UNIVERSITAT POLITÈCNICA DE VALÈNCIA

FoodUPV

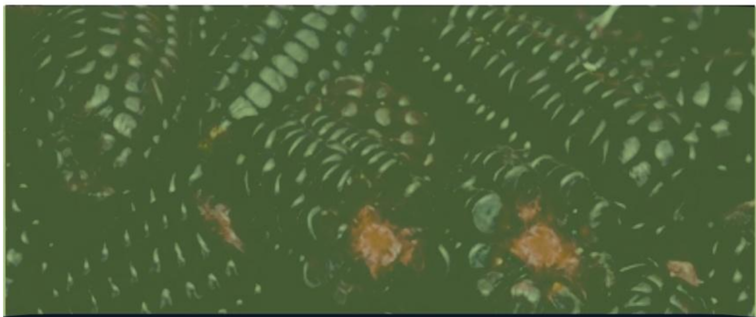

DESARROLLO DE SISTEMAS ESPECTROFOTOMÉTRICOS Y MODELIZACIÓN HÍBRIDA PARA LA MONITORIZACIÓN Y EL CONTROL DE CALIDAD DE ALIMENTOS

TESIS DOCTORAL

PRESENTADO POR:

Tony Steven Chuquizuta Trigoso

Directores:

Dr. Pedro José Fito Suñer
Dra. Marta Castro Giráldez
Dr. Wilson Manuel Castro Silupu

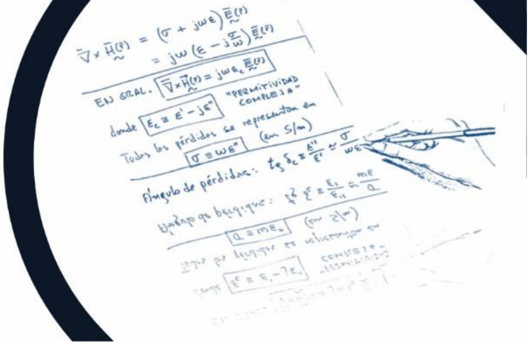

Junio 2025

TESIS DOCTORAL

Desarrollo de Sistemas Espectrofotométricos y Modelización Híbrida para la Monitorización y el Control de Calidad de Alimentos

Instituto Universitario de Ingeniería de Alimentos – FoodUPV

Universitat Politècnica de València

Presentado por:
Tony Steven Chuquizuta Trigoso

Directores:
Dr. Pedro José Fito Suñer
Dra. Marta Castro Giráldez
Dr. Wilson Manuel Castro Silupu

Junio 2025, Valencia, España

UNIVERSITAT POLITÈCNICA DE VALÈNCIA

D. PEDRO J. FITO, PROFESOR CATEDRÁTICO DE LA UNIVERSITAT POLITÈCNICA DE VALÈNCIA (ESPAÑA), PERTENECIENTE AL INSTITUTO UNIVERSITARIO DE INGENIERÍA DE ALIMENTOS FOODUPV, **Dª MARTA CASTRO GIRÁLDEZ** PROFESORA TITULAR DE LA UNIVERSITAT POLITÈCNICA DE VALÈNCIA (ESPAÑA), PERTENECIENTE AL INSTITUTO UNIVERSITARIO DE INGENIERÍA DE ALIMENTOS FOODUPV Y **D. WILSON MANUEL CASTRO SILUPU**, PROFESOR PRINCIPAL DE LA UNIVERSIDAD NACIONAL DE FRONTERA (PERÚ)

CONSIDERAN: Que la memoria titulada **DESARROLLO DE SISTEMAS ESPECTROFOTOMÉTRICOS Y MODELIZACIÓN HÍBRIDA PARA LA MONITORIZACIÓN Y EL CONTROL DE CALIDAD DE ALIMENTOS**, que presenta Don **TONY STEVEN CHUQUIZUTA TRIGOSO** para aspirar al grado de Doctor por la Universitat Politècnica de València, reúne las condiciones adecuadas para constituir su tesis doctoral, por lo que **AUTORIZAN** al interesado para su presentación.

Valencia, Junio 2025

FITO SUÑER PEDRO JOSE - 24351182R
Firmado digitalmente por FITO SUÑER PEDRO JOSE - 24351182R
Fecha: 2025.06.23 12:31:49 +02'00'

Fdo: **Pedro J. Fito Suñer**
Director de tesis

MARTA| CASTRO| GIRALDEZ
Firmado digitalmente por MARTA|CASTRO| GIRALDEZ
Fecha: 2025.06.23 12:33:50 +02'00'

Fdo: **Marta Castro Giráldez**
Directora de tesis

Firmado digitalmente por: CASTRO SILUPU Wilson Manuel FAU 20526270364 soft
Motivo: En señal de conformidad
Fecha: 23/06/2025 05:36:51-0500

Fdo: **Wilson M. Castro Silupu**
Director de tesis

“La imaginación es más importante que el conocimiento.

El conocimiento es limitado, mientras que la

imaginación abraza al mundo, impulsando

al progreso y dando a luz a la

evolución”

Albert Einstein

“*Me parece haber sido sólo un niño jugando en la*

orilla del mar, divirtiéndose y buscando una

piedra más lisa o una concha más bonita

de lo normal, mientras el gran océano

de la verdad yacía ante mis ojos

con todo por descubrir”

“*Si he visto más lejos, es porque me he parado sobre los hombros de gigantes*”

Isaac Newton

Dedicatoria

A María, mi madre, el gran amor de mi vida, por su amor incondicional, fuerza inquebrantable y sobre todo a enseñarme a luchar por nuestros sueños.

A Matthew, mi hijo, cuya existencia es mi motor y motivo en la vida.

A Nay, compañera de vida, cuyo amor, paciencia y fe me han sostenido en cada paso.

A mi familia materna por su constante apoyo motivacional y amor brindado.

Y a Joseph, Segundo, Doris, Paola, Toñi y otros amigos que han acompañado y creído en mi crecimiento, tanto personal como profesional, gracias por ser parte de este viaje.

Agradecimiento a mis mentores

A Wilson, mi gratitud profunda e infinita por haber sido el primero en acercarme al mundo de la ciencia y la tecnología. Su orientación me permitió descubrir lo que es la palabra *INGENIERÍA*, así como, la aplicación de tecnologías emergentes al control de calidad de alimentos. Gracias a su visión y confianza, pude dar mis primeros pasos en la investigación con entusiasmo y perseverancia, forjando la base de mi camino académico y científico.

A Pedro, quien supo ver en mí una vocación antes de que yo mismo la reconociera cuando me dio la oportunidad de enseñar su curso "Ingeniería del frio". Su estilo peculiar como docente universitario me inspiró a seguir el camino de la enseñanza universitaria, encontrando en ella una pasión. Además, le agradezco profundamente por enseñarme el mundo de la termodinámica irreversible, "los frikis de la termo", un campo que no solo ha enriquecido mi formación academia - científica, sino que se ha convertido en el eje central de esta tesis doctoral.

A Marta, por enseñarme que la ciencia y la ingeniería de los alimentos también puede enseñarse con pasión y paciencia. Sus clases sobre las propiedades físicas de los alimentos, en especial diagrama de estado y DSC, no solo me brindaron conocimientos fundamentales, sino que también me mostraron una forma sensible y humana de enseñar. Su estilo cercano y afectuoso dejó una huella significativa en mi manera de aprender y, más adelante, de enseñar.

Agradecimiento al Programa Nacional de Investigación Científica y de Estudios Avanzados - PROCIENCIA

Al Consejo Nacional de Ciencia, Tecnología e Innovación, a través de su Programa Nacional de Investigación Científica y de Estudios Avanzados (PROCIENCIA) – CONCYTEC, Proyectos de Investigación Básica y Aplicada [Contrato N PE501086869-2024-PROCIENCIA] "Cheese-tester: Multisensor dieléctrico para el monitoreo de maduración de queso tipo suizo", por el apoyo brindado para el cumplimiento de los objetivos de la presente tesis.

Agradecimiento al Programa Nacional de Investigación Científica y de Estudios Avanzados - PROCIENCIA

Al Consejo Nacional de Ciencia, Tecnología e Innovación, a través de su Programa Nacional de Investigación Científica y de Estudios Avanzados (PROCIENCIA) – CONCYTEC, Proyectos de Investigación Básica y Aplicada [Contrato Nº 205 - 2020 - FONDECYT] "Efecto de la bioestimulación magnética de semillas de maíz morado (*Zea Mays* L) INIA 601 sobre el rendimiento de producción y concentración de compuestos bioactivos, producidos en la región Cajamarca", por el apoyo brindado para el cumplimiento de los objetivos de la presente tesis.

Agradecimiento a la Universidad Nacional Autónoma de Chota - UNACH

Agradezco a la Universidad Nacional Autónoma de Chota - Perú, donde me desempeño como profesor asociado, por el respaldo institucional brindado, así como, el apoyo brindado mediante el uso de equipos e instalaciones de laboratorio, fundamentales para el cumplimiento de los objetivos de la presente tesis.

RESUMEN

El control de calidad, caracterización fisicoquímica y optimización de procesos de conservación de alimentos requiere actualmente del uso de herramientas analíticas avanzadas, no invasivas y adaptadas a las propiedades específicas de matrices alimentarias complejas. En esta tesis doctoral se integran diversas líneas de investigación orientadas al estudio de frutos andinos como el aguaymanto (*Physalis peruviana* L.), así como de productos cárnicos (cerdo y pescado), leguminosas y maíz morado INIA 601, a través de tecnologías emergentes como la espectrofotometría de: campos magnéticos (estático y pulsado), radiofrecuencia, microondas, termografía infrarroja e imágenes hiperespectrales, el modelado termodinámico irreversible. Estas tecnologías se agrupan en torno a tres líneas principales: (i) caracterización dieléctrica y espectral de alimentos para el análisis de calidad, (ii) modelado físico y termodinámico de procesos de conservación, y (iii) aplicación de machine learning y estímulos físicos en la monitorización y el control de alimentos. A continuación, se describen los avances más relevantes en cada una de estas áreas.

1. Caracterización dieléctrica y espectral para el análisis de calidad en alimentos

En una primera línea, se exploró el uso de espectroscopía dieléctrica en el rango de microondas para predecir propiedades fisicoquímicas clave en frutos de aguaymanto (*Physalis peruviana* L.), tales como sólidos solubles, acidez y pH. Las mediciones de la constante dieléctrica (ε’) se realizaron de 0.5 a 9 GHz a 20 °C utilizando una sonda coaxial abierta conectada a un analizador vectorial de redes. Los resultados evidenciaron que ε’ disminuye con la frecuencia, mientras que los sólidos solubles aumentaron (de 13,493 a 14,850 ºBrix), la acidez disminuyó (de 2,842 a 2,120) y el pH aumentó (de 3,468 a 3,663). Los mejores modelos de predicción se registraron a 915 MHz para sólidos solubles (R^2=0,7760), a 5800 MHz para acidez (R^2=0,4790) y a 2450 MHz para pH (R^2=0,9994), con errores de predicción aceptables, lo cual demuestra el potencial de esta técnica para el análisis de calidad interna de frutos.

De manera complementaria, la espectroscopía dieléctrica también fue aplicada al estudio de la calidad de carne de cerdo durante el periodo post-mortem. Ochenta músculos *longissimus dorsi* fueron analizados a diferentes tiempos de almacenamiento a 4 ± 1 °C, determinando propiedades dieléctricas (ε' y ε''), junto con pH, color instrumental, humedad y pérdida por goteo. Se distinguieron dos tipos de carne: RFN (Rigor Fast

Normal) y DFD (Dark, Firm and Dry), con parámetros significativamente distintos. Los modelos de predicción (PLSR) alcanzaron un R^2 de hasta 0.811 para el color L* y 0.743 para el pH en carnes DFD, lo que indica que la espectroscopía dieléctrica puede predecir moderadamente la calidad cárnica, aunque requiere mejoras para una mayor precisión en diferentes tipos de carne.

2. Modelado físico y termodinámico en procesos de conservación: secado y congelación

En una segunda línea de investigación, se abordó el estudio del secado convectivo del aguaymanto integrando un modelo termodinámico irreversible con un sistema de monitorización por termografía infrarroja. Se analizaron la cinética de secado, las isotermas de sorción y los gradientes del potencial químico del agua, evaluando el flujo de masa y energía a través de conceptos de termodinámica no lineal. Las frutas fueron sometidas a secado a 60 °C y 1,0 m/s durante 13 horas, registrando la evolución de peso, temperatura superficial y actividad de agua mediante sensores térmicos y cámaras infrarrojas. Se desarrolló un marco teórico novedoso para estimar cambios en la energía libre de Gibbs y la contribución de energía mecánica al flujo de agua, correlacionando estos parámetros con el coeficiente fenomenológico de Onsager. La termografía infrarroja permitió visualizar los patrones de deshidratación y deformación superficial de manera continua, mientras que el modelo GAB permitió ajustar las isotermas de sorción. Estos hallazgos destacan el potencial de integrar modelado termodinámico e imágenes térmicas para diseñar procesos de secado más eficientes en frutos tropicales.

En esta misma línea, se desarrolló un sistema no invasivo que combina la termografía infrarroja con la espectroscopía dieléctrica en radiofrecuencia para estudiar el proceso de congelación del aguaymanto. Esta tecnología permitió el registro simultáneo de perfiles térmicos superficiales, respuestas dieléctricas internas y cambios en la emisividad durante el congelamiento a −40 °C. Se identificaron etapas clave como el subenfriamiento, la nucleación de hielo y la vitrificación, siendo esta última registrada a −35,8 °C con un aumento de la emisividad a 0.951. Las mediciones dieléctricas evidenciaron dispersiones α y β, relacionadas con la movilidad iónica y la polarización interfacial, cuyos picos de relajación disminuyeron progresivamente durante la congelación. El análisis conjunto de estas técnicas permitió detectar transiciones de fase críticas y evaluar la movilidad del agua en tiempo real, brindando herramientas clave para mejorar los protocolos industriales de congelación y minimizar el daño estructural en frutos de alta humedad.

3. Inteligencia artificial e imagen hiperespectral en la evaluación no destructiva de alimentos

En una tercera línea, centrada en tecnologías de visión espectral y aprendizaje automático, se investigó el uso de imágenes hiperespectrales para monitorizar la hidratación de frejoles pinto. Las imágenes, adquiridas en modo reflectancia (400–800 nm), permitieron calcular el contenido de humedad durante el proceso de remojo en agua destilada. Los datos espectrales fueron ajustados mediante modelos de Peleg y sigmoidal, obteniendo un R^2 de 0.974 a 0.989 para el primero y de 0.997 a 0.999 para el segundo. El modelo sigmoidal aplicado a longitudes de onda seleccionadas (especialmente a 632 nm) mostró el mejor desempeño ($R^2 = 0.997$; RMSE = 38.3), validando el uso de imágenes hiperespectrales como herramienta no invasiva para evaluar procesos de hidratación con alta precisión.

Por otro lado, se evaluó la capacidad discriminativa de técnicas de aprendizaje profundo para identificar alteraciones inducidas por ciclos de congelación-descongelación en filetes de caballa. Se desarrolló un estudio comparativo entre redes neuronales LSTM (long short-term memory), una variante de las redes recurrentes, y redes RBNN, utilizando imágenes hiperespectrales en el rango de 400–1000 nm. Los espectros fueron procesados y optimizados mediante análisis de componentes vecinales, y los modelos fueron entrenados con validación cruzada (k=5) repetida 30 veces. Las redes LSTM superaron ampliamente a las RBNN, con una F-medida superior a 0.89 y precisión superior a 0.93. Este resultado evidencia que las técnicas de deep learning aplicadas a datos espectrales pueden ser clave para establecer sistemas de trazabilidad y monitorización en productos marinos sensibles a daños por recongelación.

4. Bioestimulación magnética para el mejoramiento de cultivos andinos

Como parte de la línea de aplicaciones físicas no convencionales en agroindustria, se evaluó el impacto de campos magnéticos sobre semillas de maíz morado (*Zea mays* L., variedad INIA 601) cultivadas en Cajamarca, Perú. Se aplicaron campos pulsados (8 mT a 30 Hz por 30 minutos) y estáticos (50 mT por 30 minutos) y se analizaron efectos sobre el desarrollo físico, rendimiento, compuestos bioactivos y actividad antioxidante. Las mazorcas tratadas presentaron mayores longitudes (16.89 y 16.53 cm frente a 15.79 cm del control). Aunque la actividad antioxidante en la bráctea fue mayor en el control (110.56 µg/mL), se observó un enriquecimiento fenólico con la bioestimulación, identificándose 14 fenoles distintos. Destacó la procyanidina B2 en bráctea y corona, mientras que epicatequina, kaempferol, vainillina y resveratrol aparecieron en menores concentraciones. Estos resultados sugieren que la estimulación magnética puede ser una estrategia viable para mejorar el perfil funcional y nutricional de cultivos tradicionales con potencial en las industrias alimentaria y farmacéutica.

ABSTRACT

Quality control, physicochemical characterization, and optimization of food preservation processes currently require the use of advanced, non-invasive analytical tools tailored to the specific properties of complex food matrices. This doctoral thesis integrates various lines of research focused on the study of Andean fruits such as goldenberry (*Physalis peruviana* L.), as well as pork, fish, legumes, and purple corn (INIA 601 variety), through emerging technologies including spectrophotometry involving magnetic fields (both static and pulsed), radiofrequency, microwaves, infrared thermography, hyperspectral imaging, and irreversible thermodynamic modeling. These technologies are grouped into three main research lines: (i) dielectric and spectral characterization of foods for quality analysis, (ii) physical and thermodynamic modeling of preservation processes, and (iii) application of machine learning and physical stimuli for food monitoring and control. The most relevant advances in each of these areas are presented below.

1. Dielectric and Spectral Characterization for Food Quality Analysis

The first research line explored the use of dielectric spectroscopy in the microwave range to predict key physicochemical properties of goldenberry (*Physalis peruviana* L.), such as soluble solids, acidity, and pH. Measurements of the dielectric constant (ε') were conducted from 0.5 to 9 GHz at 20 °C using an open-ended coaxial probe connected to a vector network analyzer. The results showed that ε' decreased with increasing frequency, while soluble solids increased (from 13.493 to 14.850 ºBrix), acidity decreased (from 2.842 to 2.120), and pH increased (from 3.468 to 3.663). The best predictive models were obtained at 915 MHz for soluble solids (R^2=0.7760), at 5800 MHz for acidity (R^2=0.4790), and at 2450 MHz for pH (R^2=0.9994), with acceptable prediction errors, demonstrating the potential of this technique for internal quality analysis of fruits.

Additionally, dielectric spectroscopy was applied to study pork quality during the post-mortem period. Eighty longissimus dorsi muscles were analyzed at different storage times at 4 ± 1 °C, measuring dielectric properties (ε' and ε''), as well as pH, instrumental color, moisture, and drip loss. Two types of meat were identified: RFN (Rigor Fast Normal) and DFD (Dark, Firm, and Dry), with significantly different quality parameters. Partial least squares regression (PLSR) models reached R^2 values of up to 0.811 for color L* and 0.743 for pH in DFD meat, indicating that dielectric spectroscopy can moderately

predict pork quality, although improvements are needed for greater accuracy across meat types.

2. Physical and Thermodynamic Modeling of Preservation Processes: Drying and Freezing

The second line of research focused on the convective drying of goldenberry by integrating an irreversible thermodynamic model with an infrared thermography monitoring system. Drying kinetics, sorption isotherms, and water chemical potential gradients were analyzed to evaluate mass and energy transfer using non-equilibrium thermodynamics. Fruits were dried at 60 °C with an air velocity of 1.0 m/s for 13 hours, and weight, surface temperature, and water activity were monitored using thermal sensors and infrared cameras. A novel theoretical framework was developed to estimate changes in Gibbs free energy and the mechanical energy contribution to water flux, correlating these parameters with the Onsager phenomenological coefficient. Infrared thermography enabled continuous visualization of dehydration patterns and surface deformation, while the GAB model was used to fit sorption isotherms. These findings highlight the potential of integrating thermodynamic modeling with thermal imaging to design more efficient drying protocols for tropical fruits.

In the same line of research, a non-invasive system was developed combining infrared thermography with radiofrequency dielectric spectroscopy to study the freezing behavior of goldenberry. This technology enabled simultaneous recording of surface thermal profiles, internal dielectric responses, and emissivity changes during freezing at −40 °C. Key freezing stages were identified, such as supercooling, ice nucleation, and vitrification—the latter observed at −35.8 °C with emissivity increasing to 0.951. Dielectric measurements revealed α- and β-dispersions related to ionic mobility and interfacial polarization, with relaxation peaks progressively decreasing during freezing. The combined analysis of these techniques allowed the detection of critical phase transitions and real-time assessment of water mobility, providing valuable tools to improve industrial freezing protocols and minimize structural damage in high-moisture fruits.

3. Artificial Intelligence and Hyperspectral Image in Non-Destructive Food Evaluation

The third research line, focused on spectral imaging and machine learning technologies, explored the use of hyperspectral imaging to monitor the hydration of pinto beans. Images were acquired in reflectance mode (400–800 nm) to calculate moisture content during soaking in distilled water. Spectral data were fitted using Peleg and sigmoidal models, obtaining R^2 values ranging from 0.974 to 0.989 for the former and from 0.997 to 0.999 for the latter. The sigmoidal model applied to selected wavelengths (especially at 632 nm) showed the best performance ($R^2 = 0.997$; RMSE = 38.3), validating hyperspectral imaging as a non-invasive tool for high-precision hydration monitoring.

In addition, the discriminative capacity of deep learning techniques was evaluated to detect changes induced by freeze-thaw cycles in mackerel fillets. A comparative study was conducted between long short-term memory (LSTM) networks—a type of recurrent neural network—and radial basis neural networks (RBNN), using hyperspectral images in the 400–1000 nm range. Spectral data were processed and optimized through neighborhood component analysis, and models were trained using 5-fold cross-validation repeated 30 times. LSTM networks significantly outperformed RBNN, achieving an F-measure above 0.89 and accuracy above 0.93. These results demonstrate that deep learning applied to spectral data can be key in establishing traceability and monitoring systems for seafood products vulnerable to quality degradation during storage.

4. Magnetic Biostimulation for the Enhancement of Andean Crops

As part of the line on unconventional physical applications in agri-food systems, the effect of magnetic fields on purple corn seeds (*Zea mays* L., INIA 601 variety) cultivated in Cajamarca, Peru, was evaluated. Pulsed (8 mT at 30 Hz for 30 minutes) and static (50 mT for 30 minutes) magnetic fields were applied, and their effects on physical development, yield, bioactive compounds, and antioxidant activity were analyzed. Treated cobs showed increased lengths (16.89 and 16.53 cm compared to 15.79 cm in the control group). Although the antioxidant activity in the bract was higher in untreated samples (110.56 μg/mL), magnetic biostimulation led to phenolic enrichment, with 14 phenolic compounds identified. Procyanidin B2 was predominant in the bract and crown, while epicatechin, kaempferol, vanillin, and resveratrol were found in lower concentrations. These findings suggest that magnetic stimulation could be a viable strategy to enhance the functional and nutritional profile of traditional crops with potential in the food and pharmaceutical industries.

RESUM

El control de qualitat, la caracterització fisicoquímica i l'optimització dels processos de conservació d'aliments requereixen actualment l'ús d'eines analítiques avançades, no invasives i adaptades a les propietats específiques de matrius alimentàries complexes. En aquesta tesi doctoral s'integren diverses línies d'investigació orientades a l'estudi de fruits andins com l'alquequengi (*Physalis peruviana* L.), així com de productes carnis (porcí i peix), lleguminoses i dacsa morada INIA 601, mitjançant tecnologies emergents com l'espectrofotometria de camps magnètics (estàtic i polsat), radiofreqüència, microones, termografia infraroja i imatges hiperespectrals, així com el modelatge termodinàmic irreversible. Aquestes tecnologies s'agrupen en tres línies principals: (i) caracterització dielèctrica i espectral d'aliments per a l'anàlisi de qualitat, (ii) modelatge físic i termodinàmic dels processos de conservació, i (iii) aplicació del machine learning i estímuls físics en la monitorització i el control d'aliments. A continuació, es descriuen els avanços més rellevants en cadascuna d'aquestes àrees.

1. Caracterització dielèctrica i espectral per a l'anàlisi de qualitat en aliments

En una primera línia, s'ha explorat l'ús de l'espectroscòpia dielèctrica en l'interval de microones per a predir propietats fisicoquímiques clau en fruits d'alquequengi (*Physalis peruviana* L.), com ara els sòlids solubles, l'acidesa i el pH. Les mesures de la constant dielèctrica (ε') es van realitzar entre 0,5 i 9 GHz a 20 °C, utilitzant una sonda coaxial oberta connectada a un analitzador vectorial de xarxes. Els resultats van mostrar que ε' disminuïa amb l'augment de la freqüència, mentre que els sòlids solubles augmentaven (de 13,493 a 14,850 ºBrix), l'acidesa disminuïa (de 2,842 a 2,120) i el pH augmentava (de 3,468 a 3,663). Els millors models de predicció es van obtindre a 915 MHz per als sòlids solubles (R^2=0,7760), a 5800 MHz per a l'acidesa (R^2=0,4790) i a 2450 MHz per al pH (R^2=0,9994), amb errors de predicció acceptables, la qual cosa demostra el potencial d'aquesta tècnica per a l'anàlisi de qualitat interna dels fruits.

De manera complementària, l'espectroscòpia dielèctrica també es va aplicar a l'estudi de la qualitat de la carn de porc durant el període post mortem. Es van analitzar huitanta músculs longissimus dorsi a diferents temps d'emmagatzematge a 4 ± 1 °C, determinant les propietats dielèctriques (ε' i ε''), juntament amb el pH, el color instrumental, la humitat i la pèrdua per degoteig. Es van distingir dos tipus de carn: RFN (Rigor Fast Normal) i DFD (Dark, Firm and Dry), amb paràmetres significativament

diferents. Els models de predicció (PLSR) van aconseguir un R^2 de fins a 0,811 per al color L* i de 0,743 per al pH en les carns DFD, la qual cosa indica que l'espectroscòpia dielèctrica pot predir de manera moderada la qualitat de la carn, tot i que es requereixen models més robusts per a millorar la precisió en diversos tipus de carn.

2. Modelatge físic i termodinàmic en processos de conservació: assecat i congelació

En una segona línia d'investigació, s'ha estudiat l'assecat convectiu de l'alquequengi mitjançant la integració d'un model termodinàmic irreversible amb un sistema de monitoratge basat en termografia infraroja. S'han analitzat la cinètica d'assecat, les isotermes de sorció i els gradients del potencial químic de l'aigua, avaluant el flux de massa i energia a través dels conceptes de la termodinàmica no lineal. Els fruits es van sotmetre a assecat a 60 °C amb una velocitat d'aire d'1,0 m/s durant 13 hores, i es va registrar l'evolució del pes, la temperatura superficial i l'activitat d'aigua mitjançant sensors tèrmics i càmeres infraroges. Es va desenvolupar un marc teòric innovador per a estimar els canvis en l'energia lliure de Gibbs i la contribució de l'energia mecànica al flux d'aigua, correlacionant aquests paràmetres amb el coeficient fenomenològic d'Onsager. La termografia infraroja va permetre visualitzar de manera contínua els patrons de deshidratació i la deformació superficial, mentre que el model GAB es va utilitzar per a ajustar les isotermes de sorció. Aquests resultats evidencien el potencial d'integrar el modelatge termodinàmic amb tècniques òptiques per a dissenyar processos d'assecat més eficients en fruits tropicals.

En aquesta mateixa línia, es va desenvolupar un sistema no invasiu que combina la termografia infraroja amb l'espectroscòpia dielèctrica en radiofreqüència per a estudiar el procés de congelació de l'alquequengi. Aquesta tecnologia va permetre el registre simultani dels perfils tèrmics superficials, les respostes dielèctriques internes i els canvis en l'emissivitat durant la congelació a −40 °C. Es van identificar fases clau com el subrefredament, la nucleació del gel i la vitrificació, aquesta darrera observada a −35,8 °C amb un augment de l'emissivitat fins a 0,951. Les mesures dielèctriques van revelar dispersions α i β, relacionades amb la mobilitat iònica i la polarització interfacial, amb freqüències de relaxació que disminuïen a mesura que avançava la congelació. L'anàlisi conjunta d'aquestes tècniques va permetre detectar transicions de fase crítiques i avaluar la mobilitat de l'aigua en temps real, proporcionant eines útils per a optimitzar els protocols industrials de congelació i reduir els danys estructurals en fruits d'elevada humitat.

3. Intel·ligència artificial i imatge hiperespectral en l'avaluació no destructiva d'aliments

En una tercera línia, centrada en tecnologies de visió espectral i aprenentatge automàtic, es va investigar l'ús d'imatges hiperespectrals per a monitorar la hidratació de fesols pinto. Les imatges, obtingudes en mode reflectància (400–800 nm), van permetre calcular el contingut d'humitat durant el procés de remull en aigua destil·lada. Les dades espectrals es van ajustar mitjançant models de Peleg i sigmoïdal, obtenint un R^2 de 0,974 a 0,989 per al primer i de 0,997 a 0,999 per al segon. El model sigmoïdal aplicat a longituds d'ona seleccionades (especialment a 632 nm) va mostrar el millor comportament ($R^2 = 0{,}997$; RMSE = 38,3), validant l'ús de la imatge hiperespectral com a eina no invasiva per a avaluar els processos de hidratació amb alta precisió.

D'altra banda, es va avaluar la capacitat discriminant de tècniques d'aprenentatge profund per a identificar alteracions causades per cicles de congelació-descongelació en filets de cavalla. Es va realitzar un estudi comparatiu entre xarxes neuronals LSTM (long short-term memory), una variant de les xarxes neuronals recurrents, i xarxes RBNN, utilitzant imatges hiperespectrals en l'interval de 400–1000 nm. Els espectres es van processar i optimitzar mitjançant anàlisi de components veïns, i els models es van entrenar amb validació creuada (k=5), repetida 30 vegades. Les xarxes LSTM van superar àmpliament les RBNN, amb una F-mesura superior a 0,89 i una precisió superior a 0,93. Aquest resultat evidencia que les tècniques de deep learning aplicades a dades espectrals poden ser clau per a establir sistemes de traçabilitat i monitoratge en productes marins sensibles als danys per recongelació.

4. Bioestimulació magnètica per a la millora de cultius andins

Com a part de la línia d'aplicacions físiques no convencionals en agroindústria, es va avaluar l'impacte de camps magnètics sobre llavors de dacsa morada (*Zea mays* L., varietat INIA 601) cultivades a Cajamarca, Perú. Es van aplicar camps polsats (8 mT a 30 Hz durant 30 minuts) i camps estàtics (50 mT durant 30 minuts), i es van analitzar els efectes sobre el desenvolupament físic, el rendiment, els compostos bioactius i l'activitat antioxidant. Les panotxes tractades van presentar longituds majors (16,89 i 16,53 cm) en comparació amb les mostres de control (15,79 cm). Tot i que l'activitat antioxidant en la bràctea va ser superior en les mostres no tractades (110,56 µg/mL), la bioestimulació magnètica va afavorir l'enriquiment fenòlic, identificant-se catorze compostos, entre els quals destaca la procyanidina B2 en bràctea i corona, mentre que epicatequina, kaempferol, vainillina i resveratrol es van detectar en menors concentracions. Aquests resultats suggereixen que l'estimulació magnètica pot ser una estratègia viable per a millorar el perfil funcional i nutricional dels cultius tradicionals amb potencial en les indústries alimentària i farmacèutica.

Índice

I. Introducción

La seguridad y el control de la calidad en la industria agroalimentaria es un objetivo primordial, con el fin de cumplir con normativas internacionales y acceder a mercados internacionales, así como, mantener altos estándares de calidad e inocuidad en los procesos de transformación agroalimentaria (Hu et al., 2019; Okpala & Korzeniowska, 2023). No obstante, la mayoría de las empresas pequeñas dedicadas a la agroindustria aun vienen realizando su monitorización y control de calidad a través de métodos de análisis físicos, químicos y bioquímicos, que si bien, son precisos, reproducibles en laboratorio y avalados por la AOAC, también presentan las siguientes desventajas: suelen ser destructivos, lentos, costosos y laboriosos (Dale et al., 2013; Huang et al., 2014a; Kumari et al., 2025; Zhu et al., 2020).

Con el avance tecnológico y científico, diversos esfuerzos se han venido dando en favor del desarrollo de técnicas fotónicas de baja energía, basadas en el grado de interacción de especies químicas con los fotones a lo largo del espectro electromagnético (desde la radiofrecuencia hasta el infrarrojo) (Chandra Roychoudhuri, 2017). Estas técnicas fotónicas no destructivas permiten monitorizar productos agroalimentarios de forma continua y en tiempo real sin dañar las muestras, lo que resulta ideal para control de procesos y trazabilidad (El Khaled et al., 2016; Elmasry et al., 2012; Liu et al., 2014; Nelson, 2005). Por ejemplo, la imagen hiperespectral en el espectro visible e infrarrojo cercano se ha consolidado como un método óptico no invasivo capaz de detectar tempranamente defectos, contaminantes o atributos de calidad en alimentos que pasarían inadvertidos por métodos convencionales (Huang et al., 2014a, 2014b; Liu et al., 2014; Zhu et al., 2020). La fotónica de baja frecuencia (radiofrecuencias, microondas e infrarrojos) combinada con modelos físicos, matemáticos y estadísticos adecuados permiten implementar sensores modernos para mejorar la calidad de los productos agroalimentarios de manera rápida y en línea (Trabelsi & Nelson, 2016; Traffano-Schiffo, Castro-Giraldez, Colom, et al., 2018a; Traffano-Schiffo, Chuquizuta, et al., 2021; Ye et al., 2023).

La presente tesis doctoral se enfoca principalmente en el desarrollo de sistemas espectrofotónicos (basados en radiación electromagnética de baja energía), así como, el uso de la modelización híbrida (modelos físicos, termodinámicos y machine learning) para la monitorización y el control de calidad de productos agroalimentarios, tales como: carne de cerdo, pescado, frejoles (alubias), aguaymanto y maíz morado. En particular, se estudiará el uso de espectrofotometría de radiofrecuencia, microondas, infrarroja e imágenes hiperespectrales, integradas con modelos de termodinámica irreversible y algoritmos quimiométricos. Este enfoque combinado busca aprovechar la sensibilidad de las técnicas fotónicas para detectar cambios fisicoquímicos en los alimentos, junto con la capacidad predictiva de modelos híbridos para interpretar esos datos y estimar parámetros de calidad relevantes. Asimismo, se estudiará la aplicación de campos magnéticos (estático y pulsado) en la mejora de las características fisiológicas y los compuestos bioactivos del maíz morado INIA 601.

Esta tesis doctoral se basa en la necesidad de la industria agroalimentaria de contar con sensores miniaturizados no invasivos y de fácil uso y acceso, los cuales permitan asegurar la calidad y seguridad de los productos de forma más eficiente. La integración de estas técnicas fotónicas ofrecen un análisis rápido, no destructivo y objetivo. Integrar estas técnicas con modelos físicos, matemáticos y estadísticos robustos permitirán no sólo monitorizar procesos en tiempo real, sino también comprender y predecir los fenómenos que ocurren en los alimentos durante diferentes operaciones unitarias. En los últimos años, los sensores que trabajan a baja frecuencia y con principios fotónicos han demostrado con éxito su aplicación en: agricultura (Nelson, 2005; Trabelsi & Nelson, 2016), operaciones unitarias (secado, congelación y osmodeshidratación) (Castro-Giráldez et al., 2014; Cuibus et al., 2014; Talens et al., 2016a, 2016b; Traffano-Schiffo et al., 2014), productos de la pesca (J.-H. Cheng et al., 2015) y legumbres (Chuquizuta et al., 2024). Esto demuestra el potencial de la fotónica para innovar el control de calidad alimentario. Sin embargo, para explotar al máximo estas tecnologías, es imprescindible el desarrollo de nuevos métodos de análisis de datos a partir de las mediciones espectrales sobre el estado del producto (humedad, actividad de agua, composición, etc.). De allí surge la motivación por investigar modelos híbridos que combinen las leyes de la física con la flexibilidad de las técnicas quimiométricas, con el fin de adaptar el modelo a datos complejos.

1.1. Justificación

La monitorización y el control de calidad en la industria agroalimentaria cada vez se enfrenta a desafíos crecientes debido a la demanda de productos más seguros, de mayor vida útil y con cualidades constantes, debido a la evolución sensorial de los consumidores (Huang et al., 2014a; Okpala & Korzeniowska, 2023). La aplicación de métodos tradicionales de análisis de calidad, como: ensayos cromatográficos, ensayos químicos – físicos y pruebas sensoriales, si bien son efectivos en laboratorio, resultan poco prácticos para inspección en línea durante la producción, por su carácter destructivo y lenta disponibilidad de resultados (Elmasry et al., 2012; Hassoun et al., 2023; Liu et al., 2014).

En este sentido, las técnicas fotónicas de baja energía (ópticas y electromagnéticas) aparece como una alternativa prometedora con soluciones innovadoras. Estas técnicas permiten obtener información interna y externa del alimento mediante interacciones de campos electromagnéticos con la materia, sin contacto físico y sin alterar la integridad del producto (Castro et al., 2018; El Khaled et al., 2016; W. Guo et al., 2015). Por ejemplo, la termografía infrarroja puede medir distribuciones de temperatura superficial de un producto en tiempo real (Harrap et al., 2018; Poirier-Pocovi et al., 2020; Shammi et al., 2023; Usamentiaga et al., 2014), destacando su potencial para la monitorización de procesos de secado y congelación de alimentos (Tomas-Egea et al., 2021, 2022; Traffano-Schiffo et al., 2014). Asimismo, la espectrofotometría dieléctrica de radiofrecuencia puede monitorizar cambios en las propiedades dieléctricas asociados a los cambios fisicoquímicas y transiciones de fase del agua en alimentos (congelación, deshidratación, etc.) (Tomas-Egea et al., 2019, 2022; Traffano-Schiffo, Castro-Giraldez, Colom, et al., 2018c, 2018a), y la espectroscopía de microondas es sensible al contenido de agua y estructura celular debido a la orientación de dipolos como el agua bajo campos de alta frecuencia (Castro-Giráldez, Aristoy, et al., 2010; Castro-Giráldez, Fito, Chenoll, et al., 2010; Talens et al., 2016b). De igual manera, la imagen hiperespectral combina la visión artificial con la espectroscopía, proporcionando para cada punto del alimento un espectro que refleja su composición; así es posible detectar zonas con distinto contenido de humedad, grasa, deterioro o contaminación que serían invisibles al ojo humano (Castro, Tene, et al., 2024; Tirado-Kulieva et al., 2024a; Vásquez et al., 2018a; Vera et al., 2025; Yoplac et al., 2019).

El uso conjunto de estas técnicas fotónicas acopladas a modelos físicos, matemáticos y estadísticos apropiados, amplía su alcance, permitiendo relacionar parámetros fisicoquímicos, estado de agregación, composición y estructura del alimento a partir de perfiles espectrales captados por los sensores fotónicos. Esta sinergia promete sistemas predictivos más robustos y precisos. En pocas palabras, los sistemas espectrofotométricos proveen una huella espectral instantánea y no destructiva del alimento, mientras que el modelo híbrido actúa como cerebro para monitorear y controlar la calidad del producto, e incluso predecir su comportamiento.

La justificación de la investigación radica entonces en que, al combinar sensores fotónicos avanzados con modelos híbridos, se podrá lograr una monitorización y control de los procesos agroalimentarios. Esto implica, por un lado, optimizar procesos en tiempo real (ajustando condiciones de secado, hidratación, congelación, etc. con base en mediciones en línea) y garantizar la seguridad alimentaria (mediante detección temprana de ruptura de la cadena de frio, predicción de parámetros de calidad y la bioestimulación de semillas para la obtención de rendimiento y compuesto biactivos altos). Por otro lado, se contribuye al avance científico al profundizar en la comprensión de cómo la radiación electromagnética de baja energía interactúa con sistemas biológicos complejos (los alimentos) y cómo estas respuestas pueden modelizarse para reflejar fenómenos de transferencia de masa y calor.

1.2. Espectro electromagnético

El fotón, o cuanto de un campo electromagnético, es una partícula elemental portadora de la interacción electromagnética, es decir es un bossón tipo gauge, sin masa, sin carga y con espín 1, con capacidad nula para almacenar energía en sus movimientos de translación o rotación, por lo que su nivel de vibración es proporcional a su nivel de energía (Raymer & Polakos, 2023). Dicha vibración conforma el espectro electromagnético o rango completo de vibración de los fotones. La teoría más moderna que describe el electromagnetismo es la electrodinámica cuántica que describe a cualquier partícula como una excitación cuántica de un campo general, siendo para el fotón el campo electromagnético. Las interacciones electromagnéticas que ejercen los fotones sobre su entorno son también denominadas radiación electromagnética. Esta radiación o, flujo de fotones, está compuesta por partículas vibrantes o cuantos excitados del campo electromagnético, que se propagan por el espacio, desde el rango de la radiofrecuencia hasta los rayos gamma (Feldman et al., 2015) (Figura1). El espectro electromagnético abarca un continuo de radiaciones clasificadas según su frecuencia (ν) o inversamente su longitud de onda (λ), relacionadas por la velocidad de la luz en el vacío (Ecuación 1)

$$c = \lambda\nu \tag{1}$$

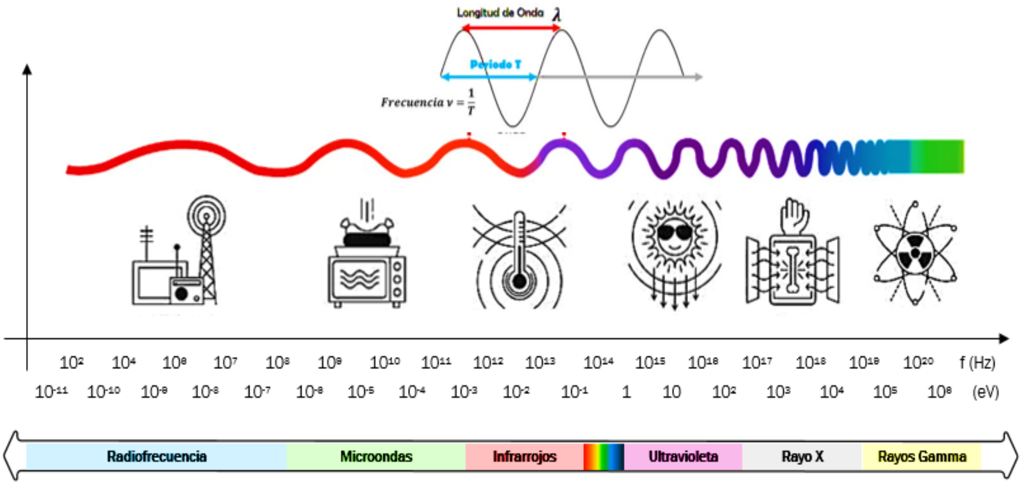

Figura 1. Espectro electromagnético completo, que muestra las distintas regiones de radiación y su clasificación en función de la frecuencia.

Nota. Adaptado de "Espectro electromagnético" por IpStore, 2024 (https://l1nq.com/Ojb68); "Electromagnetic spectrum" por 123RF, s.f. (https://l1nq.com/SedR5); "Espectro electromagnetico" por Paredes. M., 2019 (https://l1nq.com/hfNWP).

Las interacciones electromagnéticas según la electrodinámica cuántica son los intercambios de fotones entre partículas cargadas, siendo la más importante entre electrones. La radiación electromagnética al interaccionar con un elemento, cargado o no, puede sufrir absorción, reflexión o transmisión, dependiendo del grado de interacción entre la radiación y la naturaleza de las moléculas que conformen el elemento (Figura 2), siendo el sumatorio de los efectos igual a 1.

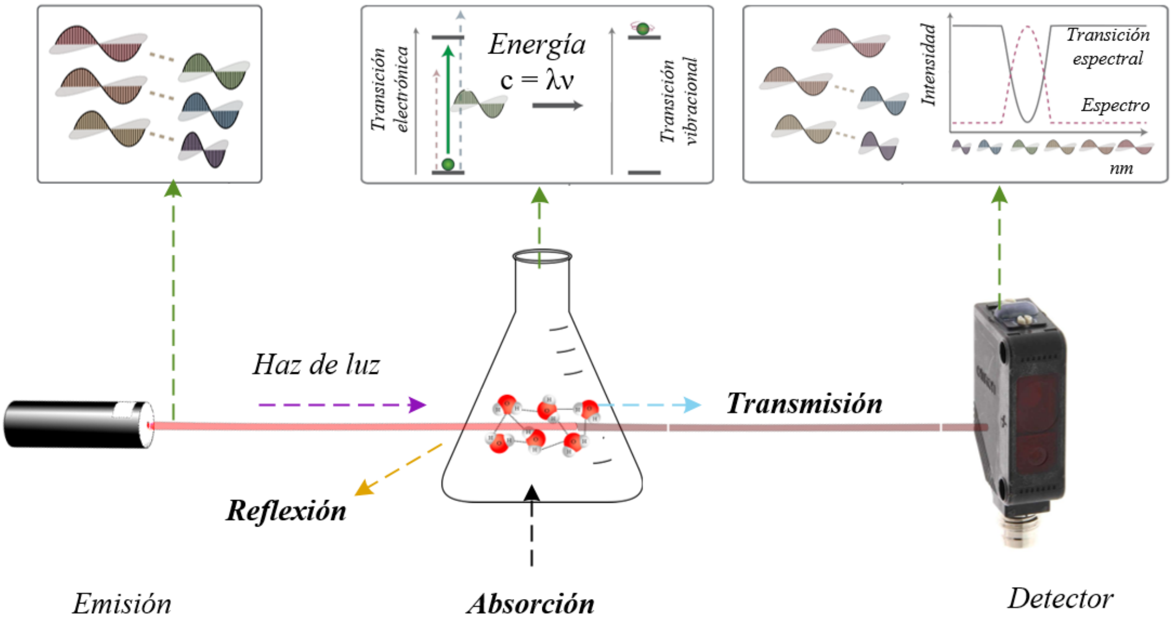

Figura 2. Fenómenos de reflexión, absorción y transmisión de la luz.

Nota. Adaptado de "Espectro de absorción" por Wikipedia, 2024 (https://es.wikipedia.org/wiki/Espectro_de_absorci%C3%B3n).

1.3. Espectrofotometría de baja energía

1.3.1. Fotónica

La fotónica es el área de la ingeniería que aprovecha la información que ofrece un flujo de fotones (cuantos del campo electromagnético o radiación electromagnética) inducido o natural después de pasar por un objeto (a través o reflejándose).

Debido a su naturaleza vibrante, el fotón presenta una longitud de onda que define su nivel de energía de partida. Sin embargo, el fotón puede interaccionar con otras partículas (Efecto Scatering en baja energía y efecto Compton en alta energía) y perder parte de su energía, bajando su frecuencia y aumentando su longitud de onda. Lo mismo ocurre a la inversa, como ocurre en la dispersión inversa de Compton en el que un electrón puede aumentar la energía de un fotón o en el efecto Doppler donde la propia velocidad del fotón puede generar acumulación de energía en el sentido de avance de la radiación (Pearsall, 2020). Estas interacciones electrón-fotón pueden ser inducidas por un dispositivo para determinar variables de estado como la temperatura, cuantificar especies químicas o para predecir propiedades físicas, siendo la base de la técnica denominada fotónica.

Dado que la energía (E) de un fotón es un cuanto de excitación del espectro electromagnético, su energía es directamente proporcional a la frecuencia, de acuerdo con la relación de Planck-Einstein (Ecuación 2):

$$E = h \times f \tag{2}$$

Dónde: E es la energía del fotón (en julios), h es la constante de Planck, $h \approx 6.626 \times 10^{-34}$ J·s, f es la frecuencia de la radiación.

Alternativamente, dado que la frecuencia está relacionada con la longitud de onda λ por la relación de la Ecuación 1, la energía del fotón también puede expresarse como la Ecuación 3:

$$E = \frac{hc}{\lambda} \tag{3}$$

Respecto a la electrodinámica cuántica (QED), la ecuación fundamental que rige el comportamiento de una partícula, adaptada al fotón es obtenida mediante la ecuación 4:

$$L_{QED} = \bar{\psi}\left(\gamma^{\mu} \cdot D_{\mu} i - m\right) - \frac{1}{4} F_{\mu\upsilon} \tag{4}$$

Donde L_{QED} es el lagrangiano que describe el comportamiento, $\bar{\psi}$ que representa el campo del electrón productor del fotón (espinor de Dirac), ($\gamma^{\mu} \cdot D_{\mu} i - m$) representa el campo cuántico del fotón, y $F_{\mu\upsilon}$que representa el campo electromagnético (Peskin, 2018)

Y la propagación de un fotón se calcula a partir de la Ecuación 5 (Schwartz, 2013):

$$D^{\mu\upsilon} = \frac{-g^{\mu\upsilon} i}{\varepsilon i} \tag{5}$$

Donde $D^{\mu\upsilon}$ es la propagación del fotón, $g^{\mu\upsilon}$es la métrica de Minkowski y el parámetro ε, es un parámetro cuantico que asegura que los efectos cuánticos respeten la causalidad.

Pese a que la fotónica moderna se rige por la electrodinámica cuántica, integrada en el modelo estándar de partícula, capaz de describir tres interacciones fundamentales, las electromagnéticas, las débiles y las fuertes, hoy en día a nivel de ingeniería se siguen usando modelos de la física clásica por su facilidad de uso y por su versatilidad en los modelos de monitorización y control. Si bien a nivel particular no son estrictamente correctos, a nivel macroscópico permiten un nivel de aproximación a la realidad suficiente, para ser de gran utilidad para la industria.

En esta simplificación de la mecánica cuántica a la física más clásica es importante hacer una diferenciación de los modelos que se utilizan en ingeniería, ya que son distintos según el rango en el que se analice el electromagnetismo. Las interacciones de los fotones con la materia a bajas frecuencias (como en radiofrecuencia y microondas), predominan los efectos ondulatorios, donde el flujo de fotones actúan como una serie de ondas electromagnéticas extendidas que induce polarizaciones e inducción en las moléculas cargadas. En cambio, a frecuencias más altas (como en el infrarrojo, visible o ultravioleta), el fotón se comporta de forma corpuscular, como un paquete discreto de energía capaz de excitar electrones o romper enlaces químicos. Así, a bajas energías domina el carácter ondulatorio, mientras que a altas energías se manifiesta su naturaleza cuántica y localizada (Saleh & Teich, 2019).

Un ejemplo de la utilización práctica de la física clásica en un tramo donde predomina el efecto corpuscular es la modelización de cuerpos radiantes en el tramo del espectro térmico (infrarrojo, visible y ultravioleta), entendiendo como radiación a un flujo de fotones incidiendo sobre una materia determinada. Todo cuerpo con una temperatura superior a 0 K, emite radiación procedente de los electrones que conforman los orbitales atómicos, que se encuentran en un continuo proceso de excitación/relajación, causado a su vez por la constante recepción de radiación. Esta radiación será proporcional a la energía cinética de estos electrones, es decir, a la temperatura la materia. En este tramo del espectro se puede definir un cuerpo negro, como un material ideal que absorbe toda la energía de radiación que recibe ($\alpha = 1$, por lo tanto $\rho = \tau = 0$), al no reflejar radiación del entorno, un cuerpo negro radiará dependiendo únicamente de su temperatura. Este fenómeno fue descrito por la ley de Planck, la cual describe un parámetro ε, denominado emisividad, que viene descrito como la relación entre la radiación absorbida y la radiación recibida (Ibarz & Barbosa-Canovas, 2002; McClelland & Mankin, 2018). Simplificando la ley de Plank, suponiendo constantes algunas variables atómicas, se obtiene la Ley de Stefan-Boltzmann, que permite calcular la energía absorbida por un cuerpo a partir de la energía emitida por un cuerpo que se encuentra radiando en frente del mismo, expresándose como (Ecuación 6):

$$E = \varepsilon \sigma T^4 \tag{6}$$

Donde: E es la energía radiada (W/m^2), la temperatura absoluta de la superficie emisora, σ es la constante de Stefan-Boltzmann (5.67×10^{-8} W/m^2K^4) y ε la emisividad del material (entre 0 y 1). Esta ecuación es fundamental para la termografía infrarroja, ya que permite convertir la energía captada por la cámara en una estimación de la temperatura superficial del objeto observado, corrigiendo por la emisividad del material (Tomás Egea, 2022; Traffano Schiffo, 2017).

Otra ley de la física clásica, muy útil en la fotónica aplicada es la Ley de Beer-Lambert, relevante sobre todo en espectroscopía en el rango de visible e infrarrojo. Esta ley relaciona la intensidad de radiación transmitida a través de un medio absorbente con la concentración de las especies absorbentes en el medio (Castro Silupu, 2016; Gowen et al., 2007; Huang et al., 2014a). En su forma habitual se expresa mediante la Ecuación 7:

$$A = \epsilon \iota c = -log_{10} \left(I_{saliente} / I_{incidente} \right) \tag{7}$$

Donde: A es la absorbancia, ϵ es el coeficiente de absortividad molar (L/(mol·cm)), ι la longitud de trayectoria de la luz a través del medio (cm) y c la concentración de la especie absorbente (mol/L) . De acuerdo con esta ley, la transmitancia disminuye exponencialmente al aumentar la concentración o la distancia recorrida por la luz. La Ley de Beer-Lambert es la base para cuantificar componentes en alimentos mediante espectroscopía NIR-VIS.

Asimismo, la reflectancia espectral es una magnitud adimensional que describe la proporción de la radiación incidente sobre una superficie que es reflejada por ésta en función de la longitud de onda (Elmasry et al., 2012). En aplicaciones espectroscópicas, como las imágenes hiperespectrales, la reflectancia se expresa generalmente como una función continua (Ecuación 8):

$$R(\lambda) = I_r(\lambda)/I_0(\lambda) \tag{8}$$

Donde: $R(\lambda)$ es la reflectancia espectral a la longitud de onda λ; $I_r(\lambda)$ es la intensidad de la luz reflejada por el objeto; $I_0(\lambda)$ es la intensidad de la luz (radiación) incidente (normalizada o referenciada)

En el caso de las técnicas de baja energía, en el tramo del espectro de radiofrecuencia y microondas, donde predominan las interacciones ondulatorias, de polarización e inducción, interesa especialmente la interacción con los dipolos dieléctricos y especies químicas cargadas en los alimentos. Los alimentos son sistemas biológicos con alto contenido de agua (molécula polar) y con iones disueltos (sales, electrolitos, entre otros), además de macromoléculas con cargas (proteínas, polisacáridos). Bajo la influencia de un campo electromagnético, estos componentes responden almacenando energía en forma de polarización eléctrica o disipándola en forma de calor (Velazquez Varela, 2014). Una simplificación de la física clásica para determinar el efecto del electromagnetismo con la materia, en este tramo del espectro son las relaciones de Maxwell. A continuación, se muestran las relaciones de Maxwell (9 y 10 - Ley de Gauss, 11 – Ley de Faraday y 12 – Ampere - Maxwell), fundamentales para entender la interacción de la radiación con la materia.

$$\nabla \cdot \vec{\boldsymbol{E}} = \rho/\varepsilon_0 \tag{9}$$

$$\nabla \cdot \vec{\boldsymbol{B}} = 0 \tag{10}$$

$$\nabla \times \vec{\boldsymbol{E}} = -\frac{\partial \vec{\boldsymbol{B}}}{\partial t} \tag{11}$$

$$\nabla \times \vec{\boldsymbol{B}} = \mu_0 \vec{\boldsymbol{J}} + \mu_0 \varepsilon_0 \frac{\partial \vec{\boldsymbol{E}}}{\partial t} \tag{12}$$

Donde: $\vec{\boldsymbol{B}}$, es el campo magnético; $\vec{\boldsymbol{E}}$, es el campo eléctrico; ρ, densidad de carga eléctrica; $\vec{\boldsymbol{J}}$, densidad de corriente; ε_0, permitividad del vacío; μ_0, permeabilidad del vacío.

Estas relaciones explican las interacciones electromagnéticas, y su efecto sobre partículas cargadas. Estas relaciones utilizan dos propiedades vectoriales para definir los efectos eléctricos o de campo eléctrico (permitividad) y para definir los efectos magnéticos o de campo magnético (permeabilidad), pudiendo potenciarse el efecto de uno u otro cambiando la geometría del equipo inductor del campo.

Cuando se trabaja con equipos inductores de señal paralelos o perpendiculares predomina el efecto eléctrico, por lo que se puede caracterizar esta respuesta mediante la permitividad dieléctrica compleja (ε_r) del material, definida como (Ecuación 13):

$$\varepsilon_r = \varepsilon' + j\varepsilon'' \tag{13}$$

Donde: ε' es la constante dieléctrica y ε'' es el factor de pérdidas dieléctricas.

Mientras que, si se utiliza un sistema circular, como una bobina, donde es posible eliminar el efecto eléctrico, se obtiene un efecto magnético, caracterizado por la permeabilidad magnética (μ_r).

1.3.2. Técnicas fotónicas

La fotónica de baja energía comprende aquellas técnicas basadas en la interacción de radiación electromagnética (no ionizante) con la materia. Estas técnicas fotónicas de baja energía están comprendidas desde campo magnético (estáticos y pulsado) de muy baja frecuencia, radiofrecuencia, microondas, infrarrojo lejano y visible - infrarrojo cercano (Figura 1). En estas regiones espectrales, la interacción fotónica con la materia se manifiesta a través de: polarizaciones eléctricas, rotación de dipolos, vibraciones moleculares, emisión térmica, entre otras, proporcionando información sobre las propiedades físicas y químicas del material (Pearsall, 2020; Raymer & Polakos, 2023).

1.3.2.1. Campo magnético o efecto magnético a baja frecuencia.

El campo magnético constituye una de las manifestaciones fundamentales del electromagnetismo. Se define como la región del espacio en la que una partícula cargada en movimiento experimenta una fuerza. Este campo es generado por cargas eléctricas en movimiento o por corrientes eléctricas, y su acción puede medirse a través de la fuerza que ejerce sobre otras cargas móviles. Se representa mediante el vector **B**, cuyas unidades en el Sistema Internacional son los teslas (T) (Greenebaum & Barnes, 2018). Asimismo, se describe mediante las Ecuaciones de Maxwell descritas en el apartado anterior.

Estas relaciones explican la interacción de campos eléctricos y magnéticos, y su efecto sobre partículas cargadas. Los campos magnéticos tienen alta capacidad de penetración en tejidos biológicos, lo que los hace útiles en aplicaciones médicas y alimentarias (Barnes & Greenebaum, 2007).

1.3.2.1.1. Tipos de campos magnéticos

Los campos magnéticos pueden ser estáticos (CME) o pulsado (CMP), generados por corriente eléctrica continua (0 Hz) o alterna (Figura 3). Las principales fuentes de estos campos son las corrientes eléctricas o generado por imanes, basado en la Ley de Ampere o Ley de Biot-Savart (Miñano et al., 2020; S. Wang et al., 2024). Dependiendo de cómo varía el campo magnético en el tiempo, este puede clasificarse como: campo magnético estático, campo alterno de baja frecuencia (AC de baja frecuencia) o campo pulsado (caracterizado por pulsos transitorios) (S. Wang et al., 2024). Asimismo, según la densidad de flujo magnético, los CME se clasifican como súper débiles (100 nT a 0,5 mT), débiles (<1 mT), moderados (1 mT a 1 T), fuertes (1 a 5 T) y ultra fuertes (>5 T) (Miñano et al., 2020). Con respecto a los EMF y PMF, los factores considerados son la densidad de flujo magnético, la frecuencia, la forma de onda, el tiempo de exposición y la polaridad (Greenebaum & Barnes, 2018). En función de la frecuencia, se consideran como frecuencia extremadamente baja (0 a 300 Hz), frecuencia intermedia (300 Hz a 1 MHz), radiofrecuencia (1 MHz a 500 MHz), frecuencia de microondas (500 MHz a 10 GHz) y alta frecuencia (>10 GHz) (Greenebaum & Barnes, 2018; Grigelmo-Miguel et al., 2010)

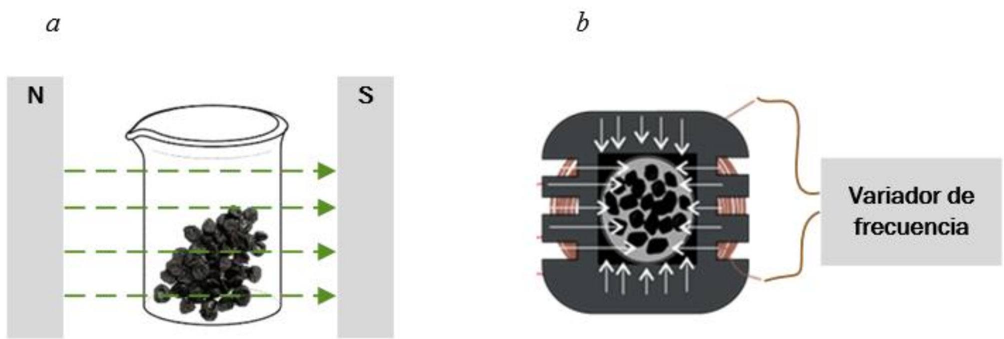

Figura 3. Aplicación de campo magnético a alimentos: a) estático y b) pulsado.

Nota. Adaptado de Chuquizuta et al. (2025).

1.3.2.1.2. Interacción del campo magnético con tejidos biológicos

La interacción de los campos magnéticos con sistemas biológicos depende fuertemente de la frecuencia y magnitud del campo, determinando los mecanismos físicos involucrados. En campos estáticos (0 Hz), no se inducen corrientes eléctricas en tejidos, pero el campo puede ejercer fuerzas directamente sobre objetos magnetizados o partículas dentro del organismo (Greenebaum & Barnes, 2018). En los campos de alta frecuencia (radiofrecuencia y microondas), la interacción dominante con los tejidos es el acoplamiento dieléctrico que resulta en calentamiento. Las moléculas polares (como el agua) oscilan al ritmo del campo alterno, y las corrientes de desplazamiento a través de tejidos conducen a disipación de energía (L. Guo et al., 2022). En frecuencias de microondas, prácticamente toda la energía absorbida en el cuerpo se convierte en calor, pudiendo elevar la temperatura tisular (S. Wang et al., 2024).

1.3.2.1.3. Aplicaciones del campo magnético en la industria alimentaria

En los últimos años, los campos magnéticos (estáticos o pulsado) vienen siendo considerados como una tecnología emergente no térmica, siendo aplicados en procesos como: congelación, inactivación de microorganismos, fermentación, secado, entre otros. Sin embargo, existen escasos estudios de la aplicación de campos magnéticos en procesos de germinación de semillas, véase la Tabla 1.

Tabla 1. Aplicación de campos magnéticos a la germinación de semillas

Muestra	Tratamiento	Resultado	Autor
Calotropis procera	2 mT y 5 días	Aumenta el rendimiento de la germinación de las semillas se intensifica con la exposición continua a campo magnético.	(Bezerra et al., 2023)
Maíz y soja	200 mT durante 1 h	Mejora los parámetros relacionados con la germinación y también las actividades de α-amilasa y proteasa.	(Kataria et al., 2017)

Habas	30 y 85 mT durante 15 s	Aumenta considerablemente la cantidad de ácido indol-3-acético y ácido giberélico en las semillas en germinación.	(Podleśna et al., 2019)
Lechuga	0.44, 0.77 y 1 T	Mejora el crecimiento, los componentes bioactivos y el rendimiento de la lechuga.	(Abdel Latef et al., 2020)
Trigo	10 y 15 mT por 15 min	Mejora el rendimiento del cultivo	(Hussain et al., 2020)
Maíz morado	8 mT a 30 Hz y 50 mT, ambos por 30 min	Mejora las propiedades nutricionales y antioxidantes del cultivo.	(Chuquizuta et al., 2025)

1.3.2.2. Espectrofotometría dieléctrica

Tal y como se ha explicado en el apartado anterior se parte de las relaciones de Maxwell (Ecuación 9 - 12) para poder describir el efecto de los campos magnéticos y/o eléctricos sobre un material. La aproximación de las relaciones de Maxwell a la teoría cuántica fue formulada por Paul Dirac en 1928, formulando el mecanismo relativista del electrón (principal productor de fotones), que al unificarlo con el principio de gauge (concepto fundamental de bossón), conformaría la electrodinámica cuántica, demostrando que la aproximación de las relaciones de maxwell para este tramo del espectro, donde los fenómenos son ondulatorios, es exacta. Para materiales dieléctricos, en especial materiales biológico como los alimentos, el flujo de fotones se ve atenuado por la resistencia del material, lo que implica una absorción parcial de la energía en la orientación de cargas. Por tanto, se origina un desplazamiento del campo eléctrico y/o magnético (Traffano Schiffo, 2017), véase la Figura 4. Estos fenómenos electromagnéticos de desplazamiento puedes ser modelizados mediante las Ecuaciones 14 y 15.

$$\overline{D} = \varepsilon^* \cdot \varepsilon_0 \cdot E = (\varepsilon' + j\varepsilon'') \cdot \varepsilon_0 \cdot \vec{\boldsymbol{E}} \tag{14}$$

$$\bar{B} = \mu^* \cdot \mu_0 \cdot E = (\mu' + j\mu'') \cdot \mu_0 \cdot \vec{\boldsymbol{B}} \tag{15}$$

Donde: $\bar{D}$ y $\bar{B}$, son desplazamiento del campo eléctrico y magnético, respectivamente; ε^*, es la permitividad vectorial del sistema (F/m), representado la respuesta de un medio ante el efecto del campo eléctrico; μ^*, es la permeabilidad vectorial del sistema (H/m), representado la respuesta de un medio ante el efecto del campo magnético.

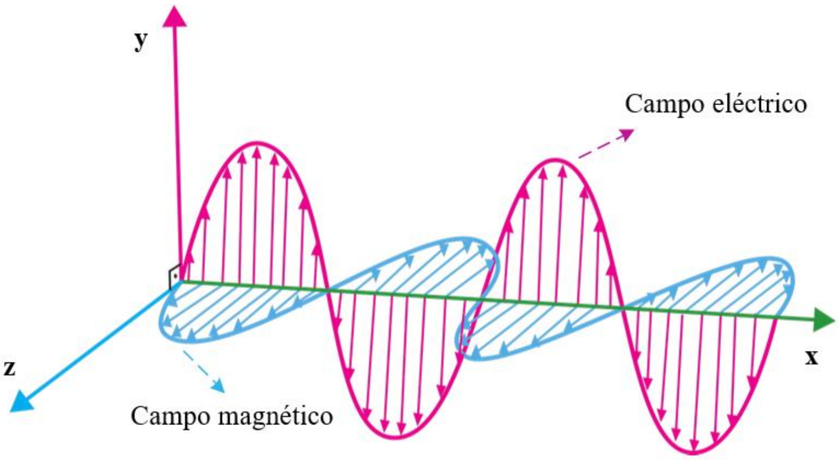

Figura 4. Campo electromagnético, formadas por las líneas campo eléctrico y magnético.

Nota. Adaptado de "Campo electromagnético" por PngWing, s.f. (https://www.pngwing.com/es/free-png-vwdei).

Los tejidos biológicos la interacción predominante está dada por el campo eléctrico. Excepto en aquellos casos donde la trayectoria del flujo de fotones conduce a una anulación del vector campo eléctrico $\vec{\boldsymbol{E}}$, se asume que la permeabilidad magnética de estos tejidos es cercana a la del vacío ($\mu_0 = \mu = 4 \cdot \pi \cdot 10^{-7}\ H/m$). Por lo tanto, es válido despreciar la interacción con el campo magnético y considerar la permitividad eléctrica como el parámetro predominante en el análisis dieléctrico del tejido (Tomás Egea, 2022).

De acuerdo con los principios de reflexión, absorción y transmisión dieléctrica, la propiedad física que describe las interacciones entre un material dieléctrico y el campo eléctrico es la permitividad compleja (Ecuación 13). Esta magnitud caracteriza el comportamiento del material cuando un flujo de fotones incide y se propaga a través de él (Tomas-Egea et al., 2022; Traffano Schiffo, 2017).

$$\varepsilon_r = \varepsilon' + j\varepsilon'' \qquad (13)$$

Donde:

Constante dieléctrica (ε'): Es la proporción de energía eléctrica almacenada al orientarse el medio respecto a la dirección del campo eléctrico (Castro-Giráldez, Fito, & Fito, 2010; Traffano-Schiffo, Castro-Giraldez, et al., 2021).

Factor de pérdidas (ε"): Es el desplazamiento del campo eléctrico inducido por las transformaciones de energía eléctrica en otras energías como la calorífica y mecánicas (Kuang & Nelson, 1998; Nelson, 2005; Traffano Schiffo, 2017).

El factor de pérdidas se asocia a la disipación de energía eléctrica dentro de un material dieléctrico, atribuida principalmente a los mecanismos de relajación relacionados con las vibraciones de especies químicas con alta movilidad iónica, fenómeno conocido como conductividad iónica. Este comportamiento puede ser cuantificado en un amplio rango de frecuencias, desde Hz hasta 1 GHz (Castro Giraldez, 2010), mediante la Ecuación 16.

$$\sigma = \omega * \varepsilon_o * \varepsilon'' \qquad (16)$$

Donde: $\boldsymbol{\omega}$, frecuencia angular ($2 * \pi * f$) ($S \times m^{-1}$); ε_o, permitividad en el vacío ($8{,}8542 \times 10^{-12}$ Fm^{-1})

1.3.2.2.1. Radiofrecuencia: interacción entre flujo de fotones y alimento (relajaciones)

Las interacciones de sistema biológico / fotones, en el rango de radiofrecuencia, muestran dos dispersiones, como la dispersión α y β (Figura 5). La dispersión α se presenta en el rango de frecuencias entre Hz y kHz, y está asociada al movimiento asociado a la orientación de las cargas móviles, como los electrolitos, dentro de los tejidos biológicos. Este fenómeno también es conocido como Efecto de Counterión (Traffano-Schiffo, Castro-Giraldez, Colom, et al., 2018a). La dispersión β tiene lugar entre los kHz y los MHz, y describe la interacción del flujo de fotones con cargas inmóviles o de escasa movilidad presentes en el tejido. En este intervalo, se pueden distinguir interacciones específicas con proteínas y carbohidratos predominantemente en el rango de los kHz, así como fenómenos de polarización interfacial, como el efecto Maxwell-Wagner, que se manifiestan en el rango de los MHz (Traffano-Schiffo, Castro-Giraldez, Herrero, et al., 2018).

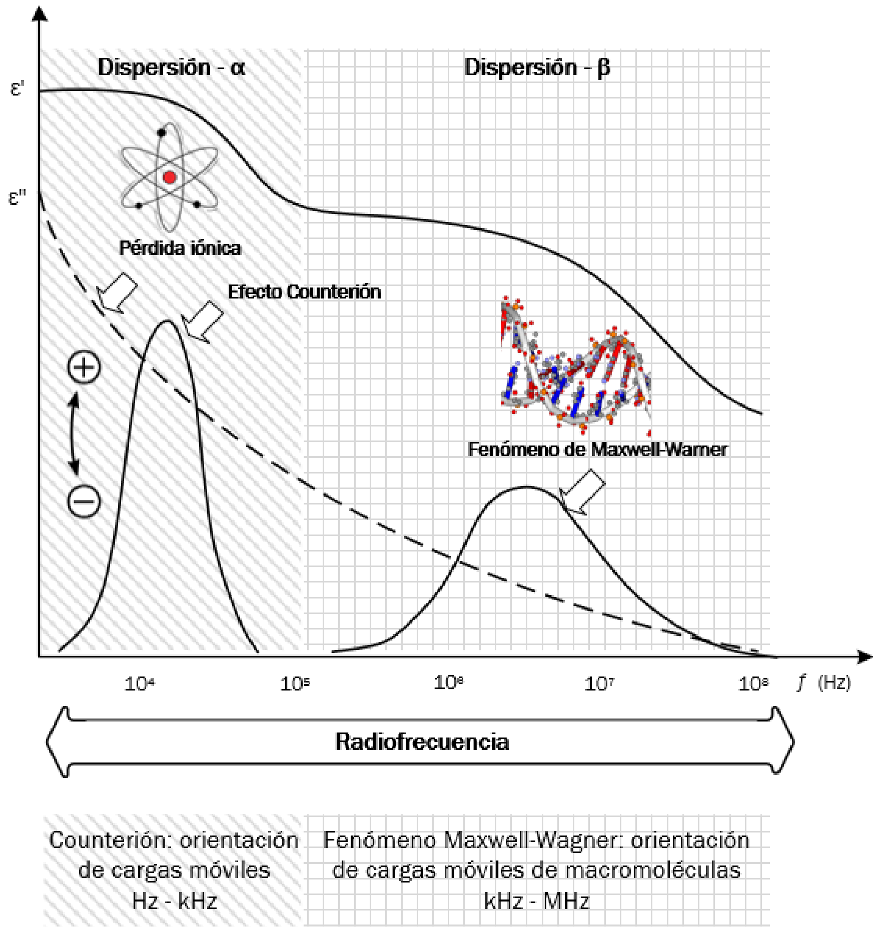

Figura 5. Relajaciones α y β en el rango de radiofrecuencia.

1.3.2.2.2. Microondas: interacción entre flujo de fotones y alimento

La denominada dispersión γ se localiza dentro del rango de microondas, desde 100 MHz hasta 300 GHz (Figura 6). Este tipo de dispersión se relaciona con la respuesta de moléculas dipolares permanentes, principalmente el agua, frente al estímulo de un flujo de fotones (Tomas-Egea et al., 2019). En condiciones normales, dichas moléculas se orientan de manera aleatoria. No obstante, al estar expuestas a un campo eléctrico o un flujo de fotones las moléculas tienden a alinearse en la dirección del estímulo aplicado. Esta reorientación del momento dipolar provoca una rotación asociada al spin molecular, fenómeno responsable del comportamiento dieléctrico característico de esta región del espectro (Tomás Egea, 2022; Tomas-Egea et al., 2019).

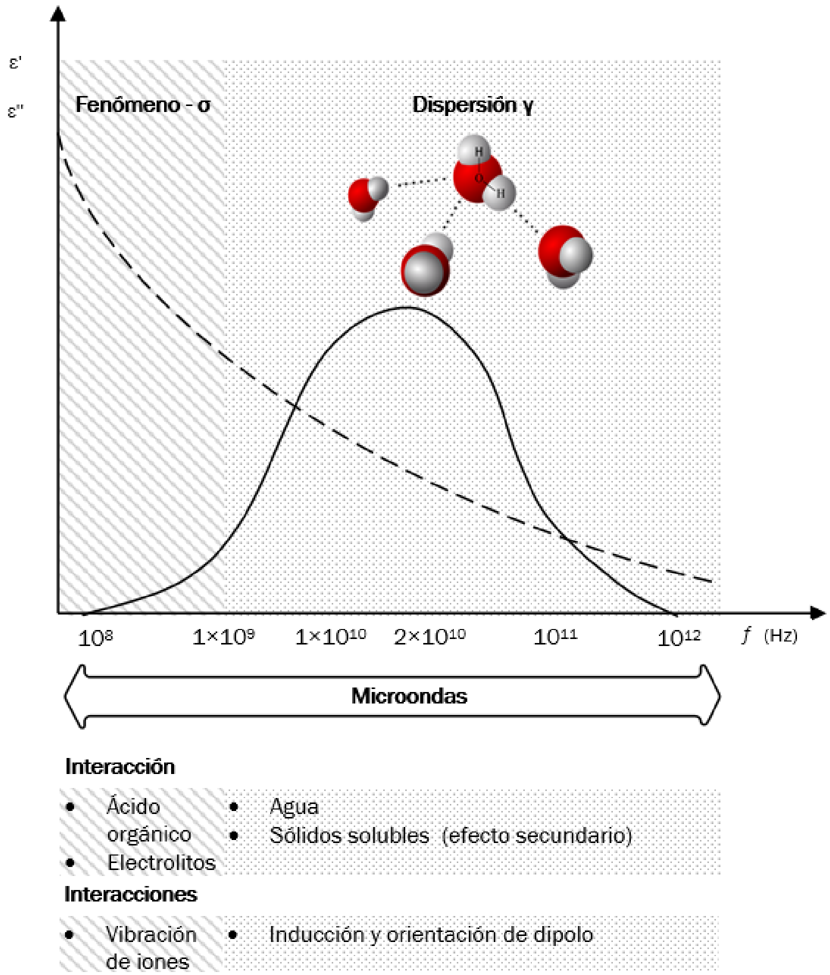

Figura 6. Relajación γ en el rango de microondas.

1.3.2.3. Espectrofotometría de infrarrojos

El infrarrojo lejano (FIR, por sus siglas en inglés) se sitúa en el extremo de baja energía del espectro infrarrojo, abarcando longitudes de onda entre 15 µm y 1 mm. Dentro del intervalo de 7 a 14 µm, se observa una ventana espectral en la cual es posible detectar la emisión de fotones térmicos provenientes de cuerpos a temperatura ambiente, así como del entorno atmosférico. Este rango coincide con el pico de emisión de radiación térmica de objetos cercanos a los 300 K (alrededor de 10 μm), de acuerdo con la ley de desplazamiento de Wien. Es precisamente en esta banda, también conocida como infrarrojo de onda larga, donde operan las cámaras termográficas empleadas para la medición de temperatura superficial sin contacto (Harrap et al., 2018).

La termografía infrarroja es una técnica no invasiva basada en la captación y análisis de la radiación electromagnética emitida por los cuerpos en el espectro infrarrojo, relacionada directamente con su temperatura superficial (Usamentiaga et al., 2014). Esta radiación térmica captada por una cámara termográfica permite generar mapas térmicos (termogramas) (Figura 7), útiles para la monitorización de procesos térmicos en alimentos (Gonçalves et al., 2016; Harrap et al., 2018). El principio físico matemático esta descrito en sección de fotónica.

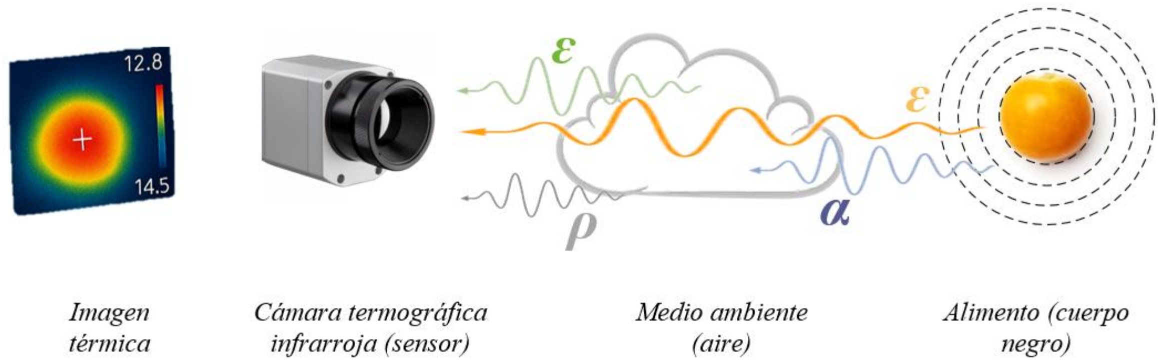

Figura 7. Sistema de termografía de infrarrojo.

1.3.2.3.1. Interacción de la termografía infrarroja con el material biológico

La interacción biológica predominante del FIR es el calentamiento superficial, cuando un objeto absorbe radiación infrarroja, aumenta la energía vibracional (Figura 8) de sus enlaces moleculares, lo cual se traduce en un incremento de su temperatura. Inversamente, al emitir radiación, el cuerpo pierde energía (Pearsall, 2020). La eficiencia de esta emisión se encuentra determinada por la emisividad (ε), que expresa cuán eficientemente un objeto irradia energía comparado con un cuerpo negro ideal (Chandra Roychoudhuri, 2017). La mayoría de los alimentos presentan valores elevados de emisividad en el FIR (en el rango de 0.8 a 0.98), debido a que son opacos y presentan superficies rugosas o no metálicas (Cuibus et al., 2014; Gonçalves et al., 2016; Shammi et al., 2022; Tomas-Egea et al., 2021; Traffano-Schiffo et al., 2014).

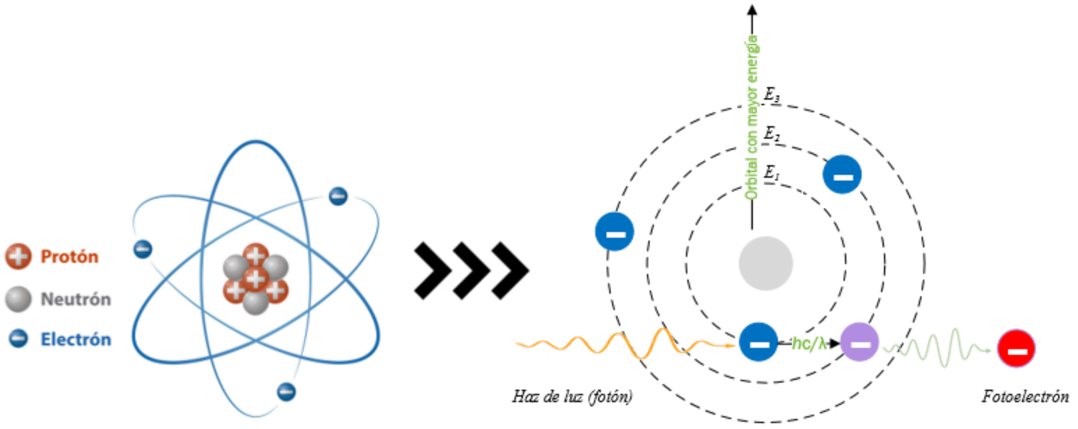

Figura 8. Grado de excitación molecular (transición electrónica o vibracional). *Nota*. Adaptado de "el átomo " por ABC, 2023. (https://www.abc.com.py/edicion-impresa/suplementos/escolar/2023/04/18/numero-atomico-y-numero-masico/).

1.3.2.4. Espectrofotometría de imágenes hiperespectrales

Las imágenes hiperespectrales (HSI, por sus siglas en inglés) constituyen una tecnología óptica avanzada que combina simultáneamente información espectral y espacial para cada píxel de una imagen (Huang et al., 2014a; Zhu et al., 2020). Este sistema genera un conjunto tridimensional de datos denominado Hipercubo (X, Y, λ) (Figura 9), donde las dimensiones espaciales X e Y representan las coordenadas de cada píxel, y la dimensión espectral λ incluye cientos de bandas espectrales contiguas que cubren desde el visible hasta el infrarrojo cercano e incluso medio (desde 400 nm hasta 2500 nm) (B. Wang et al., 2023).

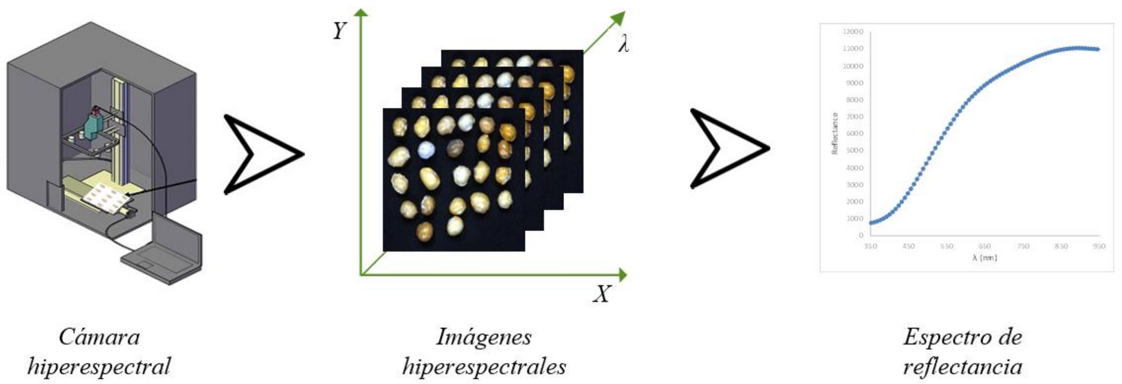

Figura 9. Sistema de adquisición de imágenes hiperespectrales.

Nota. Adaptado de Chuquizuta et al. (2024).

A diferencia de las imágenes RGB convencionales, obtenida con una cámara fotográfica común, únicamente capturan la luz reflejada en solo tres bandas (rojo, verde y azul). La imagen hiperespectral permite identificar patrones de absorción y reflexión característicos de los componentes químicos presentes en una muestra (Figura 2). Esta riqueza espectral convierte a la HSI en una técnica no destructiva y poderosa para el análisis de calidad y seguridad alimentaria (Aviara et al., 2022; Patel et al., 2024).

1.3.2.4.1. Interacción de la HSI con el material biológico

El principio físico de la imagen hiperespectral se basa en la interacción de la radiación electromagnética con la materia. Cada compuesto químico absorbe y refleja energía fotónica de manera específica a lo largo del espectro electromagnético. Esta interacción puede ser registrada como una curva espectral para cada píxel, lo que permite analizar cuantitativamente la composición química y las propiedades físicas de los alimentos (Gowen et al., 2007; Liu et al., 2014).

En diferentes rangos de longitud de onda que abarca la técnica de la HSI, podemos observar radiaciones como: ultravioleta (200–400 nm), visible (380–800 nm), visible – infrarrojo cercano (VIS-NIR, por su sigla en inglés) (400–1000 nm), infrarrojo cercano (NIR, por su sigla en inglés) (900–1700 nm) e infrarrojo de onda corta (970–2500 nm) (Marín-Méndez et al., 2024; Martínez-Domingo et al., 2024).

A nivel físico – químico, los sobretonos de las vibraciones (Figura 10) que ocurren dentro del rango de los infrarrojos producto de la estimulación y la absorción de energía de un flujo de fotones sobre un alimento, normalmente, se logran detectar vibraciones de: estiramientos del enlace C–H (metilos, metilenos y grupos aromáticos), comúnmente asociados a lípidos; estiramientos del enlace O–H, indicativos de contenido de humedad y compuestos hidroxilados; estiramientos del enlace N–H, propios de proteínas, aminas y péptidos; estiramientos C=O, relacionados con aldehídos, cetonas y ácidos carboxílicos (Marín-Méndez et al., 2024; Workman, 2014).

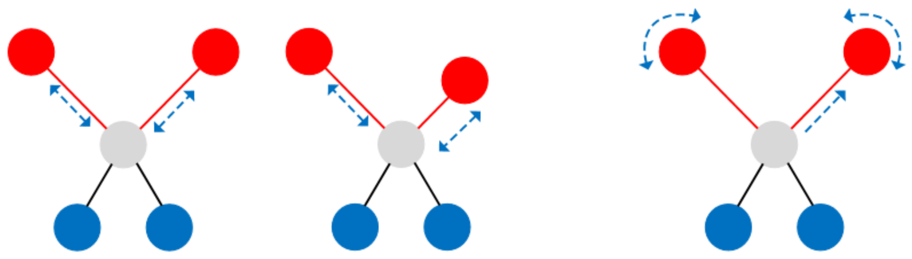

Figura 10. Tipos de vibraciones que se originan en el rango de infrarrojos

A partir de los antes mencionado, para obtener imágenes espectrales (calibradas – normalizadas) de un alimento, es necesario utilizar patrones de referencias de blanco y negro para obtener una imagen corregida. La reflectancia corregida se calcula mediante la siguiente Ecuación 17:

$$R(\lambda) = I_r(\lambda) - \ I_n(\lambda)\ /\ I_0(\lambda) - \ I_n(\lambda) \tag{17}$$

Donde: $I_n(\lambda)$ es la intensidad de la luz incidente de un cuerpo negro.

1.3.2.5. Interacción entre técnicas fotónicas

Cada técnica fotónica descrita aporta información desde una perspectiva diferente. Un enfoque prometedor es la combinación multimodal de estas técnicas para obtener un panorama completo en la monitorización y el control de calidad de alimentos. En esta investigación se ha planteado justamente esquemas híbridos de sensado, en los que dos o más técnicas se emplean simultáneamente al mismo proceso.

A continuación, se muestra la Tabla 2 con combinaciones multimodal de técnicas fotónicas a la monitorización y el control de calidad de alimentos.

Tabla 2. Combinación multimodal de técnicas fotónicas

Técnica fotónica	Muestra - Proceso de control	Resultado	Autor
Espectrofotometría de radiofrecuencia y microondas	Carne de pollo – control post mortem	Observaron que, a partir de las propiedades dieléctricas en dispersiones α, β y la conductividad iónica pueden predecir el tiempo post mortem en carne de pollo, de forma no destructiva.	(Traffano-Schiffo, Castro-Giraldez, et al., 2021)
Espectrofotometría de radiofrecuencia y microondas	Carne de pollo / Clasificación de carne	Obtuvieron un modelo físico matemático de clasificación para carne de pollo basado en análisis fotónico en rangos de radiofrecuencia y microondas	(Traffano-Schiffo, Castro-Giraldez, Colom, et al., 2018a)
Termografía infrarroja y Espectrofotometría de microondas	Papa / congelación	Consideraron que ambas técnicas son herramienta no destructiva importante para la monitorización del proceso de congelación de la papa.	(Cuibus et al., 2014)

Habiéndose realizado una búsqueda profunda de bibliografía, principalmente en bases de datos científicos, se observa una escasa y limitada combinación de las técnicas que se abordan en la presente tesis doctoral, por tanto, urge la necesidad de investigar la combinación de dichas técnicas fotónica con aplicación a los diferentes procesos agroalimentarios.

1.4. Modelización de datos espectrofotométricos

Dada la cantidad y la complejidad de los datos espectrofotométricos, y considerando que en cada intervalo del espectro electromagnético se manifiestan fenómenos físicos estrechamente relacionados con la técnica fotónica abordada en esta tesis, se hace necesario un análisis riguroso y especializado para su correcta interpretación. En esta sección se abordarán los distintos enfoques de modelado que se emplearon, abarcando desde modelos basados en primeros principios físicos, como: la termodinámica irreversible y de relajación dieléctrica. Asimismo, el desarrollo de algoritmos de machine learning aplicados a técnicas fotónicas - HSI.

1.4.1. Modelización termodinámica irreversible

Los alimentos, como sistemas biológicos altamente complejos, experimentan cambios fisiológicos, fisicoquímicos y estructurales significativos durante diversos procesos de conservación (como el secado, la congelación, entre otros) y/o transformación, los cuales están estrechamente vinculados a fenómenos de transferencia de masa y calor (Demirel & Gerbaud, 2019c, 2019a). En este contexto, la termodinámica irreversible se presenta como una herramienta robusta para describir estos fenómenos mediante flujos acoplados (de calor, masa, impulso, etc.) y sus fuerzas impulsoras (gradientes de temperatura, de potencial químico, etc.), asegurando que la producción de entropía sea positiva conforme al Segundo Principio de la Termodinámica (Demirel & Gerbaud, 2019c; Tomás Egea, 2022).

Asimismo, en las próximas secciones se describirá el principio de la termodinámica irreversible, el mismo que, integra conceptos de entropía, potenciales químicos y coeficientes fenomenológicos de Onsager, pudiendo ser aplicado a procesos agroalimentarios, como: la congelación, el secado, entre otros.

1.4.1.1. Energía libre de Gibbs

La ecuación de Gibbs constituye una relación fundamental al integrar las dos primeras leyes de la termodinámica. Cuando se utiliza en conjunto con las ecuaciones de balance (materia y energía) que asumen equilibrio termodinámico local, permite estimar la entropía del sistema (Ecuación 18). Esto resulta clave para evaluar el grado de disipación energética que ocurre durante un proceso, así como para caracterizar los fenómenos acoplados que puedan presentarse (Demirel & Gerbaud, 2019b; Demirel & Sandler, 2001).

$$\Delta G = -S\Delta T + V\Delta P + \sum_i \mu_i \,\Delta n_i \tag{18}$$

Donde: S es la entropía; V es el volumen; μ el potencial químico; n la cantidad de moles y el subíndice i representa la especia química.

En sistemas complejos como los alimentos, que contienen varios componentes y cuya composición puede cambiar respecto al tiempo, así como, la energía no solo depende de variables como la presión o la temperatura, sino también de las diferentes especies químicas presente en el alimento. Por tanto, es necesario incorporar otras fuerzas impulsoras que aportan energía libre al medio con el fin de ajustar y optimizar la ecuación de la energía libre de Gibbs (Castro Giraldez, 2010; Tomás Egea, 2022), obteniendo la Ecuación 19:

$$dG = -SdT + VdP + Fdl + \psi de + \sum_i \mu_i \; dn_i \tag{19}$$

Donde: SdT corresponde con el término entrópico y está relacionado con los flujos de calor; VdP corresponde con el término de energías mecánicas relacionadas con la variación de presión; Fdl corresponde con el término de energías mecánicas relacionadas con la fuerza de elongación; ψde corresponde con el término de energías relacionadas con el campo eléctrico inducido por los iones disueltos; $\sum_i \mu_i \; dn_i$ corresponde con el término de actividades y es el sumatorio del potencial químico de la especie "i", siendo constantes el resto de las variables de estado.

1.4.1.2. Potencial químico

Asimismo, el potencial químico (μ_i) describe la relación de energía libre asociada a cada mol de un componente "i" dentro de un sistema. El μ_i puede calcularse en condiciones de T y P contantes y cuando uno de los componentes diferentes de i no interactúan con el resto de las especies químicas. Por tanto, el μ_i se puede calcular a través de la Ecuación 20 (Castro-Giráldez et al., 2014; Tomas-Egea et al., 2021):

$$\mu_i = (\frac{G}{n_i})_{T,P,n_{j\neq i}} = RTLn(a_i) \quad (20)$$

Siendo R la constante de gases ideales (0,08205746 atm L/mol K) y a_i la actividad, definida como la relación entre la fugacidad de la especie química estudiada (i) y la fugacidad máxima.

Si integramos el termino de μ_i en la Ecuación 18, se podrá cuantificar y estudiar el efecto de las distintas fuerzas impulsoras del movimiento molecular (Ecuación 21). Para el caso de los alimentos, donde el mayor constituyente es la molécula del agua, se podrá calcular la fuerza impulsora del movimiento molecular, específicamente la del agua (Tomás Egea, 2022; Traffano Schiffo, 2017).

$$\Delta\mu_i = \frac{\Delta G}{n_i} = -\overline{s_\iota}\Delta T + \overline{v_\iota}dP + \overline{F_\iota}dl + \overline{\psi_\iota}de + \mu_{i\ T,P,n_{j\neq i}} + \sum \mu_{j\ T,P,n_{j\neq i}} \quad (21)$$

1.4.1.3. Ley fenomenológica de Onsager

En particular, cuando se aplican los principios de la termodinámica de no equilibrio a sistemas que se encuentran en las proximidades del equilibrio termodinámico global, dado la existencia de ruptura de simetría temporal de procesos irreversibles, las ecuaciones de transporte y de evolución temporal pueden representarse en forma lineal (Talens et al., 2016a; Traffano-Schiffo et al., 2014). En este régimen, se cumple la validez de las relaciones recíprocas formuladas por Onsager, relacionando para los sistemas multicomponentes, donde el flujo de la especie química i (J_i) se relaciona con todas las fuerzas impulsoras al movimiento molecular (X_i) (Onsager, 1931a, 1931b), mediante la Ecuación 22.

$$J_i = \sum_j L_{ij} X_j \quad (22)$$

Donde: L_{ij} representa una constante cinética conocida como coeficiente fenomenológico, el cual establece la relación entre el entorno y la especie química en cuanto a su capacidad para desplazarse a través de dicho medio.

Desde la perspectiva de la termodinámica irreversible no lineal, la primera relación formulada por Onsager describe el flujo de una especie química i, vinculándolo con el coeficiente fenomenológico correspondiente y con el potencial químico de esa especie dentro de un entorno específico. Esta relación se expresa mediante la siguiente Ecuación 23:

$$J_i = L_i \Delta\mu_i \tag{23}$$

1.4.2. Modelización de relajaciones dieléctricas

Para observar el efecto de algún proceso unitario en los alimentos, así como, en sus propiedades dieléctricas, es necesario obtener las relajaciones de α y β en el rango de radiofrecuencia. Para ello, se utiliza las Ecuación 24 propuesta por Traffano – Schiffo (Traffano-Schiffo, Castro-Giraldez, Colom, et al., 2018b) para determinar los parámetros de relajación α y β.

$$\log\epsilon'(\omega) = \log\epsilon'_{\infty} + \sum_{n=1}^{2} \frac{\Delta \log \epsilon'_n}{1 + e^{\left(\log\omega^2 - \log\tau_n^2\right) * \alpha_n}} \tag{24}$$

Donde n esta dado por las dispersiones de α y β, $\log\epsilon'$ representa el logaritmo de la constante dieléctrica, $\log\epsilon'_{\infty}$ es el logaritmo de la constante dieléctrica a altas frecuencias, $\log\omega$ es el logaritmo de la velocidad angular ($\omega = 2 * \pi * frecuencia$), $\Delta\log\epsilon'_n$ es la amplitud de la dispersión n, $\log\tau_n$ es el logaritmo de la velocidad angular en el tiempo de relajación para cada n, α_n es la pendiente de la dispersión.

Asimismo, a partir de los parámetros obtenidos de la Ecuación 25 se puede calcular la constante dieléctrica y la frecuencia de relajación para cada una de las dispersiones en el rango de radiofrecuencia (Ecuación 26, 27 y 28) (Traffano-Schiffo, Castro-Giraldez, Colom, et al., 2018b).

$$\epsilon'_{\alpha} = 10^{\left(\log\epsilon'_{\infty} + \Delta\log\epsilon'_{\beta} + \frac{\Delta\log\epsilon'_{\alpha}}{2}\right)} \tag{26}$$

$$\epsilon'_{\beta} = 10^{\left(\log\epsilon'_{\infty} + \frac{\Delta\log\epsilon'_{\beta}}{2}\right)} \tag{27}$$

$$f_i = 10^{\left(\frac{log\omega_{\tau i}}{2*\pi}\right)} \tag{28}$$

Siendo i el correspondiente a cada dispersión (α y β)

1.4.3. Modelización quimiométrica

La quimiometría es una disciplina que combina herramientas matemáticas y estadísticas para el análisis multivariante de datos cuantitativos y cualitativos (Fodor et al., 2024). En los últimos años, la quimiometría se ha integrado con diversas técnicas espectroscópicas (RF, MW, HSI, NIR, entre otras) para la monitorización y control de calidad de alimentos. Esto se logra mediante la reducción de la dimensionalidad de los datos, la retención de información espectral esencial y la clasificación y/o cuantificación de patrones (Amigo et al., 2013; Huang et al., 2014a; Martínez-Domingo et al., 2024; Zhu et al., 2020).

Dentro de los análisis multivariados más empleados en el ámbito del procesamiento y control de calidad de alimentos, se destacan los modelos de regresión predictiva, tanto lineales como no lineales. Entre estos se incluyen la regresión lineal múltiple (MLR, siglas en ingles), la regresión por mínimos cuadrados parciales (PLSR, siglas en ingles), las redes neuronales artificiales (ANN, siglas en ingles) y las máquinas de vectores de soporte (SVM), entre otros. Asimismo, se utilizan ampliamente modelos de clasificación lineal y no lineal, tales como Análisis Discriminante de Mínimos Cuadrados Parciales (PLS-DA, siglas en inglés), SVM, ANN, entre otros (J. H. Cheng et al., 2017; Dale et al., 2013; Saha & Manickavasagan, 2021). Diversos estudios recientes han demostrado la eficacia del modelo PLSR en aplicaciones como la detección de adulteración de leche (Chuquizuta et al., 2022), la predicción de la calidad interna de frutas (Blas Saavedra et al., 2024; W. Guo et al., 2015; Liu & Guo, 2017; Reyes et al., 2017), carne de pollo (Shen et al., 2025) y aceite (Yuan et al., 2024)

No obstante, a pesar de que los estudios sobre redes neuronales recurrentes (RNN, siglas en inglés) aplicadas a alimentos aún son limitados, el interés y la cantidad de investigaciones en esta área han experimentado un crecimiento exponencial en los últimos años. Por tanto, dada la relevancia y el potencial de los modelos PLSR y las ANN (incluidas sus variantes), en este trabajo se plantea la utilización de dichos modelos en el desarrollo de nuevas herramientas de predicción, de sistemas de monitorización y control de alimentos.

Las implementaciones de modelos requieren de pretramiento de los datos para ser utilizados, con el fin de disminuir ruido, reducir dimensionalidad, efecto del tamaño de partícula, entre otros. A continuación, se muestran detalles del preprocesamiento de las señales y la posterior modelización.

1.4.3.1. Preprocesamiento de señal

En las diferentes técnicas espectrofotónicas se viene empleando técnicas de pre procesamiento de señal, siendo estas: la normalización estándar variante (SNV, siglas en ingles) y la corrección por dispersión multiplicativa (MSC, siglas en inglés) las que corrigen efectos de dispersión y escalado en espectros hiperespectrales (Witteveen et al., 2022). También se emplean derivadas espectrales (primera, segunda), en especial el filtro Savitzky–Golay (SG, siglas en inglés), la misma que, suaviza y deriva la señal ajustando localmente un polinomio de grado k a una ventana móvil de 2m+1 puntos (Taghinezhad et al., 2025; Tirado-Kulieva et al., 2024b; Witteveen et al., 2022). A continuación, se describe la Ecuación 29 de Savitzky–Golay:

$$y_j^0 = \frac{\sum_{1=-m}^{m} C_i Y_{j+i}}{N} \tag{29}$$

Donde: Y es el perfil original, y^o el perfil suavizado, C es el coeficiente del i-ésimo término del perfil y N es el número de etapas.

1.4.3.2. Modelo de regresión de mínimos cuadrados parciales

Los valores de intensidad de una técnica espectrofotométrica, dentro de un rango de longitudes de onda o frecuencia, es primordial poder construir una matriz de datos (X, Y, Z), ordenando el valor de intensidad con su propiedad física o química como referencia.

El PLSR transforma las variables predictoras (X) en variables de respuesta (Y), asimismo, se descompone X e Y para proyectarlas en nuevas direcciones y describir el cambio de las variables en conjunto con la mayor precisión posible (Tirado-Kulieva et al., 2024; N. Vásquez et al., 2018). A continuación, se realiza una regresión con las X e Y descompuestas, cuyo modelo se muestra en la Ecuación 30:

$$Y = \beta X + e \tag{30}$$

Donde: Y representa los valores físicos o químicos de un alimento, X es la matriz de datos de intensidad de una de las técnicas espectrofotométricas (n – observaciones x m – frecuencia o longitud de onda) y β es la matriz de coeficientes.

1.4.3.3. Redes neuronales

Una red neuronal es un modelo matemático – estadístico inspirado en la estructura del cerebro humano, es decir una neurona, compuesto por capas de nodos interconectados que procesan información. Las redes neuronales son capaces de aprender patrones complejos a partir de datos mediante un proceso de entrenamiento. Su versatilidad las hace útiles en tareas como clasificación, regresión y reconocimiento de patrones. En el ámbito científico, se han consolidado como herramientas clave para el modelado no lineal y la predicción en sistemas complejos (Vásquez et al., 2018a).

1.4.3.3.1. Memoria de corto plazo

Las redes recurrentes de memoria de corto plazo (Long Short-Term Memory - LSTM), una extensión de las redes neuronales recurrentes, han demostrado alta eficacia en el modelado de datos secuenciales como los espectros hiperespectrales, debido a su capacidad para conservar información relevante a largo plazo. Cada unidad LSTM contiene puertas de entrada, olvido y salida, reguladas mediante funciones sigmoide y tanh, que controlan el flujo de información y actualizan el estado de la celda c_t (Kang et al., 2021). Las Ecuaciones 30, 31, 32 y 33 fundamentales son:

$$i_t = \sigma(W_i x_t + U_i h_{t-1} + b_i) \tag{30}$$

$$f_t = \sigma\left(W_f x_t + U_f h_{t-1} + b_f\right) \tag{31}$$

$$c_t = f_t \odot c_{t-1} + i_t \odot \tanh(W_c x_t + U_c h_{t-1} + b_c) \tag{32}$$

$$h_t = o_t \odot \tanh(c_t) \tag{33}$$

Donde: $\odot$ denota la multiplicación punto a punto.

1.4.3.3.2. Redes Neuronales de Base Radial

Las Redes Neuronales de Base Radial (RBNN, siglas en inglés) son modelos de una sola capa oculta que utilizan funciones de activación radiales (Castro, Saavedra, et al., 2024), comúnmente gaussianas, definidas como la Ecuación 34:

$$\emptyset_j(x) = \exp(-\frac{\left\|x - u_j\right\|^2}{2\sigma_j^2}) \tag{34}$$

Donde: u_j es el centro del nodo y σ_j su ancho. La salida de la red es una combinación lineal de estas funciones, véase la Ecuación 35:

$$y = \sum_j w_j \emptyset_j\,(x) \tag{35}$$

Las RBNN tienen alta capacidad de aproximación de funciones no lineales, lo que las hace efectivas para modelar relaciones complejas entre espectros y atributos químicos.

1.5. Futuro de la sensórica en la industria agroalimentaria

En las últimas décadas, la evolución de la sensórica en la industria de agroalimentaria está marcada por tendencias hacia sistemas más inteligentes, integrados y predictivos. Ante lo descrito, es posible vislumbrar varias direcciones en que avanzará la sensórica:

- Integración multi-sensorial y Gemelos Digitales: Como se describe en esta tesis, la combinación de múltiples técnicas espectrofotónicas (RF, microondas, IR, HSI) proporciona una visión integral del producto agroalimentario. En el futuro, se desarrollarán equipos híbridos capaces de medir simultáneamente diversas propiedades físicas y/o químicas (por ejemplo, túneles de procesamiento con cámaras hiperespectrales y sensores de microondas incorporados). Estos datos alimentarán en tiempo real bases de datos del proceso: réplicas virtuales que simulan de manera continua lo que ocurre dentro del alimento, facilitando la toma de decisiones. Asimismo, dichas bases de datos permitirán optimizar las condiciones de operación en tiempo real, predecir la calidad final antes de culminar el proceso y responder ante perturbaciones (por ejemplo, ajustar la potencia de secado si se detecta un retraso en la pérdida de agua), con el fin de realizar acciones preventivas o correctivas. Para lograrlo, será crucial el desarrollo de modelos híbridos altamente fidedignos y rápidos, mediante el uso de técnicas de reduced order modeling o surrogate models. Esto permitirá la implementación de plataformas de control predictivo, donde las decisiones se basen en simulaciones anticipadas en lugar de reacciones tardías.

- Sensores portátiles e IoT alimentario: La miniaturización de tecnologías fotónicas está dando lugar a sensores portables de campo: mini cámaras hiperespectrales, espectrómetros NIR de mano, sensores de radiofrecuencias y microondas integrados en dispositivos de monitorización y control de calidad. En el futuro, podríamos tener líneas de producción equipadas con redes de sensores inalámbricos (*Internet of Things*) que monitoricen en distintos puntos con distintos métodos, enviando datos a la nube para análisis en conjunto. Por ejemplo, un sensor *RFID* especial con antena microondas podrían colocarse en productos para medir propiedades fisicoquímicas durante distribución (etiquetado inteligente por resonancia). La información colectada alimentará sistemas de *Big Data* que, con algoritmos de *machine learning*, detecten patrones globales (predecir y/o clasificar propiedades fisicoquímicas de agro productos). Finalmente, la inteligencia artificial acoplada a técnicas fotónicas permitirá mejorar el procesamiento de los datos y extraer alertas útiles para la toma de medidas preventivas y/o correctivas a la monitorización y el control de calidad.

II. Objetivos y plan de trabajo

2.1. Objetivos

2.1.1. Objetivo general

- Desarrollar sistemas espectrofotométricos y modelización híbrida para la monitorización y el control de calidad de alimentos

2.1.2. Objetivos específicos

- Predecir los sólidos solubles, acidez y pH de aguaymanto (*Physalis peruviana* L) mediante propiedades dieléctricas en el rango de microondas

- Desarrollar de un sistema de monitorización y modelización termodinámica para el proceso de secado convectivo de aguaymanto (*Physalis peruviana* L) mediante termografía de infrarrojos

- Desarrollar de un sistema de monitorización del proceso de congelación de aguaymanto (*Physalis peruviana* L) mediante espectrofotometría y termografía de infrarrojos

- Identificar ruptura de cadena de frío de filetes de caballa (*Scomber japonicus peruanus*) mediante imágenes hiperespectrales acoplada a redes neuronales

- Predecir parámetros fisicoquímicos de carne de cerdo postmortem mediante espectroscopía dieléctrica (microondas) acoplada a machine learning

- Determinar la cinética de hidratación de frejoles pinto (*Phaseolus vulgaris*) mediante imágenes hiperespectrales

- Determinar el efecto de la bioestimulación magnética en las características físicas y compuestos bioactivos de maíz morado INIA 601

2.2. Plan de trabajo

A continuación, se detalla el plan de tesis doctoral, organizado por cada objetivo específico:

- Predecir los sólidos solubles, acidez y pH de aguaymanto (*Physalis peruviana* L) mediante propiedades dieléctricas en el rango de microondas

En la Figura 11, se observa la propuesta del desarrollo experimental para la predicción de propiedades fisicoquímicas de aguaymanto fresco.

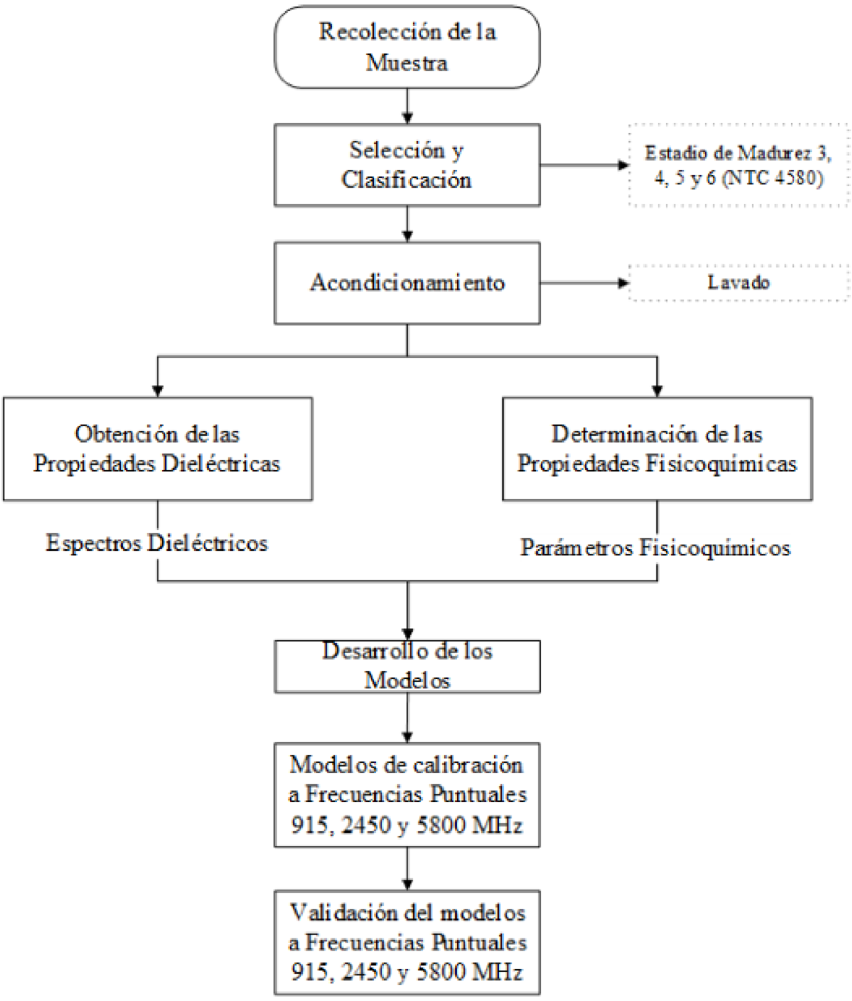

Figura 11. Propuesta del diseño experimental – calidad de aguaymanto

Se utilizaron 450 unidades de frutos de aguaymanto para la determinación de propiedades dieléctricas y fisicoquímicas, distribuidas en 150 unidades por cada estadio de madurez (4, 5 y 6), según la NTC 4580. Se obtuvieron las propiedades dieléctricas (constante dieléctrica, ε') en el rango de 0.5 a 9.0 GHz, mediante una sonda coaxial de terminación abierta (N1501A-001), conectada a un analizador de redes vectorial (modelo N9915A, Keysight Technologies). Una vez obtenidas las propiedades dieléctricas, se determinaron las siguientes propiedades fisicoquímicas: Sólidos solubles (°Brix): se colocó de dos a tres gotas de zumo sobre el lente del refractómetro (Hanna HI96800). Acidez titulable: se utilizó el método AOAC 22.008 (1984). pH: conforme al método AOAC 981.12 (AOAC, 1998), se un pH – metro (Orion Versastar Pro, Thermo Scientific) para medir el pH del zumo de aguaymanto.

- Desarrollo de un sistema de monitorización y modelización termodinámica para el proceso de secado convectivo de aguaymanto (*Physalis peruviana L*) mediante termografía de infrarrojos

En la Figura 12, se observa la propuesta del desarrollo experimental para la monitorización de secado de aguaymanto fresco.

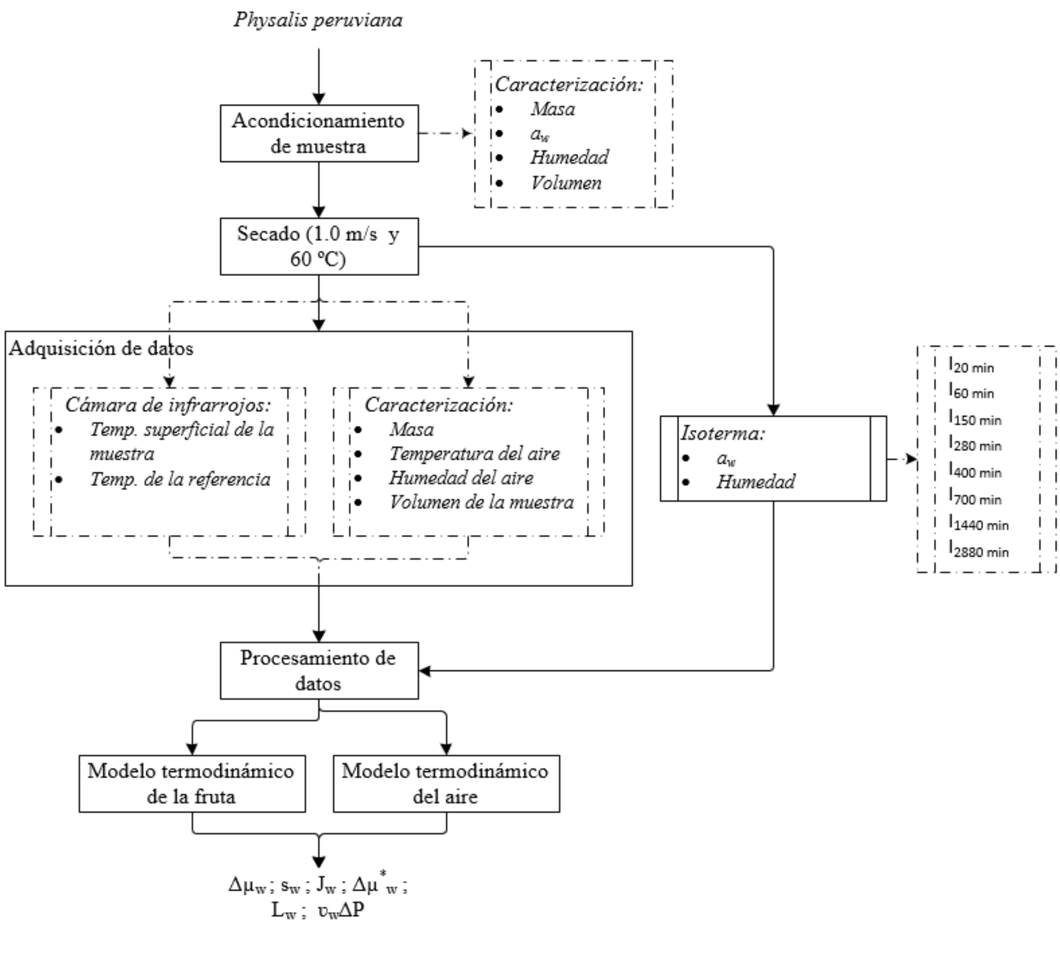

Figura 12. Propuesta del diseño experimental – secado de aguaymanto

Nota. Adaptado de Chuquizuta et al. (2025).

Se colocaron dos unidades de frutos de aguaymanto en un secador convectivo, y uno de los frutos fue suspendido de una balanza de precisión mediante un hilo de nylon para controlar la masa durante 13 horas de secado. La masa de la muestra se registró cada cinco minutos durante la primera hora, cada diez minutos entre la primera y la segunda hora, y cada 15 minutos durante el resto del período de secado. El segundo fruto de aguaymanto se colocó a la derecha del fruto suspendido.

El secador convectivo operó a una temperatura de secado de 60 ºC y una velocidad del aire de secado de 1,0 m/s. Durante el proceso de secado, la temperatura de la muestra, el aire de secado y el material de referencia (emisividad) fueron registradas con termopares (conectados a un multiplexor Agilent 34901A, Malasia). La deshidratación se realizó por triplicado.

- Desarrollo de un sistema de monitorización del proceso de congelación de aguaymanto (*Physalis peruviana* L) mediante espectrofotometría y termografía de infrarrojos

En la Figura 13, se observa la propuesta del desarrollo experimental para la monitorización de congelación de aguaymanto fresco.

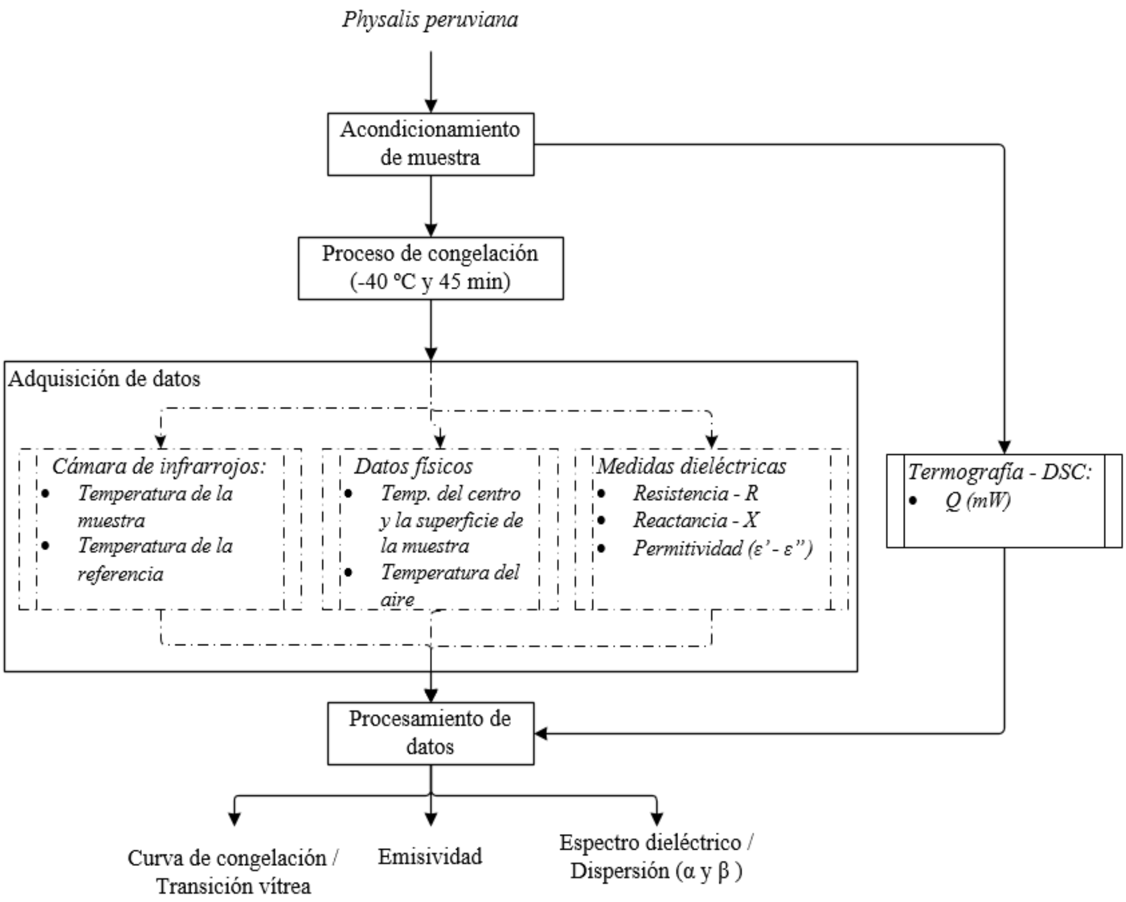

Figura 13. Propuesta del diseño experimental – congelación de aguaymanto

Nota. Adaptado de Chuquizuta et al. (2025).

Se utilizaron tres frutos de aguaymanto por cada experimental. El primer fruto se ubicó a la derecha, destinado a la monitorización de temperatura (superficial y central) mediante dos termopares tipo K, con registros cada 5 segundos. El registro de la temperatura se realizó con un sistema de adquisición de datos Agilent 34972A (Agilent Technologies, Malasia), adicionalmente, se monitoreó la temperatura superficial del material de referencia de emisividad certificada de 25 mm de diámetro (ε = 0.95) (Optris GmbH, Berlín, Alemania) y la temperatura del aire dentro del congelador. El segundo fruto se colocó en el centro, para la medición de la temperatura superficial mediante una cámara termográfica (Optris PI® 160, Optris GmbH, Berlín, Alemania) a una distancia de 30 cm, con registros cada 0.5 segundos. El tercer fruto se ubicó a la izquierda, destinado a la monitorización de las propiedades dieléctricas mediante un sensor de dos agujas insertado en el centro de la muestra, conectado a un analizador de impedancia Agilent 4294A (Agilent Technologies, Santa Clara, CA, EE. UU.)

- Identificar la ruptura de la cadena de frío de filetes de caballa (*Scomber japonicus peruanus*) mediante imágenes hiperespectrales acoplada a redes neuronales

En la Figura 14, se observa la propuesta del desarrollo experimental para identificar la ruptura de la cadena de frio de filetes de pescado.

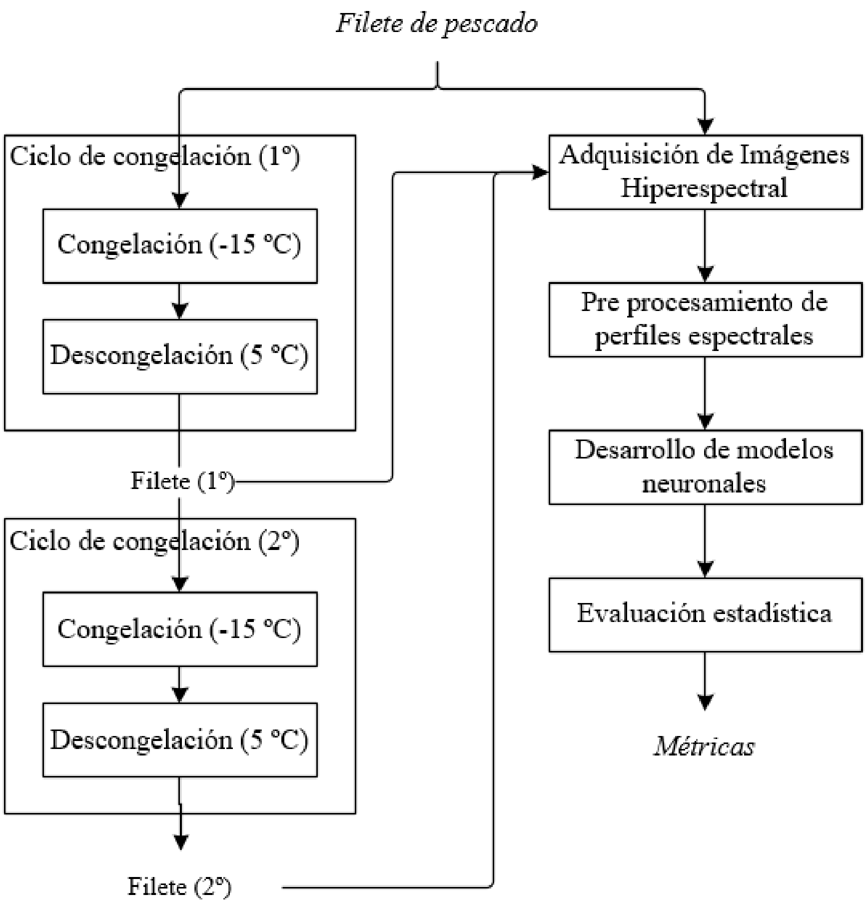

Figura 14. Propuesta del diseño experimental – ruptura de cadena de frío

Nota. Adaptado de Castro et al. (2023).

Se estudió los efectos de la rotura de la cadena de frío sobre filetes de caballa mediante ciclos de congelación-descongelación (primero y segundo ciclo). Los filetes fueron colocados en un congelador a -15 ºC (Pol-Eko-Aparatura, ZLN 85, Polonia) durante 24 h para asegurar su congelación. Posteriormente, las muestras se colocaron en un refrigerador (Daewoo, FR-146RN, China) para su descongelación gradual. Una vez completado el proceso de descongelación, se obtuvieron las imágenes hiperespectrales en el rango de 400 a 1000 nm, mediante una cámara Specim FX-10 (Finlandia). Este procedimiento se repitió para el segundo ciclo de congelación-descongelación.

- Predecir parámetros fisicoquímicos de carne de cerdo postmortem mediante espectroscopía dieléctrica (microondas) acoplada a machine learning

En la Figura 15, se observa la propuesta del desarrollo experimental para la predicción de propiedades fisicoquímicas de la carne de cerdo.

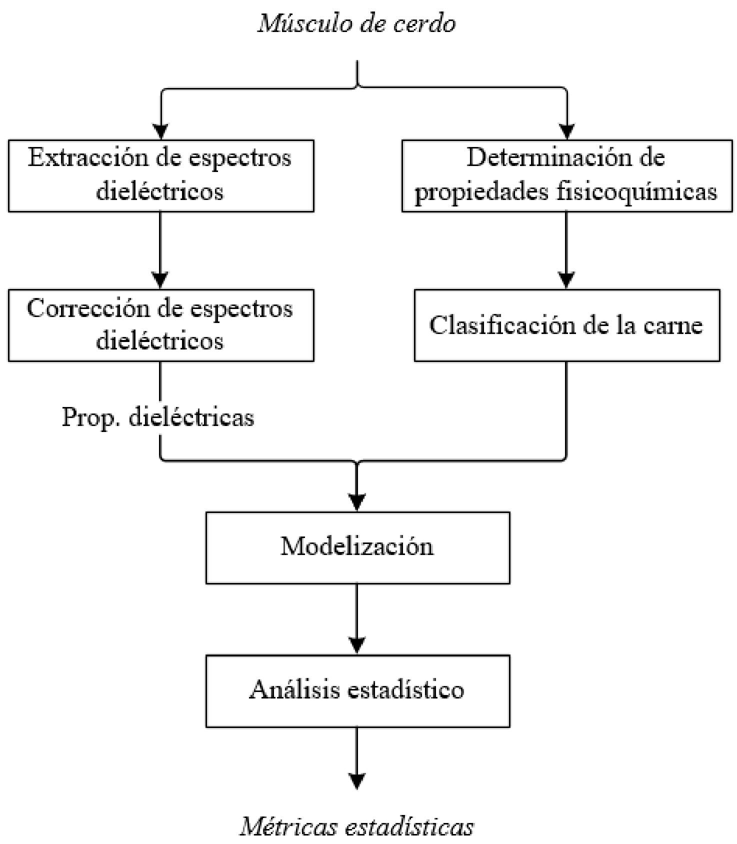

Figura 15. Propuesta del diseño experimental – calidad de carne de cerdo.
Nota. Adaptado de Chuquizuta et al. (2025).

Se utilizaron músculos Longissimus dorsi de 54 cerdos machos y 26 hembras, con un peso promedio de 85 kg y una edad comprendida entre 5 y 12 meses. Las propiedades dieléctricas se obtuvieron en el rango de 0.5 a 9 GHz, utilizando una sonda coaxial de terminación abierta (N1501A-001), conectada a un analizador de redes vectorial (KEYSIGHT N9915A). Asimismo, se determinó las siguientes propiedades de calidad:

pH: Se utilizó 10 g de muestra mezclados con 90 mL de agua destilada. La mezcla fue triturada, y el pH se medió con un pH-metro (Thermo Scientific, VSTAR50). Color (L*a*b*): Se medió el color con un colorímetro manual (3nh NR200), empleando un iluminante D65 y un ángulo de observación de 10°. Contenido de humedad: Se utilizó 5 g de muestra, los cuales se analizaron en una balanza de humedad (AE ADAM PMB 202) a 140 ºC durante 30 minutos. Pérdida por goteo: Se utilizó 100 g de muestra, y fueron colocadas en una bolsa hermética sin contacto con las paredes. Las muestras se almacenaron durante 72 horas en refrigeración a 4 ºC. Al finalizar, se registró la masa para el cálculo de la pérdida.

- Determinar la cinética de hidratación de frejoles pinto (*Phaseolus vulgaris*) mediante imágenes hiperespectrales

En la Figura 16, se observa la propuesta del desarrollo experimental para el modela de la cinética de hidratación mediante imágenes hiperespectrales.

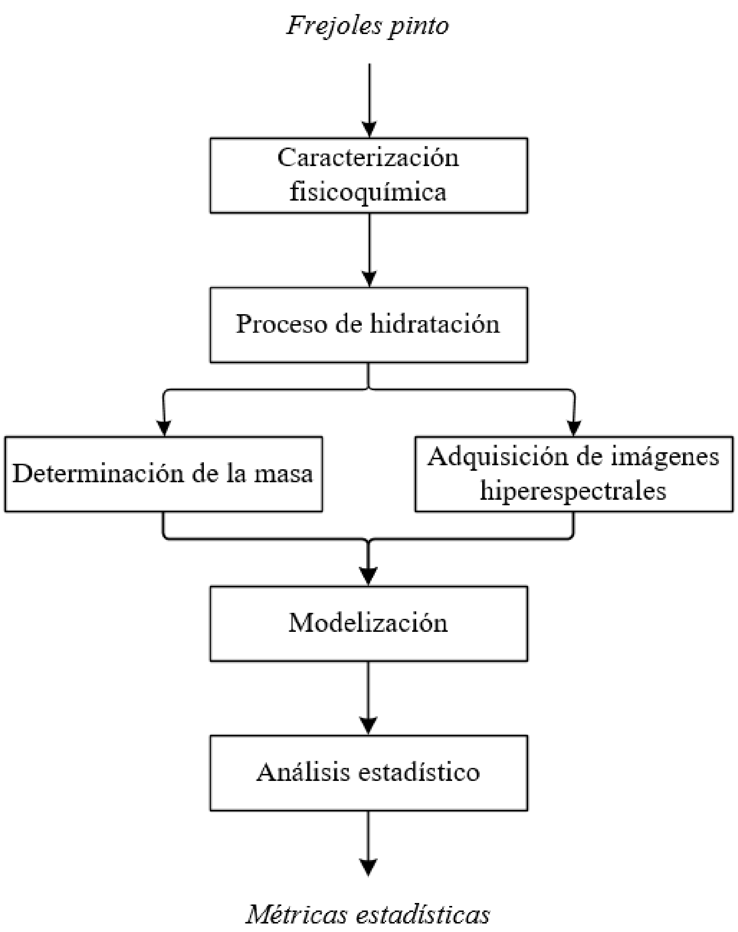

Figura 16. Propuesta del diseño experimental – modelización de cinética de hidratación.

Nota. Adaptado de Chuquizuta et al. (2024).

Se utilizó 15 g de frejoles pinto para el proceso de hidratación. Las muestras se colocaron en un matraz Erlenmeyer de 500 mL con agua destilada a 20 ºC. Durante las dos primeras horas, se registraron la masa y se obtuvieron las imágenes hiperespectrales cada 15 minutos (rango de 400 a 800 nm, utilizando una cámara Pika XC; Resonon Inc., Montana, USA). Posteriormente, la masa y las imágenes hiperespectrales fueron obtenidas cada 30 min hasta alcanzar el equilibrio de hidratación.

- Determinar el efecto de la bioestimulación magnética en las características físicas y compuestos bioactivos de maíz morado INIA 601

En la Figura 17, se observa la propuesta del desarrollo experimental para la evaluación de características físicas y compuestos bioactivos de maíz morado INIA 601.

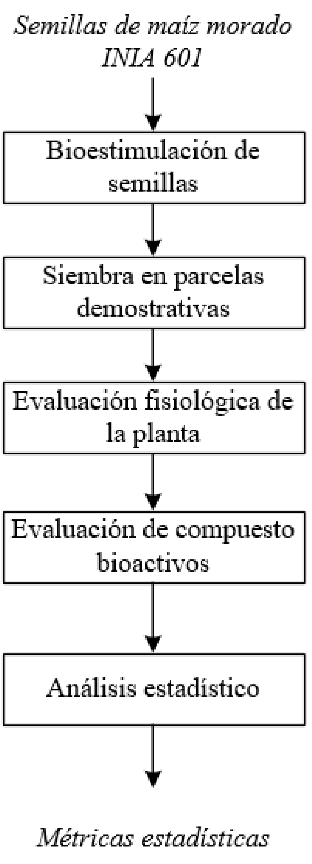

Figura 17. Propuesta del diseño experimental – compuestos bioactivos de maíz morado

Las semillas de maíz morado INIA 601 fueron bioestimuladas con campos magnéticos estáticos (50 mT) y pulsados (8 mT - 30 Hz), ambos tratamientos por un periodo de 30 min. Seguidamente, fueron sembradas en campos experimentales. Se registraron las características de desarrollo fisiológico del maíz (días de floración masculina y femenina, altura de la planta, numero de mazorcas por planta, longitud de la mazorca, rendimiento). Finalizado la cosecha, se seleccionaron las mazorcas sin daños mecánicos y biológicos, seguidamente fueron deshidratas y almacenadas en bolsas de polipropileno hasta sus análisis fisicoquímicos respectivo (fenoles totales, antocianinas y capacidad antioxidante) de la bráctea, la coronta y los granos.

III. Materiales y métodos

3.1. Muestra biológica

A continuación, se detallan las muestras biológicas que se han utilizado para el cumplimiento de la presente tesis doctoral.

3.1.1. Aguaymanto (*Physalis peruviana* L)

Los frutos de aguaymanto (*Physalis peruviana* L.) se obtuvieron de los sembríos pertenecientes al fundo "Capulí el Valle" ubicado en el C.P. San Juan de Lacamaca, provincia de Bambamarca, Región Cajamarca – Perú [UTM: -6.641845, -78.520417]. Se utilizó 450 unidades de frutos de aguaymanto para la determinación de las propiedades dieléctricas y fisicoquímicas, 150 unidades por cada estadio de madurez (4, 5 y 6) según la NTC 4580 (Figura 18). Los frutos de aguaymanto tuvieron las siguientes características de homogeneidad en peso, color y tamaño, sin presencia de magulladuras o daños mecánicos.

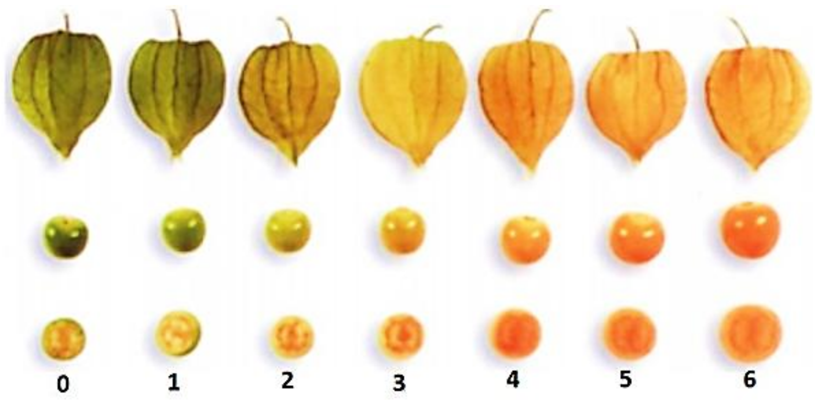

Figura 18. Estados de madurez fisiológica de aguaymanto según NTC 4580.
Nota. Adaptado de NTC 4580 (1999).

Para los experimentales de secado y congelación de frutos de aguaymanto, las muestras en madurez comercial (4), procedentes de Ecuador, se obtuvieron a través de la empresa importadora Ammarket (Orihuela, Alicante - España). Los frutos de aguaymanto llegaron en cajas refrigeradas (100 g / caja) con tamaño (diámetro) y masa uniforme, 3,8±0,21 cm y 3,9±0,4 g, respectivamente, manteniéndose en refrigeración a 6 ºC hasta su posterior análisis y ejecución del experimento.

3.1.2. Carne de cerdo (*Longissimus dorsi*)

Se seleccionaron 80 músculos "*Longissimus dorsi*" de 54 cerdos criollos machos y 26 hembras, con un peso promedio de 85 kg y un rango de edad de 5 a 12 meses (Figura 19). Una vez obtenidas las muestras, fueron colocadas en una caja isotérmica con bloques de hielo y trasladadas al laboratorio del Instituto de Investigación del Mejoramiento Productivo de la Universidad Nacional Autónoma del Chota para su posterior análisis.

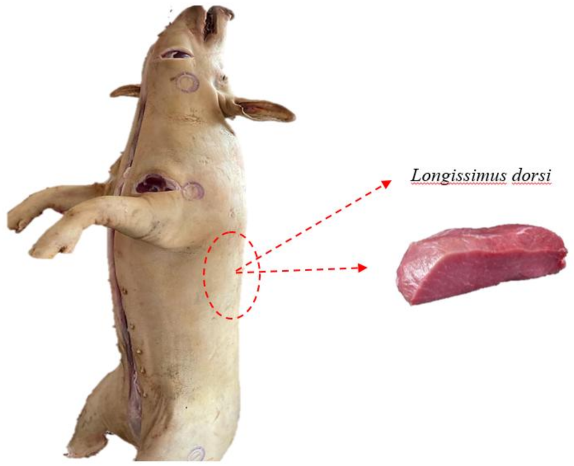

Figura 19. Músculo de *Longissimus dorsi*.

3.1.3. Caballa (*Scomber japonicus peruanus*)

Se obtuvieron 48 filetes frescos sin deshuesar de caballa (*Scomber japonicus peruanus*) (Figura 20). Estos filetes se lavaron con agua (200 ppm de cloro residual) y se almacenaron a 4 ºC hasta los análisis respectivos.

Figura 20. Filetes enteros de caballa fresca.

3.1.4. Frejol pinto (*Phaseolus vulgaris*)

Se adquirieron 3 kg de frejol común (*Phaseolus vulgaris*) de la variedad Pinto (Figura 21) en el mercado local de Chachapoyas, Amazonas, Perú. Primero, se seleccionaron los frejoles según su homogeneidad en tamaño, color y peso, descartando aquellos con daños mecánicos y biológicos. Posteriormente, las muestras se almacenaron en un recipiente hermético de plástico y seco a 15 °C, por un periodo de dos semanas para homogeneizar la humedad de los frejoles, hasta su evaluación.

Figura 21. Frejoles pinto secos.

Nota. Adaptado de "Frejoles pintos" por Amazon, s.f. (https://l1nk.dev/mHH87)

3.1.5. Maíz morado (*Zea mays* L. var. INIA 601)

En el experimento se utilizaron 3 kg de semillas de maíz morado (*Zea mays* L. var. INIA 601) (Figura 22), proporcionadas por la Estación Experimental "Baños del Inca" del Instituto Nacional de Innovación Agraria (INIA), ubicada en la cuidad de Cajamarca, Perú.

Figura 22. Mazorca de maíz morado INIA 601.

3.2. Métodos y técnicas en el análisis de alimentos

3.2.1. Predicción de parámetros fisicoquímicos de aguaymanto

- Sistemas de extracción de propiedades dieléctricas

Para medir las propiedades dieléctricas (constante dieléctrica - ε’) en un rango de 0.5 a 9.0 GHz, se utilizó una sonda coaxial de terminación abierta (N1501A-001), conectada a un analizador de redes vectorial (modelo N 9915A, Keysight Technologies), y controlada de manera remota mediante una Laptop (Lenovo HP CORE i7). Previo a la obtención de las propiedades dieléctricas, el equipo se dejó encendido por al menos 30 min con la finalidad de brindar estabilidad a los circuitos electrónicos del equipo. Seguidamente, se procedió con la calibración del equipo – sonda coaxial en aire, corto circuito y medio dieléctrico (agua destilada) sugerido por Chuquizuta et al. (2021) y Reyes et al. (2017, 2018). Para la extracción de las propiedades dieléctricas de los frutos de aguaymanto, estos se posicionaron en la parte inferior de la sonda coaxial para hacer contacto con la superficie del fruto, sin ejercer presión de penetración por parte de la sonda, y obteniendo las medidas por triplicado. Finalmente, se seleccionaron las constantes dieléctricas según los estadios de madurez de los frutos de aguaymanto a frecuencias puntuales de 0.915, 2.450 y 5.800 GHz.

- Caracterización química de frutos de aguaymanto

Posterior a la extracción de las propiedades dieléctricas de los frutos de aguaymanto, se obtuvieron las muestras de zumo de los frutos mediante el uso de un extractor de zumo (FPSTJU407W, Oster). Se determinó de los sólidos solubles (ºBrix) del zumo de aguaymanto de acuerdo con el método AOAC 932. 12 (AOAC 1980), colocando de 3 a 5 gotas sobre el lente del refractómetro (Hanna HI96800) y posterior lectura; la acidez titulable se determinó a través del método AOAC (22.008.1984), mediante la valoración con solución de NaOH (0,1 N) y expresada como porcentaje de ácido cítrico; el pH se midió de acuerdo a AOAC 981. 12 (AOAC 1998) utilizando un pH-metro (Orion Versastar pro - Thermo Scientific), previamente calibrado con tampones de 4, 7 y 10, mediante la inmersión directa del electrodo en el zumo.

3.2.2. Monitorización no invasiva de secado de aguaymanto

Se utilizó el siguiente esquema para la monitorización del secado convectivo del aguaymanto (Figura 23).

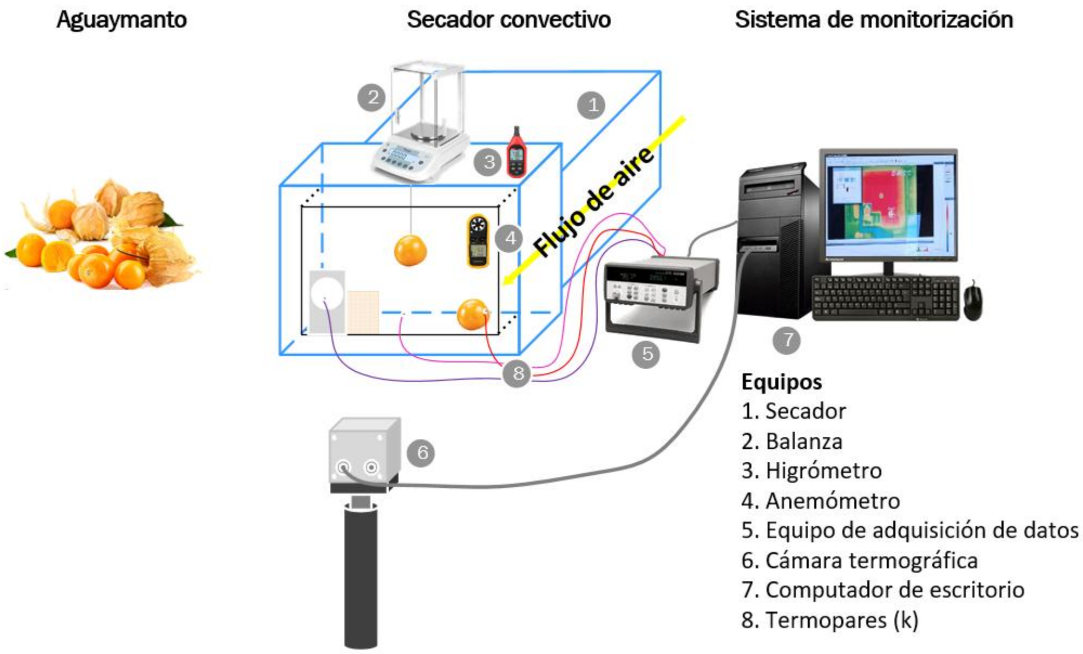

Figure 23. Sistema de monitorización de secado de aguaymanto.

Nota. Adaptado de Chuquizuta et al. (2025).

- Monitorización de la masa

Se registró la masa del fruto de aguaymanto, dentro de un secador convectivo, suspendido de una balanza de precisión (Mettler Toledo PG503-S, Spain) mediante un hilo de nylon para controlar la masa durante 13 h de secado. La masa de la muestra se registró cada cinco minutos durante la primera hora, cada diez minutos entre la primera y la segunda hora, y cada 15 min durante el resto del período de secado.

- Obtención de imágenes térmicas

Según Tomas-Egea et al. (2022) y Traffano-Schiffo et al. (2014), para obtener imágenes térmicas, la cámara térmica operó bajo las siguientes condiciones: plano focal bidimensional (matriz) de 160 x 120 píxeles, rango espectral de 7,5 - 13,0 µm, resolución de 0,05 ºC y precisión de ± 2%. La cámara térmica mide en un rango de temperatura de -

20 a 900 ºC, con un campo de visión (FOV) de 23º x 17º a una distancia mínima de 20 mm y una frecuencia de imagen de 120 Hz, conectada a un computador de sobremesa para registrar imágenes térmicas durante todo el proceso de secado utilizando el software Optris PI Connect (Optris GmbH, Berlín, Alemania). Del mismo modo, se colocó paralelamente un material emisivo de referencia (radio = 12,5 mm y ε = 0,95) al lente de la cámara termográfica a una distancia de 30 cm, con el fin de calcular la energía reflejada por la muestra y detectada por la cámara termográfica.

- Isoterma de sorción

Paralelamente al proceso de secado y bajo las mismas condiciones de operación, se utilizó un secador por convección para deshidratar 24 aguaymantos frescos sin piel. Las masas de las muestras fueron determinadas previamente utilizando una balanza de precisión (Mettler Toledo AB304-S), luego las muestras fueron colocadas en cada placa de Petri y ordenadas en tres filas y ocho columnas. Cada columna corresponde a un tiempo de secado y a una curva isotérmica diferente, a partir de la cual, se sacaron las muestras del secador y se dejaron estabilizar durante 30 min para registrar su masa y actividad de agua (Aqualab®, Serie 3 TE). A continuación, las muestras se mantuvieron a 4 ºC durante 24 h y, tras el proceso de equilibrado, se midió la masa, la actividad del agua y la humedad de las muestras equilibradas (Traffano-Schiffo et al., 2015).

3.2.3. Monitorización no invasiva de congelación de aguaymanto

Se utilizó el siguiente esquema para la monitorización de la congelación del aguaymanto (Figura 24).

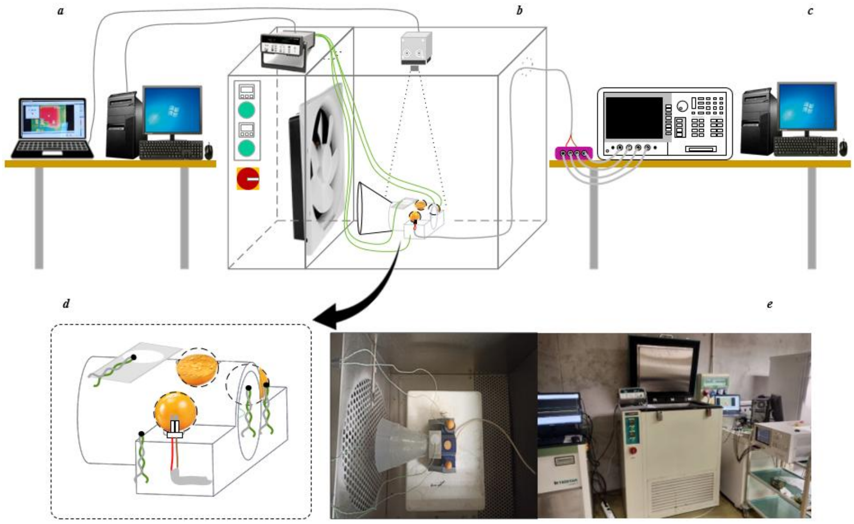

Figure 24. Sistema de monitorización de congelación de aguaymanto: a) adquisición de datos térmicos; b) proceso de congelación; c) adquisición de datos dieléctricos; d) porta muestra y e) entorno real.

Nota. Adaptado de Chuquizuta et al. (2025).

- Monitorización de la temperatura

Se registró la temperatura (tanto de la superficie como del núcleo) del fruto de aguaymanto mediante dos termopares de tipo K, los datos fueron registrados cada 5 s. Las señales digitales obtenidas por los termopares fueron convertidos a temperatura (ºC) mediante el sistema de adquisición de datos Agilent 34972A (Agilent Technologies, Malasia).

- Obtención de imágenes térmicas

El segundo fruto se colocó en posición central para medir la temperatura de la superficie. Para ello se utilizó una cámara termográfica (Optris PI® 160, Optris GmbH, Berlín, Alemania) situada a una distancia de 30 cm, y se realizaron grabaciones con un intervalo de 0.5 segundos. La cámara se conectó directamente a un ordenador portátil (PCG - 2L5M, Sony WAIO, EE.UU.) con el fin de grabar los fotogramas (vídeo) de la fruta y del material de referencia de emisividad durante el proceso de congelación en línea.

- Calorimetría diferencial de barrido

Se utilizó la metodología propuesta por Vega-Gálvez et al. (2014), con ligeras modificaciones, para determinar la temperatura de transición vítrea (Tg) y la capacidad calorífica (c_p) de muestras frescas de aguaymanto. Los perfiles térmicos de las muestras se obtuvieron utilizando un calorímetro diferencial de barrido (DSC, system 1 StarE, Mettler-Toledo, Suiza). Se calibró el equipo utilizando la función de calibración automática FlexCal, según lo recomendado por el fabricante. Cada muestra (de 10 a 15 mg) se pesó directamente en una bandeja de aluminio de 40 µL del DSC (Mettler Toledo, ME-00026763) utilizando una balanza XS-205 de Mettler Toledo, sin tener en cuenta la masa de la bandeja. Posteriormente, la bandeja se cerró herméticamente para evitar cualquier pérdida de humedad durante el análisis. Las bandejas de muestras, junto con una bandeja vacía que sirvió de control, se introdujeron en el horno DSC. Todos los experimentos se realizaron por triplicado utilizando el siguiente perfil térmico: las muestras se enfriaron desde la temperatura ambiente hasta -50°C a una velocidad de -5°C/min, y se mantuvieron durante 30 min para garantizar la congelación completa de la muestra. A continuación, las muestras se sometieron a un protocolo de calentamiento que abarcaba un intervalo de temperatura de -50°C a 80°C a una velocidad de calentamiento constante de 10°C/min. Se aplicó un periodo de mantenimiento de un minuto para garantizar la estabilidad de la temperatura antes de pasar a la siguiente fase del experimento.

- Propiedades dieléctricas

Las propiedades dieléctricas del aguaymanto se obtuvieron mediante un sensor dieléctrico de tipo aguja, tomando como referencia el trabajo realizado por Tomas-Egea et al. (2022). El sensor dieléctrico está compuesto por dos agujas de acero, cuyas dimensiones son las siguientes: Las dimensiones de la perforación se registran como 1 mm de diámetro, 2 mm de altura y 1,5 mm de separación entre ellas. La perforación penetra en la parte inferior del fruto (perpendicular a la línea ecuatorial) hasta llegar al centro (véase la Figura 24). El sensor dieléctrico se conectó a un analizador de impedancia 4294A (Agilent Technologies, Santa Clara, CA, EE.UU.), y controlado mediante un computador de mesa (ThinkCentre Tipo 7099 - 7099B8G, Lenovo, China), lo que permitió realizar el seguimiento en línea.

Antes de la calibración del analizador de impedancia, se estabilizó el equipo con un mínimo de una hora para eliminar posibles cargas estáticas o corrientes parásitas (Chuquizuta et al., 2022; W. Guo et al., 2015; Liu & Guo, 2017). La calibración se realizó de acuerdo con la siguiente metodología: medida en abierto (al aire) y en cortocircuito (mediante un conductor) descrita por Tomas-Egea et al. (2022). Se midieron los valores del espectro de impedancia compleja (resistencia - R y reactancia - X) en el rango de frecuencias (40 Hz a 1 MHz), obteniéndose 401 puntos de datos.

3.2.4. Identificación de cadena de frío de filetes de caballa

- Ciclo de congelación-descongelación

Las muestras fueron tratadas mediante ciclos de congelación-descongelación subsiguientes (C-D). Inicialmente, los filetes fueron colocados en un congelador (Marca: Pol-Eko-Aparatura, modelo: ZLN 85, origen: Polonia), programado a -25º, controlando la temperatura de los filetes hasta alcanzar -15º. Posteriormente, las muestras fueron colocadas en un refrigerador (Marca: Daewoo, modelo: FR-146RN, origen: China) a 6º, para permitir un proceso de descongelación gradual. Cuando las muestras alcanzaron los 5º, se tomaron imágenes hiperespectrales, completando así el primer ciclo de congelación-descongelación (C-D-I); Este proceso se repitió para los filetes, constituyendo el segundo ciclo (C-D-II).

- Adquisición de imágenes hiperespectrales

Se utilizó una cámara espectral (Specim FX-10, Finlandia), cuyo rango de extracción de información espectral fue de 400 a 1000 nm, una plataforma de muestra, una torre y una fuente de iluminación, todo controlado por el software Lumo Scanner de Specim LTD. El sistema operó en modo de reflectancia con una técnica de escaneo línea por línea (Pushbroom) y produce imágenes con 112 bandas. Los principales parámetros operativos fueron los siguientes: velocidad de la plataforma de muestra de 0,5 cm/s, distancia de la lente a la superficie de la muestra de 28,3 cm y apertura del diafragma de 6,4 mm

3.2.5. Predicción de calidad de carne de cerdo

- Determinación de pH

Se utilizó un pH-metro Thermo Scientific, modelo VSTAR50. La medición del pH comenzó con la calibración del equipo en tres soluciones tampón con pH 4, 7 y 10 a una temperatura de 4±0,1ºC, con un ajuste de calibración del 99,6%. Posteriormente, se pesaron 10 g de muestra, se trituró en un mortero y se homogeneizaron con 90 ml de agua destilada. El electrodo se colocó en la solución previamente preparada para determinar el pH durante 3, 4, 5, 6, 7, 8, 9, 10 y 24 horas post-mortem, la medida se realizó por triplicado.

- Determinación de color

Se utilizó un colorímetro 3nh NR200. La calibración del equipo se realizó midiendo los mosaicos en blanco y negro. La medición del color se realizó con iluminante D65 y observador de 10°. Se colocó el lente del colorímetro sobre la muestra, obteniendo las coordenadas L*, a*, y b* de las diferentes muestras a 4±1 °C, durante 3, 4, 5, 6, 7, 8, 9, 10 y 24 horas post-mortem, todas las mediciones se realizaron por triplicado y en diferentes puntos de la muestra.

- Determinación de humedad

Se utilizó una balanza de humedad AE ADAM PMB 202. Para la medición se tomaron 5 g de muestra a las 8 horas post-mortem, se colocaron en el plato de la balanza, cerrándose y sometiéndose a una temperatura de 140 °C durante 30 min. Posteriormente se registró por triplicado el porcentaje de humedad.

- Drip loss

A las 24 hpm, se cortaron tres trozos de carne de cerdo de aproximadamente 100 g cada uno y se colocaron en bolsas de polietileno previamente pesadas y se almacenaron inmediatamente en una refrigeradora (LG, modelo GT39WPPDC) a 4°C durante 72 h.

Las bolsas se mantuvieron suspendidas y completamente cerradas para evitar pérdidas por evaporación. Asimismo, se evitó que las muestras entraran en contacto con la bolsa con el fin de evitar el exudado por presión. Posteriormente, se sacaron las muestras del refrigerador y se pesaron por separado (carne y bolsa). Finalmente, se calculó el porcentaje de exudado.

- Medidas de propiedades dieléctricas

Las propiedades dieléctricas (ε' y ε'') se obtenidas en el rango de microondas, desde 0,5 GHz a 9 GHz, utilizando una sonda coaxial de extremo abierto (N1501A-001) conectada a un analizador de redes vectorial KEYSIGHT N9915A. La sonda se fijó a un soporte universal de acero inoxidable para medir las propiedades dieléctricas y evitar posibles cambios de fase debidos al movimiento del cable. Posteriormente, el equipo se calibró siguiendo las mediciones de: medida en abierto (aire), cortocircuito y agua destilada a 4°C antes de cada experimento. Una vez calibrado el equipo, se midieron las propiedades dieléctricas del agua destilada para comprobar la idoneidad de la calibración y garantizar así su estabilidad. Las propiedades dieléctricas se midieron por quintuplicado, colocando la sonda coaxial sobre la superficie de la muestra, en dirección de la fibra durante 3, 4, 5, 6, 7, 8, 9, 10 y 24 h postmortem.

3.2.6. Monitorización no invasiva de la hidratación de frejol

- Caracterización física

Se caracterizaron muestras (250 semillas) de frejol pinto (*Phaseolus vulgaris*) mediante la obtención de valores promedio de ancho (A), largo (L) y grosor (G) con un calibrador vernier (Stanley co., estándar).

- Caracterización química

La humedad, las proteínas, las grasas y las cenizas se determinaron según AOAC (2010).

- Adquisición de imágenes hiperespectrales

Previo a la obtención de la imagen hiperespectral de los granos de frejol, se programó los parámetros de funcionamiento de la cámara (Pika XC; Resonon Inc. Montana, EUA), de la siguiente manera: velocidad de la plataforma de muestra = 0.5 cm/s, apertura del diafragma = 6.4 mm y distancia a la superficie = 28.3 cm. Posteriormente, se realizó el procedimiento de calibración utilizando referencias blancas y negras. Posteriormente, se adquirieron imágenes hiperespectrales de los granos de frejol, logrando obtener cincuenta y siete imágenes de cincuenta y nueve granos en cada tiempo de hidratación mediante el software SpectrononPro 2.62 (Resonon Inc. Montana, EUA). El sistema funcionó en modo de reflectancia con escaneo línea por línea en el rango de 400 a 800 nm.

3.2.7. Aplicación de campos magnéticos a semillas de maíz morado INIA 601

- Bioestimulación de semillas de maíz morado INIA 601

Los prototipos de campo magnético estático y pulsado fueron diseñados y construidos en el Laboratorio de Tecnologías Emergentes del Instituto de Investigación de la Universidad Nacional Autónoma de Chota y el Laboratorio de Ingeniería de Alimentos de la Universidad Nacional de Jaén. El prototipo de campo magnético estático (CME) consistió en un arreglo de imanes de neodimio, que se colocaron en placas impresas de PLA. El prototipo de campo magnético pulsado (CMP) consistió en una bobina de solenoide, controladores de pulsos y una fuente de voltaje. Antes de la aplicación de los campos magnéticos, las semillas fueron seleccionadas meticulosamente, asegurando la exclusión de cualquier semilla que exhibiera signos de daño mecánico o biológico. Posteriormente, las semillas fueron transferidas al equipo para bioestimulación con campos magnéticos estáticos, con una inducción de 50 mT durante 30 min y campos magnéticos pulsados a una frecuencia de 30 Hz durante 30 min.

- Características físicas del maíz morado INIA 601

Se seleccionaron diez plantas al azar para registrar la altura de la planta y la mazorca; de los seis surcos centrales (sistema de siembra) se seleccionaron diez mazorcas al azar para medir su longitud. Se utilizó una escala de seis clases diseñada por el Centro de Investigación de Maíz y Trigo-CIMMYT para determinar el porcentaje de pudrición.

- Rendimiento de la producción de maíz morado INIA 601

El rendimiento de producción del maíz morado INIA 601 se determinó de acuerdo a las consideraciones de varios factores, entre ellos, el 14% de humedad del grano, el peso de campo, el factor de corrección de falla, el factor de falla, el factor de desgrane y el factor utilizado para expresar el rendimiento en toneladas por hectárea (t/ha).

- Obtención de extractos de maíz morado INIA 601

Las mazorcas se desgranaron para separar las brácteas, las coronas y los granos; se redujeron de tamaño con un pulverizador multifuncional (Henkel, WFA-GR1000, Düsseldorf, Alemania) y se tamizaron con un tamiz N° 35 (500 µm). La humedad de las muestras se determinó utilizando una balanza de humedad (AND MX-50) a 105 °C; se utilizó 1 g de cada muestra, junto con 20 mL de disolvente de etanol al 50% acidificado con ácido clorhídrico (HCl) al 0,01% a 6 N. Se colocó el extracto en un agitador magnético (Cimarec+ Thermo Scientific, Saint Louis, MO, EE. UU.) a 350 rpm durante 30 min a 30 °C y se centrifugó (CENTURION-Scientific Limited, Chichester, Reino Unido) a 4000 rpm durante 10 min. El sobrenadante se filtró utilizando papel Wattman No. 1 y se colocaron en recipientes ámbar, para ser almacenados a -24 °C.

- Determinación del contenido total de antocianinas (CTA)

El contenido total de antocianinas se determinó mediante el método de pH diferencial, utilizando tampón de cloruro de potasio 0,025 M a pH 1 y acetato de sodio 0,4 M a pH 4,5. Los extractos obtenidos fueron los siguientes: para la mazorca de maíz, el factor de dilución (FD) fue de 100, utilizándose 30 µL de extracto; para la bráctea, el FD fue de 50, utilizándose 60 µL de extracto; para el grano, el FD fue de 10, necesitándose 300 µL de extracto. La diferencia para cada extracto se aumentó con tampones de hasta 3 mL. Las muestras se agitaron en vórtex durante 1 min y se dejaron reaccionar durante

30 min en ausencia de luz a temperatura ambiente. Posteriormente, se dio lectura de las soluciones a longitud de onda de 520 y 700 nm utilizando un espectrofotómetro Genesys 150 UV-Visible.

- Determinación del contenido total de fenol (CTF)

Se empleó el método de Folin-Ciocalteu para determinar el contenido total de fenol. La configuración experimental implicó la utilización de 0,2 mL de las muestras diluidas, 0,1 mL de reactivo de Folin-Ciocalteu y 0,2 mL de carbonato de sodio al 10%. Estos componentes se dejaron reaccionar en un ambiente oscuro durante 1 h. Posteriormente, la reacción se midió a 765 nm utilizando un espectrofotómetro Genesys 150 UV-Visible. Previamente, se construyó una curva estándar utilizando diferentes diluciones de ácido gálico para obtener una ecuación lineal (y: a + bx; $R^2 > 0,998$). Los resultados se expresaron como mg de AGE/g bs.

- Perfil de compuesto fenólicos por HPLC

Los extractos se sometieron a análisis utilizando un cromatógrafo de ultra alta resolución (UHPLC) (Agilent 1290 Infinity II, Santa Clara, CA, EE. UU.) equipado con un detector de arreglo de diodos (DAD) y una columna Poroshell C18. El análisis se realizó a 30 °C. La separación cromatográfica se logró mediante el uso de una fase móvil que consistía en acetonitrilo y ácido fórmico al 0,1 % (fase A) y agua con ácido fórmico al 0,1 % (fase B). La separación se realizó utilizando un gradiente programado, que involucró un 95 % A + 5 % B inicial durante 15 min, seguido de una transición a 60 % A + 40 % B durante 18 min. El paso final implicó el retorno al 95 % de A + 5 % de B durante 20 min, con todos los pasos a un caudal constante de 0,3 ml/min. Los resultados se expresaron en µg/g s.

- Determinación de la actividad antioxidante

La cuantificación del método de captación del radical 2,2 difenil, 1 picrilhidrazilo (DPPH) se realizó primero el proceso de extracción implicó la dilución de 1,0 mL del extracto con metanol (200 µM), seguido de la adición de 1 mL de la solución metanólica de DPPH. Posteriormente, la mezcla se dejó reposar durante 30 min en oscuridad. Finalmente, las lecturas se obtuvieron a 517 nm utilizando un espectrofotómetro Genesys 150 UV-Visible. La CI50 se determinó a partir del gráfico del porcentaje de inhibición frente a las concentraciones utilizadas para inhibir el 50% de los radicales libres de DPPH. Los resultados se expresaron como µg de muestra/mL de la solución de DPPH.

IV. Resultados

4.1. Predicción no destructiva de sólidos solubles, acidez y pH de aguaymanto (*Physalis peruviana* L) mediante propiedades dieléctricas en el rango de microondas

Revista de investigación Agropecuaria Science and Biotechnology

Actual   Archivos   Acerca de

Inicio / Archivos / Vol. 3 Núm. 4 (2023): Octubre - Diciembre / Artículos

Predicción no destructiva de sólidos solubles, acidez y pH de aguaymanto (Physalis peruviana L) mediante propiedades dieléctricas en el rango de microondas

Tony Chuquizuta
Instituto de investigación del Mejoramiento Productivo, Universidad Nacional Autónoma de Chota, Perú.
https://orcid.org/0000-0003-3447-6296

Lesly Díaz
Instituto de investigación del Mejoramiento Productivo, Universidad Nacional Autónoma de Chota, Perú.
https://orcid.org/0009-0001-2913-9976

Tatiana Mego
Instituto de investigación del Mejoramiento Productivo, Universidad Nacional Autónoma de Chota, Perú.
https://orcid.org/0009-0002-0333-1473

Hubert Arteaga
Escuela Profesional de Ingeniería de Industrias Alimentarias, Universidad Nacional de Jaén, Carretera Jaén-San Ignacio, Km 24-Sector Yanuyacu, Jaén, Cajamarca, Perú.
https://orcid.org/0000-0003-1425-3757

Wilson Castro
https://orcid.org/0000-0001-7286-1262

DOI: https://doi.org/10.25127/riagrop.20234.935

Palabras clave: calidad, sólidos solubles, constante dieléctrica, microondas, aguaymanto

PDF   HTML

Publicado

2023-10-23

Cómo citar

Chuquizuta, T., Díaz, L., Mego, T., Arteaga, H., & Castro, W. (2023). Predicción no destructiva de sólidos solubles, acidez y pH de aguaymanto (Physalis peruviana L) mediante propiedades dieléctricas en el rango de microondas. *Revista De investigación Agropecuaria Science and Biotechnology*, *3*(4), 10–23. https://doi.org/10.25127/riagrop.20234.935

Más formatos de cita

Número

Vol. 3 Núm. 4 (2023): Octubre - Diciembre

Sección

Artículos

Condición	DOI
Aceptado (15 de agosto 2023)	**https://doi.org/10.25127/riagrop.20234.935**

PREDICCIÓN NO DESTRUCTIVA DE SÓLIDOS SOLUBLES, ACIDEZ Y PH DE AGUAYMANTO (*PHYSALIS PERUVIANA* L) MEDIANTE PROPIEDADES DIELÉCTRICAS EN EL RANGO DE MICROONDAS

Non-destructive prediction of soluble solids, acidity and pH of aguaymanto (*Physalis peruviana* L) using dielectric properties in the microwave range.

Título corto

Predicción no destructiva de calidad interna de aguaymanto

Short title

Non-destructive prediction of internal quality of goldenberry

Tony Chuquizuta[a]*, Lesly Diaz[b], Tatiana Mego[c], Hubert Arteaga[d], Wilson Castro[e]

[a] MSc. Tony Chuquizuta, Instituto de investigación del Mejoramiento Productivo, Universidad Nacional Autónoma de Chota, Perú, tchuquizuta@unach.edu.pe, https://orcid.org/0000-0003-3447-6296

[b] Bach. Lesly Díaz, Instituto de investigación del Mejoramiento Productivo, Universidad Nacional Autónoma de Chota, Perú, ldiazrafael97@gmail.com https://orcid.org/0009-0001-2913-9976

[c] Bach. Tatiana Mego, Instituto de investigación del Mejoramiento Productivo, Universidad Nacional Autónoma de Chota, Perú, tatianamego1998@gmail.com, https://orcid.org/0009-0002-0333-1473

[d] Dr. Hubert Arteaga, Escuela Profesional de Ingeniería de Industrias Alimentarias, Universidad Nacional de Jaén, Carretera Jaén-San Ignacio, Km 24-Sector Yanuyacu, Jaén, Cajamarca, Peru, hubert.arteaga@unj.edu.pe, https://orcid.org/0000-0003-1425-3757

[e] Dr. Wilson Castro, Facultad de Ingeniería en Industrias Alimentarias, Universidad Nacional de Frontera, Sullana, Piura, Perú, ing.wilsoncastro@hotmail.com, https://orcid.org/0000-0001-7286-1262

*Autor de Correspondencia: tchuquizuta@unach.edu.pe

Teléfono o celular del autor de correspondencia: +51 969637172

Resumen

La investigación tuvo como objetivo el predecir los sólidos solubles, acidez y pH de los frutos de aguaymanto (*Physalis peruviana* L.) mediante la técnica de espectroscopía dieléctrica en el rango de microondas. Las propiedades dieléctricas (constante dieléctrica – ε’) de los frutos de aguaymanto se midieron en una escala logarítmica de 0.5 a 9 GHz a 20 ºC, mediante una sonda coaxial abierta conectado a un analizador vectorial de redes, además, se determinó los sólidos solubles, acidez y pH. Los resultados mostraron que los valores medios de los espectros de la constante dieléctrica de los frutos de aguaymanto disminuyó a medida que aumentaba la frecuencia de 0,5 a 9 GHz, asimismo, los valores de sólidos solubles aumentaron de 13,493 a 14,850 ºBrix, la acidez disminuyo de 2,842 a 2,120 y el pH aumento de 3,468 a 3,663. Los mejores modelos de predicción para los sólidos solubles a 915 MHz con R^2=0.7760 y RECM=0,5185, la acidez a 5800 MHz con R^2=0,4790 y RECM=0,2391 y el pH a 2450 MHz con R^2=0,9994 y RECM=0, 0221.

Palabras clave: Calidad, sólidos solubles, constante dieléctrica, microondas, aguaymanto.

Abstract

The objective of the research was to predict the soluble solids, acidity and pH of the fruits of goldenberry (*Physalis peruviana* L.) using the dielectric spectroscopy technique in the microwave range. The dielectric properties (dielectric constant – ε ') of the aguaymanto fruits were measured on a logarithmic scale from 0.5 to 9 GHz at 20 ºC, using an open coaxial probe connected to a vector network analyzer, in addition, the soluble solids, acidity and pH were determined. The results showed that the average values of the dielectric constant spectra of the aguaymanto fruits decreased as the frequency increased from 0.5 to 9 GHz, likewise, the values of soluble solids increased from 13.493 to 14.850 ºBrix, the acidity decreased from 2.842 to 2.120 and the pH increased from 3.468 to 3.663. The best prediction models for soluble solids at 915 MHz with R^2=0.7760 and RECM=0.5185, acidity at 5800 MHz with R2=0.4790 and RECM=0.2391 and pH at 2450 MHz with R^2=0 .9994 and RECM=0.0221.

Keywords: Quality, soluble solids, dielectric constant, microwave, goldenberry.

1. Introducción

El aguaymanto (*Physalis peruviana* L.) es un fruto exótico, oriundo de la región andina del Perú, con características fisicoquímicas de: humedad (78,2 – 80%), sólidos solubles (11,6 - 13,5 ºBrix), pH (3,6 - 4,9) y acidez (1,6 – 2,4), en los estadios de madures 3, 4, 5 y 6 según la NTC 4558(Duque et al., 2011; Márquez et al., 2009; Mendoza et al., 2012; Novoa et al., 2006; Obregón-La Rosa et al., 2021; Rossi et al., 2012). Asimismo, diversos estudios manifiestan que el consumo de aguaymanto provee de vitaminas (A, B y C), carotenoides, compuestos fenólicos y fibra dietética, los mismo que, previenen enfermedades como: cáncer, diabetes, inflamaciones y del corazón (Málaga Barreda et al., 2013; Rodrigues et al., 2009; Rossi et al., 2012)

Los beneficios reportados por el consumo de aguaymanto, han incentivado a los agricultores de zonas rurales a cultivar de manera intensiva dicho fruto, permitiendo dinamizar su microeconomía rural (Sierra y Selva Exportadora, 2021). En el año 2019, Perú alcanzó 1607 t de aguaymanto fresco, reflejando un incremento de 3,47% respecto al año anterior. En el 2020 el volumen total de aguaymanto exportado fue 288 t (82% aguaymanto orgánico y el 18% convencional) a mercado estadunidenses y europeos, cuyas presentaciones fueron: aguaymanto deshidratado (92,6%), fresco (2,1%), congelado (1,65%), con chocolate (1,2%), puré (0,8%) y polvo (0,8%) (Diario - El Peruano, 2023; Léon Carrasco, 2021).

En vista del incremento de la producción de aguaymanto, los agricultores y las micro empresas dedicadas a la comercialización interna y externad de aguaymanto, vienen realizando el control de calidad de los frutos a partir de sus características fisicoquímicas (acidez, sólidos solubles, pH, color y otros) (López Nomdedeu et al., 2005). Actualmente, la calidad de los frutos de aguaymanto vienen siendo determinados a partir de sus parámetros fisicoquímicos mediante el uso de método - técnicas convencionales como penetrometría, refractometría, volumetría, colorimetría, entre otras (Villacís & Cazar, 2006; Poron, 2020), que si bien son precisas y replicables, presentan las desventajas de ser destructivas, tediosas, costosas, necesitan de pre procesamiento – acondicionamiento de muestras, generadores de desecho químicos y no son capaces de ser instaladas en líneas de producción (Brezmes-Llecha, 2000; Reyes Riofrio & Yarlequé Medina, 2018). Es por ello que, la industria frutícola, en especial la del aguaymanto, demandan de métodos y técnicas no destructivas, precisas y rápidas en la toma de decisiones, permitiendo mejorar y dinamizar el control de calidad.

Diversos esfuerzos realizados por investigadores en el desarrollo de técnicas y/o métodos no destructivos novedosos, basados en los principios fotónicos, tales como: espectroscopia de Infrarrojo cercano (NIR), Imágenes híper espectrales (HSI), y Espectroscopia dieléctrica (ED), vienen siendo aplicados al control de calidad interna de frutas (Beshah, 2014; Fito et al., 2010; Skierucha & Wilczek, 2014) La espectroscopia dieléctrica, es una técnica no destructiva, basada en la interacción del flujo de fotones con la composición química del alimento, además, de originarse dos fenómenos físicos en la dispersión gama, como la conductividad iónica (< 1GHz) y su relación con la pérdida dieléctrica causada por la vibración de especies químicas de ácidos orgánicos o electrolitos y la inducción – la orientación (> 1GHz) de moléculas dipolares como las moléculas del agua (Castro-Giráldez et al., 2013; Traffano-Schiffo et al., 2018). La aplicación de la ED ha permitido predecir el contenido de sólidos solubles [10 MHz a 1 GHz], la firmeza [20 MHz a 4500 MHz], el índice de madurez [500 MHz a 20 GHz] y el contenido de humedad [10 MHz a 4500] en caquis, manzanas, peras y melones correspondientes al rango de radiofrecuencia (Guo, Fang, et al., 2015; Guo, Shang, et al., 2015; Liu et al., 2021; Liu & Guo, 2018; Reyes et al., 2017). Así mismo, existen limitados estudios en caracterización dieléctrica de bayas, como las estudiadas por Flores-López et al., 2017; Sosa-Morales et al., 2017 quienes caracterizaron las propiedades dieléctricas (ε' y ε'') de puré de frambuesas, fresas y moras en el rango de microondas de 0,5 – 25 GHz, a temperatura de 20 – 60 °C, mas no realizaron correlación alguna con sus propiedades fisicoquímicas con las propiedades dieléctricas. Sin embargo, las predicciones realizadas a los atributos de calidad interna a las frutas antes mencionadas, ha sido realizadas mediante métodos quimiométricos y de selección de variables relevantes (frecuencias) de uso no industrial, que en su mayoría imposibilitan su escalamiento o desarrollo de sensores, así como, no se han reportado estudios en la predicción de los sólidos solubles, la acidez y el pH mediante las propiedades dieléctricas a frutos exóticos como el aguaymanto.

La utilización de herramientas matemáticas y estadísticas son cada vez más utilizadas para la predicción de atributos de calidad interna de frutos tropicales mediante propiedades dieléctricas (Guo, Fang, et al., 2015). Las técnicas quimiométricas permiten extraer la máxima información química del análisis de muestras a partir de señales (espectroscópicas) o respuestas instrumentales con muy poca selectividad (Porcel García, 2001), entre los modelos más utilizados destacan el análisis de componentes principales con regresión lineal simple (ACP-RL), la regresión lineal múltiple (RLM), la regresión de mínimos cuadrados parciales (RMCP) y regresión lineal simple (RLS), permitiendo obtener resultados prometedores en la predicción de propiedades fisicoquímicas de alimentos (Santiago Ruiz, 2020), no obstante, el uso de estos métodos de cálculo en su mayoría requieren de niveles de programación y computo avanzado y de equipos de alto rendimiento (Montero, 2016) . Por ello, el objetivo de la presenta investigación es la predicción de los sólidos solubles, la acidez y el pH de aguaymanto (*Physalis peruviana*) mediante espectroscopia dieléctrica de microondas a frecuencias puntuales de 915, 2450 y 5800 MHz.

2. Materiales y Métodos

2.1. Frutos de aguaymanto

Los frutos de aguaymanto (*Physalis peruviana* L.) se obtuvieron de los sembríos pertenecientes al fundo “Capulí el Valle” ubicado en el C.P. San Juan de Lacamaca provincia de Bambamarca, Región Cajamarca. Se utilizó 450 unidades de frutos de aguaymanto para la determinación de las propiedades dieléctricas y fisicoquímicas, 150 unidades por cada estadio de madurez (4, 5 y 6) según la NTC 4580. Los frutos de aguaymanto tuvieron las siguientes características de homogeneidad en peso, color y tamaño, sin presencia de magulladuras o daños mecánicos.

2.2. Sistemas de extracción de propiedades dieléctricas

Para medir las propiedades dieléctricas (constante dieléctrica - ε’) en un rango de 0.5 a 9.0 GHz, se utilizó una sonda coaxial de terminación abierta (N1501A-001), conectada a un analizador de redes vectorial (modelo N 9915A, Keysight Technologies), y controlada de manera remota mediante una Laptop (Lenovo HP CORE i7). Previo a la obtención de las propiedades dieléctricas, el equipo se dejó encendido por al menos 30 min con la finalidad de brindar estabilidad a los circuitos electrónicos del equipo, seguidamente se procedió con la calibración del equipo – sonda coaxial en aire, corto circuito y dieléctrico (agua destilada) sugerido por Chuquizuta et al., 2021. Para la extracción de las propiedades dieléctricas de los frutos de aguaymanto, estos se posicionaron en la parte inferior de la sonda coaxial para hacer contacto con la superficie del fruto (Figura 1), sin ejercer presión de penetración por parte de la sonda, y obteniendo las medidas por triplicado. Finalmente, se seleccionaron las constantes dieléctricas según los estadios de madurez de los frutos de aguaymanto a frecuencias puntuales de 0.915, 2.450 y 5.800 GHz.

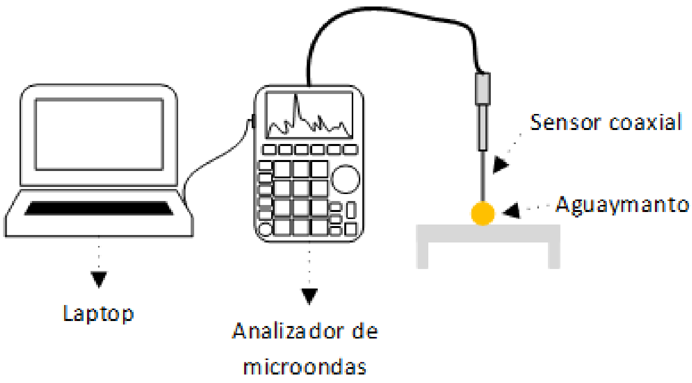

Figura 1. Sistema de adquisición de propiedades dieléctricas

2.3. Caracterización química de frutos de aguaymanto

Posterior a la extracion de las propiedades dieléctricas de los frutos de aguaymanto, se extrajo el zumo de los frutos mediante el uso de un extractor de zumo (FPSTJU407W, Oster) para las determinaciones químicas. Se determinó de los sólidos solubles (ºBrix) del zumo de aguaymanto de acuerdo con el método AOAC 932. 12 (AOAC 1980), colocando de 3 a 5 gotas sobre el lente del refractómetro (Hanna HI96800) y posterior lectura; la acidez citulable se determinó a través del método AOAC (22.008.1984), mediante la valoración con solución de NaOH (0,1 N) y expresada como porcentaje de ácido cítrico; el pH se midió de acuerdo a AOAC 981. 12 (AOAC 1998) utilizando un pH-metro (Orion Versastar pro - Thermo Scientific), previamente calibrado con tampones de 4, 7 y 10, mediante la inmersión directa del electrodo en el zumo.

2.4. Análisis estadístico

Se aplicó análisis de varianza y de comparaciones múltiple de Tukey a los resultados químicos de frutos de aguaymanto, con un margen de error de α=0.05, con la finalidad de observar diferencia significativa entre sus estadios de madurez. El procesamiento de los datos se llevó a cabo en el software Statgraphics Centurion XVIII.

Los estudios realizados por Guo et al., 2017; X. Zhu et al., 2016; Z. Zhu et al., (2019) recomiendan evaluar los modelos de predicción de los parámetros químicos utilizando el coeficiente de determinación (R^2) y la raíz del error cuadrático medio (RECM), tanto para el desarrollo del modelo de calibración como el de validación. Para el desarrollo de los modelos de predicción de las propiedades químicas del aguaymanto se tomó el 70% para la calibración y el 30% para la validación del modelo (X. Zhu et al., 2016, 2018). Para la determinación de R^2 y RECM se obtienen a través de las ecuaciones 1 y 2.

$$R^2 = 1 - \frac{\sum_{i=1}^{n} -(Y_i - \hat{Y}_i)^2}{\sum_{i=1}^{n} -(\hat{Y}_i - \bar{Y})^2} \tag{1}$$

$$RMSE = \left(\frac{\sum_{i=1}^{n} -(Y_i - \hat{Y}_i)^2}{\mathrm{n}}\right)^{0.5} \tag{2}$$

Donde $\hat{Y}_i$ e $Y_i$son los valores predichos y de referencia de una muestra (i); $\bar{Y}$ es la media de valores de referencia de todas las muestras

3. Resultados y discusión

3.1. Espectros dieléctricos – ε' de los frutos de aguaymanto (Physalis peruviana L.) en sus estadios de madurez 4, 5 y 6 (NTC 4580), en el rango de 0,5 a 9 GHz.

En la Figura 2, se muestran los espectros dieléctricos medidos de la constante dieléctrica – ε', de los frutos (Physalis peruviana L.) en los estadios de madurez 4, 5 y 6 según la NTC 4580, los espectros dieléctricos ε', de los estadios de madurez disminuyen 30,5 a 23,0 con el incremento de la frecuencia, asimismo los espectros del estadio 4 presentaron valores más altos debido a que el fruto adquiere diferentes especies químicas, como ácidos débiles, minerales, proteínas, calcio y vitaminas como resultado de la modificación de su estructura celular y los cambios fisicoquímicos que experimenta durante el ciclo de maduración. Fito et al., 2010; Talens et al., 2016; Traffano-Schiffo et al., 2018 observaron que la permitividad disminuye en estudios realizados en frutas como: naranja, mandarina y manzana en el rango de radiofrecuencias y microondas producto de la inducción u orientación (relajación dipolar) de las moléculas de agua y la conductividad iónica de los electrolitos y ácidos orgánicos débiles.(Fito et al., 2010; Talens et al., 2016) puesto que la aplicación de un flujo de fotones al tejido aumenta la energía interna de las moléculas a consecuencia de la vibración de los iones, produciendo pérdidas de energía eléctrica. Igualmente, en investigaciones hechas por Fang & Guo, 2016; Guo et al., 2011; Guo, Fang, et al., 2015; Guo, Shang, et al., 2015; Liu et al., 2021; Liu & Guo, 2018; Reyes et al., 2017en frutas como caquis, manzanas, peras y melones respectivamente observaron el mismo comportamiento de los espectros dieléctricos medidos.

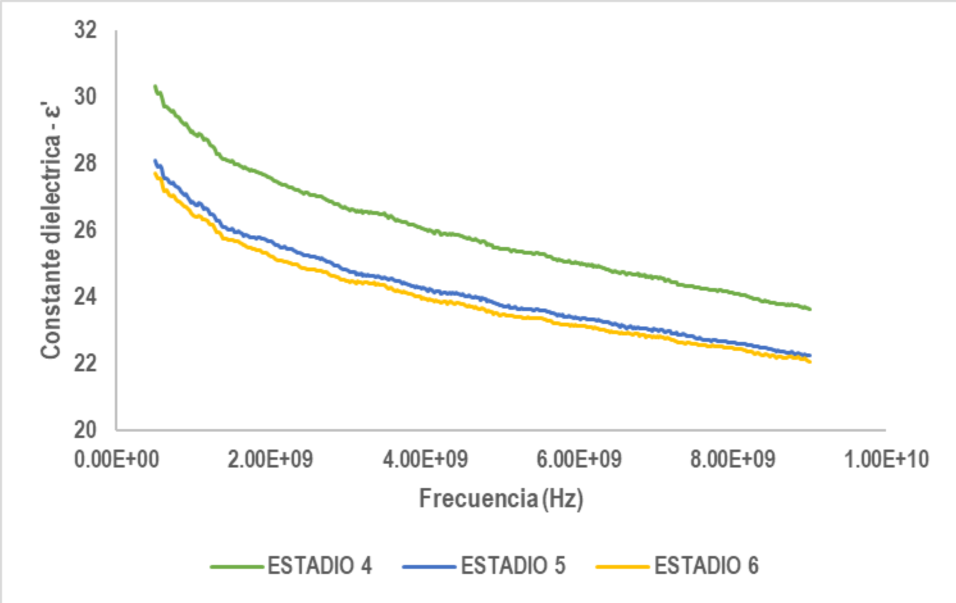

Figura 2. Espectros dieléctricos medidos de la constante dieléctrica – ε’, de los frutos de aguaymanto (*Physalis peruviana* L.) en sus estadios de madurez 4, 5 y 6 (NTC 4580), en un rango de 0,5 a 9 GHz.

3.2. Caracterización química de los frutos de aguaymanto (*Physalis peruviana* L.) en sus estadios de madurez 4, 5 y 6 (NTC 4580).

En la Tabla 1, se muestran los resultados de los sólidos solubles, la acidez y el pH de los frutos de aguaymanto (*Physalis peruviana* L.) en sus estadios de madurez 4, 5 y 6 (NTC 4580), asimismo se observa una tendencia ascendente de los sólidos solubles y pH en relación con el avance del grado de madurez del fruto, coincidiendo con los reportes (Duque et al., 2011; Fischer et al., 2005; Mendoza et al., 2012; Velasquez Cristobal & Velasquez Cristobal, 2017), tendencia atribuible a la formación de azúcares como: la sacarosa, glucosa y fructosa a partir de la hidrolisis de cadenas de almidón por intermedio de las enzimas (deshidrogenasas) (Fischer et al., 2005; Tapia, 2019). Además, de la capacidad de translocar sacarosa del cáliz al fruto (Balaguera et al., 2014) y la reducción de los ácidos orgánicos (cítrico, málico y oxálico) en aras de estabilidad celular durante la maduración (García Pesantez, 2015). Sin embargo, la acidez disminuye a mayor grado de madurez con o menor diferencia significativa en diferentes estudios, en este caso nuestros valores de acidez no concuerdan con las investigaciones de (Duque et al., 2011; Fischer et al., 2005; Mendoza et al., 2012; Restrepo et al., 2009) quienes reportaron un intervalo de acidez entre 2,0% a 1,5% para los estadios de 3 – 6, provocado por la disminución de los ácidos orgánicos durante el periodo de maduración, y el consumo de los ácidos orgánicos por enzimas deshidrogenasas para mantener la estabilidad celular y el proceso respiratorio del fruto.

Tabla 1. Propiedades fisicoquímicas de los frutos de aguaymanto (*Physalis peruviana* L.) en sus estadios de madurez 4,5 y 6.

Propiedades químicas	**n[1]**	**Estadio de Madurez (NTC 4580)**		
		4	**5**	**6**
Sólidos Solubles (ºBrix)	150	14.636 ± 0.516 [a]	14.643 ± 0.292 [a]	14.850 ± 0.444 [b]
Acidez titulable (%)	150	2.230 ± 0.240 [a]	2.105 ± 0.115 [b]	2.219 ± 0.189 [a]
pH	150	3.568 ± 0.039 [a]	3.630 ± 0.026 [b]	3.663 ± 0.012 [c]

[1]Número de unidades experimentales por estadio de madurez; los superíndices de las mismas letras de los valores medios en cada estadio de madures, indican la no existencia de diferencias significativas según la prueba de Tukey (pvalor < 0.05).

3.3. Relación estadística de los sólidos solubles, la acidez y el pH de los frutos de aguaymanto (*Physalis peruviana* L.) con la ε', a frecuencias puntuales de 915, 2450 y 5800 MHz.

La relación entre los sólidos solubles, la acidez y el pH de los frutos de aguaymanto con la ε', a frecuencias puntuales de 915, 2450 y 5800 MHz, se determinaron por del coeficiente de determinación (R^2), para el posterior desarrollo de los modelos de predicción a partir de los espectros de ε', según la metodología propuesta por Chuquizuta et al., 2022.

En la Tabla 2, se muestran las ecuaciones de relación directa mediante regresiones lineales simples de los sólidos solubles, la acidez y el pH en función de las propiedades dieléctricas (ε') a frecuencias puntuales de 915, 2450 y 5800 MHz, obteniendo una alta relación directa para sólidos solubles a 915 MHz con R^2 = 0,8951 (Figura 3a), acidez titulable a 5800 MHz con R^2 = 0,9807 (Figura 4c) y pH a 2450 MHz con R^2 = 0,9071 (Figura 5b), indicando que las tres frecuencias evaluadas tienen un buen desempeño para la predicción de las propiedades químicas estudiadas.

Tabla 2. Relación entre los sólidos solubles, la acidez y el pH y la ε', de los frutos de aguaymanto.

Propiedades Fisicoquímicas	Frecuencia		
	915 (MHz)	2450 (MHz)	5800 (MHz)
Sólidos solubles	y=0,0748X+12,636 R^2=0,8951	y=0,0807X+12,625 R^2=0,8561	y=0,0099X+14,947 R^2=0,0311
Acidez titulable	y=−0,0003X+2,1318 R^2=0,0002	y=−0,002X+2,1741 R^2=0,0052	y=−0,0177X+2,5651 R^2=0,9807
pH	y=−0,03X+4,4476 R^2=0,87	y=−0,338X+4887 R^2=0,9071	y=−0,0114X+3,9048 R^2=0,2482

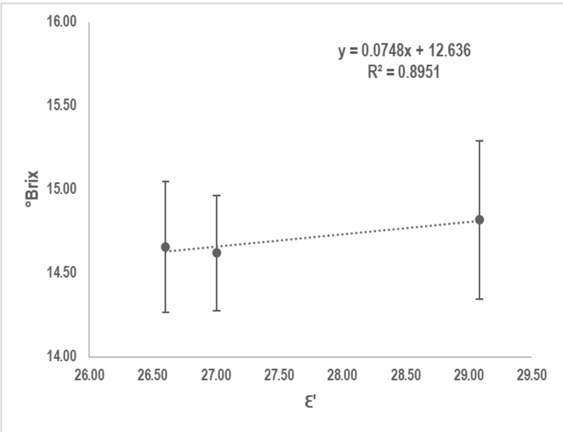

(a)

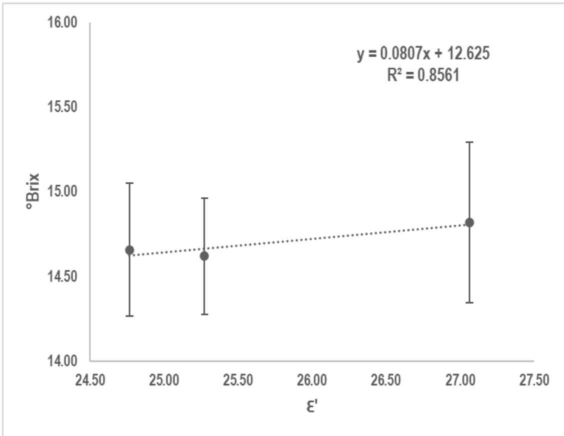

(b)

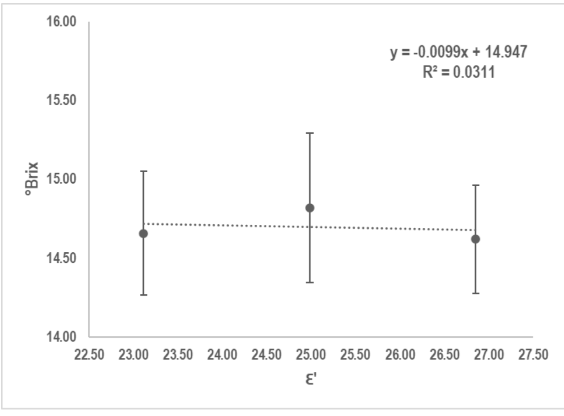

(c)

Figura 3. Relación lineal entre los sólidos solubles y ε’ de los frutos de aguaymanto, a frecuencias puntuales de 915, 2450 y 5800 MHz.

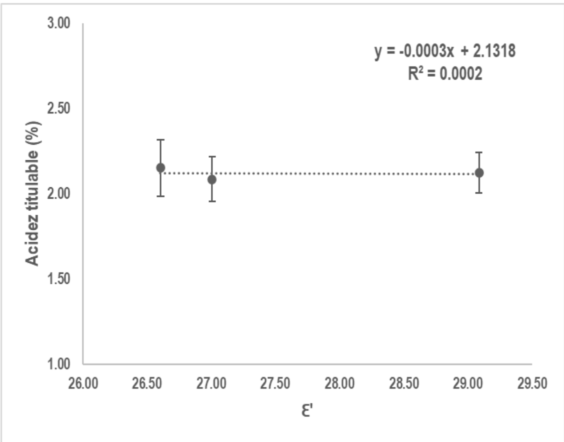

(a)

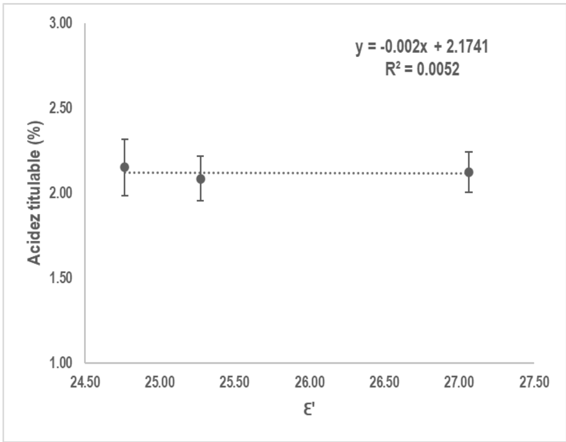

(b)

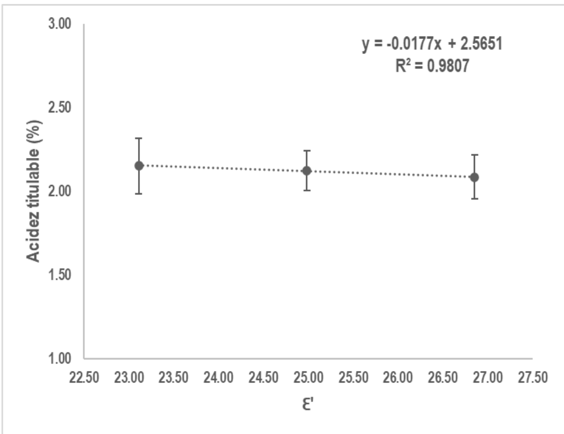

(c)

Figura 4. Relación lineal entre la cidez titulable (%) y ε’ de los frutos de aguaymanto, a frecuencias puntuales de 915, 2450 y 5800 MHz.

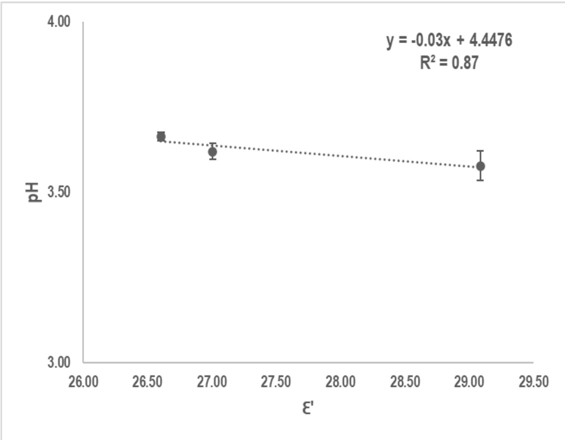

(a)

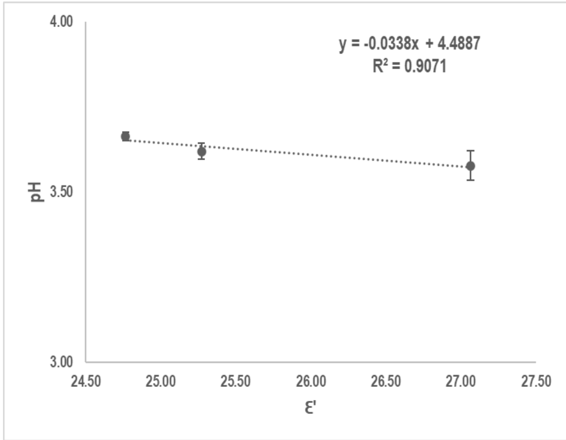

(b)

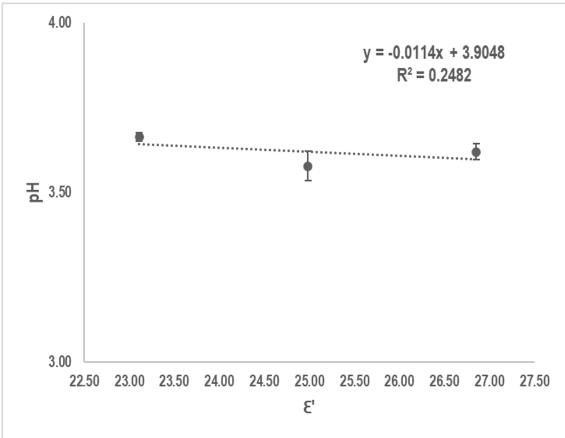

(c)

Figura 5. Relación lineal entre el pH y ε' de los frutos de aguaymanto, a frecuencias puntuales de 915, 2450 y 5800 MHz.

3.4. Predicción de los parámetros químicos de los frutos de aguaymanto a frecuencias puntuales

Luego de haber obtenido los modelos de calibración (Tabla 2) para cada uno de los parámetros químicos del aguaymanto, estas modelos fueron utilizados para obtener los valores predichos a partir del grupo de valores ε' restantes (30% del total de datos). Las correlaciones entre los valres predichos y los valores reales de referencia (parámetros químicos) se muestran en la Tabla 3, resultando el mejor modelo de predicción para los sólidos solubles a 915 MHz con R^2 = 0.7760 y RECM = 0,5185 (Figura 6a), la acidez a 5800 MHz con R^2 = 0,4790 y RECM = 0,2391 (Figura 7c) y el pH a 2450 MHz con R^2 = 0,9994 y RECM = 0,0221 (Figura 7b). Los rendimientos de la predicción obtenidos mediante la técnica de ED son similares a estudios previos realizados por Guo, Shang, et al., 2015; Liu et al., 2021; Liu & Guo, 2018; Nelson et al., 2007 en melones, caquis y manzanas obteniendo R^2 =0,80 y RECM ≤ 1,00; R^2 = 0,970, RECM =0,494 y R^2 =0,908, RECM =0,822 respectivamente; Baiano et al., 2012 en uvas acidez $R^2 \geq 0, 82$, sólidos solubles R^2 =0,94 y pH $R^2 \geq 0,80$;Weng et al., 2020 y Amodio et al., 2017 en fresas sólidos solubles totales R^2 = 0,9370, RECM = 0,1145, pH R^2 = 0,8493, RECM = 0,0501; SST R^2 = 0,85, RECM = 0,58, pH R^2 = 0,86; RECM = 0,09 respectivamente y Louw & Theron, 2010 en ciruelas sólidos solubles totales $R^2 \geq 0,817$, RECM ≤ 0,610, acidez $R^2 \geq 0,608$, RECM ≤ 0,194, sin embargo, estos estudios han utilizado técnicas espectroscópicas como: imágenes hiperespectrales, espectroscopia de reflectancia de infrarrojo - transformada por Fourier y espectroscopia de infrarrojo cercano, además, de la utilización de técnicas de pre procesamiento de señal, que si bien son precisas pero a menudo requieren algoritmos de programación más complejos para procesar y analizar los datos espectrales, lo que puede hacer que su implementación sea más desafiante en una línea de producción, a diferencia del método utilizado de regresión lineal simple es más sencillo de ser implementado en entornos de producción debido a su bajo requerimiento de cómputo y de inversión en equipos con mayor capacidad de procesamiento de datos.

Tabla 3. Predicción de los parámetros químicos de los frutos de aguaymanto a frecuencia puntual de 915, 2450 y 5800 MHz.

Propiedades Fisicoquímicas	**Frecuencia**		
	915 (MHz)	**2450 (MHz)**	**5800 (MHz)**
Sólidos solubles	R^2=0.7760	R^2=0,7604	R^2=0,7470
	RECM=0,5185	RECM=0,5166	RECM=0,4385
Acidez titulable	R^2=0,4452	R^2=0,4635	R^2=0,4790
	RECM=2466	RECM=0,2482	RECM=0,2391
pH	R^2=1,0000	R^2=0,9994	R^2=0,9984

	RECM=0,0222	RECM=0,0221	RECM=0,0445

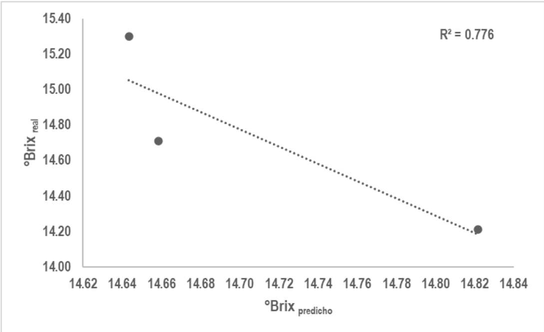

(a)

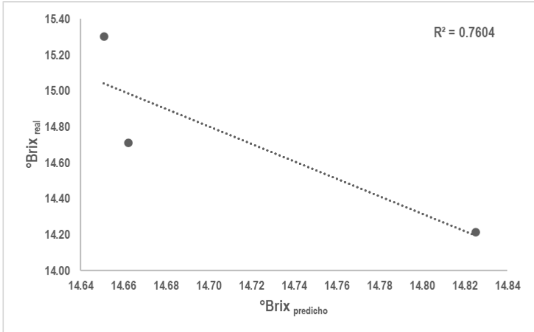

(b)

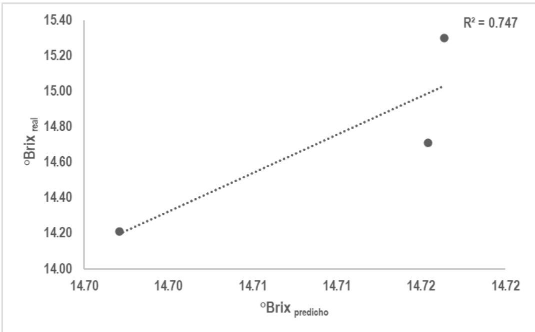

(c)

Figura 6. Modelos de validación de los sólidos solubles a frecuencias puntuales de 915, 2450 y 5800 MHz.

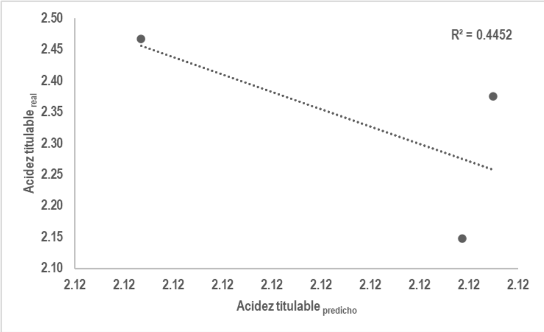

(a)

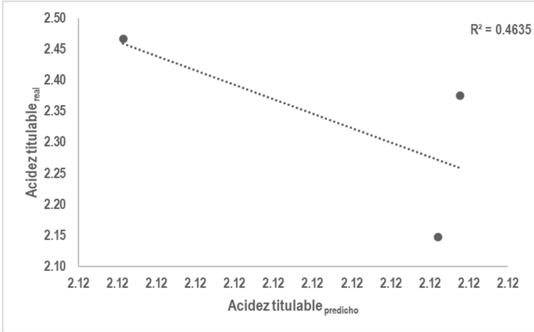

(b)

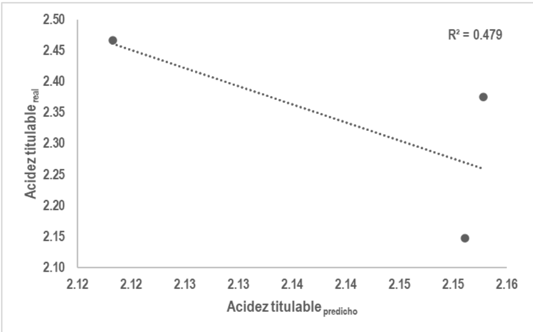

(c)

Figura 7. Modelos de validación de la acidez titulable frecuencias puntuales de 915, 2450 y 5800 MHz.

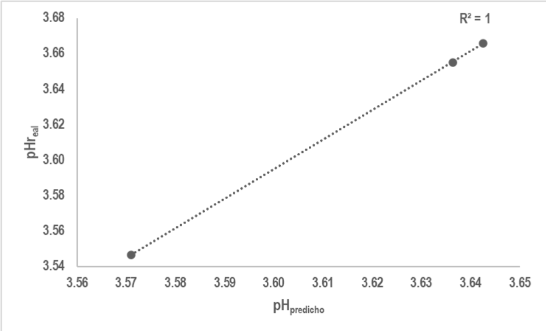

(a)

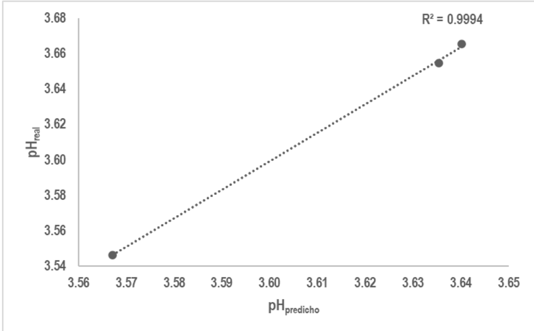

(b)

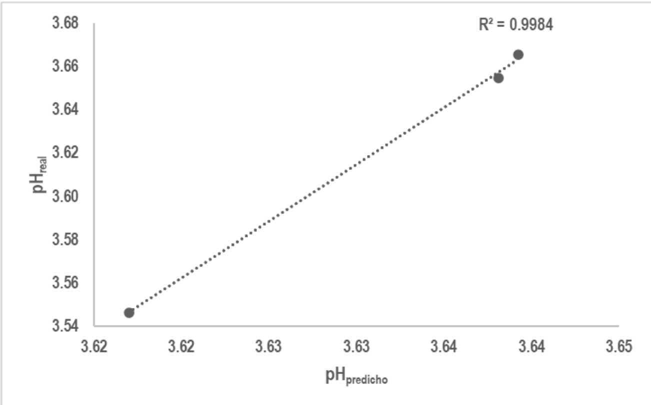

(c)

Figura 8. Modelos de validación del pH a frecuencias puntuales de 915, 2450 y 5800 MHz.

4. Conclusiones

La técnica de la espectroscopia dieléctrica ha demostrado ser una herramienta prometedora para la predicción de los sólidos solubles (R^2 = 0.7760 y RECM = 0,5185), la acidez (R^2 = 0.479 y RECM = 0,2391) y el pH (R^2 = 0.9994 y RECM = 0,0221) de los frutos aguaymanto a frecuencias puntuales 915, 5800 y 2450 MHz respectivamente, permitiendo a futuro desarrollar sensores dieléctricos miniaturizados para evaluaciones rápidas y no destructivas de la calidad interna de los frutos de aguaymanto.

Declaración de intereses

Ninguna.

Agradecimientos

A la Universidad Nacional Autónoma de Chota por el financiamiento otorgado a través del Proyecto: “Desarrollo de un sistema no destructivo para la determinación de las propiedades fisicoquímicas en frutas nativas y derivados de la región Cajamarca, usando espectroscopía dieléctrica”, con resolución de ganador “Resolución Nº 432-2018-C.O./UNACH”. Asimismo, al Instituto de Investigación del Mejoramiento Productivo – UNACH por brindar el apoyo, la instalación y el soporte técnico en la ejecución de la presente investigación.

5. Referencias

Amodio, M. L., Ceglie, F., Chaudhry, M. M. A., Piazzolla, F., & Colelli, G. (2017). Potential of NIR spectroscopy for predicting internal quality and discriminating among strawberry fruits from different production systems. *Postharvest Biology and Technology, 125*. https://doi.org/10.1016/j.postharvbio.2016.11.013

Baiano, A., Terracone, C., Peri, G., & Romaniello, R. (2012). Application of hyperspectral imaging for prediction of physico-chemical and sensory characteristics of table grapes. *Computers and Electronics in Agriculture, 87*. https://doi.org/10.1016/j.compag.2012.06.002

Balaguera, H., Martínez, C., & Herrera, A. (2014). Papel del cáliz en el comportamiento poscosecha de frutos de uchuva (*Physalis peruviana* L.) ecotipo Colombia. *Revista Colombiana De Ciencias Hortícolas, 8(2).*

Beshah, W. B. (2014). Calidad de la carne de cerdo, efecto de la congelacion y descongelacion, uso del calentamiento dielectrico para la descongelacion y la espectroscopia dielectrica para evaluar la calidad tecnologica. *SCIENCE*.

Brezmes-Llecha, J. (2000). Técnicas de control de calidad en fruta. Control de Calidad.

Castro-Giráldez, M., Fito, P. J., Ortolá, M. D., & Balaguer, N. (2013). Study of pomegranate ripening by dielectric spectroscopy. *Postharvest Biology and Technology, 86*. https://doi.org/10.1016/j.postharvbio.2013.07.024

Chuquizuta, T., Colunche, Y., Rubio, M., Oblitas, J., Arteaga, H., & Castro, W. (2022). Prediction of Quality Attributes of Fresh Unpasteurized Milk Using Dielectric Spectroscopy Coupled to Chemometric Tools. *Progress in Electromagnetics Research Symposium, 2022-April*. https://doi.org/10.1109/PIERS55526.2022.9792687

Chuquizuta, T., Oblitas, J., Arteaga, H., Yarleque, M., & Castro, W. (2021). Dielectric Spectral Profiles for Andean Tubers Classification: A Machine Learning Techniques Application. 2021 *International Conference on Electromagnetics in Advanced Applications, ICEAA 2021*. https://doi.org/10.1109/ICEAA52647.2021.9539623

Diario - El Peruano. (2023, September 14). Más del 80% de aguaymanto que exportó Perú en el 2020 fue orgánico. Https://Elperuano.Pe/Noticia/118480-Mas-Del-80-de-Aguaymanto-Que-Exporto-Peru-En-El-2020-Fue-Organico.

Duque, A. L., Giraldo, G. A., & Quintero, V. D. (2011). Caracterización de la fruta, pulpa y concentrado de uchuva (Physalis peruviana L.) Caracterization of fruit, pulp and concentrate uchuva (*Physalis peruviana* L.).

Fang, L. J., & Guo, W. C. (2016). Nondestructive measurement of sugar content and firmness in Korla fragrant pears by using their dielectric spectra. *Modern Food Science and Technology, 32(5).* https://doi.org/10.13982/j.mfst.1673-9078.2016.5.044

Fischer, G., Miranda, D., Wilson, P., & Jorge, R. (2005). Avances en cultivo, poscosecha y exportación de la uchuva *(Physalus peruviana* L.) en Colombia.

Fito, P., Castro-Giráldez, M., Fito, P. J., & Chenoll, C. (2010). Development of a dielectric spectroscopy technique for the determination of apple (Granny Smith) maturity. *Innovative Food Science and Emerging Technologies*, *11(4)*, 749–754. https://doi.org/10.1016/j.ifset.2010.08.002

Flores-López, T., Miranda-Estrada, D. E., K. T. , O.-C. J. L. , C.-C. A., Sosa-Morales, M. E., & Rojas-Laguna, R. (2017). Propiedades dieléctricas de frambuesa y mora de 0,5 a 25 GHz a 20ºC y 48ºC.

García Pesantez, D. A. (2015). Cambios físico-químicos durante el proceso de maduración de uvilla (Physalis peruviana) orgánica. Universidad Tecnológica Equinoccial.

Guo, W., Fang, L., Dong, J., & Wang, Z. (2015). Nondestructive detection of internal qualities for pears using dielectric spectra. Nongye Jixie Xueba. *Transactions of the Chinese Society for Agricultural Machinery, 46(9)*. https://doi.org/10.6041/j.issn.1000-1298.2015.09.034

Guo, W., Lin, B., Liu, D., & Zhu, X. (2017). A Novel Technique on Determining Water Content in Milk Using Radio-Frequency/Microwave Dielectric Spectroscopy and Chemometrics. *Food Analytical Methods, 10(12).* https://doi.org/10.1007/s12161-017-0946-7

Guo, W., Shang, L., Zhu, X., & Nelson, S. O. (2015). Nondestructive Detection of Soluble Solids Content of Apples from Dielectric Spectra with ANN and Chemometric Methods. *Food and Bioprocess Technology*, *8(5)*, 1126–1138. https://doi.org/10.1007/s11947-015-1477-0

Guo, W., Zhu, X., Nelson, S. O., Yue, R., Liu, H., & Liu, Y. (2011). Maturity effects on dielectric properties of apples from 10 to 4500 MHz. LWT, 44(1), 224–230. https://doi.org/10.1016/j.lwt.2010.05.032

Léon Carrasco, J. C. (2021, May 4). Exportaciones peruanas de aguaymanto alcanzaron las 288 toneladas por US$ 2.659.000 en 2020. Https://Agraria.Pe/Noticias/Exportaciones-Peruanas-de-Aguaymanto-AlcanzaronLas288Tone24284#:~:Text=Exportaciones%20de%20aguaymanto%20en%202020,3.460.000%20despachadas%20en%202019.

Liu, D., & Guo, W. (2018). Nondestructive determination of soluble solids content of persimmons by using dielectric spectroscopy. *International Journal of Food Properties, 20*. https://doi.org/10.1080/10942912.2017.1381114

Liu, D., Wang, E., Wang, G., Wang, P., Wang, C., & Wang, Z. (2021). Non-destructive sugar content assessment of multiple cultivars of melons by dielectric properties. *Journal of the Science of Food and Agriculture, 101(10)*, 4308–4314. https://doi.org/10.1002/jsfa.11070

López Nomdedeu, C., Vázquez Martínez, C., & Cos Blanco, A. I. (2005). Alimentación y nutrición manual teórico-práctico (2° EDICIÓN).

Louw, E. D., & Theron, K. I. (2010). Robust prediction models for quality parameters in Japanese plums (Prunus salicina L.) using NIR spectroscopy. *Postharvest Biology and Technology, 58(3).* https://doi.org/10.1016/j.postharvbio.2010.07.001

Málaga Barreda, R., Guevara Pérez, A., & Vargas, M. A. (2013). efecto del procesamiento de puré de aguaymanto (Physalis peruviana l.), sobre los compuestos bioactivos y la capacidad antioxidante. In Rev Soc Quím Perú (Vol. 79, Issue 2).

Márquez, C. J. C., Trillos, O. G., Cartagena, J. R. V, & Cotes, J. M. T. (2009). Evaluación físico-quimica y sensorial de frutos de uchuva (Physalis peruviana L.). Vitae, 16(1).

Mendoza, H. J. C., Rodríguez S, A. DE, & Millán, P. C. (2012). Caracterización físico química de la uchuva (physalis peruviana) en la región de silvia cauca physical and chemical characterization of golden berry fruit (Physalis peruviana) in the region of silvia cauca caracterização físico-química da groselhacapa (Physalis peruviana) na região de Silvia Cauca. In Biotecnología en el Sector Agropecuario y Agroindustrial (Vol. 10, Issue 2). Julio-Diciembre.

Montero, R. (2016). Modelos de regresión lineal múltiple. Documentos de Trabajo En Economía Aplicada.

Nelson, S. O., Guo, W. C., Trabelsi, S., & Kays, S. J. (2007). Dielectric spectroscopy of watermelons for quality sensing. *Measurement Science and Technology, 18(7).* https://doi.org/10.1088/0957-0233/18/7/014

Novoa, R., Bojacá, M., Galvis, J., & Fischer, G. (2006). La madurez del fruto y el secado del cáliz influyen en el comportamiento poscosecha de la uchuva, almacenada a 12 °C (*Physalis peruviana* L) *. *Agronomía Colombiana, 24(1).*

Obregón-La Rosa, A. J., Augusto-Elías-Peñafiel, C. C., Contreras-López, E., Arias-Arroyo, G. C., & Bracamonte-Romero, M. (2021). Características fisicoquímicas, nutricionales y morfológicas de frutas nativas. *Revista de Investigaciones Altoandinas - Journal of High Andean Research, 23(1),* 17–25. https://doi.org/10.18271/ria.2021.202

Porcel García, M. (2001). Aplicación de técnicas quimiométricas para el desarrollo de nuevos métodos cinético-espectrofotométricos de análisis.

Restrepo, A. M., Cortes, M., & Marquez, C. J. (2009). Cape Gooseberry (Physalis peruviana L.) minimally processed fortified with vitamin e. *Vitae-Revista De La Facultad De Quimica Farmaceutica, 16(1).*

Reyes, A., Yarlequé, M., Castro, W., & Chuquizuta, S. (2017). Determination of dielectric properties of the red delicious apple and its correlation with quality parameters. *Progress in Electromagnetics Research Symposium*, 2017-November. https://doi.org/10.1109/PIERS-FALL.2017.8293478

Reyes Riofrio, A. C., & Yarlequé Medina, Dr. M. A. (2018). Determinación de constantes dieléctricas por espectroscopia de microondas para el análisis de calidad de productos hortofrutículas. In Lima, Noviembre.

Rodrigues, E., Rockenbach, I. I., Cataneo, C., Gonzaga, L. V., Chaves, E. S., & Fett, R. (2009). Minerals and essential fatty acids of the exotic fruit Physalis peruviana L. *Ciência e Tecnologia de Alimentos, 29(3).* https://doi.org/10.1590/s0101-20612009000300029

Rossi, D., Fuentes, R., Pardo, F., Reyes, D., & Urbina, E. (2012). Efecto de la temperatura y sinergismo de sacarosa, sacarina y sugar light en la deshidratación osmótica de aguaymanto (*Physalis peruviana*).

Efecto de La Temperatura y Sinergismo de Sacarosa, Sacarina y Sugar Light En La Deshidratación Osmótica de Aguaymanto (Physalis Peruviana), 2(1).

Santiago Ruiz, M. B. (2020). Espacio de diseño con métodos de inversión de modelos de regresión sobre variables latentes . Universidad de Burgos.

Sierra y Selva Exportadora. (2021, March 9). Análisis de Mercado - Aguaymanto 2015 - 2020. Https://Www.Gob.Pe/Institucion/Sse/Informes-Publicaciones/1745797-Analisis-de-Mercado-Aguaymanto-2015-2020.

Skierucha, W., & Wilczek, A. (2014). Comparison of Open-Ended Coax and TDR sensors for the measurement of soil dielectric permittivity in microwave frequencies. https://www.researchgate.net/publication/26552052

Sosa-Morales, M. E., Flores-López, T., Miranda-Estrada, D. E., Kaur Kataria, T., Abraham-Juárez, M. D. R., Cerón-García, A., Corona-Chávez, A., Olvera-Cervantes, J. L., & Rojas-Laguna, R. (2017). Dielectric properties of berries in the microwave range at variable temperature. *Journal of Berry Research, 7(4)*, 239–247. https://doi.org/10.3233/JBR-170161

Talens, C., Castro-Giraldez, M., & Fito, P. J. (2016). Study of the effect of microwave power coupled with hot air drying on orange peel by dielectric spectroscopy. *LWT, 66*. https://doi.org/10.1016/j.lwt.2015.11.015

Tapia, T. (2019). Evaluación del perfil de color, características fisicoquímicas y capacidad antioxidante de tres estados de madurez comercial del aguaymanto (*Physalis peruviana* L.). In Universidad Nacional del Altiplano.

Traffano-Schiffo, M. V., Castro-Giraldez, M., Colom, R. J., & Fito, P. J. (2018). New Spectrophotometric System to Segregate Tissues in Mandarin Fruit. *Food and Bioprocess Technology, 11(2).* https://doi.org/10.1007/s11947-017-2019-8

Velasquez Cristobal, E. J., & Velasquez Cristobal, K. I. (2017). Evaluación de las características fisicoquímicas del aguaymanto (*Physalis peruviana* L.) de la zona andina y selva en diferentes estados de madurez. Universidad Nacional del Centro del Perú.

Villacís, I., & Cazar, M. (2006). Análisis físico-químico para la determinación de la calidad de las frutas. In Pontificia Universidad Católica Del Ecuador (Issue December).

Weng, S., Yu, S., Guo, B., Tang, P., & Liang, D. (2020). Non-destructive detection of strawberry quality using multi-features of hyperspectral imaging and multivariate methods. Sensors (Switzerland), 20(11). https://doi.org/10.3390/s20113074

Zhu, X., Guo, W., Kang, F., Kong, F., & Zhu, Q. (2016). Determination of Protein Content of Raw Fresh Cow's Milk Using Dielectric Spectroscopy Combined with Chemometric Methods. *Food and Bioprocess Technology, 9(12).* https://doi.org/10.1007/s11947-016-1791-1

Zhu, X., Guo, W., Liu, D., & Kang, F. (2018). Determining the Fat Concentration of Fresh Raw Cow Milk Using Dielectric Spectroscopy Combined with Chemometrics. *Food Analytical Methods, 11(5).* https://doi.org/10.1007/s12161-017-1140-7

Zhu, Z., Zhu, X., Kong, F., & Guo, W. (2019). Quantitatively determining the total bacterial count of raw goat milk using dielectric spectra. *Journal of Dairy Science, 102(9).* https://doi.org/10.3168/jds.2019-16666

4.2. Modelo termodinámico y sistema de monitorización por termografía infrarroja para el secado convectivo de la uchuva (*Physalis peruviana*)

ELSEVIER

Journal of Food Engineering

Volume 404, February 2026, 112773

Thermodynamic model and infrared thermography monitoring system for convective drying of goldenberry (*Physalis peruviana*)

T. Chuquizuta [a b], W. Castro [c], M. Castro-Giraldez [a], P.J. Fito [a]

Show more

Add to Mendeley Share Cite

https://doi.org/10.1016/j.jfoodeng.2025.112773

Get rights and content

Condición	DOI
Aceptado (06 de agosto, 2025)	**https://doi.org/10.1016/j.jfoodeng.2025.112773**

THERMODYNAMIC MODEL AND INFRARED THERMOGRAPHY MONITORING SYSTEM FOR CONVECTIVE DRYING OF GOLDENBERRY (*Physalis peruviana*)

T. Chuquizuta[1,2]; W. Castro[3]; M. Castro-Giraldez[1]; P.J. Fito[1*]

[1] Instituto Universitario de Ingeniería de Alimentos FoodUPV, Universitat Politècnica de València, Camino de Vera s/n, Valencia 46022, Spain

[2] Instituto de Investigación del Mejoramiento Productivo, Universidad Nacional Autónoma de Chota, Chota 06120, Perú

[3] Facultad de Ingeniería de Industrias Alimentarias y Biotecnología, Universidad Nacional de Frontera, Sullana 20100, Perú

*author for correspondence: pedfisu@tal.upv.es

Abstract

The goldenberry (*Physalis peruviana*) is a highly perishable Andean fruit with valuable nutritional and functional properties. Its preservation poses a challenge due to its high moisture content. This study presents an integrated method combining infrared thermography (IR) and irreversible thermodynamics to characterize the convective drying process of goldenberry.Samples were dried at 60 °C and 1.0 m/s air velocity. Weight loss, surface temperature, and water activity were recorded over 13 h using thermocouples, precision balances, and IR imaging. An irreversible thermodynamic model was applied to estimate water flux, free energy changes, and chemical potential gradients, including mechanical energy effects. The phenomenological coefficient from Onsager's relation was correlated with water flux to describe internal water migration. IR thermography enabled real-time, non-invasive monitoring of temperature and emissivity, correlating with morphological changes during drying. Sorption isotherms were fitted using the GAB model, and thermodynamic analysis allowed separation of physical and mechanical contributions to water potential. This approach provides a deeper understanding of moisture transport during drying and demonstrates the usefulness of combining IR monitoring with thermodynamic modeling. It offers a promising tool for optimizing drying protocols in high-moisture tropical fruits like goldenberry.

Keywords: Thermodynamic, infrared thermography, physalis, drying and monitoring.

Highlights

- An irreversible thermodynamic model was developed to characterize water flux, and water transport mechanism, during goldenberry drying.
- Different physical properties of goldenberry were obtained, such as specific heat, emissivity, water activity and entropy.
- The evolution of air properties (energy and moisture) throughout the drying treatment of goldenberry is shown.
- Infrared thermography enabled non-invasive, real-time monitoring of surface temperature.
- The Onsager phenomenological coefficient was correlated with water flux, allowing the decoupling of physical and mechanical energy contributions to water transport.

1. Introduction

The goldenberry (*Physalis peruviana*), also known as uchuva (caspe goldberry or goldberry) in several Latin American countries, is a fruit that originated in the Andean region and is widely regarded as an exotic fruit, especially appreciated when consumed fresh (Bazalar Pereda et al., 2019; Blas Saavedra et al., 2024; Hidayat et al., 2021; Yıldız et al., 2015). The goldenberry is composed of 75–85 % (w/w) moisture, 11–16 g of carbohydrates, 0.3–1.9 g of protein, 0–0.5 g of fat, and 43 mg of ascorbic acid per 100 g of the edible portion (Puente et al., 2011; Rossi et al., 2012). The fruit contains various bioactive components, including vitamin C, β-carotenes, total phenols, phenolic acids, and flavonoids. These compounds confer beneficial properties to the consumer, such as anti-inflammatory effects. The goldenberry fruit has been demonstrated to possess antioxidant, anticarcinogenic, antidiabetic, and cardiovascular disease prevention properties (Ordóñez-Santos et al., 2017; Pasten et al., 2024; Vega-Gálvez et al., 2015). However, the physicochemical and nutritional properties of the fruit vary according to its stage of maturity and the technical and post-harvest conditions under which it is cultivated (Avendaño et al., 2022; Hidayat et al., 2021; Lopez et al., 2024; Muñoz et al., 2021).

In recent years, Colombia and Peru have emerged as prominent players in the marketing and export of fresh goldenberry fruits to Europe, Asia, and North America, driven by the fruit's recognised nutritional benefits for human health (Obregón La Rosa et al., 2021; Ramirez-Hernandez et al., 2020). However, due to the respiration rate (influenced by temperature), high moisture content and water activity, goldenberry fruits are considered highly perishable fruits and therefore have a limited shelf life (Garavito et al., 2021). Additionally, they are susceptible to fungal and yeast contamination (Fischer et al., 2011; Fischer & Martinez, 1999), underscoring the necessity for preservation techniques aimed at reducing moisture content and, consequently, prolonging the shelf-life of the product (İzli et al., 2014).

Drying is a preservation method that is employed extensively in the agri-food sector, particularly in the context of fruit dehydration. This process enables the extension of fruit shelf-life by reducing moisture content and water activity, thereby minimising and/or inhibiting spoilage, enzymatic activity and microbial growth (Doymaz, 2008; Vásquez-Parra et al., 2013; Vega-Gálvez et al., 2015). Moreover, the process of fruit dehydration involves a series of concurrent operations, including mass and heat transfer (Lopez et al., 2013; Pasten et al., 2024), improving water diffusion conditions from the interior to the surface in contact with the circulating air has been demonstrated (Barbosa-Cánovas & Vega-Mercado, 1996; İzli et al., 2014; Vega-Gálvez et al., 2015). Consequently, this leads to changes and deterioration in the cell wall, collapse and stiffness (texture) of cell tissues (Cabrera Ordoñez et al., 2017; Nawirska-Olszańska et al., 2017; Vega-Gálvez et al., 2015).

Conversely, the convective drying method is more extensively employed in the agri-food industry, where numerous endeavours have been made to model the drying kinetics and ascertain the effective water diffusion of goldenberry fruits. The mathematical models most commonly used to predict the behaviour of drying kinetics are: Newton, Wang and Sing, Henderson-Pabis, Page, Logarithmic, Midilli and Kucuk (İzli et al., 2014; Junqueira et al., 2017; L. Puente et al., 2020, 2021; Uribe et al., 2022; Vega-Gálvez et al., 2014). In a similar vein, Yasin et al. (2016), Vásquez-Parra et al. (2013) and Vega-Gálvez et al. (2014) have obtained the effective diffusion assuming a finite plate and sphere geometry. However, it should be noted that the equations employed in modelling kinetics and determining effective diffusion have certain limitations, such as the failure to consider additional factors (such as relative humidity), variations in operating temperature and interactions between fruit components. Furthermore, the aforementioned equations are based on empirical and simplified models, which may have a detrimental effect on the accuracy of the calculations for the design of a dryer and the dehydration process.

Thermodynamics is the scientific study of energy transfer and mass movement during the process of food dehydration. In this context, the analysis of sorption isotherms is considered a fundamental tool for the design, modelling and optimization of technological processes (Aviara N, 2020; Kraiem et al., 2023). These isotherms are also pivotal in analysing the thermodynamic interactions between food components and water, as well as in quantifying the energy requirements of the dehydration process. Conversely, several researchers advocate the utilisation of the Guggenheim-Anderson-de Boer (GAB) and Brunauer-Emmett-Teller (BET) models to predict avocado sorption isotherms (Pasten et al., 2024; L. Puente et al., 2020; Vega-Gálvez et al., 2015; Vega-Gálvez et al., 2014). However, such predictions are often limited to parameters such as critical humidity, isosteric heat, entropy and enthalpy (Aviara N, 2020; Akpinar et al., 2006; Junqueira et al., 2017; Pasten et al., 2024; L. Puente et al., 2020; Ruan et al., 2022; Yasin et al., 2016). It is therefore necessary to study new thermodynamic variables such as exergy and the optimization of energy loss minimization, in order to enrich the understanding of the dehydration process.

Moreover, the examination of energy interactions and thermodynamic behaviour between air and food during dehydration in a drying chamber, based on the second law of thermodynamics, remains under-explored in the scientific literature. This paucity of research is due to the intricacy of studying enthalpy and exergy changes that occur in both reversible and irreversible processes (Akpinar et al., 2006; Talens et al., 2016). The surface temperature of the food is a primary factor influencing these changes, arising from convective heat transfer. The most common method to measure the temperature of a food during dehydration is through the use of calibrated thermocouples (types K, T or Pt), data loggers and computers. However, this method is destructive and restricts temperature recording to a single point (Motahayyer et al., 2019; Yilmaz et al., 2008). Consequently, there is a clear need to develop non-destructive systems that facilitate the monitoring of surface temperature during fruit drying, thus improving upon the aforementioned problems (Kylili et al., 2014).

Recent studies have demonstrated the efficacy of infrared thermography (IR) as a valuable tool for two-dimensional, non-contact temperature diagnosis of biological materials during the drying process, providing relevant information on heat transfer (Kylili et al., 2014; Motahayyer et al., 2019; Traffano-Schiffo et al., 2014). The underlying principle of infrared thermography is the measurement of infrared radiation emitted by a surface, thereby generating an image of the thermal distribution (Gowen et al., 2010). This technology has been extensively employed in the control of processes such as the drying of pork (Traffano-Schiffo et al., 2014a), potatoes (Tomas-Egea et al., 2021a), coffee beans (Reyes-Chaparro et al., 2024), mushrooms (Lombraña et al., 2010), rice (ElGamal et al., 2017) and wood (Lerman & Scheepers, 2023). Its application in freezing potatoes (Cuibus et al., 2014a) and water stress analysis in citrus (Pappalardo et al., 2023) has also been documented. However, there is a paucity of studies on its use in the drying of berries, such as grapes (Reyes-Chaparro et al., 2024), and even more so in tropical berries such as goldenberry.

The initial objective of this study was to provide a comprehensive overview of the advantages of the first and second laws of thermodynamics in the drying process, and to explore non-invasive methods of monitoring, such as infrared thermography. The subsequent aim was to develop a thermodynamic model to facilitate a more in-depth understanding of the mechanisms of internal heating and water transport in goldenberry fruit during hot air drying. This was to be achieved by monitoring the process with infrared thermography.

2. Materials and methods

The experimental procedure is shown in Fig. 1. Likewise, each step of the flowchart is explained in the following paragraphs. Each experimental condition was tested with three replicates (n = 3).

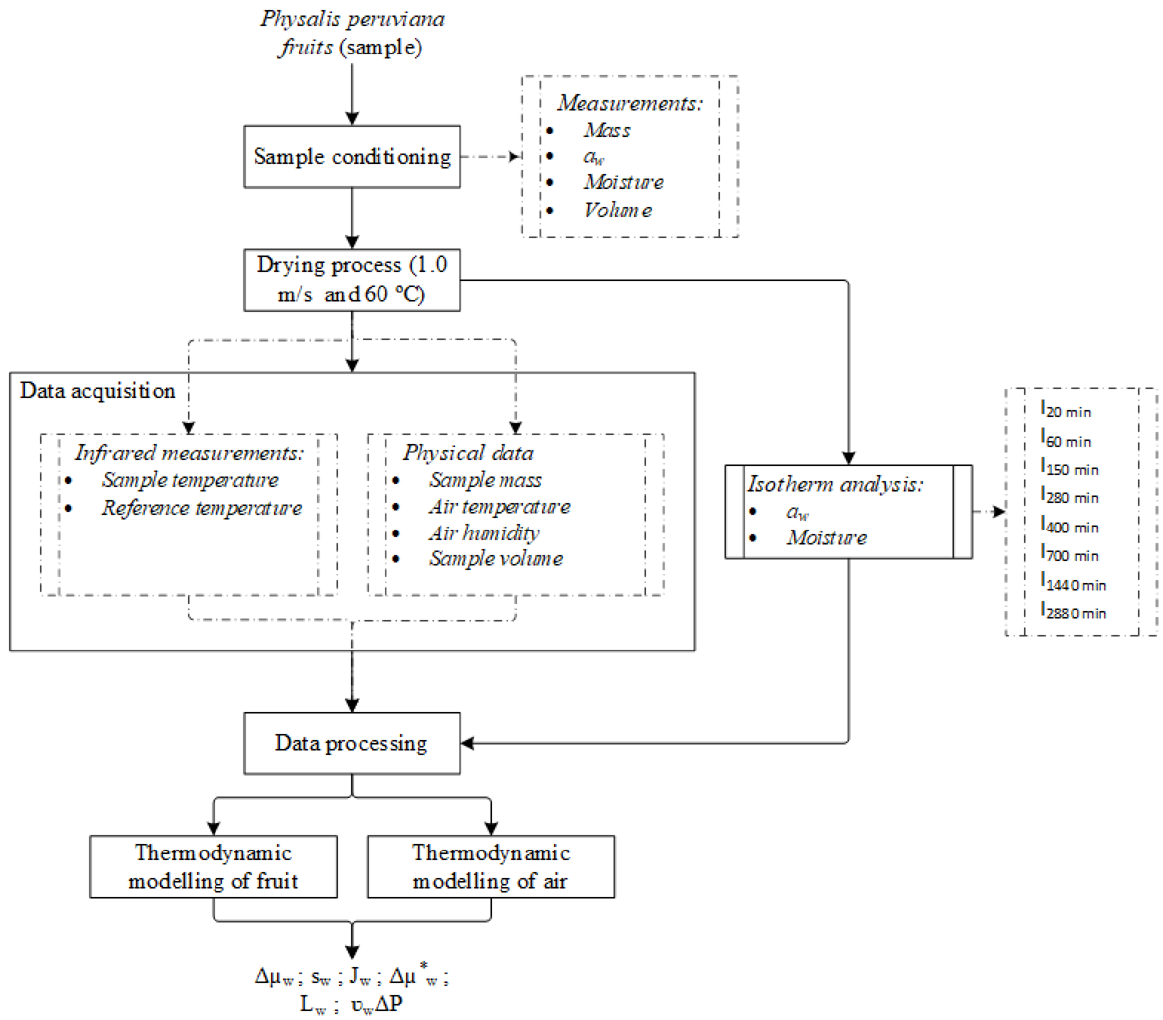

Figure 1. Experimental procedure in drying process of *Physalis peruviana*.

2.1. Sample goldenberry fruits.

The samples of fresh goldenberry fruit at commercial ripeness, coming from Ecuador, were obtained through the importing company Ammarket (Orihuela, Alicante - Spain). The goldenberry fruits arrived in refrigerated boxes (100 g / box) with uniform size (diameter) and weight, 3.8±0.21 cm and 3.9±0.4 g, respectively, which were kept in a refrigerator at 6 °C until later analysis and execution of the experiment.

2.2. Sample conditioning.

Before drying the goldenberry fruit, the skin of two fruits (for each replicate) was removed manually using tweezers. The fruit's moisture content (dry basis) was also characterized using the methodology of AOAC Method 934.06, 2000.

2.3. Drying process

Before drying, the works of (Cuibus et al., 2014; Talens et al., 2017; Traffano-Schiffo et al., 2014) were used as a reference to install and locate the following equipment in the dryer: a precession balance (Mettler Toledo PG503-S, Spain), a thermal imaging camera (infrared camera) (Optris PI® 160, Germany), a data logger (Agilent 34972A, Malaysia) and a desktop computer. In addition, type K thermocouples, reference emissivity material ($\varepsilon = 0.95$ - Optris GmbH, Germany), and graph paper (9 cm^2) were placed as shown in Fig. 2.

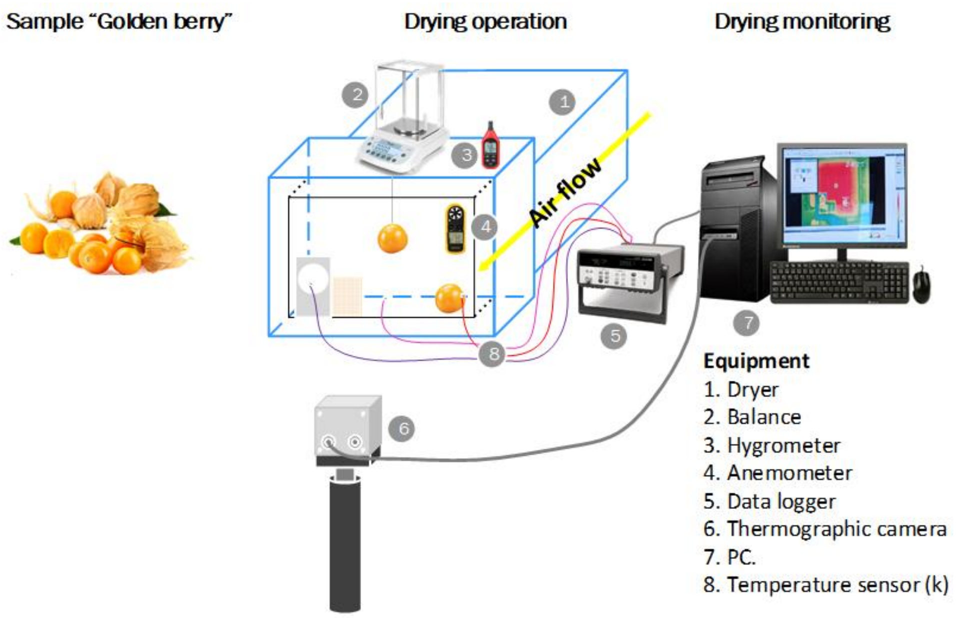

Fig. 2. Equipment for convective drying operation of *Physalis peruviana* must be assembled.

Two units of goldenberry fruit were placed in a convective dryer, and one of the fruits was suspended from a precision balance by means of a nylon thread to monitor the mass during 13 hours of drying. The mass of the sample was recorded every five minutes during the first hour, every ten minutes between the first and second hours, and every 15 minutes for the rest of the drying period. The second goldenberry fruit was also placed to the right of the suspended fruit, in order to measure the surface emissivity.

The convective dryer was operated at a temperature of 60 ºC and a drying air velocity of 1.0 m/s (monitored with a Proster anemometer, model HT 383, China). During the drying process, the temperatures of the sample, drying air and reference emissivity material were recorded with thermocouples (connected to an Agilent 34901A multiplexer, Malaysia) to correct the emissivities recorded by the thermal camera. Dehydration was performed in triplicate.

2.4. Infrared thermography

According to (Tomas-Egea et al., 2022; Traffano-Schiffo et al., 2014, in order to obtain thermal images, the thermal camera operates under the following conditions: two-dimensional focal plane (matrix) of 160 x 120 pixels, spectral range of 7.5 – 13.0 µm, resolution of 0.05 ºC and accuracy of ± 2%. The thermal camera measures in a temperature range of -20 to 900 ºC, with a field of view (FOV) of 23º x 17º at a minimum distance of 20 mm and a frame rate of 120 Hz, which is connected to a desktop computer to record thermal images throughout the drying process using the Optris PI Connect software (Optris GmbH, Berlin, Germany). Similarly, the reference emissivity material (radius = 12.5 mm and ε = 0.95) was placed parallel to the lens of the thermographic camera at a distance of 40 cm to calculate the reflected energy received by the thermographic camera.

2.5. Sorption isotherm modelling

In parallel with the drying process and under the same operating conditions, a convection dryer was used to dehydrate 24 fresh skinless goldenberry. The masses of the samples were previously determined using a precision balance (Mettler Toledo AB304-S), then each sample was placed on each petri dish and arranged in three rows and eight columns. Each column corresponds to a different drying time and isothermal curve (see Fig. 1), from which the samples were taken out of the dryer and allowed to stabilize for 30 min to record their mass and water activity (Aqualab®, Series 3 TE). The samples were then kept at 4 ºC for 24 h, and after the equilibration process, the mass, water activity, and moisture of the equilibrated samples were measured (Traffano-Schiffo et al., 2015).

The experimental moisture values and their respective water activities were adjusted with the GAB model by Equation (1).

$$X_W = \frac{X_{W0}\ C\ a_w}{(1-K\ a_w)(1+(C-1)a_w)} \quad (1)$$

Where: X_w corresponds to the meat sample moisture (kg_w/kg_{dm}), X_{w0} the monomolecular moisture layer (kg_w/kg_{dm}), *C* corresponds to the Guggenheim constant (dimensionless) and *K* is the correlation factor (dimensionless).

2.6. Differential Scanning Calorimetry (DSC)

The methodology proposed by (Vega-Gálvez, López, et al., 2014a), with slight modifications, was used to determine the heat capacity (Cp) of fresh goldenberry samples. The thermal profiles of the samples were obtained using a differential scanning calorimeter (DSC, System 1 StareE, Mettler-Toledo, Switzerland), which was calibrated using the automatic calibration function FlexCal, as recommended by the manufacturer. Each sample (10 - 15 mg) was weighed directly into a 40 µL DSC aluminium pan (Mettler Toledo, ME-00026763) using a Mettler Toledo XS-205 balance, excluding the mass of the pan. The pan was then hermetically sealed to prevent moisture loss during the analysis. The sample pans, along with an empty pan used as a reference, were placed in the DSC oven. All experiments were performed in triplicate, following the thermal profile described below: samples were cooled from room temperature to −50 °C at a rate of −5 °C/min and held at this temperature for 30 minutes to ensure complete freezing. Subsequently, the samples were heated from −50 °C to 80 °C at a rate of 10 °C/min, and held at 80 °C for 1 min.

3. Results and discussion

3.1. Drying kinetics of Physalis peruviana

To better understand the drying kinetics of goldenberry, it is essential to first describe the internal tissue structure through which water is transported. The fruit consists of approximately 1 % epidermal tissue (which is removed prior to drying), around 15 % cortical parenchyma near the skin, 3 %–5 % vascular tissue, and between 70 % and 85 % spongy parenchyma, with the remainder corresponding to seeds (Balaguer et al., 2024). These anatomical features imply that water transport involves multiple coordinated pathways: apoplastic (extracellular), symplastic (intracellular, via plasmodesmata), and transmembrane (connection extra and intra cellular transport), all primarily occurring within parenchymal tissues. The coexistence of these transport mechanisms, along with structural events such as plasmolysis, results in multiple internal water transport rates operating simultaneously during drying.

Fig. 3 shows the classic drying curve of the goldenberry sample, which started with an initial moisture of 4.102±0.043 (kgw/kgt) and reached a final moisture of 0.298 ± 0.108 d.b. in 13 h of continuous drying, corresponding to a mass loss of 74.55% (± 2.11). It should be noted that the surface moisture of the goldenberry sample evaporates first, then the water moves from the inside of the sample to the surface by diffusion principles (Doymaz, 2008), in agreement with the work reported by (Vásquez-Parra et al., 2013; Lopez et al., 2013).

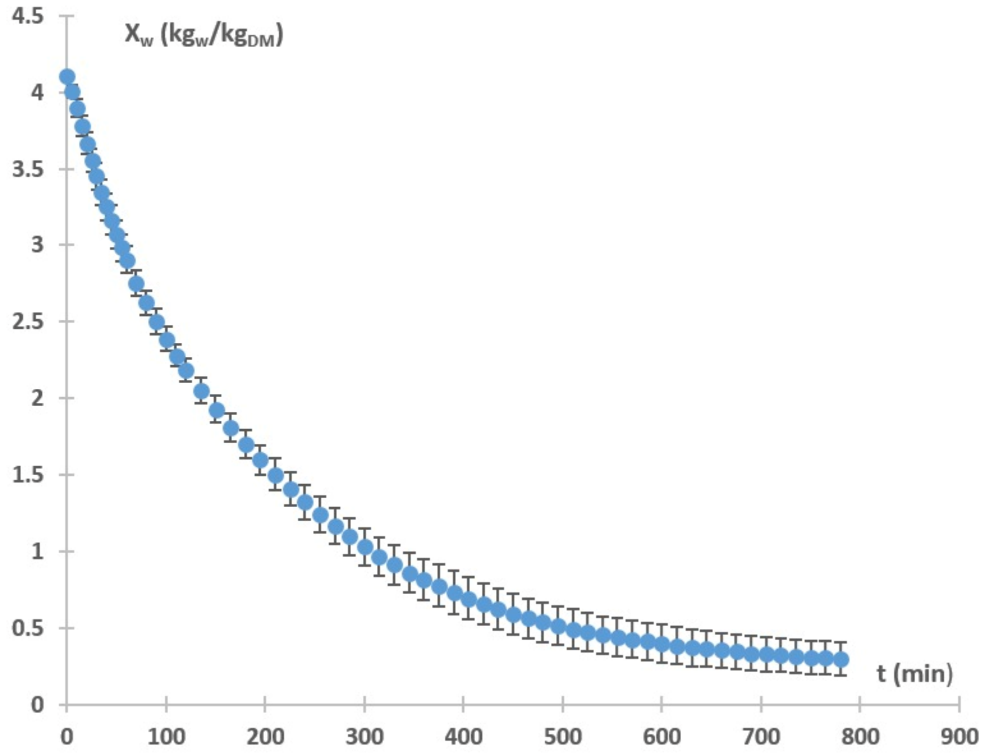

Fig. 3. Drying curve of *Physalis peruviana* at 60 ºC.

Nevertheless, given the inherent difficulty in observing the drying stages undergone by the goldenberry, it is essential to plot the drying speed curve (Fig. 4) in order to gain insight into this process.

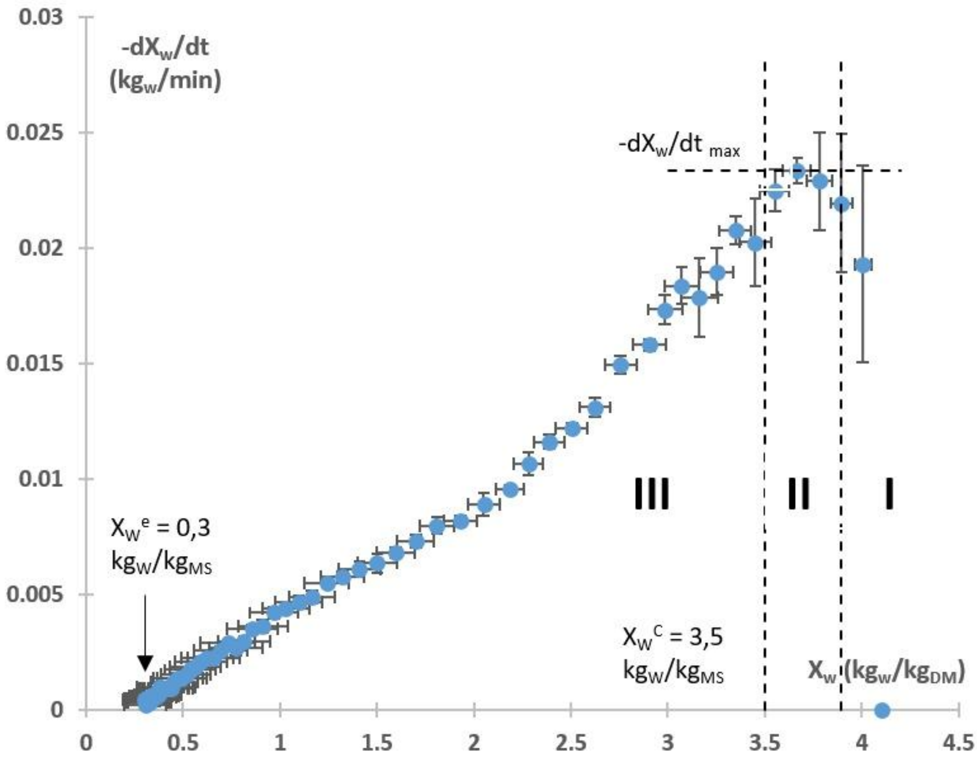

Fig. 4. Drying speed of *Physalis peruviana*; drying stage: I - induction, II – constant speed and III – decreasing speed.

The drying rate curve illustrates the variation in drying rate in relation to the dry-base moisture content and allows the observation of three distinct drying phases. A brief induction phase (I) is evident during the initial three points, succeeded by a phase of constant drying rate (II) at 0.024 kg_w/min with a critical moisture content of 3.5 kg_w/kg_{DM}. Subsequent to the critical moisture content, a decline in the drying rate is observed until equilibrium moisture is reached (0.3 kg water/kg dry matter), which occurs 45 minutes after the commencement of the drying process.

Additionally, during the drying process, the goldenberry exhibits deformation associated with water loss and morphological transformations resulting from internal cellular plasmolysis of the fruit, as evidenced by volume variation (Fig. 5).

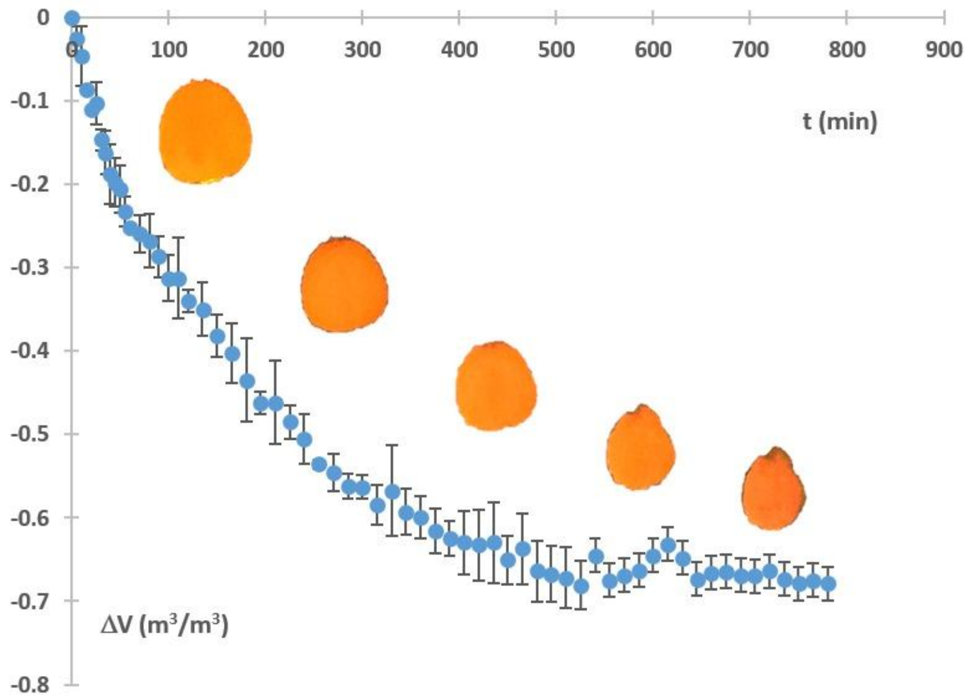

Fig. 5. Volume variation curve of *Physalis peruviana* during the drying process at 60 ºC.

Goldenberry consists mainly of parenchymatic tissue, characterized by thin primary cell walls, high vacuole content, and loosely packed cells. During drying, the removal of water from this tissue leads to plasmolysis, collapse of cell walls, and progressive loss of turgor pressure. These structural changes contribute to the distinct phases observed in the drying rate curve. In the initial constant-rate period, free water from intercellular spaces and vacuoles is easily evaporated. As drying progresses and water must diffuse through increasingly rigid and collapsed cell matrices, the drying rate decreases, marking the transition to the falling-rate period.

It is important to note that the loss of volume is directly proportional to the water loss, resulting in an overall volume reduction of 68 %. If the tissue volume were to shrink exactly in proportion to the volume of water lost, the expected shrinkage would be approximately 95 %. However, part of the space formerly occupied by water becomes filled with air, leading to a partial swelling or expansion of the tissue matrix.

The drying process is a complex operation, and existing empirical and/or physical models are inadequate for describing and explaining the transfer of mass and heat in the dehydration of food. In recent studies such as Traffano-Schiffo et al. (2014), Talens et al. (2016a, 2016b), the importance of using irreversible thermodynamics to describe the phenomenon of water transport during drying based on the structure of the food has been demonstrated. Therefore, it is crucial to determine the flow of water extracted from the fruit using Equation (2).

$$J_W = \frac{\Delta M_W \cdot M_0}{\Delta t \cdot S \ \ Mr_W} \tag{2}$$

In this equation, ΔM_w represents the mass variation of water in the sample, M_0 denotes the initial mass, Δt signifies the variation in drying time, and S is the surface obtained from the volume (Figure 5), assuming that the goldenberry is a sphere. M_{rW} represents the molecular mass of water (18 g /mol).

Fig. 6 shows the water flow extracted from the goldenberry sample exhibits an increase until reaching 0.01831 ± 0.00089 ($kmol_W/m^2$ s), which is caused by the appearance of the drying induction stage and is almost non-existent in other fruits. Once the drying induction stage is complete, the water flow declines throughout the remainder of the drying process, reaching a final value of 0.000611 ± 0.000091 ($kmol_W/m^2$ s), as anticipated, coinciding with work carried out on samples of goldenberry by (Vega-Gálvez, López, et al., 2014b; Vega-Gálvez, Puente-Díaz, et al., 2014).

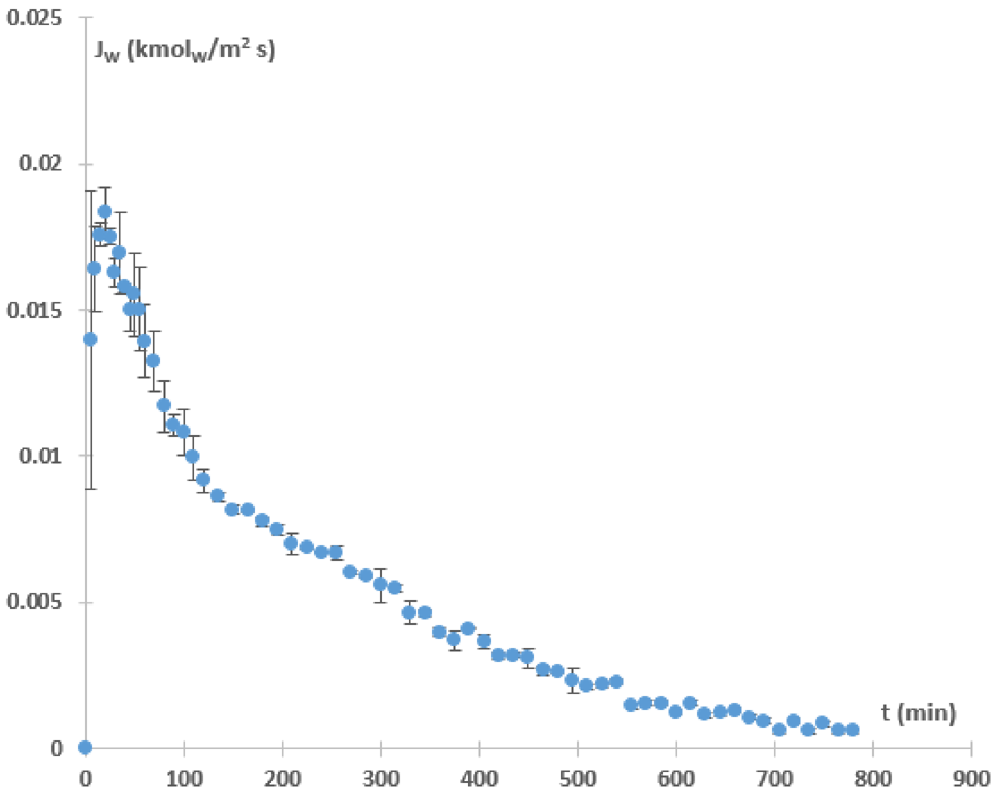

Fig. 6. The evolution of water flux during the drying process of *Physalis peruviana*.

3.2. Thermographic monitoring of the drying process of *Physalis peruviana*

The importance of monitoring the temperature variation in the boundary layer between the surface temperature of the goldenberry sample and the temperature of the drying air using a thermal imager during the drying process allows the surface phenomena affecting drying to be identified and described (Traffano-Schiffo et al., 2015). It should be noted that the thermal imager detects the energy flow through its pyroelectric detector, which is based on the Stefan-Boltzmann law for heat transfer by radiation (Talens et al., 2017).

In order to interpret the measurements of the radiant energy flux recorded by the thermal camera, and therefore calculate the emissivity of the goldenberry sample during drying, it is important to carry out a radiant energy balance based on the Stefan-Boltzmann law, taking into account the following terms: the first term represents the energy flux emitted by the goldenberry sample, the second term represents the energy flux emitted by the environment and the third term represents the energy flux absorbed by the air (Traffano-Schiffo et al., 2014), see Equation (3).

$$E_T = \varepsilon_C \sigma {T_C}^4 = F \cdot \varepsilon_{obj} \sigma T_{obj}^4 + E_{ent} - (1 - \tau_{air}) F \cdot \sigma T_{air}^4 \qquad (3)$$

Where E_T is the total energy received by the camera (W/m^2), ε_C is the emissivity set in the thermographic camera ($\varepsilon_C = 1$), σ is the Stefan-Boltzman constant (5.67×10^{-8} W/m^{2}K^4), T_C is the temperature calculated by the thermographic camera, F is the geometric factor that can be taken as 1 when the camera is placed perpendicular to the samples, ε_{obj} is the emissivity of the goldenberry, T_{obj} is the surface temperature of the golden berry, E_{ent} is the energy of the environment on the object obtained with the reference material, τ_{air} is the air permeability which, when it is less than 40 cm from the fruit and the RH of the environment is less than saturation, can be considered equal to 1, leaving this term as zero.

As observed in Fig. 7, the average emissivity of the goldenberry sample decreases to a value of 0.834 ± 0.070 during the first 45 min, this phenomenon is due to the absorption of radiant energy by the water molecules present on the surface of the goldenberry sample (degree of excitation) in the infrared range, therefore as the humidity decreases, its emissivity will be lower, in agreement with that reported by (Traffano-Schiffo et al.,

2014) in the dehydration of pork. After the critical drying humidity (45 min), which is the beginning of the decreasing drying stage, the drying rate decreases due to the decrease in the water flow from the center to the surface of the sample, as well as the mobility (diffusion) of the soluble solids (Uribe et al., 2022; Vega-Gálvez, Puente-Díaz, et al., 2014). It is also noteworthy to observe the effect of temperature on the emissivity, the latter increasing to 0.889 ± 0.015 as the temperature of the sample surface increases after 13 h of drying.

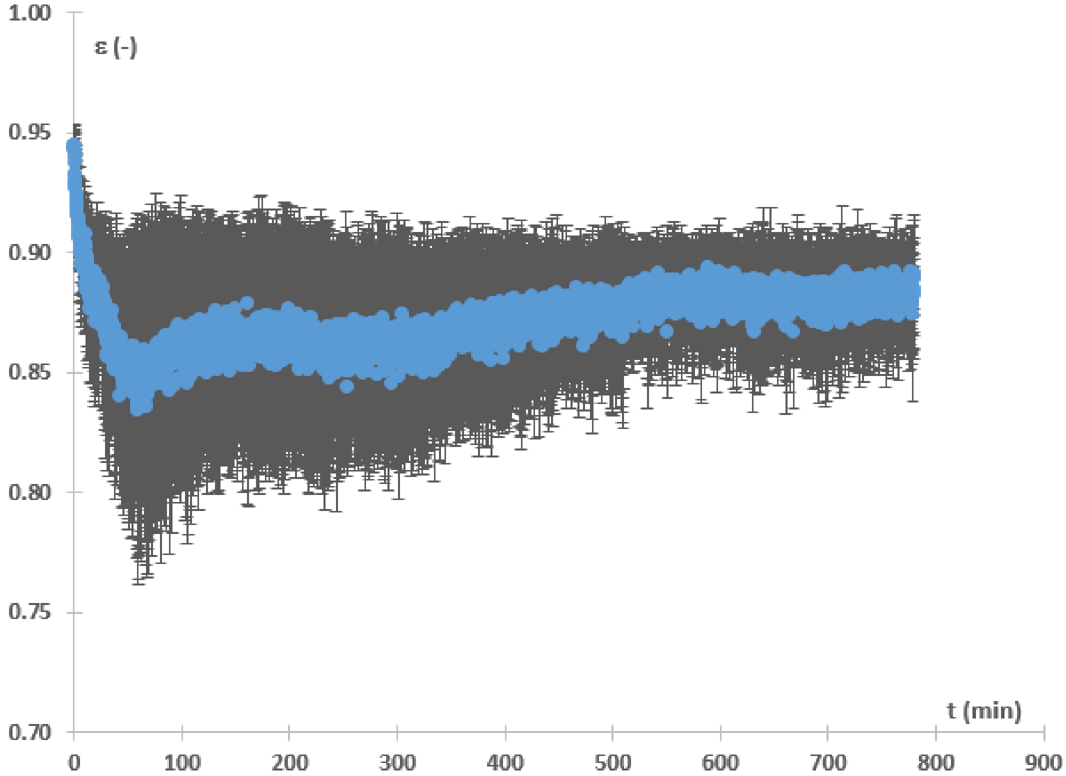

Fig. 7. Evolution of the mean emissivity values during the drying process of *Physalis peruviana*.

Once the surface temperature of the goldenberry sample was obtained, it was compared with the evolution of the air temperature during drying using a Mollier psychrometric chart. Fig. 8 shows two examples in different atmospheric conditions (cold and hot day) that cause the surface temperature of the goldenberry samples to change through different isenthalpic conditions, as observed in the orange peel drying process (Talens et al., 2016a, 2016b, 2017).

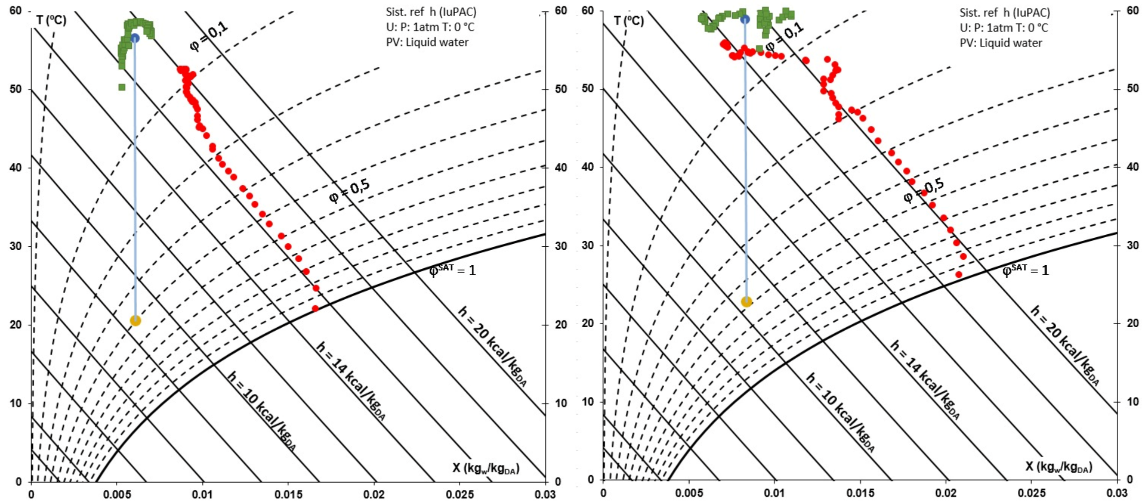

Fig. 8. Evolution of the mean emissivity values during the drying process of *Physalis peruviana*.

These two examples in Fig. 8, as limits of the experiment (cold and warm day), start the drying process with enthalpies of 16 and 20 kCal/kg$_{DA}$. It can also be seen that the drying process is initially adiabatic. The surface temperature of the sample starts from the wet temperature and rises to the drying temperature. However, the sample undergoes adiabatic heating and cooling as it approaches the drying temperature.

3.3. Sorption isotherm of Physalis peruviana

In order to determine the mechanisms that intervene and affect the drying (boundary layer), it is first necessary to obtain the relationship between humidity and water activity, so the sorption isotherm was carried out. The experimental data of the sorption isotherms of goldenberry at a temperature of 60ºC are shown in Fig. 9.

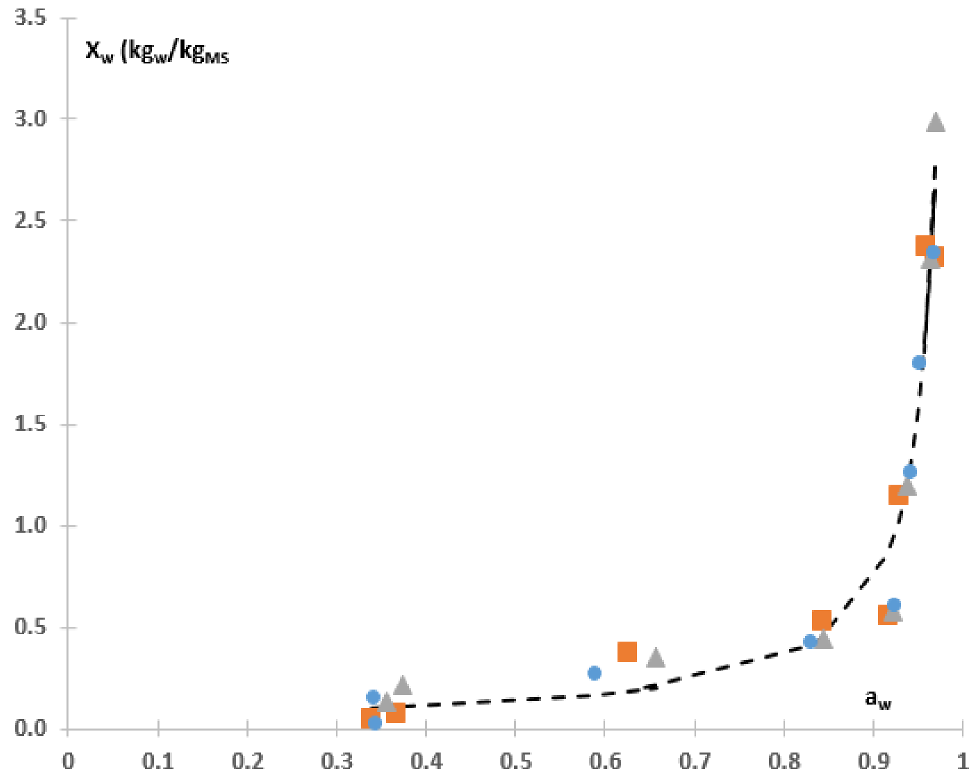

Fig. 9. Sorption isotherm of *Physalis peruviana* carried out in triplicate, where: ■ corresponds to the first experiment, ▲ corresponds to the second experiment and ● corresponds to the third experiment.

From the experimental data of the sorption isotherm, the values of: X_{w0}, C, K, Δ0, τ, α and ef have been obtained according to the GAB model, allowing a direct relationship between water activity and humidity based on the Gompertz transformation during drying, see Table 1.

Table 1. GAB and Gompertz model parameters

GAB (60 ºC)				Gompertz (60 ºC)	
$X_W = \frac{X_{W0}\, C\, a_w}{(1-K\, a_w)(1+(C-1)a_w)}$				$a_w = e_f + \frac{\Delta 0}{1+(e^{\tau^2-\log(X_w)^2\cdot\alpha})}$	
Parameters	Experimental	(Cortés et al., 2012)	(Vega-Gálvez, et al., 2014b)	Parameters	Experimental
X_{w0}	0.067	0.231	0.086	**Δ0**	0.8
				τ	-1.0
C	4.678	2.419	32.88	**α**	1.4
K	1.006	0.760	0.956	**ef**	1.1

The GAB model parameters provide insights into the water-binding behavior of goldenberry during drying. The monolayer moisture (Xw0) represents the amount of water adsorbed to specific active sites on the fruit surface, which is essential for product stability. A low Xw0 indicates that goldenberry retains a relatively small amount of adsorbed water, consistent with its high sugar and acid content. The Guggenheim constant (C) reflects the strength of interaction between the first layer of water molecules and the food matrix. Higher C values suggest stronger binding forces. The K parameter accounts for multilayer water sorption beyond the monolayer; values of K closer to 1 indicate more homogeneous multilayer water binding. These parameters collectively help to understand the moisture adsorption and desorption behavior of goldenberry, relevant for optimizing storage and drying strategies.

In Table 1, GAB parameters have been compared with previous parameters obtained by Cortes et al. (2012). Compared to the data reported by Cortes et al. (2012), the monolayer moisture values obtained in this study appear more consistent with the expected behavior of fruits, which generally exhibit a lower water adsorption capacity than other foods such as meat. The values of parameter C are similarly low in both studies, indicating moderate isosteric heat values that align with the limited ability of fruit tissues to bind water molecules. In contrast, the K parameter typically approaches 0.99 in fruits, due to the steep slopes observed in isotherm curves under high turgor conditions, an aspect that appears inconsistent with the values reported by Cortes et al. (2012).

3.4. Thermodynamic modeling of drying of *Physalis peruviana*

The irreversible thermodynamics has the ability to describe the mechanical phenomena involved in the drying process of goldenberry; that is, it takes into account the structure of the food in the transport of water during drying and its interaction with the air (Fig. 10). In order to better understand the behaviors involved in the drying process, a thermodynamic model, based in the free energy variation, was developed and described by Equation (4) (Talens et al., 2016a).

$$dG = -SdT + VdP + Fdl + \psi de + \sum_i \mu_i \, dn_i \qquad (4)$$

Where: SdT corresponds to the entropic term and is related to the heat flows; VdP corresponds to the mechanical energy term related to the pressure variation; Fdl

corresponds to the mechanical energy term related to the tensile force; ψde corresponds to the energy term related to the electric field induced by the dissolved ions; $\sum_i \mu_i \, dn_i$ corresponds to the activity term and is the sum of the chemical potential of the species "i", the rest of the state variables being constant.

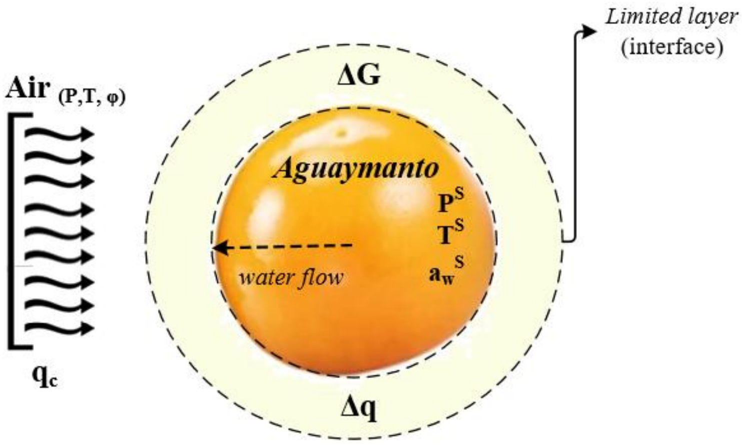

Fig. 10. Schematic diagram of the thermodynamic equilibrium.

Considering the hypothetical existence of an interface between the air flow and the surface of the goldenberry, it is possible to calculate the increase in free energy between the two systems. Furthermore, in order to determine the water transport engine, it is necessary to obtain the water chemical potential, where it is defined as the free energy by water mol (Equation (5)).

$$\Delta\mu_w = \frac{\Delta G}{\Delta n_w} \tag{5}$$

Where: $\Delta\mu_w$ = water chemical potential (J mol^{-1}); ΔG = Gibbs free energy change (J); Δn_w = moles of water (mol). Equation (6) is obtained from equations (4), (5). The terms Fdl and ψde in equation (4) can be neglected, since the plant tissue is a rigid system and there is no great effect of ions, since the sample contains only native ions of goldenberry.

$$\Delta\mu_w = -s_w\left(T^{air} - T^S\right) + \upsilon_w\left(P^{air} - P^S\right) + RT^S \ln\frac{a_w^S}{\varphi^{air}} \tag{6}$$

Where: s_w = partial molar entropy of water (J K^{-1} mol^{-1}); T = temperature (K); υ_w = partial molar volume of water (m^3 mol^{-1}); P = pressure (atm); R = ideal gas constant (8.314472

J K^{-1} mol^{-1}); a_w = water activity; φ = relative humidity. The superscripts *s* and *air* refer to the surface of the goldenberry and the surrounding air, respectively.

Before obtaining the extended chemical potential of water, it is necessary to calculate the partial molar enthalpy of water (Equation (7)).

$$s_W = \frac{C_p \cdot (T^S - T^{air}) \cdot M_t + \Delta G_{vap} \cdot M_0 \Delta M_w}{M_t \cdot T^S \cdot x_w \cdot Mr_W} \qquad (7)$$

Where: C_p= specific heat of goldenberry 3.96 ± 0.02 kJ kg^{-1} K^{-1} obtained by differential scanning calorimetry explained in material and methods section; T^s = surface temperature of the sample (K); T^{air} = temperature of the air surrounding the goldenberry (K); M_t = mass of goldenberry at each time of the drying process (kg); ΔG_{vap} = latent heat of vaporization 2494.4 kJ kg^{-1} (Fletcher, 1970); M_0^m= initial mass of the sample (kg); ΔM_w= mass variation of water in the sample during drying (-); x_w= mass fraction of water in the sample during drying (kg kg-1); Mr_W= molecular mass of water (18 g mol^{-1}).

However, the limited information on the mechanical energy ($v_w \Delta P$) of the goldenberry fruit during the drying process makes it impossible to calculate all the terms of the chemical potential of water. It is therefore necessary to relate the available information to the water flow.

As the system is unstable and out of equilibrium, it is essential to understand the water flow and the thermodynamic forces involved in drying. The first Onsager relation (Traffano-Schiffo et al., 2014) can be used to describe the molar flow of water from the food, driven by the gradient of the chemical potential of water between the interior and the surface (Equation (8)). The phenomenological coefficient is constant in reversible processes and helps to quantify how easily water moves in response to this gradient. However, if mechanical energy stores cause irreversible fractures in the medium, the phenomenological coefficient will evolve according to the transformation undergone by the tissue.

$$J_w = L_W \cdot \Delta\mu_w \qquad (8)$$

Where: J_w= molar flow of water (mol s^{-1} m^{-2}); L_w = phenomenological coefficient (mol^2 J^{-1} s^{-1} m^{-2}); $\Delta\mu_w$ = chemical potential of water (J mol^{-1}).

Since it is not possible to obtain the mechanical gradient, it is possible to calculate the rest of the components of the chemical potential of water. That is, a chemical potential can be defined without the effect of mechanical transformations in transport, using the following Equation (9) obtained from Equation (6).

$$\Delta\mu_w^* = -s_w\left(T^{air} - T^S\right) + RT^S \ln\frac{a_w}{\varphi^{air}} \qquad (9)$$

Although it is not possible to obtain the mechanical gradient in the figure, it is possible to calculate the remaining components of the chemical potential of water. That is, a water potential gradient can be defined without the mechanical energy term ($\Delta\mu_w^*$), as shown in Fig. 11, across the air/golden grass surface interface. Furthermore, the chemical potential gradient of the water over the surface of the goldenberry shows an increase until it reaches a maximum value of 7500 J/mol during the first 450 min, after which it begins to decrease until the end of the drying process.

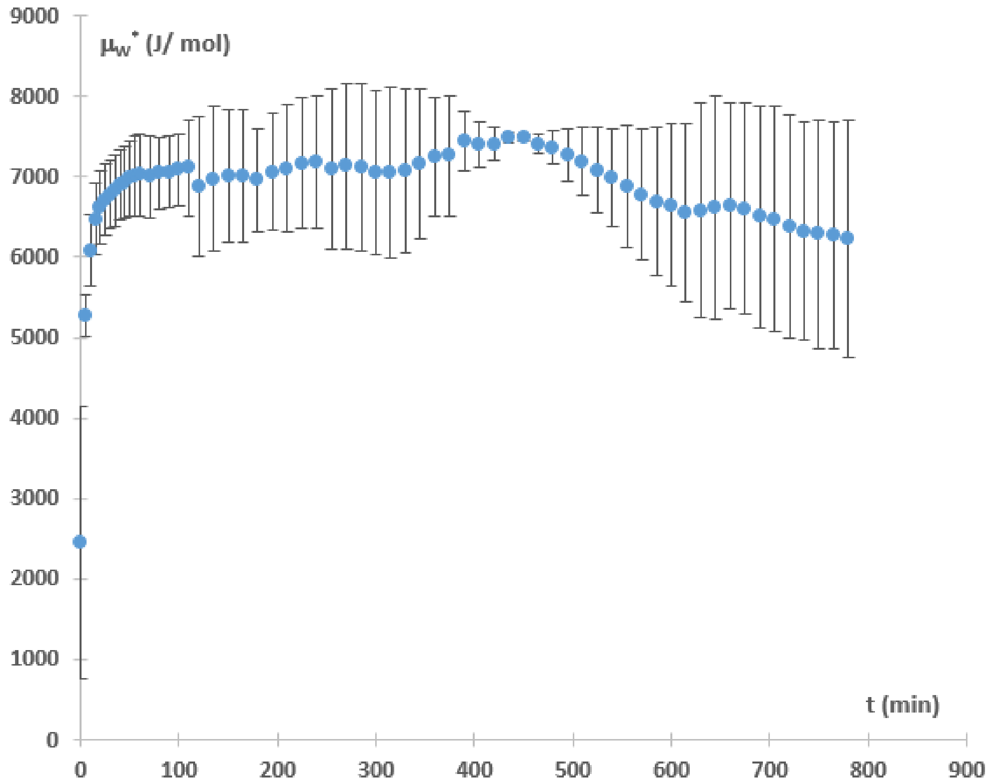

Fig. 11. Evolution of the water chemical potential gradient, without mechanical energy term, between the air and the *Physalis peruviana* surface.

Using Equation (9), it is possible to determine the phenomenological coefficient using the definition of potential in Equation (10). This phenomenological coefficient will be more accurate the smaller the influence of the variation in mechanical energy at the interface is compared to the energies associated with the variation in water activity and temperature. According to the Traffano-Schiffo et al. (2014), the relationship between the phenomenological coefficient and the water flow will be more linear the smaller the effect of the pressure term (mechanical). Fig. 12 shows this relationship and indicates that it is possible to establish a linear relationship between the two.

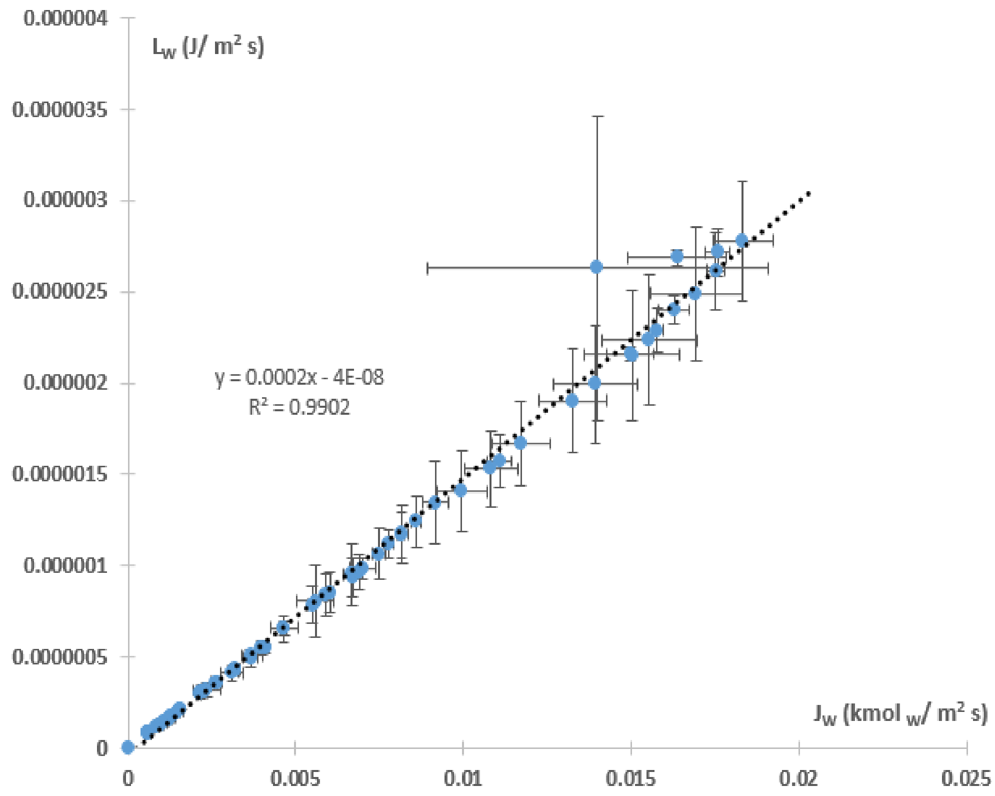

Fig. 12. Relationship between phenomenological coefficient and water flow.

With the linear relationship between the coefficient and the flow, the chemical potential can be recalculated from the equation obtained. By subtracting this chemical potential of water from that calculated in Equation (9), as shown in Equation (10), it is possible to determine the mechanical term.

$$v_w \, \Delta P = \Delta\mu_w - \Delta\mu_w^* \tag{10}$$

Fig. 13 shows the evolution of the mechanical term over the drying time. In the first 100 minutes, the mechanical term decreases from 1556.259 ± 273.661 to -210.977 ± 175.256, which is related to a large storage of mechanical energy due to the initial contraction of the goldenberry structure caused by the high water loss. From 100 to 600 min, a phase of zero mechanical term is observed, associated with the cellular plasmolysis process. Subsequently, the mechanical energy reaches a value of 2280.527 ± 223.763 at the end of the drying process, releasing mechanical energy to the system.

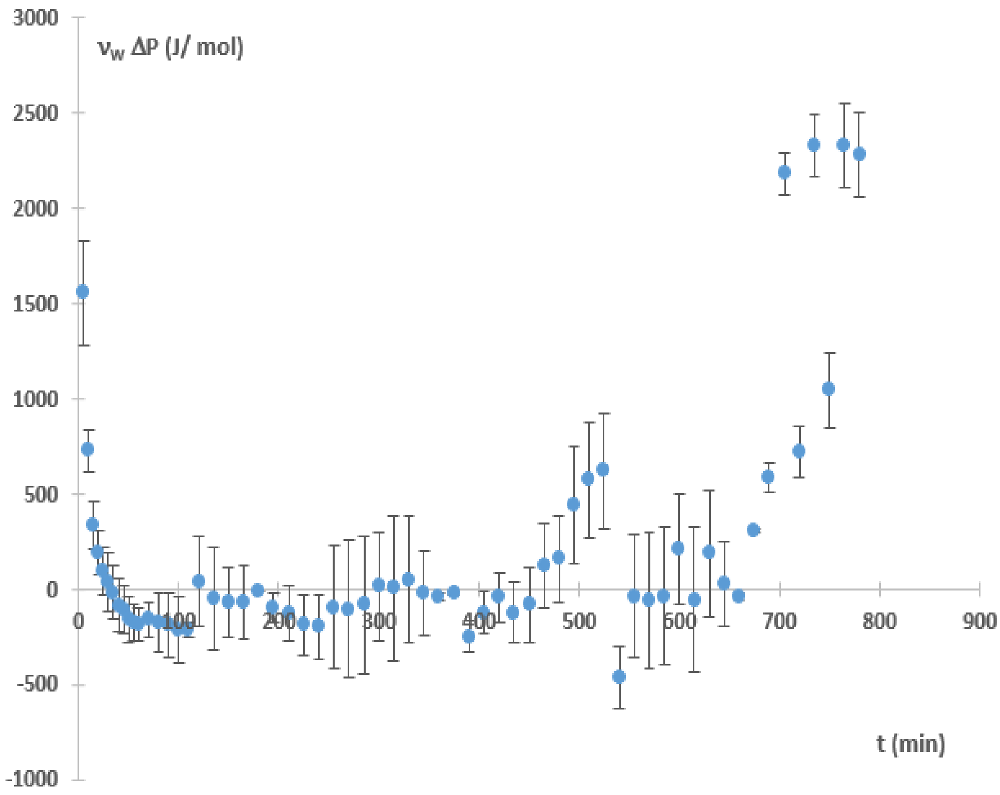

Figure 13. Evolution of the mechanical energy term of the chemical potential of the water during the whole drying process.

4. Conclusions

A drying monitoring system using infrared thermography has been developed to follow the drying process of goldenberry to optimum conditions. To this end, the evolution of the emissivity of the fruit surface during the process was obtained.

The evolution of the phenomenological coefficient of goldenberry drying during the process has been obtained, which will allow this operation to be predicted in the future.

The mechanical effect (internal fractures, plasmolysis and storage of mechanical energy) in the goldenberry dehydration process has been observed. This will allow both the rehydration capacity of the fruit and its effect on a formulated food system to be predicted.

Engineering tools such as the sorption isotherm, emissivity and phenomenological coefficient were obtained, which will facilitate future modelling of goldenberry drying.

The integration of infrared thermography with thermodynamic modeling provides a powerful tool for improving the efficiency and control of convective drying processes in the food industry. By enabling non-invasive, real-time monitoring of surface temperature and emissivity, this system allows for better identification of critical drying stages and optimization of process parameters. Furthermore, the quantification of water flux and chemical potential gradients supports a more accurate prediction of moisture migration, which is crucial for minimizing energy consumption, reducing drying time, and preserving product quality. These findings offer a valuable basis for the development of more sustainable and cost-effective drying protocols for high-moisture fruits such as goldenberry.

5. Bibliographical references

A. Aviara, N. (2020). Moisture Sorption Isotherms and Isotherm Model Performance Evaluation for Food and Agricultural Products. In Sorption in 2020s. *IntechOpen*. https://doi.org/10.5772/intechopen.87996

Akpinar, E. K., Midilli, A., & Bicer, Y. (2006). The first and second law analyses of thermodynamic of pumpkin drying process. *Journal of Food Engineering, 72(4)*, 320–331. https://doi.org/10.1016/j.jfoodeng.2004.12.011

Avendaño, W. A., Muñoz, H. F., Leal, L. J., Deaquiz, Y. A., & Castellanos, D. A. (2022). Physicochemical characterization of cape gooseberry (*Physalis peruviana* L.) fruits ecotype Colombia during preharvest development and growth. *Journal of Food Science, 87(10),* 4429–4439. https://doi.org/10.1111/1750-3841.16318

Balaguer, H.E., Fischer, G., Magnitskiy, S., 2024. Chapter 11 - physiology and biochemistry of the Physalis peruviana fruit. In: Fawzy Ramadan, Mohamed (Ed.), Handbook of Goldenberry (Physalis Peruviana). Academic Press, pp. 121–137. https://doi.org/10.1016/B978-0-443-15433-1.00011-X.

Barbosa-Cánovas, G. V., & Vega-Mercado, H. (1996). Dehydration of Foods. *Springer US*. https://doi.org/10.1007/978-1-4757-2456-1

Bazalar Pereda, M. S., Nazareno, M. A., & Viturro, C. I. (2019). Nutritional and Antioxidant Properties of Physalis peruviana L. Fruits from the Argentinean Northern Andean Region. *Plant Foods for Human Nutrition, 74(1),* 68–75. https://doi.org/10.1007/s11130-018-0702-1

Blas Saavedra, R., Cruz-Tirado, J. P., Figueroa-Avalos, H. M., Barbin, D. F., Amigo, J. M., & Siche, R. (2024). Prediction of physicochemical properties of cape gooseberry (*Physalis peruviana* L.) using near infrared hyperspectral imaging (NIR-HSI). *Journal of Food Engineering, 371*, 111991. https://doi.org/10.1016/j.jfoodeng.2024.111991

Cabrera Ordoñez, Y. A., Estrada Mesa, E. M., & Cortés Rodríguez, M. (2017). The influence of drying on the physiological quality of cape gooseberry (*Physalis peruviana* L.) fruits added with active components. *Acta Agronómica, 66(4),* 512–518. https://doi.org/10.15446/acag.v66n4.59507

Cuibus, L., Castro-Giráldez, M., Fito, P. J., & Fabbri, A. (2014). Application of infrared thermography and dielectric spectroscopy for controlling freezing process of raw potato. *Innovative Food Science & Emerging Technologies*, *24,* 80–87. https://doi.org/10.1016/j.ifset.2013.11.007

Doymaz, İ. (2008). Convective drying kinetics of strawberry. *Chemical Engineering and Processing: Process Intensification*, *47(5)*, 914–919. https://doi.org/10.1016/j.cep.2007.02.003

ElGamal, R. A., Kishk, S. S., & ElMasry, G. M. (2017). Validation of CFD models for the deep-bed drying of rice using thermal imaging. *Biosystems Engineering, 161*, 135–144. https://doi.org/10.1016/j.biosystemseng.2017.06.018

Fischer, G., Herrera, A., & Almanza, P. J. (2011). Cape gooseberry (*Physalis peruviana* L.). In *Postharvest Biology and Technology of Tropical and Subtropical Fruits* (pp. 374–397e). Elsevier. https://doi.org/10.1533/9780857092762.374

Fischer, G., & Martinez, O. (1999). Calidad y madurez de la uchuva (*Physalis peruviana* l.) en relación con la coloración del fruto. *Agronomía Colombiana, 16(1–3)*, 35–39.

Fletcher, N. H. (1970). The Chemical Physics of Ice. *Cambridge University Press*. https://doi.org/10.1017/CBO9780511735639

Garavito, J., Herrera, A. O., & Castellanos, D. A. (2021). A combined mathematical model to represent transpiration, respiration, and water activity changes in fresh cape gooseberry (*Physalis peruviana*) fruits. *Biosystems Engineering, 208*, 152–163. https://doi.org/10.1016/j.biosystemseng.2021.05.015

Gowen, A. A., Tiwari, B. K., Cullen, P. J., McDonnell, K., & O'Donnell, C. P. (2010). Applications of thermal imaging in food quality and safety assessment. *Trends in Food Science & Technology, 21(4),* 190–200. https://doi.org/10.1016/j.tifs.2009.12.002

Hidayat, D. D., Luthfiyanti, R., Iwansyah, A. C., Herminiati, A., Rahman, T., Rahman, N., & Andriansyah, R. C. E. (2021). Identification and evaluation of physical and mechanical properties of Physalis peruviana L. *IOP Conference Series: Earth and Environmental Science, 672(1),* 012056. https://doi.org/10.1088/1755-1315/672/1/012056

İzli, N., Yıldız, G., Ünal, H., Işık, E., & Uylaşer, V. (2014). Effect of different drying methods on drying characteristics, colour, total phenolic content and antioxidant capacity of Goldenberry (*Physalis peruviana* L.). International *Journal of Food Science & Technology, 49(1),* 9–17. https://doi.org/10.1111/ijfs.12266

Junqueira, J. R. de J., Corrêa, J. L. G., de Oliveira, H. M., Ivo Soares Avelar, R., & Salles Pio, L. A. (2017). Convective drying of cape gooseberry fruits: Effect of pretreatments on kinetics and quality parameters. *LWT - Food Science and Technology, 82,* 404–410. https://doi.org/10.1016/j.lwt.2017.04.072

Kraiem, A., Madiouli, J., Shigidi, I., & Sghaier, J. (2023). Experimental Analysis of Drying Conditions' Effect on the Drying Kinetics and Moisture Desorption Isotherms at Several Temperatures on Food Materials: Corn Case Study. *Processes, 11(1),* 184. https://doi.org/10.3390/pr11010184

Kylili, A., Fokaides, P. A., Christou, P., & Kalogirou, S. A. (2014). Infrared thermography (IRT) applications for building diagnostics: A review. *Applied Energy, 134*, 531–549. https://doi.org/10.1016/j.apenergy.2014.08.005

Lerman, P., & Scheepers, G. (2023). Determination of a mass-transfer coefficient for wood drying by means of thermography. *Wood Material Science & Engineering, 18(6),* 2104–2111. https://doi.org/10.1080/17480272.2023.2243473

Lombraña, J. I., Rodríguez, R., & Ruiz, U. (2010). Microwave-drying of sliced mushroom. Analysis of temperature control and pressure. *Innovative Food Science & Emerging Technologies, 11(4),* 652–660. https://doi.org/10.1016/j.ifset.2010.06.007

Lopez, H. E. B., Fischer, G., & Magnitskiy, S. (2024). Physiology and biochemistry of the Physalis peruviana fruit. In Handbook of Goldenberry (*Physalis Peruviana*) (pp. 121–137). Elsevier. https://doi.org/10.1016/B978-0-443-15433-1.00011-X

Lopez, J., Vega-Gálvez, A., Torres, M. J., Lemus-Mondaca, R., Quispe-Fuentes, I., & Di Scala, K. (2013). Effect of dehydration temperature on physico-chemical properties and antioxidant capacity of goldenberry (*Physalis peruviana* L.). *Chilean Journal of Agricultural Research, 73(3),* 293–300. https://doi.org/10.4067/S0718-58392013000300013

Motahayyer, M., Arabhosseini, A., & Samimi-Akhijahani, H. (2019). Numerical analysis of thermal performance of a solar dryer and validated with experimental and thermo-graphical data. *Solar Energy, 193,* 692–705. https://doi.org/10.1016/j.solener.2019.10.001

Muñoz, P., Parra, F., Simirgiotis, M. J., Sepúlveda Chavera, G. F., & Parra, C. (2021). Chemical Characterization, Nutritional and Bioactive Properties of *Physalis peruviana* Fruit from High Areas of the Atacama Desert. *Foods, 10(11),* 2699. https://doi.org/10.3390/foods10112699

Nawirska-Olszańska, A., Stępień, B., Biesiada, A., Kolniak-Ostek, J., & Oziembłowski, M. (2017). Rheological, Chemical and Physical Characteristics of Golden Berry (*Physalis peruviana* L.) after Convective and Microwave Drying. *Foods, 6(8),* 60. https://doi.org/10.3390/foods6080060

Obregón La Rosa, A., Talledo Rodríguez, G., & Pinedo Taco, R. (2021). Native fruits of Peru as a potential source of nutrients, bioactive compounds and antioxidant capacity in the nutritional requirements of vulnerable groups. Revista de La Facultad de Agronomía, Universidad Del Zulia, 38(2), 421–440. https://doi.org/10.47280/RevFacAgron(LUZ).v38.n2.11

Ordóñez-Santos, L. E., Martínez-Girón, J., & Arias-Jaramillo, M. E. (2017). Effect of ultrasound treatment on visual color, vitamin C, total phenols, and carotenoids content in Cape gooseberry juice. *Food Chemistry, 233*, 96–100. https://doi.org/10.1016/j.foodchem.2017.04.114

Pappalardo, S., Consoli, S., Longo-Minnolo, G., Vanella, D., Longo, D., Guarrera, S., D'Emilio, A., & Ramírez-Cuesta, J. M. (2023). Performance evaluation of a low-cost thermal camera for citrus water status estimation. *Agricultural Water Management*, *288,* 108489. https://doi.org/10.1016/j.agwat.2023.108489

Pasten, A., Gomez-Perez, L. S., Vega-Galvez, A., Uribe, E., & Puente, L. (2024). Drying technologies of Physalis peruviana. In Handbook of Goldenberry (*Physalis Peruviana*) (pp. 351–372). Elsevier. https://doi.org/10.1016/B978-0-443-15433-1.00034-0

Puente, L. A., Pinto-Muñoz, C. A., Castro, E. S., & Cortés, M. (2011). Physalis peruviana Linnaeus, the multiple properties of a highly functional fruit: A review. *Food Research International, 44(7),* 1733–1740. https://doi.org/10.1016/j.foodres.2010.09.034

Puente, L., Vega-Gálvez, A., Ah-Hen, K. S., Rodríguez, A., Pasten, A., Poblete, J., Pardo-Orellana, C., & Muñoz, M. (2020). Refractance Window drying of goldenberry (*Physalis peruviana* L.) pulp: A comparison of quality characteristics with respect to other drying techniques. *LWT, 131*, 109772. https://doi.org/10.1016/j.lwt.2020.109772

Puente, L., Vega-Gálvez, A., Fuentes, I., Stucken, K., Rodríguez, A., & Pastén, A. (2021). Effects of drying methods on the characterization of fatty acids, bioactive compounds and antioxidant capacity in a thin layer of physalis (*Physalis peruviana* L.) pulp. *Journal of Food Science and Technology, 58(4),* 1470–1479. https://doi.org/10.1007/s13197-020-04659-0

Ramirez-Hernandez, A., Galagarza, O. A., Álvarez Rodriguez, M. V., Pachari Vera, E., Valdez Ortiz, M. del C., Deering, A. J., & Oliver, H. F. (2020). Food safety in Peru: A review of fresh produce production and challenges in the public health system. Comprehensive Reviews in *Food Science and Food Safety, 19(6),* 3323–3342. https://doi.org/10.1111/1541-4337.12647

Reyes-Chaparro, J. E., Arballo, J. R., & Campañone, L. A. (2024). Experimental study of parchment coffee drying using the combined fluidization and microwave process: Analysis of drying curves and thermal imaging. *Journal of Food Engineering, 383*, 112214. https://doi.org/10.1016/j.jfoodeng.2024.112214

Rossi, D., Fuentes, R., Pardo, F., Reyes, D., Tirado, R., Urbina, E., & Vega, J. (2012). Effect of temperature and synergism of sucrose, saccharin and sugar light in osmotic dehydration aguaymanto (*Physalis peruviana*). *Agroindustrial Science*, 100–109. https://doi.org/10.17268/agroind.science.2012.01.03

Ruan, J., Li, M., Liu, Y., Ye, B., & Ling, C. (2022). Adsorption isotherm and thermodynamic properties of microwave vacuum dried tilapia fillets. *LWT, 166*, 113766. https://doi.org/10.1016/j.lwt.2022.113766

Talens, C., Arboleya, J. C., Castro-Giraldez, M., & Fito, P. J. (2017). Effect of microwave power coupled with hot air drying on process efficiency and physico-chemical properties of a new dietary fibre ingredient obtained from orange peel. *LWT, 77*, 110–118. https://doi.org/10.1016/j.lwt.2016.11.036

Talens, C., Castro-Giraldez, M., & Fito, P. J. (2016a). A thermodynamic model for hot air microwave drying of orange peel. *Journal of Food Engineering, 175*, 33–42. https://doi.org/10.1016/j.jfoodeng.2015.12.001

Talens, C., Castro-Giraldez, M., & Fito, P. J. (2016b). Study of the effect of microwave power coupled with hot air drying on orange peel by dielectric spectroscopy. *LWT - Food Science and Technology, 66*, 622–628. https://doi.org/10.1016/j.lwt.2015.11.015

Tomas-Egea, J. A., Castro-Giraldez, M., Colom, R. J., & Fito, P. J. (2022). New technique for determining the critical freezing temperatures of chicken breast based on radiofrequency photospectrometry. *Journal of Food Engineering, 333*, 111155. https://doi.org/10.1016/j.jfoodeng.2022.111155

Tomas-Egea, J. A., Traffano-Schiffo, M. V., Castro-Giraldez, M., & Fito, P. J. (2021). Hot Air and Microwave Combined Drying of Potato Monitored by Infrared Thermography. *Applied Sciences, 11(4)*, 1730. https://doi.org/10.3390/app11041730

Traffano-Schiffo, M. V., Castro-Giraldez, M., Colom, R. J., & Fito, P. J. (2015). Study of the application of dielectric spectroscopy to predict the water activity of meat during drying process. *Journal of Food Engineering, 166*, 285–290. https://doi.org/10.1016/j.jfoodeng.2015.06.030

Traffano-Schiffo, M. V., Castro-Giráldez, M., Fito, P. J., & Balaguer, N. (2014). Thermodynamic model of meat drying by infrarred thermography. *Journal of Food Engineering, 128*, 103–110. https://doi.org/10.1016/j.jfoodeng.2013.12.024

Uribe, E., Gómez-Pérez, L. S., Pasten, A., Pardo, C., Puente, L., & Vega-Galvez, A. (2022). Assessment of refractive window drying of physalis (*Physalis peruviana* L.) puree at different temperatures: drying kinetic prediction and retention of bioactive components. *Journal of Food Measurement and Characterization, 16(4)*, 2605–2615. https://doi.org/10.1007/s11694-022-01373-7

Vásquez-Parra, J. E., Ochoa-Martínez, C. I., & Bustos-Parra, M. (2013). Effect of chemical and physical pretreatments on the convective drying of cape gooseberry fruits (Physalis peruviana). *Journal of Food Engineering, 119(3)*, 648–654. https://doi.org/10.1016/j.jfoodeng.2013.06.037

Vega-Gálvez, A., López, J., Ah-Hen, K., Torres, M., & Lemus-Mondaca, R. (2014a). Thermodynamic Properties, Sorption Isotherms and Glass Transition Temperature of Cape Gooseberry (*Physalis peruviana* L.). *Food Technology and Biotechnology, 52(1)*, 83–92.

Vega-Gálvez, A., Puente-Díaz, L., Lemus-Mondaca, R., Miranda, M., & Torres, M. J. (2014). Mathematical Modeling of Thin-Layer Drying Kinetics of Cape Gooseberry (*Physalis peruviana* L.). *Journal of Food Processing and Preservation, 38(2),* 728–736. https://doi.org/10.1111/jfpp.12024

Vega-Gálvez, A., Zura-Bravo, L., Lemus-Mondaca, R., Martinez-Monzó, J., Quispe-Fuentes, I., Puente, L., & Di Scala, K. (2015). Influence of drying temperature on dietary fibre, rehydration properties, texture and microstructure of Cape gooseberry (Physalis peruviana L.). *Journal of Food Science and Technology, 52(4)*, 2304–2311. https://doi.org/10.1007/s13197-013-1235-0

Yasin, O., Aysun, O., & Senem, T. uuml fek ccedil i. (2016). Effect of two dipping pretreatment on drying kinetics of golden berry (*Physalis peruviana* L.). *African Journal of Agricultural Research, 11(1),* 40–47. https://doi.org/10.5897/AJAR2014.8937

Yilmaz, N., Gill, W., Donaldson, A. B., & Lucero, R. E. (2008). Problems Encountered in Fluctuating Flame Temperature Measurements by Thermocouple. *Sensors, 8(12),* 7882–7893. https://doi.org/10.3390/s8127882

Yıldız, G., İzli, N., Ünal, H., & Uylaşer, V. (2015). Physical and chemical characteristics of goldenberry fruit (*Physalis peruviana* L.). *Journal of Food Science and Technology, 52(4),* 2320–2327. https://doi.org/10.1007/s13197-014-1280-3

4.3. Sistema de monitorización de la congelación de aguaymanto (*Physalis peruviana*) mediante espectrofotometría de radiofrecuencia y termografía infrarroja.

ELSEVIER

Innovative Food Science & Emerging Technologies
Volume 104, August 2025, 104134

Non-invasive monitoring of goldenberry freezing using infrared thermography and radiofrequency dielectric spectroscopy

T. Chuquizuta [a b], W. Castro [c], M. Castro-Giraldez [a], P.J. Fito [a]

Show more

Add to Mendeley Share Cite

https://doi.org/10.1016/j.ifset.2025.104134 Get rights and content

Condición	DOI
Aceptado (28 de julio de 2025)	**https://doi.org/10.1016/j.ifset.2025.104134**

NON-INVASIVE MONITORING OF GOLDENBERRY FREEZING USING INFRARED THERMOGRAPHY AND RADIOFREQUENCY DIELECTRIC SPECTROSCOPY

T. Chuquizuta[1,2]; W. Castro[3]; M. Castro-Giraldez[1*]; P.J. Fito[1]

[1] Instituto Universitario de Ingeniería de Alimentos FoodUPV, Universitat Politècnica de València, Camino de Vera s/n, Valencia 46022, Spain

[2] Instituto de Investigación del Mejoramiento Productivo, Universidad Nacional Autónoma de Chota, Chota 06120, Perú

[3] Facultad de Ingeniería de Industrias Alimentarias y Biotecnología, Universidad Nacional de Frontera, Sullana 20100, Perú

*author for correspondence: marcasgi@upv.es

Abstract

This study presents a non-invasive monitoring system combining infrared thermography and radiofrequency dielectric spectroscopy to characterize the freezing behavior of goldenberry (*Physalis peruviana*). The system enabled simultaneous acquisition of surface temperature profiles, internal dielectric responses, and emissivity changes during freezing at −40 °C. Thermal imaging revealed distinct freezing stages, including subcooling, ice nucleation, and vitrification, with emissivity decreasing to 0.837 during initial dehydration and increasing to 0.951 near the glass transition (−35.8 °C). Dielectric measurements identified α- and β-dispersions linked to ionic mobility and interfacial polarization, with relaxation frequencies decreasing progressively as freezing advanced. The integration of both techniques allowed the detection of critical phase transitions, including the onset and completion of ice crystallization, supported by differential scanning calorimetry. These findings provide insight into structural changes and water mobility in high-moisture fruits, enabling real-time assessment of freezing kinetics. The approach demonstrates significant potential for optimizing industrial freezing protocols, improving the preservation of delicate fruits by minimizing structural damage and degradation of bioactive compounds.

Keywords: infrared thermography, radiofrequency, spectrophotometry and freezing.

Highlights

A non-invasive system monitors goldenberry freezing using IR thermography and RF sensing.

Emissivity profiling detects critical thermal transitions, including vitrification.

Dielectric spectroscopy reveals α/β relaxations linked to ionic mobility and ice formation.

Combined thermal-dielectric data enable precise identification of phase change points.

1. Introduction

Goldenberry (*Physalis peruviana*) is an exotic fruit native to the Peruvian Andes, recognised for its nutritional value and its high content of bioactive compounds, such as carotenoids, polyphenols, flavonoids and vitamin C (Olivares-Tenorio et al., 2016; L. A. Puente et al., 2011). A substantial body of research has demonstrated that these compounds possess antioxidant, anti-inflammatory, and immunomodulatory properties (L. Puente et al., 2021b; L. A. Puente et al., 2011; Vasco et al., 2008). Notwithstanding its nutritional benefits and growing demand in the agri-food industry, goldenberry is considered a highly perishable fruit (Balaguera-López et al., 2017; H. E. B. Lopez et al., 2024; Ozcelik et al., 2024). This is attributed to its rapid postharvest metabolism and high enzymatic activity, which generates losses of mass, texture and bioactive compounds along the marketing chain. In this context, the implementation of effective preservation techniques is imperative to extend their shelf life and maintain their nutritional and sensory properties.

Freezing is one of the most commonly applied preservation methods for fruits, offering extended shelf life and minimal nutrient loss. This method involves subjecting the food to temperatures below 0 °C, which has been shown to reduce water mobility (intra- and extracellular) and water activity (a_w) (Chi Khang, Le Dang, Van Muoi, & Thanh Truc, 2022; Da Silva, Silveira, Ronzoni, & Hermes, 2022). This, in turn, has been demonstrated to decrease chemical reactions, as well as enzymatic and microbial activity (De Ancos, Sánchez-Moreno, De Pascual-Teresa, & Cano, 2012; Delgado & Sun, 2001; Loayza-Salazar et al., 2024). In this context, freezing has been shown to preserve the sensory quality (i.e. odour, colour and taste) and nutritional value of the product (Ojha, Kerry, Tiwari, & O'Donnell, 2016).

During the freezing process, the phenomena of heat and mass transfer are contingent on the properties of the foodstuff, including its composition, porosity, density and surface area (Delgado & Sun, 2001). Consequently, the freezing process can be categorized into three distinct stages: initial cooling, phase change (nucleation and ice formation), and tempering. The subsequent cooling stage involves the reduction of the initial temperature to the sub cooling temperature, below the freezing point, where the nuclearization is produced. The phase change stage is characterized by the initiation of nucleation and the subsequent growth of ice crystals, a consequence of the surface tension of water ice Ih, and its state transition (liquid – solid). Finally, the tempering stage begins after the completion of the phase change and concludes when thermal equilibrium is established between the sample and the ambient freezing conditions (Ben Haj Said, Bellagha, & Allaf, 2016; De Ancos et al., 2012; Tomas-Egea, Castro-Giraldez, Colom, & Fito, 2022). However, the efficiency of the freezing process is closely related to a number of phenomena, including the kinetics of formation and agglomeration of ice crystals of the type Ih, as well as the vitrification processes undergone by the fruit. Among these critical phenomena are sub cooling, the initial freezing point (T_{m0}), the freezing temperature of the maximally cryoconcentrated sample (T_m') and the glass transition temperature (T_g') of the sample. These phenomena are instrumental in determining the structural and biochemical stability of the product during frozen storage (Fan & Roos, 2017; Roos, 1993; Talja & Roos, 2001). In view of this, the monitoring of ice formation in food is of utmost importance, as is the determination of technical parameters such as those mentioned above, which are to be transferred to the industry dedicated to freezing processes of exotic fruits, due to the paucity of research in this area.

The present study investigates the monitoring of ice formation in plant tissues using thermocouples. Despite their accuracy and low measurement error, these techniques are destructive due to their insertion into the food tissue (surface and/or center), causing damage to the structure (cells), leakage of intra- and extra-cellular liquid, and contamination of the samples (Cuibus, Castro-Giraldez, Fito, & Fabbri, 2014; Li, Cheng, & Cheng, 2025). Consequently, the frozen fruit industry (predominantly the goldenberry industry) has been demanding novel non-invasive methods to monitor the surface temperature of the food.

Infrared thermography technology (deriving from infrared radiation) constitutes a component of thermal analysis methods, with a focus on the acquisition and processing of thermal images (Gonçalves et al., 2018; Usamentiaga et al., 2014). This technique has been shown to have several advantages, including being non-invasive, fast and objective for the analysis of non-contact surface temperature profiles (Gonçalves, Giarola, Pereira, Vilas Boas, & de Resende, 2016; Harrap, Hempel de Ibarra, Whitney, & Rands, 2018; Shammi et al., 2022). Recent advances in the field have also explored the integration of thermal imaging and spectroscopic techniques to characterize internal structural heterogeneity and firmness distribution in fruits (Lan et al., 2024; Wang et al., 2024), supporting the relevance of advanced non-invasive tools for assessing quality attributes in plant-based systems. In recent years, there has been a concerted effort to apply infrared thermography to a variety of contexts. For instance, Gonçalves et al. (2018) have used the technique to monitor the heat transfer process during the freeze-drying of gelatin solutions with ethanol, while Shammi et al. (2022); Shammi, Sohel, Diepeveen, Zander, and Jones (2023) have employed infrared thermography to detect frost in crops. In the following years, research has been conducted on the estimation of freeze-dryer plate temperature (Li et al., 2025), the detection of water stress in almond plants (Poirier-Pocovi, Volder, & Bailey, 2020), the analysis of heat stress in insects (Gallego, Verdú, Carrascal, & Lobo, 2016) and the assessment of lesions in cold-stored guava (Gonçalves et al., 2016). The extant literature demonstrates the potential of using thermal imaging cameras in agricultural and biological applications. However, the majority of these investigations do not consider the determination of emissivity and do not make corrections to accurately estimate the real temperature of the object under study.

In this context, the determination of the emissivity of a body from its radiant energy becomes relevant, considering that the thermal camera sensor captures not only the energy emitted by the object under study, but also the energy of the surrounding air and the radiation reflected from the environment (Usamentiaga et al., 2014). A paucity of studies has been identified that address the determination and/or correction of object emissivity in agri-food processes. The following studies are notable in this respect: the drying of pork (Traffano-Schiffo, Castro-Giraldez, Fito, & Balaguer, 2014); the drying of potatoes (Tomas-Egea, Traffano-Schiffo, Castro-Giraldez, & Fito, 2021); the freezing of pork (Castro-Giraldez, Balaguer, Hinarejos, & Fito, 2014); and the freezing of potatoes (Cuibus et al., 2014). However, research applying infrared thermography to small and structurally complex fruits such as goldenberry has not yet been reported.

Spectrophotometry is a technique based on the interaction of photons with matter along the electromagnetic spectrum, the behavior of which can be modelled from quantum theory via the Schrödinger equation (Chandra Roychoudhuri, 2017). At the macroscopic level, Maxwell's equations facilitate the description of the interaction between electric and magnetic fields and materials, represented respectively through the complex permittivity and the material complex permeability (Tomas-Egea et al., 2022; Traffano-Schiffo, Castro-Giraldez, Colom, & Fito, 2018; Traffano-Schiffo, Castro-Giraldez, Colom, Talens, & Fito, 2021). Permittivity is a vectorial property consisting of a real part (ε'), which is associated with the material's capacity to store electrical energy, and an imaginary part (ε''), which is related to dielectric losses. Within the radiofrequency range, the dielectric behavior facilitates the identification of three primary contributions across the spectrum: two associated with molecular orientation effects (α and β dispersions), and one linked to molecular vibration and ionic conduction (σ) (Heileman, Daoud, & Tabrizian, 2013; Kuang & Nelson, 1998; Liu & Guo, 2017). The α- dispersions (Hz-kHz range) has been shown to be associated with charged molecules that exhibit low mobility and high ionic strength, such as electrolytes and organic acids. Conversely, β- dispersions (kHz-MHz) has been observed to be associated with charged macromolecules, such as proteins and carbohydrates, in addition to interactions at interfacial surfaces that exhibit charges with high surface tension (Cuibus et al., 2014; Tomas-Egea et al., 2022; Traffano-Schiffo et al., 2018, Traffano-Schiffo et al., 2021).

Recent studies have demonstrated that dielectric analysis (α- and β-dispersions) can detect changes in molecular structure associated with the glass transition (T_g'), thus providing a non-destructive tool for monitoring product stability during the freezing process (Fan & Roos, 2017; Tomas-Egea et al., 2022). Despite the advances in the individual use of these technologies, their joint application to monitor and understand freezing processes in fruits such as goldenberry remains limited. The integration of infrared thermography and radiofrequency spectrophotometry has the potential to provide a more comprehensive understanding of thermal and dielectric events during the freezing process. This, in turn, could facilitate a more precise characterization of physical transitions, thereby contributing to the development of enhanced preservation protocols.

2. Materials and methods

The experimental procedure is shown in Fig. 1. Likewise, each step of the flowchart is explained in the following paragraphs.

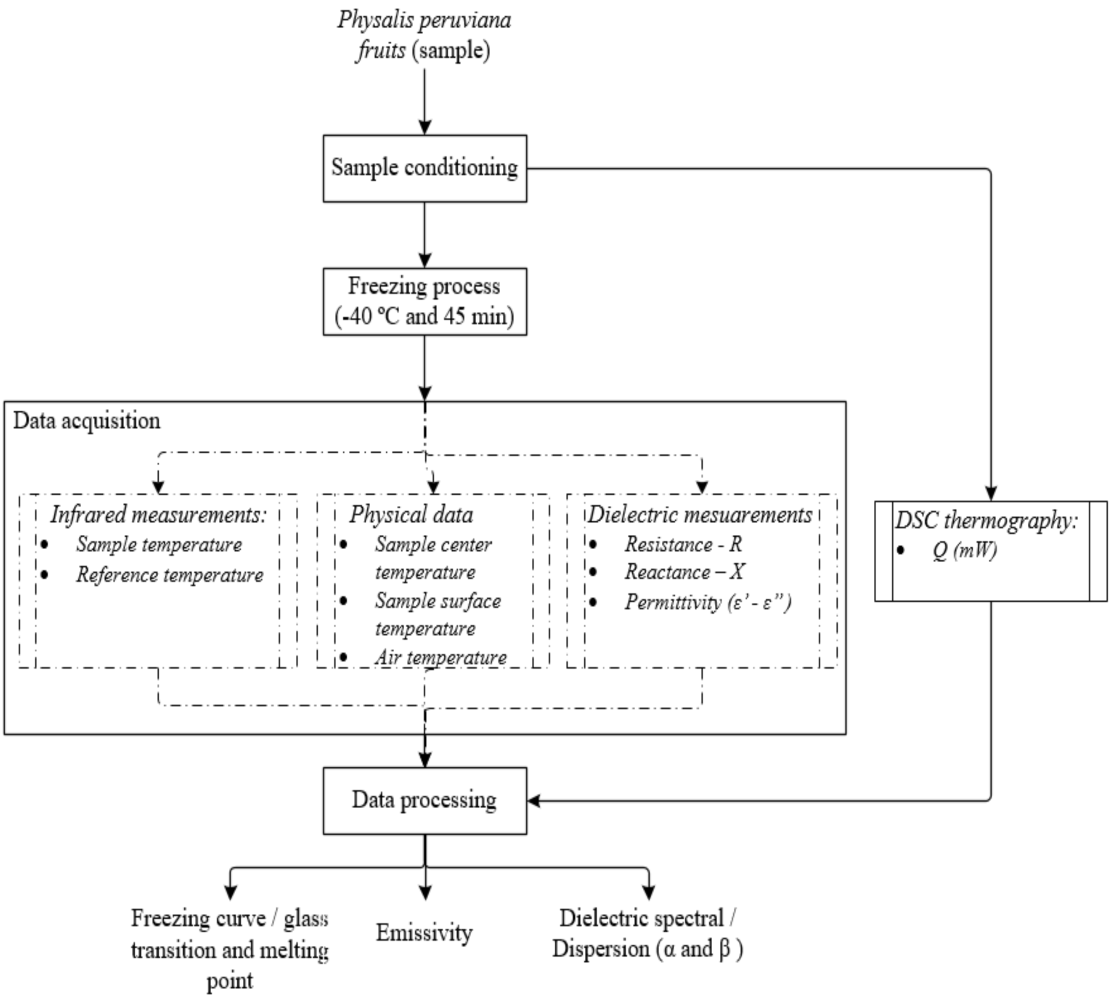

Fig. 1. Experimental procedure in freezing process of *Physalis peruviana*.

2.1. Sample goldenberry fruits

The samples of fresh goldenberry fruit at commercial ripeness, coming from Ecuador, were obtained through the importing company Ammarket (Orihuela, Alicante - Spain). The goldenberry fruits arrived in refrigerated boxes (100 g / box) with uniform size (diameter) and weight, 3.8±0.21 cm and 3.9±0.4 g, respectively, which were kept in a refrigerator at 6 ºC until later analysis and execution of the experiment.

2.1.1. Soluble solids content

The soluble solids (°Brix) of the goldenberry juice were determined using the AOAC method 932. This involved placing 3 to 5 drops of the juice on the lens of the Hanna HI96800 refractometer and taking a reading.

2.1.2. Moisture

The fruit's moisture (in dry basis) was characterized using the methodology of AOAC Method 934.06, 2000.

2.2. Sample conditioning

Prior to the experiment, the goldenberry fruits were removed from the refrigerator and acclimatized at room temperature (18.5 ± 0.6 °C) for a period of 24 h. Furthermore, a sample holder was designed and printed in PLA) with a 3D printer to facilitate the monitoring of the freezing process of the fruits (Fig. 2). The order in which the fruits were placed in the sample holder was as follows: on the right side, the first fruit was used for temperature monitoring using K-type thermocouples (surface and center); in the center, the second fruit was used for surface temperature monitoring using an infrared camera; and on the left side, the third fruit was used for the measurement of dielectric properties.

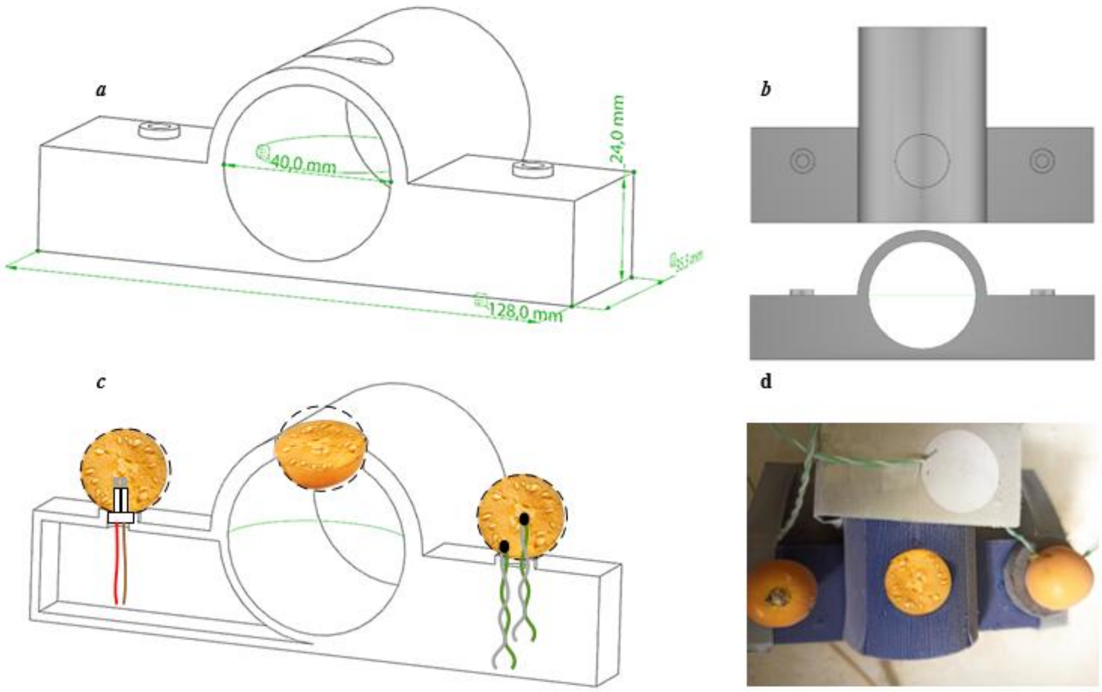

Figure 2. Sample conditioning by sample holder: a) Isometric drawing of the sample holder; b) top and side views of the sample holder; c) location of the samples for the extraction of information (temperature and dielectric properties) and d) conditioning of the fruit in the holder.

2.3. Freezing process

In the present study, data acquisition systems were installed for the purpose of monitoring the freezing process of godenberry fruit. This work is founded upon the contributions of Tomas-Egea et al. (2022) and Cuibus et al. (2014) the installation of the systems involved the measurement of surface and core temperature of the sample, surface temperature by thermographic camera, and dielectric properties (Fig. 2). Prior to the initiation of the freezing process, the sample holder was positioned on an expanded polystyrene box, which was then situated in the center of a horizontal convective air freezer (model ACR-45/87, Dycometal, SL, Barcelona, Spain), with no-frost technology. This configuration ensured that the forced cold airflow would directly contact the fruit (Fig. 2, b and d). This approach facilitated effective convective heat transfer from the air to the fruit, as well as radial conduction heat transfer (from the surface to the center) within the fruit.

In addition, three goldenberry fruits were utilized in each experiment, positioned within the designated sample holder (Fig. 2, c). The initial fruit was positioned on the right, with the objective of conducting temperature monitoring (both surface and core) through the utilization of two K-type thermocouples, with data recorded at an interval of 5 s. The temperature was recorded using an Agilent 34972A data acquisition system (Agilent Technologies, Malaysia). Additionally, the surface temperature of the 25 mm diameter certified emissivity reference material (ε = 0.95) (Optris GmbH, Berlin, Germany) and the air temperature inside the freezer were monitored. The second fruit was positioned centrally for measuring surface temperature. This was accomplished by means of a thermographic camera (Optris PI® 160, Optris GmbH, Berlin, Germany) positioned at a distance of 30 cm, with recordings being conducted at an interval of 0.5 s. The camera was connected directly to a laptop (PCG - 2L5M, Sony WAIO, USA) for the purpose of recording frames (video) of the goldenberry fruit and emissivity reference material during the online freezing process. The third fruit was positioned on the left, with the objective of monitoring the dielectric properties by means of a two-needle sensor that was inserted in the center of the sample. This was connected to an Agilent 4294A impedance analyzer (Agilent Technologies, Santa Clara, CA, USA).

Following the installation of the data acquisition systems and the placement of the goldenberry fruits in the sample holder, an extruded polystyrene sheet (Chovafoam type 4I, Leroy Merlin SL, Valencia, Spain) was utilized as thermal insulation. The sheet, measuring 68 cm × 52 cm × 3 cm, was utilized as the lid of the chest freezer and was affixed with adhesive tape to minimize heat ingress from the external environment. Furthermore, the apparatus featured a central aperture measuring 7 cm in diameter, which served as the site for the integration of the thermographic camera. The freezing process of the goldenberry fruits was conducted at a temperature of -40 °C for a duration of 45 min, with an air flow of 1 m/s, within a horizontal freezer equipped with forced air ventilation (model ACR-45/87, Dycometal, SL, Barcelona, Spain) (Fig. 3).

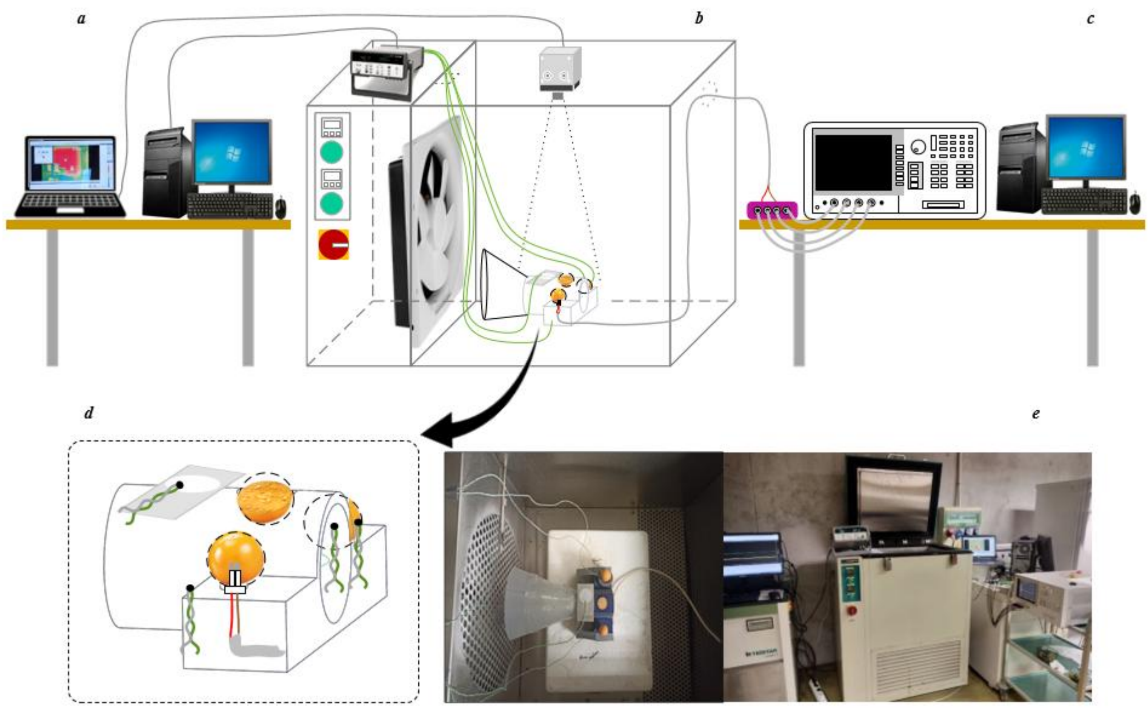

Fig. 3. The freezing process monitoring system is comprised of the following components: a) Thermal data acquisition; b) Freezing process; c) Dielectric data acquisition; d) Sample holder and e) Real environment.

2.4. Infrared thermography

According to Tomas-Egea et al. (2022) and Traffano-Schiffo et al. (2014), in order to obtain thermal images, the thermal camera operates under the following conditions: two-dimensional focal plane (matrix) of 160 x 120 pixels, spectral range of 7.5 – 13.0 µm, resolution of 0.05 ºC and accuracy of ± 2%. The thermal camera measures in a temperature range of -20 to 900 ºC, with a field of view (FOV) of 23º x 17º at a minimum distance of 20mm and a frame rate of 120 Hz, which is connected to a desktop computer to record thermal images throughout the freezing process using the Optris PI Connect software (Optris GmbH, Berlin, Germany). Similarly, the reference emissivity material (radius = 12.5 mm and ε = 0.95) was placed parallel to the lens of the thermographic camera at a distance of 30 cm to calculate the reflected energy received by the thermographic camera (Fig. 3, b).

2.5. Dielectric properties

The dielectric properties of the goldenberry were obtained by means of a needle-type dielectric sensor, taking as a reference the work carried out by Tomas-Egea et al. (2022). The dielectric sensor is composed of two steel needles, the dimensions of which are as follows: The dimensions of the perforation are recorded as 1 mm diameter, 2 mm height and 1.5 mm separation between them (Fig. 4). The perforation penetrates the lower part of the fruit (perpendicular to the equatorial line) until reaching the center (see Fig. 2c). The dielectric sensor was connected to a 4294A impedance analyzer (Agilent Technologies, Santa Clara, CA, USA), which was operated remotely via a desktop computer (ThinkCentre Type 7099 - 7099B8G, Lenovo, China), allowing online monitoring.
Prior to the calibration of the impedance analyzer, it was required to stabilize for a minimum of one hour in order to eliminate possible static charges or stray current (Chuquizuta et al., 2022; Guo, Fang, Liu, & Wang, 2015; Liu & Guo, 2017). The calibration was conducted in accordance with the open-air and short-circuit methodologies outlined by Tomas-Egea et al. (2022). The values of the complex impedance spectrum (resistance - R and reactance - X) were measured in the frequency (f) range (40 Hz to 1 MHz), with 401 data points obtained. The impedance values thus

obtained permitted the calculation of dielectric properties using Eqs. (1), (2), (3) (Traffano-Schiffo et al., 2018).

$$C_0 = \frac{\varepsilon_0 \, S}{d} \tag{1}$$

$$\varepsilon' = \frac{-X}{(R^2 + X^2)} \, \frac{1}{2\pi f C_0 10^{-12}} \tag{2}$$

$$\varepsilon'' = \frac{R}{R^2 + X^2} \, \frac{1}{2\pi f C_0 \, 10^{-12}} \tag{3}$$

Where C0 is the vacuum capacitance (pF), e0 is the vacuum permittivity (C2/Nm2), S is the sensor poles surface (m2), d is the distance between poles (m).

In order to observe the influence of the freezing process on the fruit, as well as on its dielectric properties, it is necessary to obtain the α and β relaxations in the radiofrequency range. To this end, eqs. (4), (5), (6), (7) proposed by Traffano-Schiffo et al. (2018) were utilized to ascertain the α and β relaxation parameters.

$$\log \epsilon'(\omega) = \log \epsilon'_\infty + \sum_{n=1}^{2} \frac{\Delta \log \epsilon'_n}{1 + e^{(\log \omega^2 - \log \tau_n^2) * \alpha_n}} \tag{4}$$

Where n is given by the dispersions of α and β, $\log \epsilon'$represents the logarithm of the dielectric constant, $\log \epsilon'_\infty$ is the logarithm of the dielectric constant at high frequencies, $\log \omega$ is the logarithm of the angular frequency (rad/s) and $\Delta\log\epsilon'_n$ is the amplitude of the dispersion n, $\log \tau_n$ is the logarithm of the angular frequency at relaxation time $(t_{rel} = 1/t_n)$ for each dispersion, α_n is the slope of the dispersion.

Also, from the parameters obtained from Eq. 4, the dielectric constant and the relaxation frequency for each of the dispersion in the radio frequency range have been calculated (Eq. (5), (6), (7)) (Traffano-Schiffo et al., 2018).

$$\epsilon'_\alpha = 10^{\left(\log \epsilon'_\infty + \Delta \log \epsilon'_\beta + \frac{\Delta \log \epsilon'_\alpha}{2}\right)} \tag{5}$$

$$\epsilon'_\beta = 10^{\left(\log \epsilon'_\infty + \frac{\Delta \log \epsilon'_\beta}{2}\right)} \tag{6}$$

$$f_i = 10^{\left(\frac{log \omega_{\tau i}}{2 * \pi}\right)} \tag{7}$$

Where i corresponds to each dispersion (α and β)

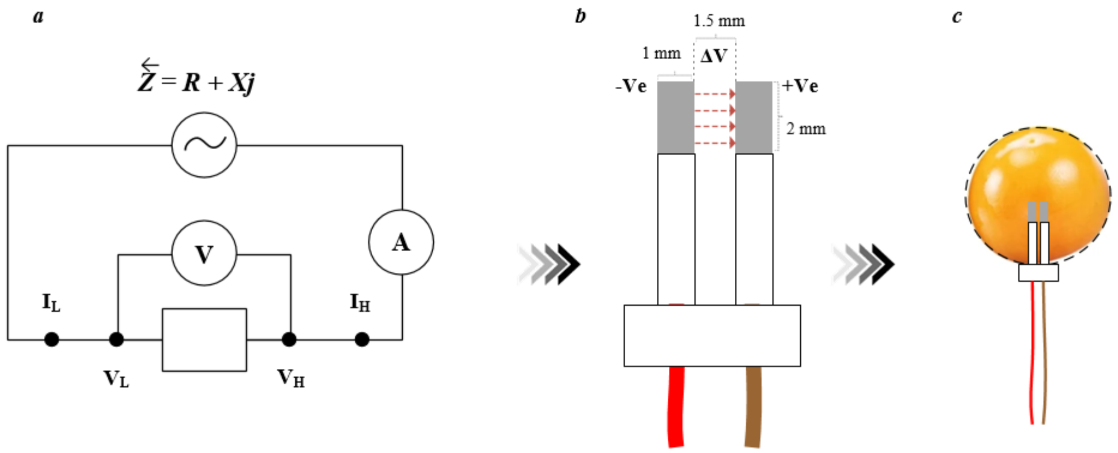

Fig. 4. Schematic representation of the experimental setup used to measure the dielectric properties at the center of the goldenberry sample during the freezing process. a) Electrical circuit diagram for impedance measurement; b) Sensor configuration showing the applied electric field; and c) Sensor positioning at the core of the fruit.

2.6. Differential scanning calorimeter

The methodology proposed by Vega-Gálvez, López, Ah-Hen, Torres, and Lemus-Mondaca (2014), with slight modifications, was utilized to ascertain the glass transition temperature (T_g) and heat capacity (c_p) of fresh goldenberry samples. The thermal profiles of the samples were obtained using a differential scanning calorimeter (DSC, system 1 StarE, Mettler-Toledo, Switzerland), which was calibrated using the automatic calibration function FlexCal, as recommended by the manufacturer. Each sample (10 to 15 mg) was weighed directly onto a 40 µL DSC aluminum tray (Mettler Toledo, ME-00026763) using a Mettler Toledo XS-205 balance, without considering the mass of the tray. Subsequently, the tray was hermetically sealed in order to prevent any loss of moisture during the analysis. The sample trays, in conjunction with an empty tray that served as a control, were placed in the DSC oven. All experiments were performed in triplicate using the following thermal profile: samples were cooled from room temperature to -50°C at a rate of -5°C/min, and held for 30 min to ensure complete freezing of the sample. Subsequently, the samples were subjected to a heating protocol, encompassing a temperature range from -50°C to 80°C at a constant heating rate of 10°C/min. A maintenance period of one minute was implemented to ensure the stability of the temperature before proceeding to the subsequent stage of the experiment.

2.7. Statistic

The Levenberg-Marquardt algorithm, as implemented in the MATLAB 2024b software (MathWorks), was utilised to fit the data to the Traffano-Schiffo model and subsequently calculate the dielectric relaxations α and β. Furthermore, the implemented algorithm was constrained to a maximum of 400 interactions, with a convergence threshold set at 1×10^{-6}. For the purpose of statistical analysis, the coefficient of determination (R^2) and root mean square error (RMSE) were evaluated at the 95% confidence level, with eqs (8), (9) being employed for this purpose.

Furthermore, a univariate analysis of variance (ANOVA) and a Tukey's post hoc test ($\alpha = 0.05$) were conducted on goldenberry heat capacity, utilising Statgraphics Centurion V.19 software.

$$R^2 = \frac{\sum_{i=1}^{n}(\hat{y}_i - y_i)^2}{\sum_{i=1}^{n}(\hat{y}_i - y_t)^2} \tag{8}$$

$$RMSE = \sqrt{\frac{1}{n}\sum_{i=1}^{n}(y_i - \hat{y}_i)^2} \tag{9}$$

Where, $\hat{y_i}$ is the experimental value, y_i is the predicted value and n is the number of observations.

3. Results and discussion

3.1. Freezing kinetics

Figure 5 shows the freezing curve pertaining to both the surface and center of the goldenberry that was obtained by means of K-type thermocouples over the course of a 45 min period. Three distinct stages were identified during the freezing process: After the initial cooling of the sample, a subcooling stage occurs, followed by a phase change (nucleation and freezing), and concluding with a tempering stage until thermal equilibrium with the freezing air is reached. During the cooling stage, a decrease in temperature was observed at the surface and in the center of the sample at different times. In the surface, the subcooling stage was reached at 3.3 ± 0.4 min and at -2.28 ± 0.03 ºC, and in the center of the sample, this stage was reached at 7 ± 1 and -1.93 ± 0.07 ºC. This temperature difference is attributed to variations in the freezing rate, resulting from both convective and conductive heat transfer mechanisms (Guizani, Al-Saidi, Rahman, Bornaz, & Al-Alawi, 2010; Struchaiev, Postol, Stopin, & Borokhov, 2019). These effects are further influenced by changes in solute concentration during the freezing process, which lead to a progressive decrease in the freezing temperature and involve simultaneous variations in internal energy and phase change energy (Ben Haj Said et al., 2016; Hajji et al., 2022). Thus, marking the initiation of nucleation and the formation of ice crystals within the fruit tissue. During this period, most of the water solidifies, while the remaining liquid phase, primarily composed of non-electrolyte solutes, undergoes cryoconcentration, leading to a gradual decrease in the freezing temperature. In the subsequent phase, the supersaturated liquid phase induces a sudden drop in freezing temperature, and a tempering process in which the sample equilibrates with the temperature of the freezing air (Cuibus et al., 2014; Struchaiev et al., 2019). This decrease corresponds to the third stage of the process in which the sample reaches the thermal equilibrium with the air medium (Auleda, Raventós, Sánchez, & Hernández, 2011; Da Silva et al., 2022; Struchaiev et al., 2019).

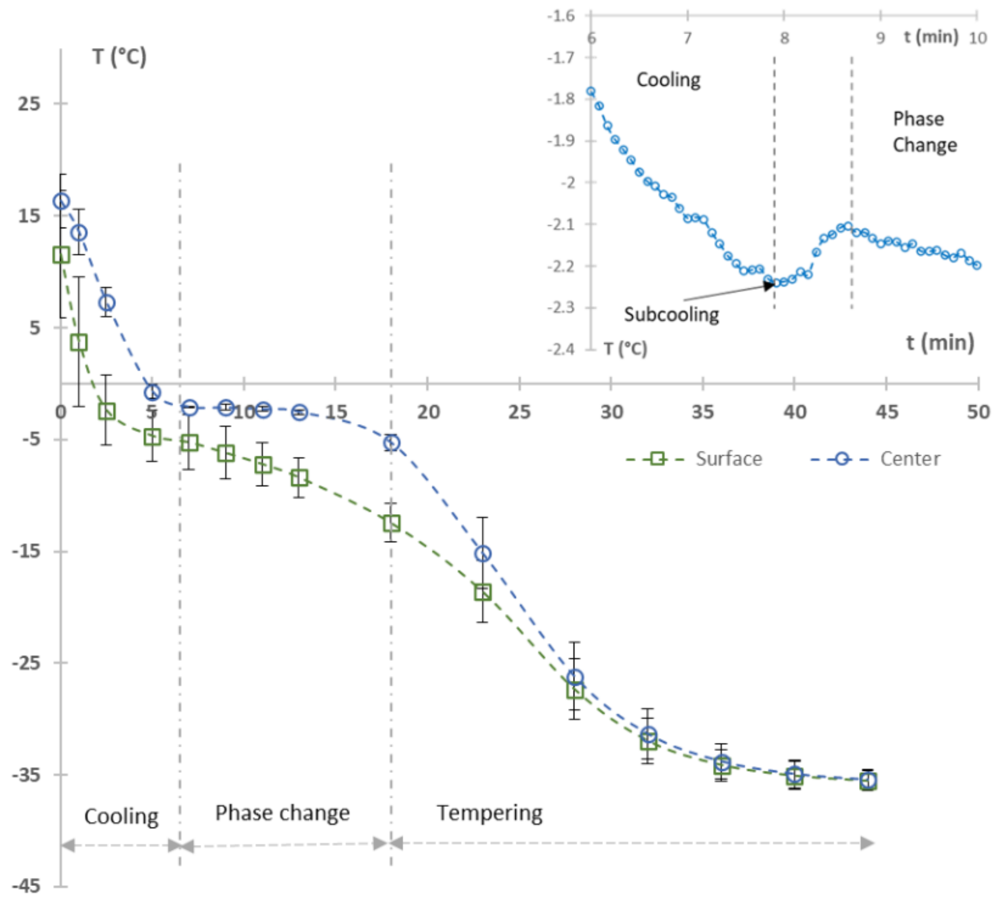

Fig. 5. Freezing curve of fresh goldenberry. The dashed lines represent the critical points of the freezing curve of the center of the sample and the upper magnification represents a specific sample, where the subcooling and initial freezing point are observed.

3.2. Differential scanning calorimetry

Figure 6 shows the thermogram of fresh goldenberry pulp (moisture 4.10 ± 0.04 kg_w/kg_T), where both an endothermic behavior and a glass transition are observed. The glass transition temperature range is detailed in Table 1, with the midpoint (T'_g) identified at -35.8 ± 0.2°C. This T'_g value is close to those reported for other fruits, including Deglet Nour (Guizani et al., 2010), blueberries (Díaz, Henríquez, Enrione, & Matiacevich, 2011; Vásquez, Díaz-Calderón, Enrione, & Matiacevich, 2013), Chinese gooseberries (Wang, Zhang, & Chen, 2008), and raspberries (Syamaladevi, Sablani, Tang, Powers, & Swanson, 2009), which exhibit T'_g values of -42.5, [-44.0 to -40.3], -55.8 and -62.1 °C, respectively. The variation in T'_g among these matrices is primarily attributed to differences in water content and the molecular weight of solutes (Guizani et al., 2010), since higher moisture content generally leads to lower T'_g values (Collares, Finzer, & Kieckbusch, 2004; Roos, 1993; Roos & Drusch, 2016). In the case of goldenberry, these differences can be further explained by the predominant carbohydrate composition of its cell wall, particularly the presence of sucrose (35 g/100 g total sugars), fructose (29 g/100 g), and glucose (25 g/100 g) (Ramadan & Moersel, 2007). These low molecular weight sugars have been shown to significantly influence T'_g, as evidenced in similar food matrices such as mango (Yamamoto, Fong-in, & Kawai, 2021). Moreover, the T'_g for sucrose, glucose and fructose are -41 °C, -53 °C and -53 °C respectively (Roos & Drusch, 2016). These values are comparable to the values obtained for goldenberry pulp.

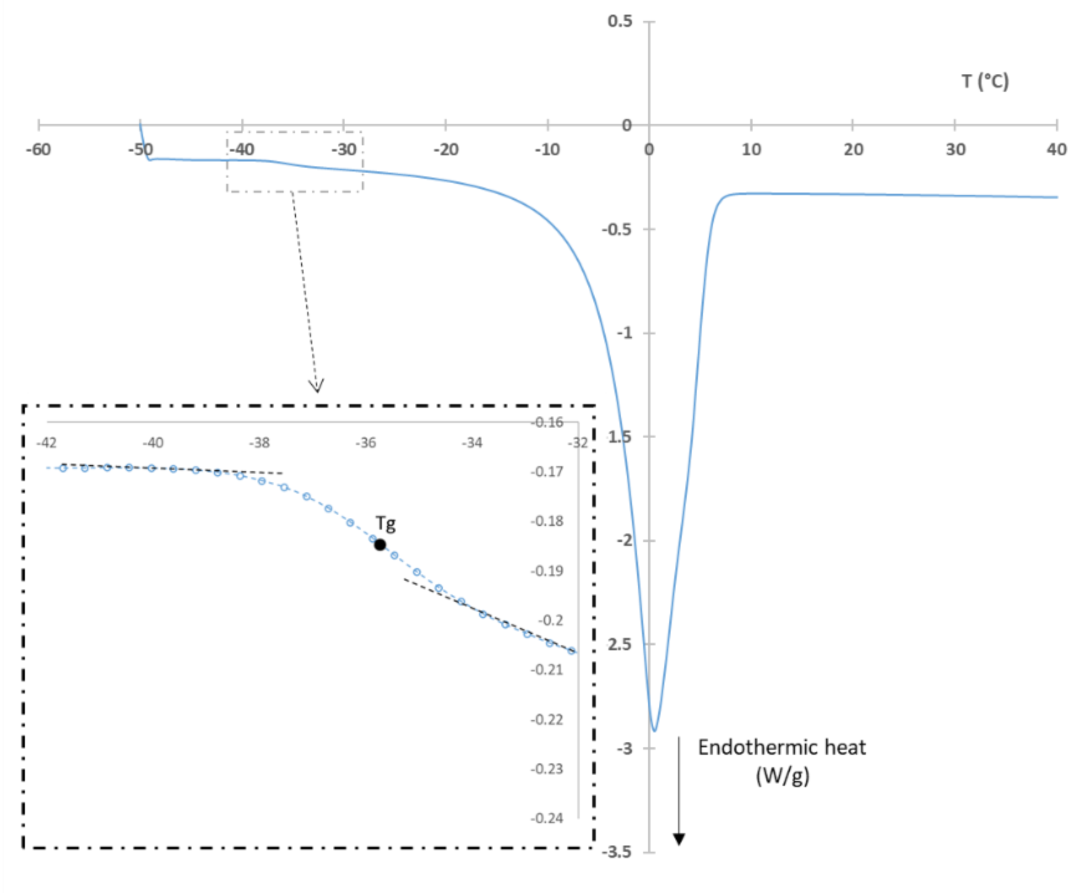

Figure 6. Thermogram of goldenberry pulp.

Table 1. Glass transition of maximally concentrated sample range. Initial, mean and final temperature of goldenberry pulp T_g'.

T_{gi} (°C)	T_g (°C)	T_{ge} (°C)
-33.9 ± 0.2	-35.8 ± 0.2	-37.7 ± 0.2

To date, limited research has been conducted on the thermal properties of high Andean berries, particularly regarding the specific heat capacity (c_p) of goldenberry. The specific heat capacity is a critical parameter in heat transfer calculations and plays a key role in the design and optimization of refrigeration, freezing, and cold storage systems, as well as in defining the operational parameters for these processes.

The Table 2 presents the c_p values of fresh goldenberry pulp across different temperature ranges. These values were derived from the thermal profile (Fig. 6) and calculated using Eq. 10. A Statistically significant difference in c_p was observed between temperature ranges ($p < 0.05$), which may be attributed to variations in moisture and/or water mobility (Farinu & Baik, 2007; Murakonda, Patel, & Dwivedi, 2022). At temperatures above 0 °C, the c_p values obtained for goldenberry pulp were comparable to those reported for other fruits such as murtilla (3.78 kJ/kg·°C), cashew (3.816 kJ/kg·°C), and bael (3.2512 kJ/kg·K). The values for murtilla were determined using differential scanning calorimetry (DSC) (Lemus-Mondaca, Ah-Hen, Vega-Gálvez, & Zura-Bravo, 2016), whereas those for cashew and bael were estimated from proximate composition based on moisture (Singh, Abdullah, Pradhan, & Mishra, 2019; Sonawane, Pathak, & Pradhan, 2020).

$$c_p = \frac{q}{m * \Delta T} \quad (10)$$

In the Table 2 shows, the c_p values of the frozen sample were measured over three distinct periods: the rubbery state, the glass transition, and the glassy state.

Table 2. Specific heat (kJ/kg K) of goldenberry pulp

$\leq T_{ge}$	$T_{ge} \leq \quad \leq T_{gi}$	$\geq T_{gi}$	Fresh *	Fresh **	p value
1.988 ± 0.023^{d}	2.195 ± 0.096^{c}	2.605 ± 0.138^{b}	3.975 ± 0.013^{a}	3.953 ± 0.021^{a}	0.000

Nota. Superscripts of the same letters of the mean c_p values indicate no significant differences according to Tukey's test (pvalue < 0.05); (*) heating; (**) cooling.

3.3. Surface thermal analysis by Infrared thermography.

In the frozen food industry, accurate recording and monitoring of temperature during the fruit freezing process is critically important, as it ensures both the completeness and uniformity of freezing by promoting thermal equilibrium between the sample and the surrounding freezing air. Infrared (IR) thermography has proven to be an effective non-invasive tool for thermal analysis in a variety of food matrices, including pork (Castro-Giraldez et al., 2014) and fresh potatoes (Cuibus et al., 2014), and has been successfully applied in freezing operations.

To accurately interpret the radiant energy emitted from the fruit surface as photon flux, captured by the pyrosensor of the infrared camera during the freezing process, it is essential to apply a radiative heat transfer model. In this context, the Stefan–Boltzmann law provides the theoretical framework required for such modeling. This model should enable the estimation of the fruit's surface emissivity, the radiative energy received from the surrounding environment, and the energy absorbed by the air layer between the fruit and the infrared camera. (Castro-Giraldez et al., 2014; Cuibus et al., 2014; Tomas-Egea et al., 2022; Traffano-Schiffo et al., 2014). These terms are integrated in Eq. 11.

$$E_T = \varepsilon_C \sigma {T_C}^4 = F \cdot \varepsilon_{obj} \sigma T_{obj}^4 + E_{ent} - (1 - \tau_{air}) F \cdot \sigma T_{air}^4 \tag{11}$$

Where E_T is the total energy received by the camera (W/m^2), ε_C is the emissivity set in the thermographic camera ($\varepsilon_C = 1$), σ is the Stefan-Boltzman constant (5.67×10^{-8} W/m^{2}K^4), T_C is the temperature obtained by the thermographic camera, F is the geometric factor that can be taken as 1 when the camera is placed perpendicular to the samples, ε_{obj} is the emissivity of the goldenberry, T_{obj} is the surface temperature of the goldenberry, E_{ent} is the energy of the environment on the object obtained with the reference material, τ_{air} is the air permeability which, when it is less than 30 cm from the fruit and the RH of the environment is less than saturation, can be considered equal to 1, leaving this term as zero.

Figure 7 shows the emissivity profile of fresh goldenberry during the freezing process. In the initial cooling phase (0–5 minutes), a significant decrease in emissivity is observed, from 0.959 ± 0.019 to 0.837 ± 0.002. This reduction may be attributed to surface dehydration of the fruit, likely caused by the low relative humidity conditions within the convective freezer equipped with a no-frost system (Fig. 8). The dehydration phenomenon is driven by a water activity gradient established between the fruit surface and the surrounding air, which promotes the migration of both intracellular and extracellular water to the surface. During the subsequent freezing phase, the emissivity remains relatively stable at approximately 0.845 ± 0.007. This stability is associated with the onset of nucleation and the formation of ice, which induces a chemical potential gradient in the water, leading to both internal and surface ice crystallization (Castro-Giraldez et al., 2014). Concurrently, the surface temperature of the fruit drops rapidly from -4.94 ± 0.17 °C to -28.68 ± 0.12 °C over a 13 min period. Between 18 and 28 min, corresponding to the final stage of the freezing phase, an increase in emissivity is observed from 0.8317 ± 0.003 to 0.93 ± 0.03 (Fig. 7, Fig. 9). This rise may be attributed to the progressive reduction in surface temperature as the fruit approaches thermal equilibrium with the surrounding freezing air. From 28 min until the end of the process, the emissivity of the goldenberry remains stable at approximately 0.9506 ± 0.010. Notably, this stage coincides with the sample reaching its vitrification temperature, recorded at -35.8 ± 0.2 °C (Fig. 9). Similar trends in emissivity variation during freezing processes have been reported in previous studies. Cuibus et al. (2014) and Castro-Giráldez et al. (2014) observed an initial decrease in emissivity, from 0.97 to 0.87 in potatoes and from 0.90 to 0.96 in pork, followed by a subsequent increase after freezing. This behavior aligns with the pattern observed in the present study. In contrast, (Arnoldussen et al., 2022). reported a continuous decline in emissivity during the freezing of sweet cherry reproductive shoots, with values dropping from 0.88 to 0.46 as the temperature decreased from 14 °C to -10 °C.

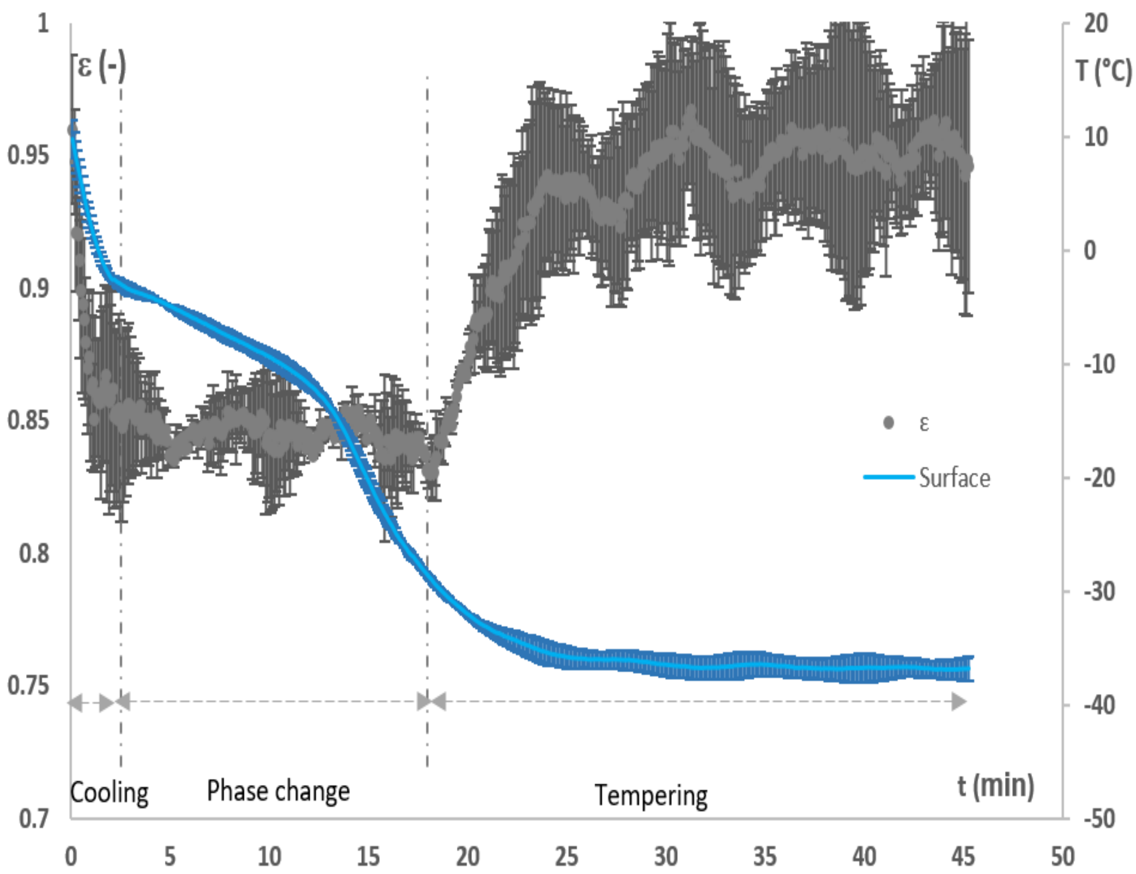

Fig. 7. Kinetics of goldenberry emissivity during the freezing process

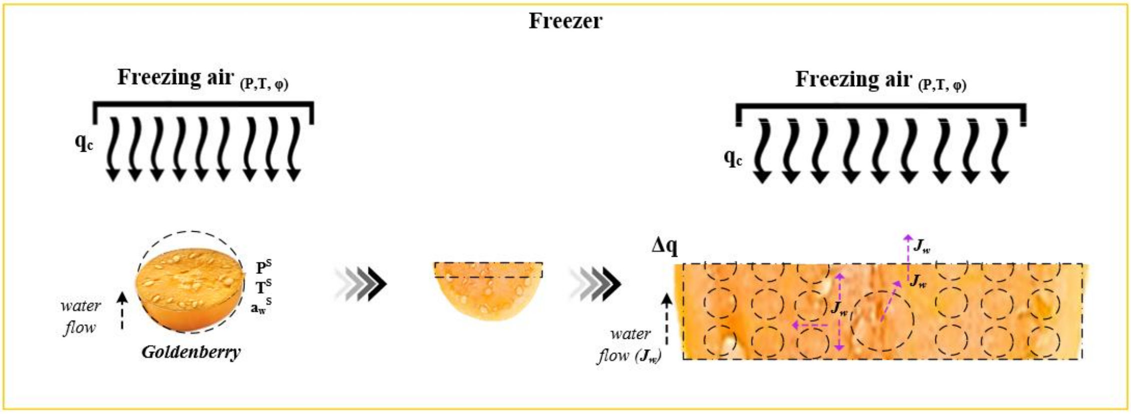

Fig. 8. Thermal analysis and water mobility during freezing of goldenberry.

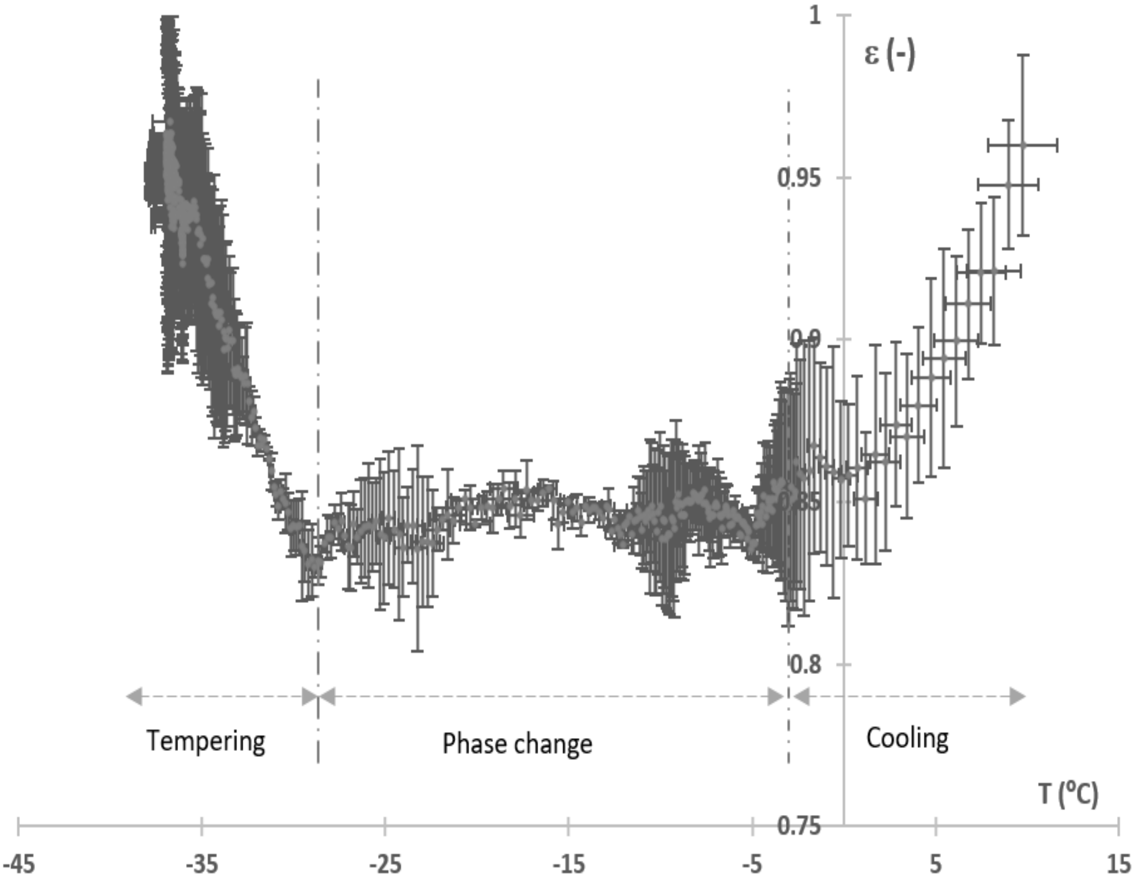

Fig. 9. Emissivity profile of goldenberry as a function of temperature

3.4. Dielectric properties in radiofrequency range.

During the freezing process of goldenberry, a progressive decrease in the dielectric constant (log ε') is observed over time and with an increasing angular frequency (log ω) (Fig. 10). The figure shows the exponential stage of α- and β-dispersions, with relaxation frequencies shifting to lower values during freezing. The dielectric constant declines in both cases due to reduced molecular mobility in the liquid phase and in absorbed water, associated with dehydration driven by ice formation., The dielectric spectra in Fig. 10 exhibit a clear β-dispersion (within the 5.5 to 7.5 log(rad/s) during the first 13 minutes of freezing. This dispersion is attributed to the orientation of fixed charges associated with macromolecules and/or interfacial polarization phenomena, such as the Maxwell–Wagner effect, commonly observed in biological tissues (Albelda Aparisi, Fortes Sanchez, Contat Rodrigo, Masot Peris, & Laguarda-Miro, 2021; Tomas-Egea et al., 2022). The orientation capacity of fixed charges on tissue proteins and carbohydrates is modulated by adsorbed water, and thus, any water-reducing mechanism directly impacts their dielectric behavior. In addition, α-dispersion is also observed, primarily resulting from the orientation of mobile charges. In goldenberry, this mechanism is fundamentally associated with native ions of the fruit (Kuang & Nelson, 1998). From minute 18 until the end of the freezing process, the ε' values continue to decrease, reaching a stabilization phase. This behavior is consistent with the reduced ability of biological materials to store electrical energy as a result of decreased water mobility and availability during the liquid–solid phase transition (Heileman et al., 2013). Such limitations hinder the detection of dielectric spectra, as previously described in studies on frozen biological matrices (Alexander, Shaw, & Muckenhirn, 1937; Auty & Cole, 1952; Pandey, Vandermeiren, Dimiccoli, & Stiens, 2018; Zhang, Shen, & Luo, 2010).

Our findings align with prior observations reported by Arteaga et al. (2021) in the monitoring of blueberry freezing, and by Tomas-Egea et al. (2022), who used radiofrequency spectrophotometry to determine the critical freezing point of chicken meat. In both cases, a consistent decrease in ε' values was reported across different frequencies and freezing durations, a trend similarly observed in our study.

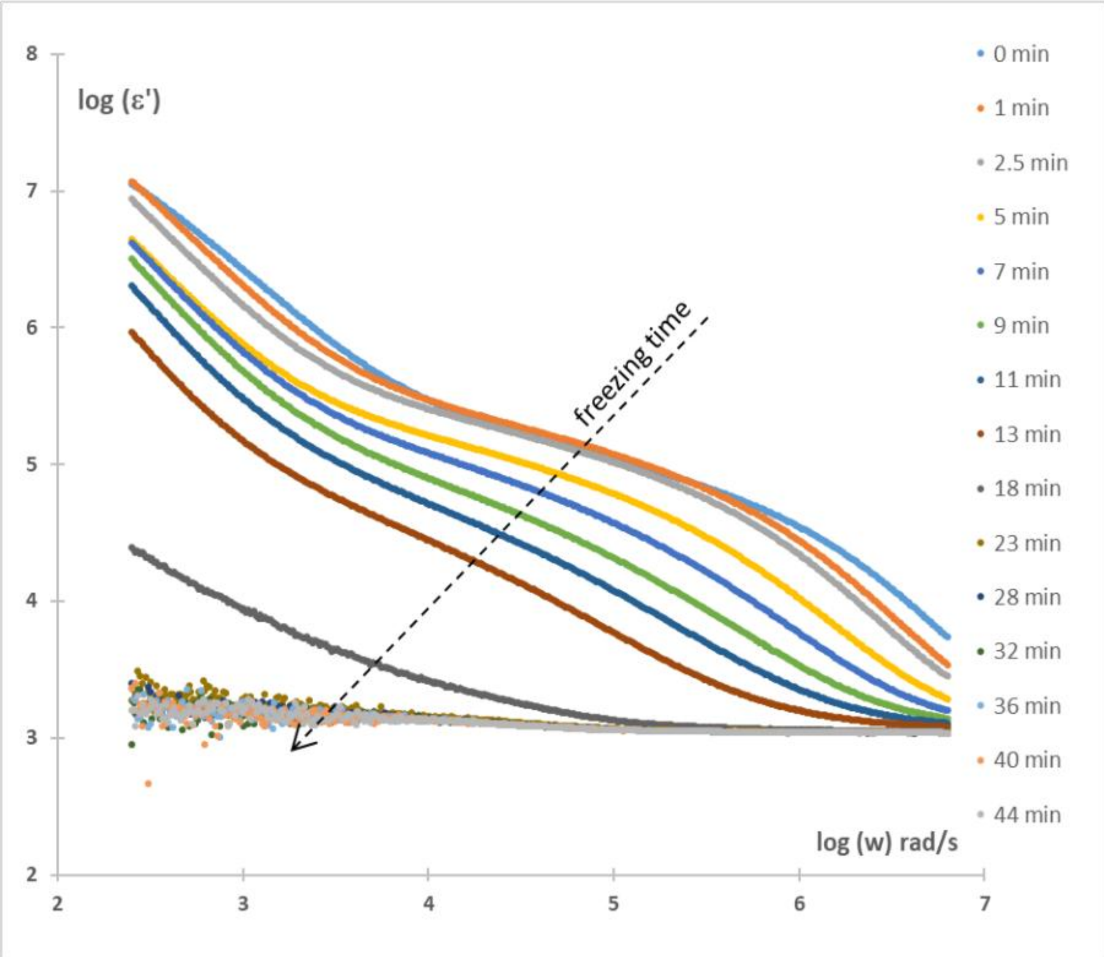

Fig. 10. Evolution of the dielectric spectra of goldenberry during the freezing process.

3.5. Kinetics of α and β dispersions

To identify the critical points of the goldenberry freezing process and to elucidate the influence of tissue structure and chemical composition on photon flux, it is essential to analyze α- and β-relaxations using Eqs. (5), (6). Fig. 11 illustrates these critical transitions, consistent with descriptions by Fan and Roos (2017) and Roos (2010). Specifically, the onset of freezing can be inferred from the maximum of the real part of the dielectric constant (ε') within the β-dispersion region, as shown in Fig. 11(a). This behavior is associated with the high surface tension of agglomerated ice cristal Ih, which produces a high Maxwell Wagner effect, allowing to detect the initial ice crystal formation (Agranovich, Ben Ishai, Katz, Bezman, & Feldman, 2016; Cuibus et al., 2014; Tomas-Egea et al., 2022). A similar trend is observed in the α-dispersion region (Fig. 11(c)), where a sharp increase in ε' is attributed to the ionic concentration. In goldenberry tissue, the liquid phase is rich in electrolytes and sugars; as ice crystals form, cryoconcentration initially increases electrolyte concentration, amplifying the α-dispersion response. However, upon reaching saturation and supersaturation, the exponential rise in viscosity restricts ionic mobility, thereby diminishing the α-dispersion effect (Bittelli, Flury, & Roth, 2004; Fan & Roos, 2017; Kono, Imamura, & Nakagawa, 2021; Sasaki et al., 2017). The final freezing point can also be clearly determined. As demonstrated in Fig. 11(c), corresponding to α-dispersion, ε'exhibits a pronounced trend change around −5.27 °C, marking the completion of ice crystal formation. This trend is also corroborated by Fig. 11(b), which shows the loss factor (ε") in the β-dispersion region. A progressive decline in ε" is observed after the maximum peak, indicating a diminished ability of the system to dissipate energy due to increased rigidity of the frozen matrix (Roos, 2010; Talja & Roos, 2001; Tomas-Egea et al., 2022).

During the freezing process, initial ice nuclei typically form at the fruit surface. This induces surface dehydration and creates a gradient in the water chemical potential, which drives water migration from the interior toward the surface. Under atmospheric pressure conditions, the formation of ice Ih crystals is favored. These crystals exhibit high surface tension, which further attracts nearby liquid water molecules, promoting the growth of agglomerated ice structures. As a result, water is simultaneously attracted to the surface and to nucleation centers, leading to high water mobility throughout the freezing process.

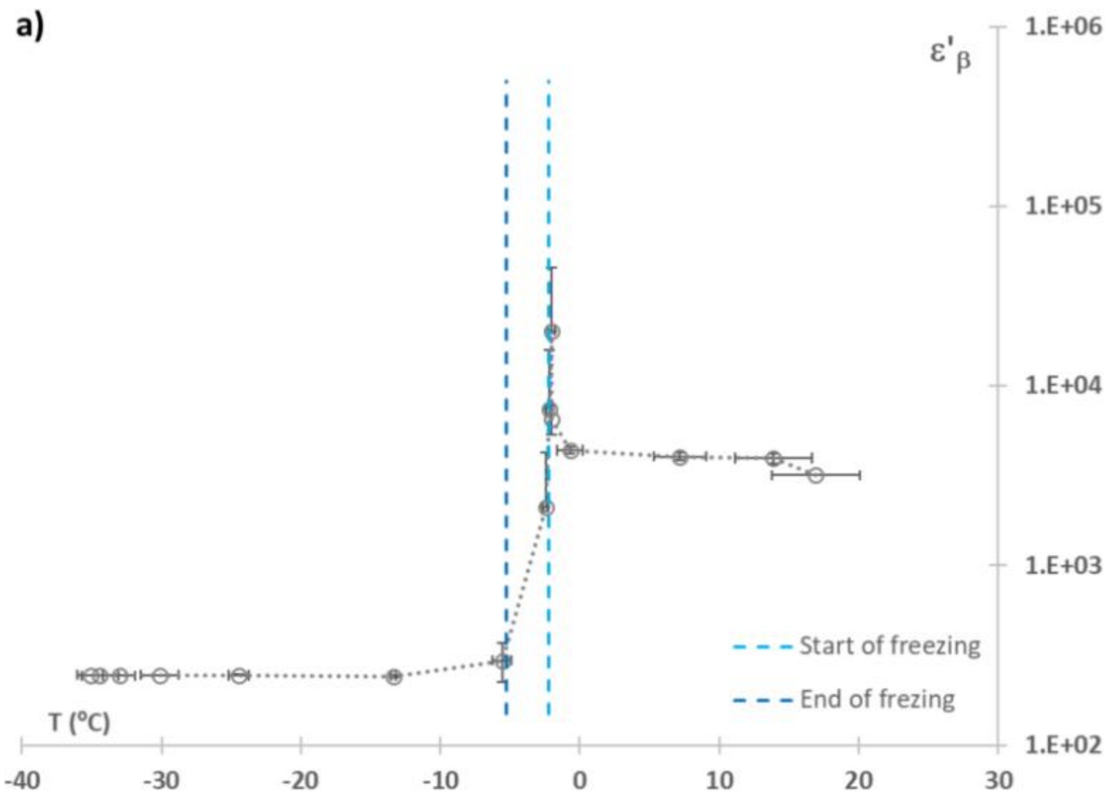

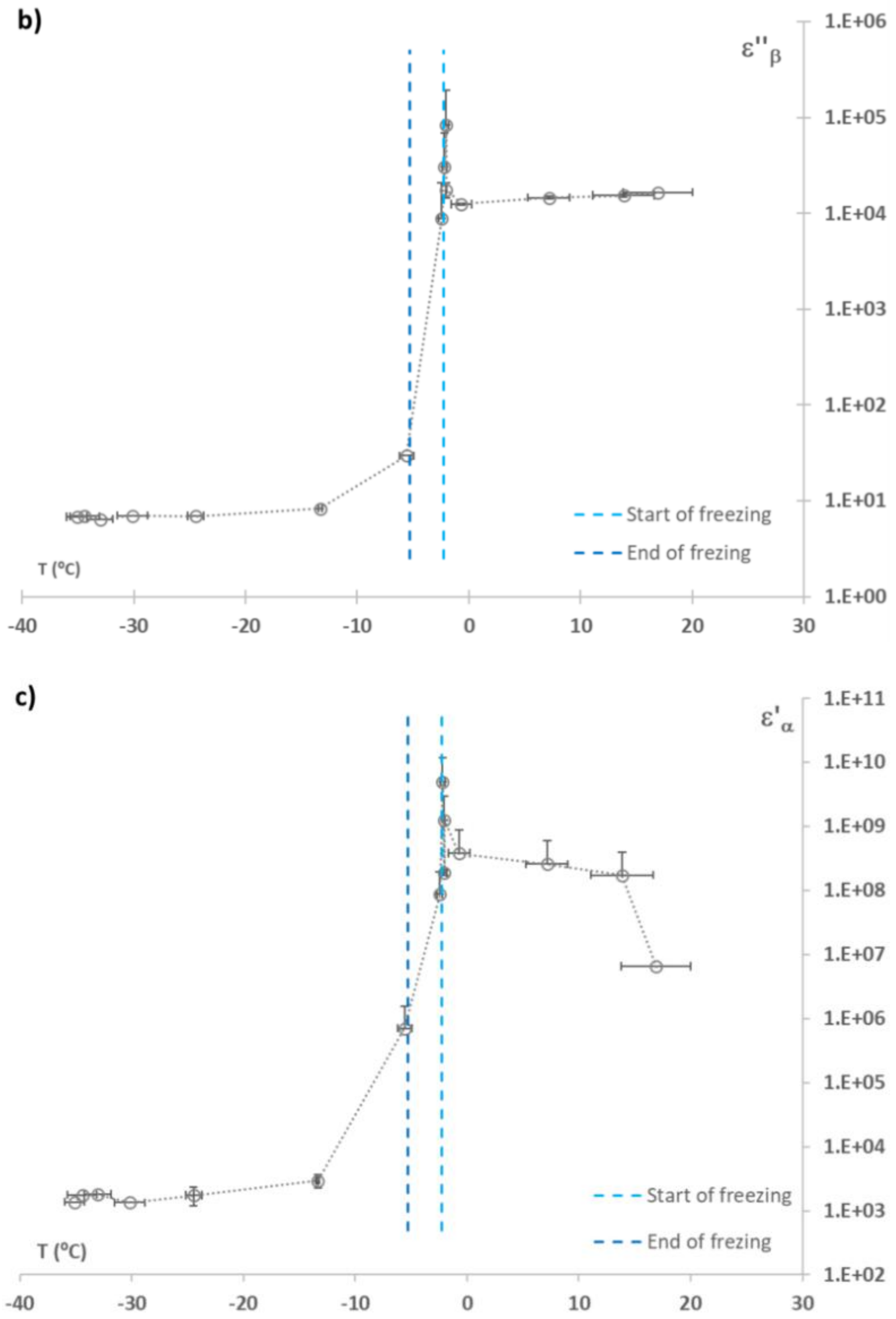

Fig. 11. Dielectric properties with respect to internal temperature, where a) dielectric constant in β relaxation, b) dielectric loss factor in β relaxation and c) dielectric constant in α relaxation.

3.6. Water mobility role

The location of ice nucleation plays a critical role in the extent of cellular damage. When ice nucleation occurs extracellularly (in the apoplastic space), water is drawn out of the cells, and the resulting ice crystal growth tends to cause minimal structural disruption. In contrast, intracellular nucleation (e.g., within the vacuole) leads to expansion and rupture of cell membranes, significantly increasing tissue damage.

In our study, changes in surface emissivity were associated with dehydration and water migration dynamics, while dielectric α-dispersion reflected alterations in ionic mobility, likely due to membrane disruption and solute concentration changes. β-dispersion, on the other hand, captured interfacial polarization effects related to ice crystal growth and macromolecular rearrangements. Together, these thermal and dielectric parameters provide a non-invasive means of assessing structural changes during freezing, offering valuable information for optimizing processing protocols.

4. Conclusions

The findings indicate that infrared thermography is a viable method for monitoring the freezing process of goldenberry, as it facilitates the observation of surface temperature variations. This tool facilitates the identification of critical points in the process, such as the glass transition, from the estimation of the emissivity at different stages of freezing; supercooling stage: Detected by a continuous temperature drop without phase change, and a sharp decrease in emissivity from ∼0.959 to 0.837. This stage ends with the onset of nucleation. Ice nucleation and crystallization stage: Identified by a plateau or slight rebound in temperature due to latent heat release, along with stable emissivity (∼0.845) and changes in dielectric α- and β-dispersions, reflecting structural changes (β) and cryoconcentration (α). And finally, Vitrification stage: Occurs after ice crystallization is completed. Emissivity increases again (∼0.93 to 0.951) as the system approaches the glass transition. The glass transition temperature (−35.8 °C) marks the point where molecular mobility becomes severely restricted, thus preserving cellular structure by preventing further ice growth and solute migration. This enhances long-term structural and biochemical stability during frozen storage.

Conversely, the utilization of sensors founded upon radiofrequency spectrophotometry facilitates the acquisition of not merely surface information, as is the case in thermography, but also the internal properties of samples undergoing the freezing process. This is imperative for the precise detection of the critical points of the process (melting point and glass transition), thereby ensuring uniform and efficient freezing of the goldenberry.

5. References

Agranovich, D., Ben Ishai, P., Katz, G., Bezman, D., & Feldman, Y. (2016). Dielectric spectroscopy study of water dynamics in frozen bovine milk. *Colloids and Surfaces B: Biointerfaces*, *141*, 390–396. https://doi.org/10.1016/j.colsurfb.2016.01.031

Albelda Aparisi, P., Fortes Sanchez, E., Contat Rodrigo, L., Masot Peris, R., & Laguarda-Miro, N. (2021). A Rapid Electrochemical Impedance Spectroscopy and Sensor-Based Method for Monitoring Freeze-Damage in Tangerines. *IEEE Sensors Journal, 21(10),* 12009–12018. https://doi.org/10.1109/JSEN.2021.3065846

Alexander, L. T., Shaw, T. M., & Muckenhirn, R. J. (1937). Detection of Freezing Point by Dielectric Measurements. *Soil Science Society of America Journal, 1(C)*, 113–119. https://doi.org/10.2136/sssaj1937.036159950001000000014x

Arnoldussen, B., Alhamid, J., Wang, P., Mo, C., Zhang, X., Zhang, Q., & Whiting, M. (2022). Internal freezing and heat loss of apple (Malus domestica Borkh.) and sweet cherry (*Prunus avium* L.) reproductive buds are decreased with cellulose nanocrystal dispersions. *Frontiers in Plant Science*, *13*. https://doi.org/10.3389/fpls.2022.949537

Arteaga, H., Robleto-Martinez, E., Carolina de Sousa Silva, A., Souto, S., Batista, J., & Xavier Costa, E. J. (2021). Postharvest freezing process assessment of the blueberry structure in three acts: Bioimpedance, color, and granulometry analysis. *LWT, 151,* 112237. https://doi.org/10.1016/j.lwt.2021.112237

Auleda, J. M., Raventós, M., Sánchez, J., & Hernández, E. (2011). Estimation of the freezing point of concentrated fruit juices for application in freeze concentration. *Journal of Food Engineering, 105(2),* 289–294. https://doi.org/10.1016/j.jfoodeng.2011.02.035

Auty, R. P., & Cole, R. H. (1952). Dielectric Properties of Ice and Solid D2O. *The Journal of Chemical Physics, 20(8)*, 1309–1314. https://doi.org/10.1063/1.1700726

Balaguera-López, H. E., Espinal-Ruiz, M., Zacarías, L., & Herrera, A. O. (2017). Effect of ethylene and 1-methylcyclopropene on the postharvest behavior of cape gooseberry fruits (*Physalis peruviana* L.).

Food Science and Technology International, 23(1), 86–96. https://doi.org/10.1177/1082013216658581

Ben Haj Said, L., Bellagha, S., & Allaf, K. (2016). Dehydrofreezing of Apple Fruits: Freezing Profiles, Freezing Characteristics, and Texture Variation. *Food and Bioprocess Technology, 9(2),* 252–261. https://doi.org/10.1007/s11947-015-1619-4

Bittelli, M., Flury, M., & Roth, K. (2004). Use of dielectric spectroscopy to estimate ice content in frozen porous media. *Water Resources Research, 40(4).* https://doi.org/10.1029/2003WR002343

Castro-Giráldez, M., Balaguer, N., Hinarejos, E., & Fito, P. J. (2014). Thermodynamic approach of meat freezing process. *Innovative Food Science & Emerging Technologies, 23*, 138–145. https://doi.org/10.1016/j.ifset.2014.03.007

Chandra Roychoudhuri, A. F. K. K. C. (2017). The Nature of Light What is a Photon? (Thompson Brian J., Ed.). *CRC Press*.

Chi Khang, V., Le Dang, T., Van Muoi, N., & Thanh Truc, T. (2022). Evaluation of freezing temperatures and ripeness levels on the quality characteristics of frozen pineapple fruits. *Journal of Microbiology, Biotechnology and Food Sciences, 12(3),* e5439. https://doi.org/10.55251/jmbfs.5439

Chuquizuta, T., Colunche, Y., Rubio, M., Oblitas, J., Arteaga, H., & Castro, W. (2022). Prediction of Quality Attributes of Fresh Unpasteurized Milk Using Dielectric Spectroscopy Coupled to Chemometric Tools. *2022 Photonics & Electromagnetics Research Symposium (PIERS)*, 776–782. https://doi.org/10.1109/PIERS55526.2022.9792687

Collares, F. P., Finzer, J. R. D., & Kieckbusch, T. G. (2004). Glass transition control of the detachment of food pastes dried over glass plates. *Journal of Food Engineering*, *61(2),* 261–267. https://doi.org/10.1016/S0260-8774(03)00098-0

Cuibus, L., Castro-Giráldez, M., Fito, P. J., & Fabbri, A. (2014). Application of infrared thermography and dielectric spectroscopy for controlling freezing process of raw potato. *Innovative Food Science & Emerging Technologies*, *24*, 80–87. https://doi.org/10.1016/j.ifset.2013.11.007

Da Silva, D. L., Silveira, A. S., Ronzoni, A. F., & Hermes, C. J. L. (2022). Effect of freezing rate on the quality of frozen strawberries (Fragaria x ananassa). *International Journal of Refrigeration, 144*, 46–54. https://doi.org/10.1016/j.ijrefrig.2022.07.006

De Ancos, B., Sánchez-Moreno, C., De Pascual-Teresa, S., & Cano, M. P. (2012). Freezing Preservation of Fruits. In *Handbook of Fruits and Fruit Processing* (pp. 103–119). Wiley. https://doi.org/10.1002/9781118352533.ch7

Delgado, A. E., & Sun, D.-W. (2001). Heat and mass transfer models for predicting freezing processes – a review. *Journal of Food Engineering, 47(3),* 157–174. https://doi.org/10.1016/S0260-8774(00)00112-6

Díaz, P., Henríquez, O., Enrione, J., & Matiacevich, S. (2011). Thermal transitions of pulp and cuticle of blueberries. *Thermochimica Acta, 525(1–2),* 56–61. https://doi.org/10.1016/j.tca.2011.07.021

Fan, F., & Roos, Y. H. (2017). Glass Transition-Associated Structural Relaxations and Applications of Relaxation Times in Amorphous Food Solids: a Review. *Food Engineering Reviews, 9(4),* 257–270. https://doi.org/10.1007/s12393-017-9166-6

Farinu, A., & Baik, O.-D. (2007). Thermal Properties of Sweet Potato with its Moisture Content and Temperature. *International Journal of Food Properties, 10(4),* 703–719. https://doi.org/10.1080/10942910601137482

Gallego, B., Verdú, J. R., Carrascal, L. M., & Lobo, J. M. (2016). A protocol for analysing thermal stress in insects using infrared thermography. *Journal of Thermal Biology, 56,* 113–121. https://doi.org/10.1016/j.jtherbio.2015.12.006

Gonçalves, B. J., Giarola, T. M. de O., Pereira, D. F., Vilas Boas, E. V. de B., & de Resende, J. V. (2016). Using infrared thermography to evaluate the injuries of cold-stored guava. *Journal of Food Science and Technology, 53(2),* 1063–1070. https://doi.org/10.1007/s13197-015-2141-4

Gonçalves, B. J., Lago, A. M. T., Machado, A. A., Giarola, T. M. de O., Prado, M. E. T., & de Resende, J. V. (2018). Infrared (IR) thermography applied in the freeze-drying of gelatin model solutions added with ethanol and carrier agents. *Journal of Food Engineering, 221,* 77–87. https://doi.org/10.1016/j.jfoodeng.2017.10.004

Guizani, N., Al-Saidi, G. S., Rahman, M. S., Bornaz, S., & Al-Alawi, A. A. (2010). State diagram of dates: Glass transition, freezing curve and maximal-freeze-concentration condition. *Journal of Food Engineering, 99(1),* 92–97. https://doi.org/10.1016/j.jfoodeng.2010.02.003

Guo, W., Fang, L., Liu, D., & Wang, Z. (2015). Determination of soluble solids content and firmness of pears during ripening by using dielectric spectroscopy. *Computers and Electronics in Agriculture, 117,* 226–233. https://doi.org/10.1016/j.compag.2015.08.012

Hajji, W., Gliguem, H., Bellagha, S., & Allaf, K. (2022). Structural and textural improvements of strawberry fruits by partial water removal prior to conventional freezing process. *Journal of Food Measurement and Characterization, 16(5),* 3344–3353. https://doi.org/10.1007/s11694-022-01443-w

Harrap, M. J. M., Hempel de Ibarra, N., Whitney, H. M., & Rands, S. A. (2018). Reporting of thermography parameters in biology: a systematic review of thermal imaging literature. *Royal Society Open Science, 5(12),* 181281. https://doi.org/10.1098/rsos.181281

Heileman, K., Daoud, J., & Tabrizian, M. (2013). Dielectric spectroscopy as a viable biosensing tool for cell and tissue characterization and analysis. *Biosensors and Bioelectronics, 49,* 348–359. https://doi.org/10.1016/j.bios.2013.04.017

Kono, S., Imamura, H., & Nakagawa, K. (2021). Non-destructive monitoring of food freezing process by microwave resonance spectroscopy with an open-ended coaxial resonator. *Journal of Food Engineering, 292*, 110293. https://doi.org/10.1016/j.jfoodeng.2020.110293

Kuang, W., & Nelson, S. O. (1998). Low-frequency dielectric properties of biological tissues: A review with some new insights. *Transactions of ASAE*, 41(1), 173–184. https://doi.org/10.13031/2013.17142

Lan, W., Hui, X., Nicolaï, B., Verboven, P., Qin, J., Renard, C. M. G. C., … Pan, L. (2024). Visualizing the structural and chemical heterogeneity of fruit and vegetables using advanced imaging techniques: Fundamentals, instrumental aspects, applications and future perspectives. *Critical Reviews in Food Science and Nutrition*. https://doi.org/ 10.1080/10408398.2024.2384650

Lemus-Mondaca, R., Ah-Hen, K., Vega-Gálvez, A., & Zura-Bravo, L. (2016). Effect of high hydrostatic pressure on rheological and thermophysical properties of murtilla (*Ugni molinae* Turcz) berries. *Journal of Food Science and Technology, 53(6)*, 2725–2732. https://doi.org/10.1007/s13197-016-2244-6

Li, H.-C., Cheng, H.-P., & Cheng, C.-C. (2025). Shelf temperature estimation of a vacuum freeze dryer by infrared thermal imaging camera. *Quantitative InfraRed Thermography Journal, 1–16.* https://doi.org/10.1080/17686733.2025.2463264

Liu, D., & Guo, W. (2017). Nondestructive determination of soluble solids content of persimmons by using dielectric spectroscopy. *International Journal of Food Properties, 20(3),* S2596–S2611. https://doi.org/10.1080/10942912.2017.1381114

Loayza-Salazar, S., Siche, R., Vegas, C., Chávez-Llerena, R. T., Encina-Zelada, C. R., Calla-Florez, M., & Comettant-Rabanal, R. (2024). Novel Technologies in the Freezing Process and Their Impact on the Quality of Fruits and Vegetables. *Food Engineering Reviews, 16(3),* 371–395. https://doi.org/10.1007/s12393-024-09371-9

Lopez, H. E. B., Fischer, G., & Magnitskiy, S. (2024). Physiology and biochemistry of the Physalis peruviana fruit. In *Handbook of Goldenberry* (*Physalis Peruviana*) (pp. 121–137). Elsevier. https://doi.org/10.1016/B978-0-443-15433-1.00011-X

Murakonda, S., Patel, G., & Dwivedi, M. (2022). Characterization of engineering properties and modeling mass and fruit fraction of wood apple (*Limonia acidissima*) fruit for post-harvest processing. *Journal of the Saudi Society of Agricultural Sciences, 21(4),* 267–277. https://doi.org/10.1016/j.jssas.2021.09.005

Ojha, K. S., Kerry, J. P., Tiwari, B. K., & O'Donnell, C. (2016). Freezing for Food Preservation. In Reference Module in Food Science. Elsevier. https://doi.org/10.1016/B978-0-08-100596-5.03108-5

Olivares-Tenorio, M.-L., Dekker, M., Verkerk, R., & van Boekel, M. A. J. S. (2016). Health-promoting compounds in cape gooseberry (*Physalis peruviana* L.): Review from a supply chain perspective. *Trends in Food Science & Technology, 57*, 83–92. https://doi.org/10.1016/j.tifs.2016.09.009

Ozcelik, M. M., Ozcelik, A., Aksu, M., & Ozkan, G. (2024). Postharvest technology and packing of *Physalis peruviana*. In *Handbook of Goldenberry* (*Physalis Peruviana*) (pp. 291–298). Elsevier. https://doi.org/10.1016/B978-0-443-15433-1.00031-5

Pandey, G., Vandermeiren, W., Dimiccoli, L., & Stiens, J. (2018). Contactless monitoring of food drying and freezing processes with millimeter waves. *Journal of Food Engineering, 226*, 1–8. https://doi.org/10.1016/j.jfoodeng.2018.01.003

Poirier-Pocovi, M., Volder, A., & Bailey, B. N. (2020). Modeling of reference temperatures for calculating crop water stress indices from infrared thermography. *Agricultural Water Management, 233,* 106070. https://doi.org/10.1016/j.agwat.2020.106070

Puente, L. A., Pinto-Muñoz, C. A., Castro, E. S., & Cortés, M. (2011). Physalis peruviana Linnaeus, the multiple properties of a highly functional fruit: A review. *Food Research International, 44(7),* 1733–1740. https://doi.org/10.1016/j.foodres.2010.09.034

Puente, L., Vega-Gálvez, A., Fuentes, I., Stucken, K., Rodríguez, A., & Pastén, A. (2021). Effects of drying methods on the characterization of fatty acids, bioactive compounds and antioxidant capacity in a thin layer of physalis (*Physalis peruviana* L.) pulp. *Journal of Food Science and Technology, 58(4),* 1470–1479. https://doi.org/10.1007/s13197-020-04659-0

Ramadan, M. F., & Moersel, J. T. (2007). Impact of enzymatic treatment on chemical composition, physicochemical properties and radical scavenging activity of goldenberry (*Physalis peruviana* L.) juice. *Journal of the Science of Food and Agriculture, 87(3),* 452–460. https://doi.org/10.1002/jsfa.2728

Roos, Y. H. (1993). Water activity and physical state effects on amorphous food stability. *Journal of Food Processing and Preservation, 16(6),* 433–447. https://doi.org/10.1111/j.1745-4549.1993.tb00221.x

Roos, Y. H. (2010). Glass Transition Temperature and Its Relevance in Food Processing. *Annual Review of Food Science and Technology, 1(1),* 469–496. https://doi.org/10.1146/annurev.food.102308.124139

Roos, Y. H., & Drusch, S. (2016). Food components and polymers. In *Phase Transitions in Foods* (pp. 115–172). Elsevier. https://doi.org/10.1016/B978-0-12-408086-7.00005-X

Sasaki, K., Panagopoulou, A., Kita, R., Shinyashiki, N., Yagihara, S., Kyritsis, A., & Pissis, P. (2017). Dynamics of Uncrystallized Water, Ice, and Hydrated Protein in Partially Crystallized Gelatin–Water Mixtures Studied by Broadband Dielectric Spectroscopy. *The Journal of Physical Chemistry B, 121(1),* 265–272. https://doi.org/10.1021/acs.jpcb.6b04756

Shammi, S., Sohel, F., Diepeveen, D., Zander, S., & Jones, M. G. K. (2023). Machine learning-based detection of frost events in wheat plants from infrared thermography. *European Journal of Agronomy, 149,* 126900. https://doi.org/10.1016/j.eja.2023.126900

Shammi, S., Sohel, F., Diepeveen, D., Zander, S., Jones, M. G. K., Bekuma, A., & Biddulph, B. (2022). Machine learning-based detection of freezing events using infrared thermography. *Computers and Electronics in Agriculture, 198,* 107013. https://doi.org/10.1016/j.compag.2022.107013

Singh, S. S., Abdullah, S., Pradhan, R. C., & Mishra, S. (2019). Physical, chemical, textural, and thermal properties of cashew apple fruit. *Journal of Food Process Engineering, 42(5).* https://doi.org/10.1111/jfpe.13094

Sonawane, A., Pathak, S. S., & Pradhan, R. C. (2020). Physical, thermal, and mechanical properties of bael fruit. *Journal of Food Process Engineering, 43(6).* https://doi.org/10.1111/jfpe.13393

Struchaiev, N., Postol, Y., Stopin, Y., & Borokhov, I. (2019). Determination of the Duration of Spherical-Shaped Berries Freezing Under the Conditions Stationary Heat Flow. In *Modern Development Paths of Agricultural Production* (pp. 405–414). Springer International Publishing. https://doi.org/10.1007/978-3-030-14918-5_42

Syamaladevi, R. M., Sablani, S. S., Tang, J., Powers, J., & Swanson, B. G. (2009). State diagram and water adsorption isotherm of raspberry (Rubus idaeus). *Journal of Food Engineering, 91(3),* 460–467. https://doi.org/10.1016/j.jfoodeng.2008.09.025

Talja, R. A., & Roos, Y. H. (2001). Phase and state transition effects on dielectric, mechanical, and thermal properties of polyols. *Thermochimica Acta, 380(2),* 109–121. https://doi.org/10.1016/S0040-6031(01)00664-5

Tomas-Egea, J. A., Castro-Giraldez, M., Colom, R. J., & Fito, P. J. (2022). New technique for determining the critical freezing temperatures of chicken breast based on radiofrequency photospectrometry. *Journal of Food Engineering, 333*, 111155. https://doi.org/10.1016/j.jfoodeng.2022.111155

Tomas-Egea, J. A., Traffano-Schiffo, M. V., Castro-Giraldez, M., & Fito, P. J. (2021). Hot Air and Microwave Combined Drying of Potato Monitored by Infrared Thermography. *Applied Sciences, 11(4),* 1730. https://doi.org/10.3390/app11041730

Traffano-Schiffo, M. V., Castro-Giraldez, M., Colom, R. J., & Fito, P. J. (2018). Innovative photonic system in radiofrequency and microwave range to determine chicken meat quality. *Journal of Food Engineering, 239,* 1–7. https://doi.org/10.1016/j.jfoodeng.2018.06.029

Traffano-Schiffo, M. V., Castro-Giraldez, M., Colom, R. J., Talens, P., & Fito, P. J. (2021). New methodology to analyze the dielectric properties in radiofrequency and microwave ranges in chicken meat during postmortem time. *Journal of Food Engineering, 292*, 110350. https://doi.org/10.1016/j.jfoodeng.2020.110350

Traffano-Schiffo, M. V., Castro-Giráldez, M., Fito, P. J., & Balaguer, N. (2014). Thermodynamic model of meat drying by infrarred thermography. *Journal of Food Engineering, 128*, 103–110. https://doi.org/10.1016/j.jfoodeng.2013.12.024

Usamentiaga, R., Venegas, P., Guerediaga, J., Vega, L., Molleda, J., & Bulnes, F. (2014). Infrared Thermography for Temperature Measurement and Non-Destructive Testing. *Sensors, 14(7),* 12305–12348. https://doi.org/10.3390/s140712305

Vasco, C., Ruales, J., & Kamal-Eldin, A. (2008). Total phenolic compounds and antioxidant capacities of major fruits from Ecuador. *Food Chemistry, 111(4),* 816–823. https://doi.org/10.1016/j.foodchem.2008.04.054

Vásquez, C., Díaz-Calderón, P., Enrione, J., & Matiacevich, S. (2013). State diagram, sorption isotherm and color of blueberries as a function of water content. *Thermochimica Acta, 570,* 8–15. https://doi.org/10.1016/j.tca.2013.07.029

Vega-Gálvez, A., López, J., Ah-Hen, K., Torres, M., & Lemus-Mondaca, R. (2014). Thermodynamic Properties, Sorption Isotherms and Glass Transition Temperature of Cape Gooseberry (*Physalis peruviana* L.). Food Technology and Biotechnology, 52(1), 83–92.

Wang, H., Zhang, S., & Chen, G. (2008). Glass transition and state diagram for fresh and freeze-dried Chinese gooseberry. *Journal of Food Engineering, 84(2),* 307–312. https://doi.org/10.1016/j.jfoodeng.2007.05.024

W. Kuang, & S. O. Nelson. (1998). Low-frequency dielectric properties of biological tissues: a review with some new insights. *Transactions of the ASAE, 41(1),* 173–184. https://doi.org/10.13031/2013.17142

Wang, Z., Ding, F., Ge, Y., Wang, M., Zuo, C., Song, J., Tu, K., Lan, W., & Pan, L. (2024). Comparing visible and near infrared 'point' spectroscopy and hyperspectral imaging techniques to visualize the variability of apple firmness. *Spectrochimica Acta Part A: Molecular and Biomolecular Spectroscopy,* 316, Article 124344. https://doi.org/ 10.1016/j.saa.2024.124344

Yamamoto, Y., Fong-in, S., & Kawai, K. (2021). Optimum physical properties of fruit puree for freeze-drying: Effect of pulp content on freeze-concentrated glass transition temperature and yield stress of mango puree. *Journal of Food Engineering, 307,* 110649. https://doi.org/10.1016/j.jfoodeng.2021.110649

Zhang, L., Shen, H., & Luo, Y. (2010). Study on the electric conduction properties of fresh and frozen–thawed grass carp (*Ctenopharyngodon idellus*) and tilapia (*Oreochromis niloticus*). *International Journal of Food Science & Technology, 45(12),* 2560–2564. https://doi.org/10.1111/j.1365-2621.2010.02428.x

4.4. Uso de redes neuronales recurrentes para identificar filetes de pescado con cadena de frío rota a partir de perfiles espectrales.

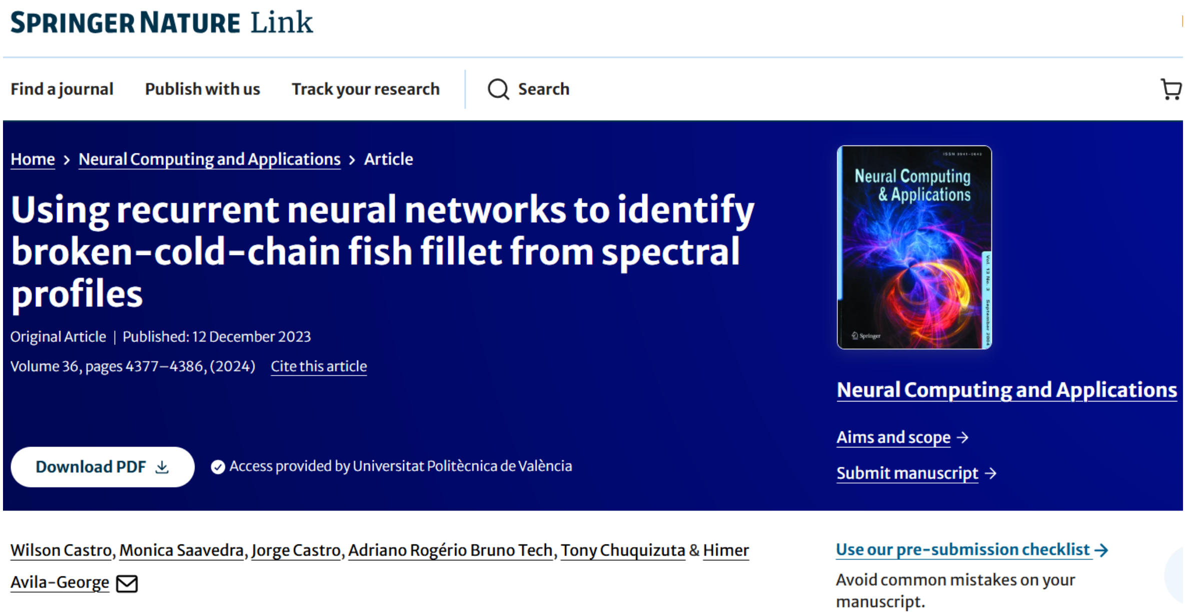
SPRINGER NATURE Link

Find a journal | Publish with us | Track your research | Search

Home > Neural Computing and Applications > Article

Using recurrent neural networks to identify broken-cold-chain fish fillet from spectral profiles

Original Article | Published: 12 December 2023

Volume 36, pages 4377–4386, (2024) Cite this article

Download PDF

Access provided by Universitat Politècnica de València

Neural Computing and Applications

Aims and scope →

Submit manuscript →

Wilson Castro, Monica Saavedra, Jorge Castro, Adriano Rogério Bruno Tech, Tony Chuquizuta & Himer Avila-George

Use our pre-submission checklist →

Avoid common mistakes on your manuscript.

Condición	DOI
Aceptado (12 de diciembre, 2023)	https://doi.org/10.1007/s00521-023-09311-4

USING RECURRENT NEURAL NETWORKS TO IDENTIFY BROKEN-COLD-CHAIN FISH FILLET FROM SPECTRAL PROFILES

Wilson Castro [1], Monica Saavedra [1], Jorge Castro [2], Adriano Rogério Bruno Tech [3], Tony Chuquizuta [4,5] & Himer Avila-George [6]

[1] Facultad de Ingeniería de Industrias Alimentarias, Universidad Nacional de Frontera, Av. San Hilarión 101, Sullana, 20101, Piura, Peru

[2] Facultad de ingeniería, Universidad Nacional de Cuyo, Centro Universitario, Mendoza, M5500, Mendoza, Argentina

[3] Department of Basic Sciences, Faculty of Animal Science and Food Engineering, University of São Paulo, R. Duque de Caxias 225, Pirassununga, São Paulo, 13635-900, Brazil

[4] Instituto de Investigación del Mejoramiento Productivo, Universidad Nacional Autónoma de Chota, Chota 06120, Perú

[5] Instituto Universitario de Ingeniería de Alimentos FoodUPV, Universitat Politècnica de València, Camino de Vera s/n, Valencia 46022, Spain

[6] Departamento de Ciencias Computacionales e Ingenierías, Universidad de Guadalajara, Carretera Guadalajara-Ameca km 45.5, 46600, Ameca, Jalisco, Mexico

*author for correspondence: wcastro@unf.edu.pe

Abstract

In the last two decades, hyperspectral images have been studied for use in food quality analysis using neural network-based chemometric techniques such as radial basic neural network (RBNN) in classification tasks or multilayer perceptron (MLP) for prediction ones. However, recently, deep learning techniques are receiving special interest as those based on recurrent neural networks (RNN) or gated recurrent units for their feature extraction capacity. A kind of RNN are networks based on long short-term memory (LSTM), which are promising for improving the capabilities of hyperspectral images in food analysis. In this sense, a comparative study on using LSTM-based networks is done, comparing it to RBNN in the discrimination of fish fillets subjected to freeze-thaw cycles. The samples for the study were fresh mackerel fillets subjected to two successive cycles

of freezing and thawing. Hyperspectral images of fillets were acquired, both fresh and in each freeze-thaw cycle, and spectral profiles were acquired in the range of 400–1000 nm. Complete spectral profiles were used to generate classification models; these were subsequently optimized using the relevant wavelengths determined by feature selection neighborhood component analysis. The models were trained using a k-cross-fold validation strategy (k = 5), repeating the process thirty times. The models were evaluated, confusion matrices were determined, and their classification metrics were compared. The training process results showed that the LSTM networks had superior potential to the RBNN networks, achieving an average F-measure greater than 0.89 and an accuracy greater than 0.93. This study shows that deep learning techniques can be used to tell the difference between fish fillets that have been frozen and thawed several times. These techniques could also be used to establish systems to control the transport and conservation processes of this type of food.

1. Introduction

Fish and its sub-products play a vital role in the diets of many countries, serving as valuable sources of protein, vitamins, and fat. However, due to their perishable nature, it is crucial to ensure their quality before they reach consumers [1, 2]. Freezing and a properly maintained cold chain are the most common methods of preserving fish quality [3, 4]. However, if the cold chain is disrupted, tissue damage accelerates deterioration processes, making it necessary to have effective and fast methods for detecting when the cold chain has been compromised [5]. This is particularly important because the changes caused by these processes are not readily visible to the naked eye [6].

In this regard, hyperspectral imaging (HSI) technology has been proposed as a suitable alternative to detect changes in fish quality and its sub-products [4]. HSI is capable of capturing high-resolution images in both visible and near-infrared (NIR) spectrum, allowing users to obtain information about the chemical composition of each pixel and detect any changes in the food structure [7]. In this order, researchers such as [8] have applied HIS and different chemometric techniques to predict quality parameters in seafood. Similarly, [1] and [4] performed models for the discrimination of fresh and frozen/cooled seafood, such as Atlantic salmon, Chinese white shrimp, abalone fillets, and Japanese mackerel, respectively. The use of HIS to study food quality implies the processing of large volumes of data, commonly redundant or with overlapping information [9]. To address these challenges, chemometric tools have been applied relatively effectively, many of them based on machine learning [1, 10, 11]. Traditionally, machine learning techniques are used to estimate outputs based on feature extraction and training models [12]. However, more recently, deep learning techniques, a particular type of machine learning, have become a large field in the machine learning domain [13]. This kind of technique uses a cascade of multiple nonlinear processing layers to extract information corresponding to different levels of abstraction, which are used to modify connections in their structures [14,15,16,17]. Then, using its capacity for information extraction, machine learning, and deep learning-based models can learn complex relationships and make predictions [18]. During the last few years, a special one has gained importance among the different models in deep learning, which uses long short-term memory (LSTM) units for time series analysis. These LSTM-based networks have the ability to preserve information from previous states in hidden layers to incorporate it into their prediction and classification processes [14].

The LSTM networks, initially developed for speech recognition, have received special attention due to their ability to adapt to the analysis of 1-D information, such as spectral profiles [14, 19]. In summary, the combination of models based on networks LSTM and spectral profiles has been shown to be efficient in a wide variety of food analyses, such as the prediction of storage time in black tea [20], the discrimination of cumin and fennel [14], the classification of apples [21], the quantification of spores of Clostridium sporogenes in food products [22], the detection of defective eggs [23], the classification of citrus [24], the detection of moisture levels in individual corn seeds [25], determination of seafood quality [26], identification of different types of cheese [27], degree of cooking of shrimp [28], recognition of oils [29], differentiation of wines [30], among others. However, the literature review on the applications of LSTM-based networks has yet to produce studies on the differentiation of fish fillets exposed to broken cold chains.

Consequently, this study suggests a deep learning technique for discriminating fish fillets subjected to a broken cold chain. The performance of LSTM-based models was compared to RBNN. In this sense, the study was divided into the following steps: (a) Sample conditioning, (b) Spectral profile extraction, (c) Model building, and (d) Model comparison.

2. Materials and methods

The methodology used in this study is based on previous research by [3] and [31]. The main steps of the methodology are presented in Fig. 1.

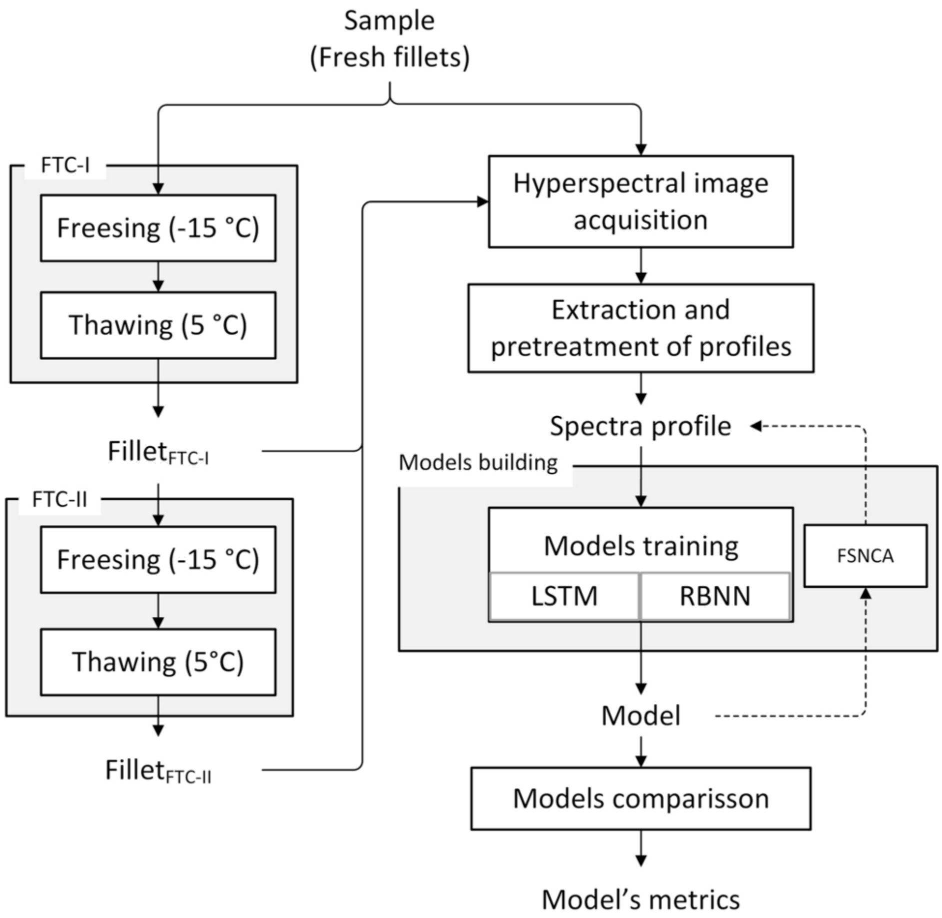

Fig. 1. Using recurrent neural networks to identify broken-cold-chain fish fillet from spectral profiles

The methodology involves two stages of freezing and thawing, which simulate the effect of two breaks in a cold chain. Hyperspectral images of the fresh samples were acquired in the 400 to 1000 nm range at each rupture in the cold chain. The acquired images were corrected for noise, and their spectral profiles were extracted. Subsequently, several classification models were developed and tested using different techniques, such as radial basis neural networks, linear discriminant analysis, and LSTM-based networks. The classifiers were evaluated using metrics such as accuracy and F-measure to ensure their robustness and reliability. Models were optimized using feature selection methods, such as neighborhood component analysis (NCA), to identify the most relevant features for classification.

All sequences were implemented using functions and graphical user interfaces (GUIs) developed in MATLAB 2019a (The MathWorks Inc., USA). The following subsections provide further details on each step of the flowchart.

2.1. Sample

The sample consisted of 48 fresh unbone fillets of mackerel (Scomber japonicus peruanus). These fillets were thoroughly washed with water containing 200 ppm residual chlorine and stored at 4º prior to the following steps.

2.2. Freezing – thawing cycle

In order to study broken-cold-chain effects over samples, they were treated by subsequent freezing-thawing cycles (FTC); this FCTs were carried out in accordance with the work of [3] and [8]. Initially, the fillets were placed in a freezer (Brand: Pol-Eko-Aparatura, model: ZLN 85, origin: Poland), programmed at -25º, controlling the temperature of the fillets until reaching -15º. Subsequently, the samples were placed in a refrigerator (Brand: Daewoo, model: FR-146RN, origin: China) in the zone of 6º in order to allow a gradual thawing process. When the samples reached 5º, hyperspectral images were taken, thus completing the first freezing-thawing cycle (FTC-I); this process was repeated for the fillets, constituting the second cycle (FTC-II).

2.3. Hyperspectral images acquisition

The hyperspectral imaging system used in this study operates in the wavelength range of 400 to 1000 nm and consists of a spectral camera (Specim FX-10, Finland), a sample platform, a tower, and a lighting source, all controlled by the Lumo Scanner software from Specim LTD. The system operates in reflectance mode with a line-by-line scanning technique (Pushbroom) and produces images with 112 bands. The main operating parameters were set as follows: sample platform speed of 0.5 cm/s, lens-to-sample surface distance of 28.3 cm, and diaphragm opening of 6.4 mm. After the images were captured, the correction was performed using Eq. 1, which is defined as follows:

$$I_c = \frac{I-D}{W-D} \tag{1}$$

where I is the raw image, I_c is the corrected image, W is the white reference obtained from a Teflon pattern with a reflectance value of 99.9%, and D is the dark reference obtained by blocking the lens with a reflectance value of 0.0%. The correction method was described in detail in the studies by [32] and [33]. Finally, all the corrected images were stored in an eight-terabyte network-attached storage for further analysis.

2.4. Extraction and pretreatment of profiles

Pseudo-RGB images were created using intensity images taken at 644, 584, and 483 nm (Layers 47, 36, and 17), as shown in Fig. 2(a). The sample pixels were then segmented in the intensity image taken at 552 nm (Layer 30) using threshold, as this provided greater contrast between the sample and the background. For each sample, the major and minor axes were determined and a rectangular region of interest (ROI) was defined with its major and minor sides corresponding to 60% of the respective major and minor axes (as seen in Fig. 2(b)).

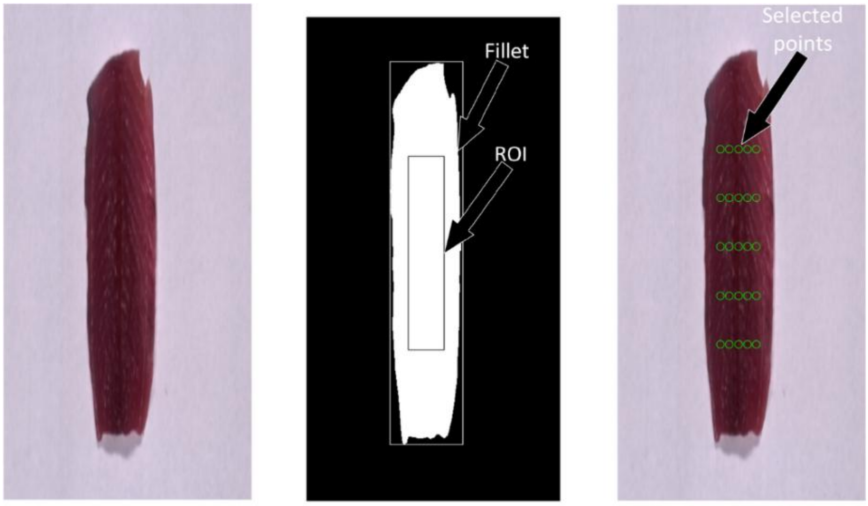

(a) Pesudo-RGB (b) Segmented (c) ROI

Fig. 2. Using recurrent neural networks to identify broken-cold-chain fish fillet from spectral profiles

Next, following the method described by [34] and [33], 25 acquisition points for spectral profiles were located within the ROI, as illustrated in Fig. 2c, for each of the 48 fillets and treatments. This resulted in a total of 3600 spectral profiles, which were divided into the following classes: fresh fillets, FTC-I, and FTC-II. Each profile was then smoothed using the Savitzky-Golay filter, as described in Eq. 2. The filter had a second order and 11 steps per frame, which were used to smooth the original profile and produce a smooth profile.

$$Y_j^{\circ} = \frac{\sum_{i=-m}^{m} C_i, Y_{j+1}}{N} \qquad (2)$$

Where Y is the original profile, Y_o is the smooth profile, C is the coefficient of the i^{th} term of the profile, and N is the number of convolution stages.

2.5. Models building

2.5.1. Models training

Two different models were implemented based on LSTM and RBNN, as shown in Fig. 3. The details of each model are outlined in the following sections.

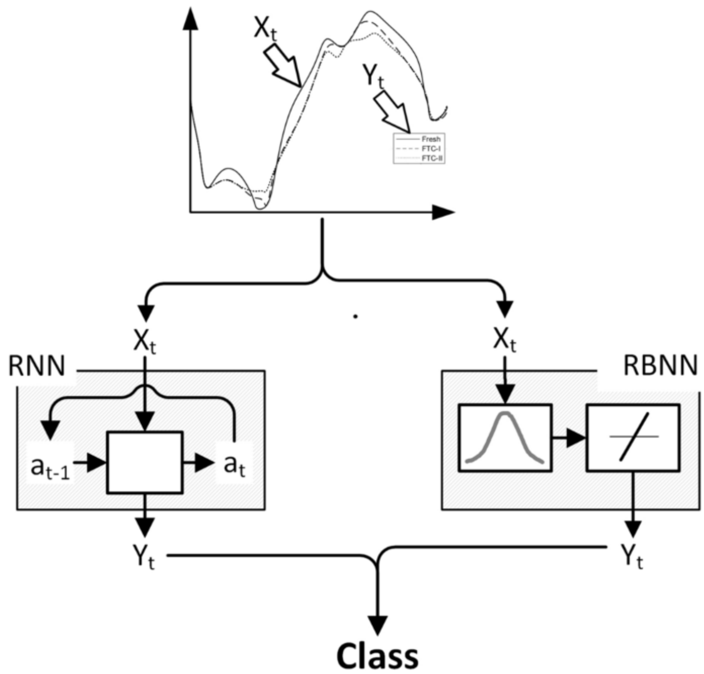

Fig. 3. Implement models in the study

- The LSTM architecture introduced the input gate, the forget gate, and the output gate to control the memory cell and record additional information, as shown in Fig. 4(a) [20, 35]; according to [19], these networks are cyclic neural networks. The proposed structure was based on the proposals of [35], which comprises an input layer with 112 neurons (NIL), an LSTM layer with 18 hidden units (NHU), a fully connected layer with three output units (OSFC), a softmax layer, and an output layer of three neurons (OSOL). The number of hidden units in the LSTM layer was calculated as $NHU = \sqrt{NIL * OSOL}$
- The RBNN model, depicted in Fig. 4(b), is a specialized classification network that uses a radial basis transfer function [36,37,38]. It consists of an input layer with 112 neurons and an output layer with three neurons (NOL). The model is designed to learn complex patterns and data structures to better classify and predict labels. It uses a radial

basis function, which allows the model to classify data points with high accuracy. The model allows for the extraction of nonlinear features and patterns, which are then used to classify data points into their respective classes. This model is especially useful in cases where the data contain multiple nonlinear features and the underlying structure of the data is difficult to discern. The ability of the model to extract complex patterns makes it a preferred choice for classifying difficult data sets.

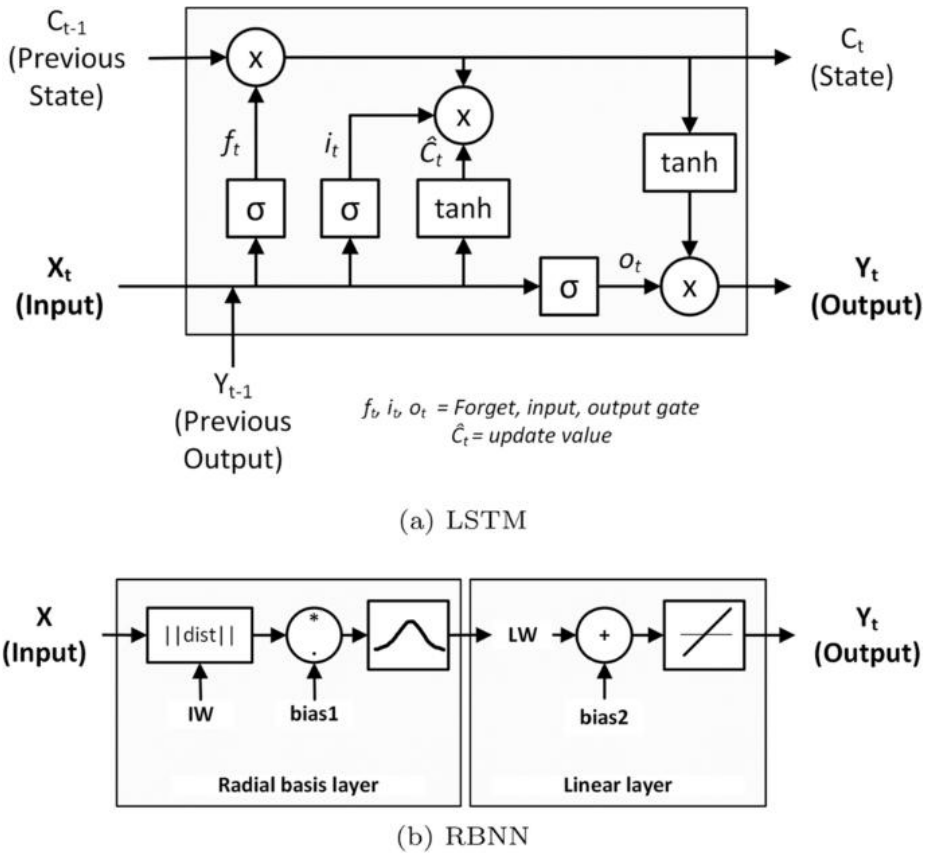

Fig.4. Neural network structures used in the study

The algorithms used in this research were implemented using functions and graphical user interfaces in MATLAB 2019a. First, the models were built using the functions lstmLayer and newpnn for LSTM and RBNN models, respectively. A fixed number of neurons was used for each model based on the number of inputs and outputs. Next, for the training step, the LSTM and RBNN networks used the trainNetwork function; likewise, the training algorithm used was a stochastic gradient descent approach.

To calculate the robustness and reliability of the model, these models were trained 30 times, applying the cross-validation strategy of K-segments (K = 5). This strategy is beneficial because it helps prevent overfitting by splitting the data into multiple subsets, which can then be used to train and test the model. After each training was completed, the results were stored for the calculation of performance metrics. This helps to ensure that the model is able to make accurate predictions and generalize well to unseen data.

Similarly, as previously mentioned, the models were built, setting the input number as the number of full spectra profiles. However, to optimize the models, feature selection neighborhood component analysis (FSNCA) was used to identify the number of relevant wavelengths. This number was then used as the new input size to help improve the model's accuracy and performance. This approach also allowed the parameters of the model to be adjusted, such as the number of epochs, the learning rate, the momentum rate, and the regularization rate; this helps to ensure that the model is able to make more accurate and reliable predictions.

2.5.2. Feature selection neighborhood component analysis

According to [39], the FSNCA uses the Mahalanobis distance through the KNN classification algorithm. This technique uses a feature weighting scheme to select the best subset of features by maximizing an objective function that evaluates the average leave-one-out classification accuracy over the training data. This approach is beneficial because it helps identify the most important features that can be used to train and test the model, resulting in a more accurate prediction. Additionally, this method also helps reduce the complexity of the data by removing redundant or irrelevant features, which then helps improve the performance of the model. Furthermore, this technique also helps prevent overfitting by ensuring that the model can generalize well to unseen data.

2.6. Models comparison

The results of the model training were placed in bidimensional arrays called confusion matrices (CM). This CM contains information on the true and predicted classes of the elements of a sample, organized in a square array [n x n], where n is the number of classes.

Statistical metrics, based on the CM, for classifier comparison, were then determined using Eqs. 3 and 4. ACC is the overall precision and F-measure is the harmonic mean between PR (precision) and RC (recall). Additionally, TP–TN are the total positive and negative cases, respectively, while FP–FN are the false positive and negative cases, respectively.

$$ACC = \frac{TF+TN}{TP+FP+FN+TN} \quad (3)$$

$$F_{Measure} = 2\left(\frac{PRxRC}{PR+RC}\right) \quad (4)$$

3. Results and discussion

3.1. Median profiles

In Fig. 5, the mean spectra of the treatments are plotted, which demonstrates the varying effects of broken cold chains, expressed as freeze–thaw cycles on the shape of the profile, which is in agreement with the findings of [40], which state that other storage methods can affect fish quality and its characteristics of the spectral profile.

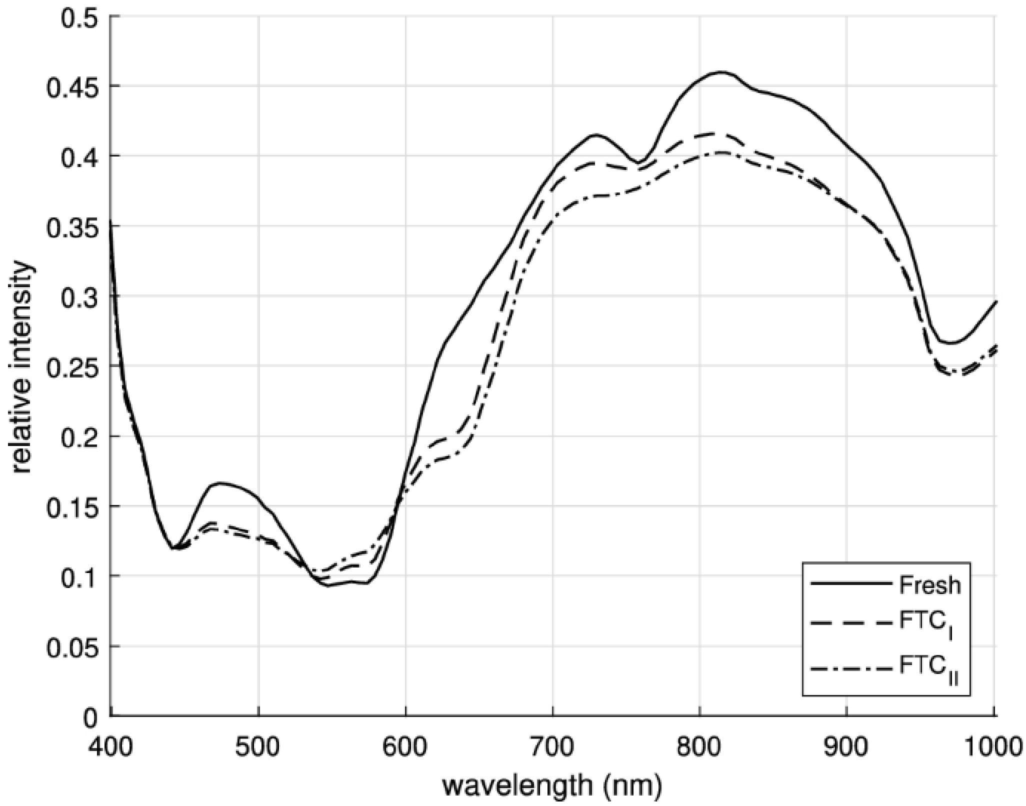

Fig.5. Median spectral profiles per treatment

Previous studies by [2, 3], and [34] have reported differences in fresh samples and those subjected to different types and cycles of freezing-thawing. Differences may be attributed to the varying composition of the different varieties of fish.

It can be observed that the average profiles of the samples subjected to successive freezing-thawing processes had a decrease in the reflectance value of their spectral profiles, with a notable decrease around the wavelengths of 467, 627, 725, and 813 nm in accordance to the number of applied FTC. Additionally, different peaks can be seen throughout the profile, such as the one at approximately 470, 560, 620, 720 and 810 nm. For example, the peak at 560 nm is associated with the absorption of heme pigments, and the peak at 620 nm is linked to methemoglobin absorption regions. Furthermore, the peaks at approximately 729 and 928 nm correspond to the second and third vibrations of the O–H bond of water, which could indicate the loss of water from the product due to the freezing-thawing cycles [2, 31].

Furthermore, tissue degradation in fish may be a consequence of the freezing-thawing process, as it disrupts the cell membrane, leading to an increase in the solubility of intracellular and extracellular components [41]; this could manifest in the spectra as a decrease in the reflectance value in the spectral profile. Furthermore, the peak at 627 nm can indicate protein decomposition, highlighting the need for proper handling and storage of fish to ensure minimal degradation [40].

3.2. Network training

3.2.1. Full spectra based models

The results of the training process using the full spectra of the classifiers are summarized in Fig. 6. Classifiers demonstrated exceptional performance in discrimination tasks, with positive percentages of numbers ranging from 71 to 100% per class. These results are comparable to those reported by [3].

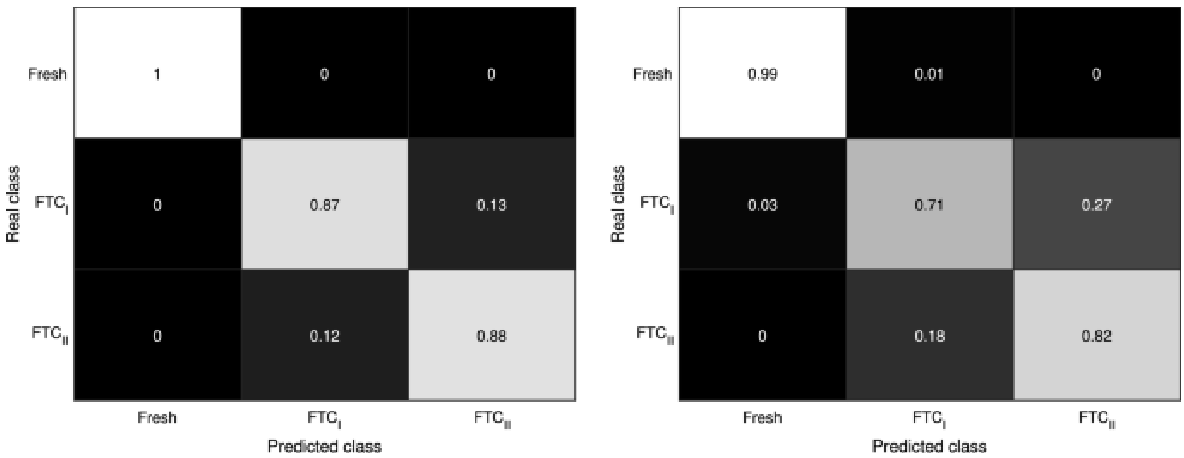

(a) LSTM-Full (b) RBNN-Full

Fig. 6. Mean confusion matrices of full classifiers

Furthermore, the accuracy plotted in Fig. 7 shows that the process required around eight hundred epochs until reaching stable LSTM models. This is a larger number than the one reported by [42], who obtained stability in the training process around one hundred and fifty epochs, although, as commented by [9], the number of epochs is related to CNN training parameters such as learning transfer.

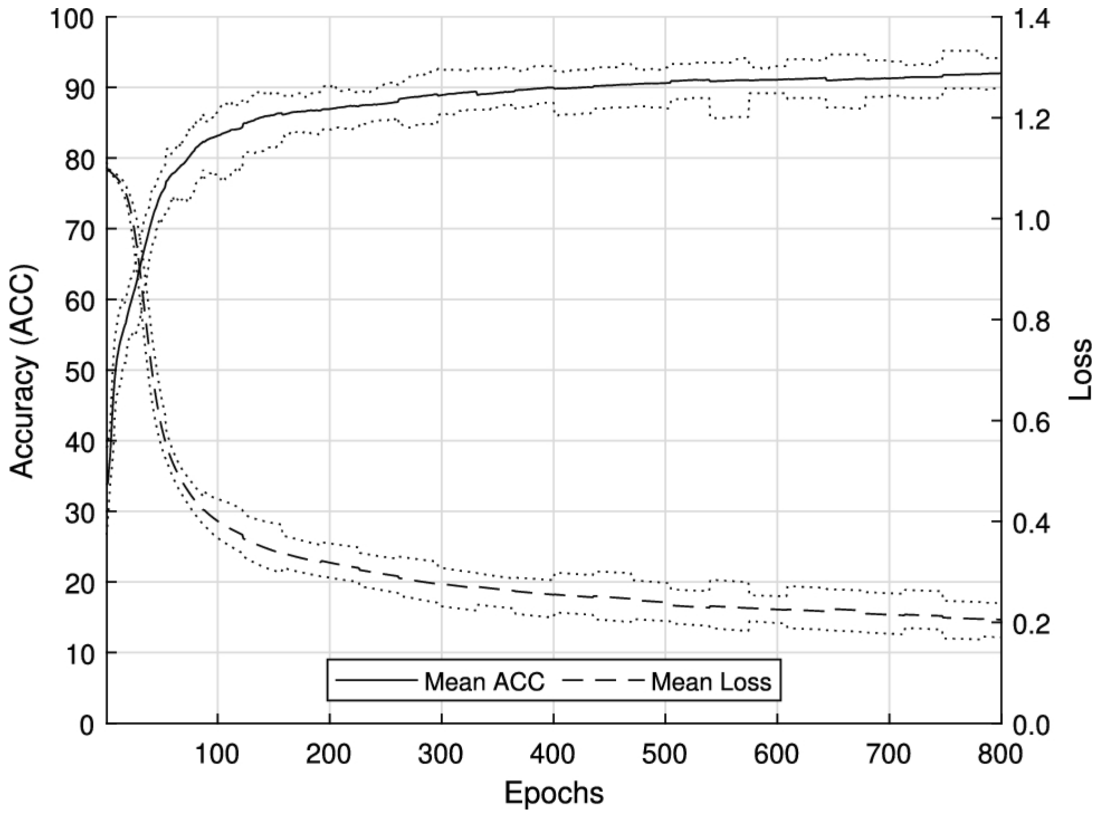

Fig. 7. Accuracy and loss during training process

Consequently, as demonstrated in Fig. 7, a significant number of epochs are necessary to reach a stable state of the models, making the adaptation capacity to the used spectra less efficient than in the previously mentioned works.

3.2.2. Selected features

The FSNCA algorithm was employed to determine the optimal number of relevant features, which was found to be 18. The selected wavelengths corresponding to these features were then plotted in Fig. 8. The mean spectra are represented by the solid dark line, whereas the relevant features are shown as dark points overlaid on top. These relevant features correspond to all wavelengths (points shown on a white background) whose feature weight exceeded the threshold value specified by the FSNCA algorithm.

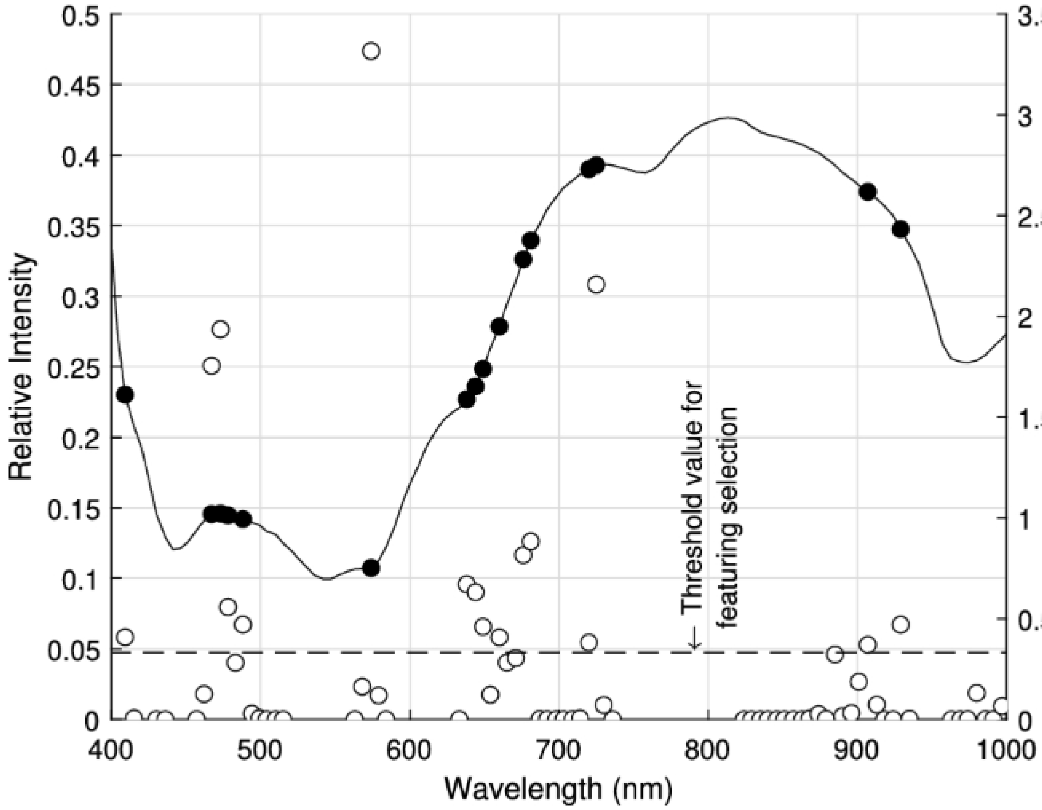

Fig. 8. Relevant variables

The selected number was higher than the one reported by [43], who used the successive projections algorithm to obtain five to seven relevant variables from the first derived reflectance spectra. Meanwhile, the second-derived reflectance spectra yielded twenty-two relevant variables for the same objective.

3.2.3. Optimized spectra based models

Figure 9 shows only two mean matrices, as the main objective was to compare techniques, in contrast to [4], who compared techniques (soft independent modeling of class analogy—SIMCA, least squares support vector machine—LS-SVM, and probabilistic neural network—PNN) and pretreatments (standard normalization variance, first derivative, among others).

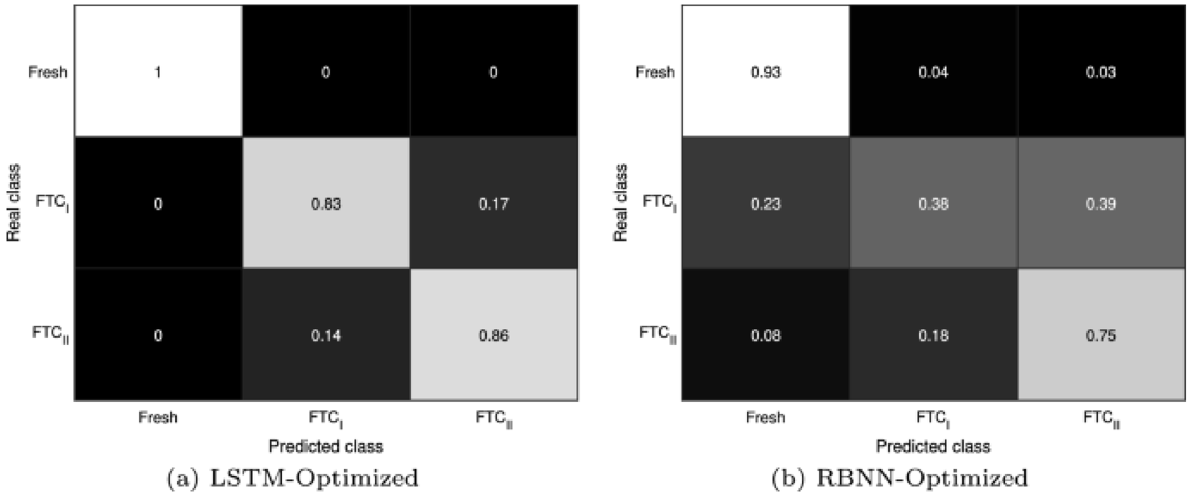

Fig. 9. Mean confusion of optimized classifiers

3.3. Comparison of metrics

The performance comparison presented in Table 1 highlights the superior accuracy achieved by LSTM networks compared to the RBNN models. Specifically, the LSTM models achieved an accuracy of 0.944 and 0.928 for the full and optimized models, respectively, while the corresponding figures for the RBNN models were 0.890 and 0.789.

Table 1. Classification metrics per model

Model	Accuracy		$F_{Measure}$	
2-5	Full	Optimized	Full	Optimized
LSTM	0.944 ± 0.04	0.928 ± 0.005	0.915 ± 0.005	0.892 ± 0.0007
RBNN	0.890 ± 0.02	0.789 ± 0.002	0.835 ± 0.003	0.664 ± 0.003

The accuracy of the LSTM networks was remarkably similar to that reported in [31], which used images in the same range and obtained an accuracy of 97.2% when distinguishing between a single freeze–thaw cycle and fresh fillets. Furthermore, [2] were able to achieve the accuracies of 87% to 94% with the RBNN networks when discriminating between carp fillets subject to different storage conditions, which are close to the results obtained in this research. However, when only fresh fillets and fillets subjected to a freeze–thaw cycle were compared, the precision obtained by the LSTM network was 100%. This result points toward the LSTM networks having the edge over probabilistic networks when it comes to distinguishing between different treatments applied to fillets.

4. Conclusions

The findings of this study indicate that the LSTM networks were superior to the RBNN networks for discriminating between fish fillets subjected to different FTC, achieving an average F-measure greater than 0.89 and accuracy greater than 0.93. Based on these findings, it is feasible to implement systems that utilize this technique to manage the transportation and preservation of this particular type of food. In order to improve the effectiveness of the LSTM networks, it would be beneficial for future research to investigate how modifying their layers and adjusting the training parameters can impact their training speed. It is crucial to develop an automated system to keep a check on the condition of fish fillets while they are being transported and stored. The system can notify the authorities immediately in case of any abnormalities to guarantee compliance with food safety regulations.

5. References

1. Pu H, Sun D-W, Ma J, Cheng J-H (2015) Classification of fresh and frozen-thawed pork muscles using visible and near-infrared hyperspectral imaging and textural analysis. Meat Sci 99:81–88. https://doi.org/10.1016/j.meatsci.2014.09.001

2. Chen S, Zhang F, Ning J, Liu X, Zhang Z, Yang S (2015) Predicting the anthocyanin content of wine grapes by NIR hyperspectral imaging. Food Chem 172:788–793. https://doi.org/10. 1016/j.foodchem.2014.09.119

3. Anderssen K, Stormo S, Ska˚ra T, Skjelvareid M, Heia K (2020) Predicting liquid loss of frozen and thawed cod from hyperspectral imaging. LWT 133:110093. https://doi.org/10.1016/j.lwt. 2020.110093

4. Cheng J-H, Sun D-W, Pu H-B, Chen X, Liu Y, Zhang H, Li J-L (2015) Integration of classifiers analysis and hyperspectral imaging for rapid discrimination of fresh from cold-stored and frozen-thawed fish fillets. J Food Eng 161:33–39. https://doi.org/ 10.1016/j.jfoodeng.2015.03.011

5. Xie A, Sun D-W, Zhu Z, Pu H (2016) Nondestructive measurements of freezing parameters of frozen porcine meat by NIR hyperspectral imaging. Food Bioprocess Technol 9(9):1444–1454. https://doi.org/10.1007/s11947-016-1766-2

6. Kiani H, Sun D-W (2011) Water crystallization and its importance to freezing of foods: a review. Trends Food Sci Technol 22(8):407–426. https://doi.org/10.1016/j.tifs.2011.04.011

7. Fracarolli JA, Pavarin FFA, Castro W, Blasco J (2021) Visa˜o computacional aplicada a alimentos e produtos agrı´colas. Revista Cieˆncia Agrono ˆmica. 20200087 https://doi.org/10.5935/1806-6690.

8. Cheng J-H, Sun D-W (2014) Hyperspectral imaging as an effective tool for quality analysis and control of fish and other seafoods: current research and potential applications. Trends Food Sci Technol 37(2):78–91. https://doi.org/10.1016/j.tifs. 2014.03.006

9. Chen X, Li J, Liu H, Wang Y (2022) A fast multi-source information fusion strategy based on deep learning for species identification of boletes. Spectrochim Acta Part A Mol Biomol Spectrosc 274:121137. https://doi.org/10.1016/j.saa.2022.121137

10. Zhuang Q, Peng Y, Yang D, Wang Y, Zhao R, Chao K, Guo Q (2022) Detection of frozen pork freshness by fluorescence hyperspectral image. J Food Eng 316:110840. https://doi.org/10. 1016/j.jfoodeng.2021.110840

11. Saha D, Manickavasagan A (2021) Machine learning techniques for analysis of hyperspectral images to determine quality of food products: a review. Curr Res Food Sci 4:28–44. https://doi.org/ 10.1016/j.crfs.2021.01.002

12. Shammi S, Sohel F, Diepeveen D, Zander S, Jones MG (2022) A survey of image-based computational learning techniques for frost detection in plants. Inform Process Agric. https://doi.org/10. 1016/j.inpa.2022.02.003

13. Zhang Y, Deng L, Zhu H, Wang W, Ren Z, Zhou Q, Lu S, Sun S, Zhu Z, Gorriz JM et al (2023) Deep learning in food category recognition. Inform Fusion. https://doi.org/10.1016/j.inffus.2023. 101859

14. Chen C, Yang B, Si R, Chen C, Chen F, Gao R, Li Y, Tang J, Lv X (2021) Fast detection of cumin and fennel using NIR spectroscopy combined with deep learning algorithms. Optik 242:167080. https://doi.org/10.1016/j.ijleo.2021.167080

15. Han T, Kuo Y (2018) Developing a system for three-dimensional quantification of root traits of rice seedlings. Comput Electron Agric 152:90–100. https://doi.org/10.1016/j.compag.2018.07.001

16. Wu L, Liu Z, Bera T, Ding H, Langley D, Jenkins-Barnes A, Furlanello C, Maggio V, Tong W, Xu J (2019) A deep learning model to recognize food contaminating beetle species based on elytra fragments. Comput Electron Agric 166:105002. https://doi. org/10.1016/j.compag.2019.105002

17. Zhang WJ, Yang G, Lin Y, Ji C, Gupta MM (2018) On definition of deep learning. In: 2018 World automation congress (WAC) pp. 1–5 . https://doi.org/10.23919/WAC.2018.8430387

18. Paudel D, Wit A, Boogaard H, Marcos D, Osinga S, Athanasiadis IN (2023) Interpretability of deep learning models for crop yield forecasting. Comput Electron Agric 206:107663. https://doi.org/ 10.1016/j.compag.2023.107663

19. Pang L, Wang L, Yuan P, Yan L, Yang Q, Xiao J (2021) Feasibility study on identifying seed viability of sophora japonica with optimized deep neural network and hyperspectral imaging. Comput Electron Agric 190:106426. https://doi.org/10.1016/j. compag.2021.106426

20. Hong Z, Zhang C, Kong D, Qi Z, He Y (2021) Identification of storage years of black tea using near-infrared hyperspectral imaging with deep learning methods. Infrared Phys Technol 114:103666. https://doi.org/10.1016/j.infrared.2021.103666

21. Shi X, Chai X, Yang C, Xia X, Sun T (2022) Vision-based apple quality grading with multi-view spatial network. Comput Electron Agric 195:106793. https://doi.org/10.1016/j.compag.2022. 106793

22. Soni A, Al-Sarayreh M, Reis MM, Brightwell G (2021) Hyperspectral imaging and deep learning for quantification of clostridium sporogenes spores in food products using 1d-convolutional neural networks and random forest model. Food Res Int 147:110577. https://doi.org/10.1016/j.foodres.2021.110577

23. Turkoglu M (2021) Defective egg detection based on deep features and bidirectional long-short-term-memory. Comput Electron Agric 185:106152. https://doi.org/10.1016/j.compag.2021. 106152

24. Yu Y, AnX,LinJ, Li S, Chen Y (2022) A vision system based on cnn-lstm for robotic citrus sorting. Inform Process Agric. https:// doi.org/10.1016/j.inpa.2022.06.002

25. Zhang L, Zhang Q, Wu J, Liu Y, Yu L, Chen Y (2022) Moisture detection of single corn seed based on hyperspectral imaging and deep learning. Infrared Phys Technol 125:104279. https://doi.org/ 10.1016/j.infrared.2022.104279

26. Tran T, Nguyen L, Hoai P, Pham Q, Huyen P, Dong N, Hieu H, Hien N (2022) Long short-term memory (lstm) neural networks for short-term water level prediction in mekong river estuaries. Songklanakarin J Sci Technol https://doi.org/10.14456/sjst-psu. 2022.138

27. Ebrahimpour M, Yu W, Young B (2021) Artificial neural network modelling for cream cheese fermentation ph prediction at lab and industrial scales. Food Bioprod Process 126:81–89. https://doi.org/10.1016/j.fbp.2020.12.006

28. Liu Z, Jia X, Xu X (2019) Study of shrimp recognition methods using smart networks. Comput Electron Agric 165:104926. https://doi.org/10.1016/j.compag.2019.104926

29. Yuan L, Meng X, Xin K, Ju Y, Zhang Y, Yin C, Hu L (2023) A comparative study on classification of edible vegetable oils by infrared, near infrared and fluorescence spectroscopy combined with chemometrics. Spectrochim Acta Part A Mol Biomol Spectroscop 288:122120. https://doi.org/10.1016/j.saa.2022. 122120

30. Katumullage D, Yang C, Barth J, Cao J (2022) Using neural network models for wine review classification. J Wine Econ 17(1):27–41. https://doi.org/10.1017/jwe.2022.2

31. Zhu F, Zhang D, He Y, Liu F, Sun D-W (2013) Application of visible and near infrared hyperspectral imaging to differentiate between fresh and frozen-thawed fish fillets. Food Bioprocess Technol 6(10):2931–2937. https://doi.org/10.1007/s11947-0120825-6

32. Va´squez N, Maga´n C, Oblitas J, Chuquizuta T, Avila-George H, Castro W (2018) Comparison between artificial neural network and partial least squares regression models for hardness modeling during the ripening process of swiss-type cheese using spectral profiles. J Food Eng 219:8–15. https://doi.org/10.1016/j.jfoodeng. 2017.09.008

33. Castro W, Prieto J, Guerra R, Chuquizuta T, Medina W, Acevedo-Jua´rez B, Avila-George H (2018) Feasibility of using spectral profiles for modeling water activity in five varieties of white quinoa grains. J Food Eng 238:95–102. https://doi.org/10. 1016/j.jfoodeng.2018.06.012

34. Cheng J-H, Qu J-H, Sun D-W, Zeng X-A (2014) Visible/nearinfrared hyperspectral imaging prediction of textural firmness of grass carp (ctenopharyngodon idella) as affected by frozen storage. Food Res Int 56:190–198. https://doi.org/10.1016/j.foodres. 2013.12.009

35. Gao J, Zhao L, Li J, Deng L, Ni J, Han Z (2021) Aflatoxin rapid detection based on hyperspectral with 1d-convolution neural network in the pixel level. Food Chem 360:129968. https://doi. org/10.1016/j.foodchem.2021.129968

36. Oblitas J, Mejia J, De-la-Torre M, Avila-George H, Seguı ´ Gil L, Mayor Lo ´pez L, Ibarz A, Castro W (2021) Classification of the microstructural elements of the vegetal tissue of the pumpkin (cucurbita pepo l.) using convolutional neural networks. Appl Sci 11(4):1581. https://doi.org/10.3390/app11041581

37. Ferna´ndez-Navarro F, Herva´s-Martı´nez C-, Gutie´rrez P, Carbonero-Ruz M (2011) Evolutionary q-gaussian radial basis function neural networks for multiclassification. Neural Netw 24(7):779–784. https://doi.org/10.1016/j.neunet.2011.03.014

38. Huang W, Oh S, Pedrycz W (2014) Design of hybrid radial basis function neural networks (hrbfnns) realized with the aid of hybridization of fuzzy clustering method (fcm) and polynomial neural networks (pnns). Neural Netw 60:166–181. https://doi.org/ 10.1016/j.neunet.2014.08.007

39. Malan N, Sharma S (2019) Feature selection using regularized neighbourhood component analysis to enhance the classification performance of motor imagery signals. Comput Biol Med 107:118–126. https://doi.org/10.1016/j.compbiomed.2019.02.009

40. Cheng J-H, Dai Q, Sun D-W, Zeng X-A, Liu D, Pu H-B (2013) Applications of non-destructive spectroscopic techniques for fish quality and safety evaluation and inspection. Trends Food Sci Technol 34(1):18–31. https://doi.org/10.1016/j.tifs.2013.08.005

41. Yu D, Xu Y, Jiang Q, Yang F, Xia W (2017) Freshness assessment of grass carp (ctenopharyngodon idellus) fillets during stroage at 4 c by physicochemical, microbiological and sensorial evaluations. J Food Saf 37(2):12305. https://doi.org/10.1111/jfs. 12305

42. Agarwal M, Al-Shuwaili T, Nugaliyadde A, Wang P, Wong KW, Ren Y (2020) Identification and diagnosis of whole body and fragments of trogoderma granarium and trogoderma variabile using visible near infrared hyperspectral imaging technique coupled with deep learning. Comput Electron Agric 173:105438. https://doi.org/10.1016/j.compag.2020.105438

43. Dai Q, Cheng J-H, Sun D-W, Zeng X-A (2015) Advances in feature selection methods for hyperspectral image processing in food industry applications: a review. Critic Rev Food Sci Nutr 55(10):1368–1382. https://doi.org/10.1080/10408398.2013. 871692

4.5. Espectroscopia dieléctrica para la predicción de la calidad de la carne de cerdo durante el periodo post mortem

ELSEVIER

Journal of Food Composition and Analysis

Volume 148, Part 1, December 2025, 108128

Dielectric spectroscopy for the prediction of pork quality during the post-mortem time

Tony Chuquizuta [a] [f], Magaly Peralta [a], Sideli Medina [a], Hubert Arteaga [b], Jimy Oblitas [c], Segundo G. Chavez [d], Wilson Castro [e], Marta Castro-Giraldez [f], Pedro J. Fito [f]

Show more

Add to Mendeley Share Cite

https://doi.org/10.1016/j.jfca.2025.108128

Get rights and content

Condición	DOI
Aceptado (09 de noviembre, 2024)	**https://doi.org/10.1016/j.jfca.2025.108128**

DIELECTRIC SPECTROSCOPY FOR THE PREDICTION OF PORK QUALITY DURING THE POST-MORTEM TIME

Tony Chuquizuta[1,6]*, Magaly Peralta[1], Sideli Medina[1], Hubert Arteaga[2], Jimy Oblitas[3], Segundo G. Chavez[4]*, Wilson Castro[5], Marta Castro-Giraldez[6] and Pedro J. Fito[6]

[1] Instituto de Investigación Del Mejoramiento Productivo, Universidad Nacional Autónoma de Chota, Chota, 06121, Perú; tchuquizuta@unach.edu.pe

[2] Instituto de Investigación de Ciencia y Tecnología de Alimentos, Universidad Nacional de Jaén, Carretera Jaén-San Ignacio, Km 24-Sector Yanuyacu, Jaén, Cajamarca, Perú;

[3] Facultad de Ingeniería, Universidad Privada del Norte, Perú;

[4] Instituto de Investigación, Innovación y Desarrollo para el Sector Agrario y Agroindustrial de la región Amazonas (IIDAA), Universidad Nacional Toribio Rodríguez de Mendoza, Perú;

[5] Facultad de Ingeniería en Industrias Alimentarias, Universidad Nacional de Frontera, Perú;

[6] Instituto Universitario de Ingeniería de Alimentos para el Desarrollo, Universidad Politécnica de Valencia, Camino de Vera s/n, 46022 Valencia, Spain;

* Correspondence: segundo.quintana@untrm.edu.pe

Abstract

Dielectric spectroscopy was used in this study to predict and classify pork quality during the post-mortem time. Eighty ~1 kg- *longissimus dorsi* muscles were collected and stored at 4 ± 1 °C and pH, instrumental color, and dielectric properties (ε' and ε'') were subsequently determined in the microwave range (0.5 - 9 GHz) at 3, 4, 5, 6, 7, 8, 9, 10 and 24 hours post-mortem (hpm), as well as moisture at 8 hpm and drip weight loss at 24 hpm. Of the 80 pork samples, two types of meat were found. RFN (33) and DFD (47) between males and females. Quality parameters: RFN (pH=5.708-5.714; L*=43.341-43.692; moisture (%) = 68.857-69.604; drip loss = 1.655-1.833) and DFD (pH=6.154-6.177; L*=40.152-41.91; moisture (%) = 69.032-69.9; drip loss = 1.129-1.693). Quality parameter predictions during muscle-to-meat transformation showed R^2 of 0.743 (pH), 0.811 (L*) and 0.603 (C*) for DFD meats with PLSR (full) and R^2 of 0.359 (pH), 0.558 (L*) and 0.284 (C*) for RNF meats with PLSR (optimized) from male pigs. R^2_{cv} of 0.412 - 0.637 for pH, L* and c* for RFN and DFD meats from female pigs with PLSR (optimized). Dielectric spectroscopy predicts pork quality moderately well, but models that are more robust are needed to improve predictions of internal pork quality.

Keywords: Meat; Quality; Prediction; Dielectric spectroscopy

1. Introduction

In Peru, pork production has increased over the last 20 years to such an extent that it has become one of the three most consumed types of meat after chicken and beef, reaching a per capita consumption of 5.5 kg/year per person due to its nutritional properties such as proteins, vitamins, fats, and minerals, which are essential for the proper functioning of the human body. The principal pork-producing regions are Lima (45%), Libertad (11%), Arequipa (7%), Huánuco (4%), and Cajamarca (4%) (MIDAGRI, 2020).

In the Cajamarca region, approximately 6.3 thousand tons of pork are produced annually (MIDAGRI, 2020). Chota is one of the provinces with the highest production and commercialization of pork; however, this product is consumed without a previous physicochemical analysis to determine its physicochemical quality and the type of meat that the population consumes, which leads to the consumption of meat that does not meet quality standards.

The conversion from muscle to meat is a complex process involving a series of physical, chemical, and biochemical transformations responsible for the meat quality (Gispert et al., 2000). Likewise, when blood flow is interrupted, the muscle stops receiving oxygen supply, glucose, fatty acids, amino acids, and glycogen metabolism changes from aerobic to anaerobic, producing the accumulation of lactic acid, ATP depletion, pH decrease, protein denaturation, and temperature decrease, originating new intracellular conditions which are responsible for meat quality (Barbut et al., 2008, Huff-Lonergan, 2010).

Meat quality is given by a set of characteristics, such as organoleptic (color, tenderness, flavor, and odor), nutritional and technological (pH, color, water retention capacity, drip loss, and texture), which are determined by traditional methods that often have disadvantages such as being destructive, costly, time-consuming and requiring trained personnel for such analyses (Gispert et al., 2000, Novgorodska and Verbytskyi, 2023).

For this reason, it is necessary to look for new alternative technologies to the traditional ones, such as Near Infrared Spectroscopy (NIR), Hyper Spectral Imaging (HSI), Raman Spectroscopy (RS), Visible Reflectance Spectroscopy (VIS) and Dielectric Spectroscopy (DS). These methods have the advantage of being non-destructive, obtaining results quickly and with greater accuracy; they are environmentally friendly, and, above all, they can be used in production lines as a tool for quality control of different agri-food products (Castro-Giraldez et al., 2010). DS is a technique based on the rotation of molecules in the presence of electromagnetic field stimulation in the frequency ranges of 30 Hz- 300 GHz (radiofrequency) and 0.3-300 GHz (microwave) (Blakey and Morales-Partera, 2016). DS is also described by the complex permittivity ($\varepsilon^* = \varepsilon' + \varepsilon''$), where the dielectric constant (ε') and the loss factor are the real and imaginary parts of the complex permittivity, respectively. The dielectric constant is related to the ability of the material to store energy, and the dissipation factor is related to the absorption and dissipation of electromagnetic energy into other types of energy (Castro-Giráldez et al., 2010, Castro-Giráldez et al., 2010).

In the last decade, several efforts have been made in the application of the DS technique, such as detection of quality defects in pork muscle during the post mortem period (Castro-Giráldez, Aristoy, et al., 2010), determination of key biochemical markers of pork quality (Castro-Giráldez et al., 2011), salting processes of pork meat (Castro-Giráldez, Fito, et al., 2010), determination of added water in pork products (Kent et al., 2002), it has been applied in chicken meat to know the relationship between dielectric properties with biochemical metabolism (M. V. Traffano-Schiffo et al., 2021), dielectric characterization of chicken meat during post-mortem period (M. V. Traffano-Schiffo et al., 2021), determination of internal quality of chicken meat (M. V. Traffano-Schiffo, Castro-Giraldez, Colom, et al., 2018), determination of deep pectoral myopathy in chicken meat (M. V. Traffano-Schiffo, Castro-Giraldez, Herrero, et al., 2018), it has also been applied to detect defects in chicken breast (M. Traffano-Schiffo et al., 2017). However, no recent studies have been identified on the application of chemometric techniques in the prediction of internal quality during muscle-to-meat processing. In this context, and in order to broaden the application of dielectric spectroscopy in meat types, the aim of this research is to analyze the feasibility of using microwave dielectric spectroscopy as a tool for grading pork meat according to its quality

2. Materials and methods

The experimental diagram shown in Fig. 1 was used to obtain the data, described in detail in the following paragraphs.

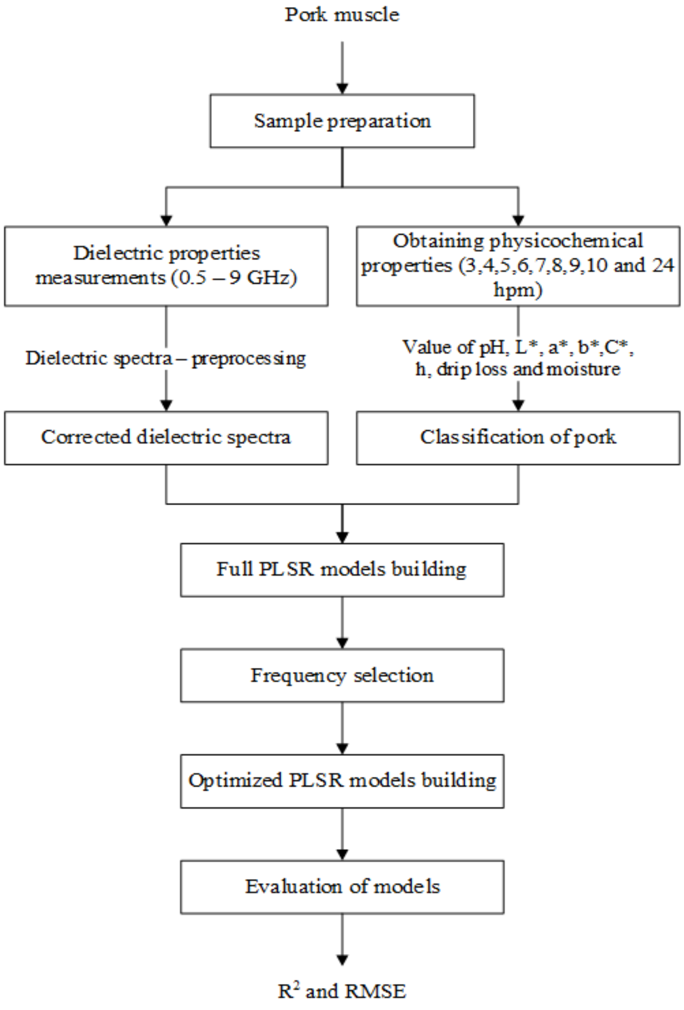

Fig. 1. The experimental diagram

2.1. Sample preparation

Eighty "*Longissimus dorsi*" muscles were selected from 54 male and 26 female Creole pigs, with an average weight of 85 kg and an age range of 5 to 12 months. Once the samples were obtained, they were placed in an isothermal box with blocks of ice and transferred to the Research Institute for Productive Improvement laboratory of the National Autonomous University of Chota for subsequent analysis.

Likewise, the samples were classified in relation to parameters of pH, color (L*) and drip loss obtained at 24 h, agreeing with studies realized by Castrillón et al. (1978; Castro-Giráldez et al. (2010 y Torres et al. (2018) for obtain meat as PSE (Pale, Soft, and Exudative), RSE (Red, Soft, and Exudative), DFD (Dark, Firm, and Dry), and RFN (Red, Firm, and Non-exudative).

2.2. Obtaining physicochemical properties

2.2.1. pH determination

A Thermo Scientific pH meter, model VSTAR50, was used. The pH measurement began with the equipment calibration in three buffer solutions with pH 4, 7 and 10 at a temperature of 4±0.1ºC, with a calibration adjustment of 99.6%. Subsequently, 10 g of sample were weighed, crushed in a mortar, and homogenized with 90 ml of distilled water. The electrode was placed in the previously prepared solution in triplicate to determine the pH during 3, 4, 5, 6, 7, 8, 9, 10, and 24 hours post-mortem (Castro-Giraldez et al., 2010).

2.2.2. Color determination

A 3nh NR200 colorimeter was used. The equipment calibration was carried out by measuring the black and white mosaics. Color measurement was realized with D65 illuminant and 10° observer, placing the colorimeter lens on the sample, obtaining L*, a*, and b* coordinates of the different samples at 4±1 °C, during 3, 4, 5, 6, 7, 8, 9, 10 and 24 hours post-mortem, all measure was realized per triplicate and different points of the sample (Castro-Giráldez et al., 2010, Castro-Giraldez et al., 2010).

2.2.3. Moisture determination

An AE ADAM PMB 202 Moisture Balance was used. For the measurement, 5 grams of sample were taken at 8 hours post-mortem, placed on the balance plate, closed, and subjected to a temperature of 140 °C for 30 minutes (Yang et al., 2009). The moisture percentage obtained automatically by this equipment was then recorded in triplicate.

2.2.4. Drip water loss

At 24 hpm, three pieces of pork of approximately 100 g each were cut and placed in pre-weighed polyethylene bags and immediately stored in a refrigerator (LG, model GT39WPPDC) at 4°C for 72 h. The bags were kept suspended and completely closed to avoid evaporation losses. The bags were kept suspended and completely closed to avoid evaporation losses. Likewise, the samples were prevented from coming into contact with the bag to avoid exudate by pressure. Subsequently, the samples were removed from the refrigerator and weighed separately (meat and bag), and, finally, the percentage of exudate was calculated through Eq. 1 (Castro-Giráldez et al., 2010, Qiao et al., 2007).

$$\text{Drip loss (\%)} = \frac{\text{weight of the bag with exudate} - \text{bag weight}}{\text{initial sample weight}} \text{x } 100 \qquad (1)$$

2.3. Dielectric properties measurements

The dielectric properties (ε' and ε") were acquired in the microwave range, at a frequency from 0.5 GHz to 9 GHz, using an open-ended coaxial probe (N1501A-001) connected to a KEYSIGHT N9915A vector network analyzer. The probe was fixed to a universal stainless steel support to measure the dielectric properties to avoid possible phase changes due to cable movement. Subsequently, the equipment was calibrated using three types of loads: air, short circuit, and distilled water at 4°C before each experiment (Castro-Giráldez, Aristoy, et al., 2010). Once the equipment was calibrated, the dielectric properties of the distilled water were measured to check the calibration suitability and thus ensure that it was stable. The dielectric properties were measured in quitupled by placing the coaxial probe on the sample surface in line with the fiber during 3, 4, 5, 6, 7, 8, 9, 10, and 24 hours post-mortem (Castro-Giráldez et al., 2011).

2.4. Statistics Analysis

A one-way analysis of variance was carried out on the physicochemical parameters of the types of pork followed by Tukey's multiple comparisons test with a margin of error of α=0.05 to determine remarkable distinctions among maturity stages. The data was processed in Statgraphics Centurion XVIII software.

Before the statistical analysis of the modeling of quality prediction during the muscle-to-meat conversion, data matrices were created in *.xlsx format in MS Excel according to the type of meat. Each data matrix consisted of each spectrum of ε' and ε" with its respective physicochemical reference value. Then, the algorithm proposed by Chuquizuta et al. (2022) for data processing was modified and carried out in Matlab 2022b software.

2.4.1. Modeling according to PLSR

2.4.1.1. Data pre-processing

A second-order Savitzky-Golay filter, with 9 points, was used for the dielectric spectra of the dielectric constant (ε') and the loss factor (ε") to eliminate the noise generated by the electronic devices during the data collection. This filter consists of performing the least squares fitting of a small set of consecutive data to a polynomial and taking the center point of the fitted polynomial curve as new smoothed data (Flores et al., 2017; Geesink et al., 2003).

2.4.1.2. Modeling according to PLSR

The partial least squares regression (PLSR) model was used to model the dielectric spectra and physicochemical characteristics. This statistical model, popular in multivariate analysis, aims to obtain a linear model which predicts a response variable, Y, from a large set of X variables, as shown in Eq. 2 (Andersen et al., 2021; Khan et al., 2020).

$$Y = X\beta + E \qquad (2)$$

Where X is a size matrix (n x m), n is the intensity value according to the hours post-mortem, and m is the intensity value according to the frequency regarding the dielectric constant (ε'); Y is the reference information (n x1) of the physical-chemical properties, β is the vector of regression coefficients or beta coefficients (m x 1) and E is the error of the vector.

2.4.1.3. Evaluation of models

The prediction models were constructed on the complete dataset, utilising the five-fold (k-fold) cross-validation methodology to prevent over-fitting. To assess the accuracy of both the full and optimised models derived from PLSR, (3), (4) were used to determine the coefficient of determination (R^2_{cv}) and the mean square error (Andersen et al., 2021, Khan et al., 2020; Y. Yang et al., 2021; Zhao et al., 2016).

$$R^2 = 1 - \frac{\sum_{i=1}^{n} -(Y_i - \widehat{Y}_i)^2}{\sum_{i=1}^{n} -(\widehat{Y}_i - \bar{Y})^2} \tag{3}$$

$$RMSE = \left(\frac{\sum_{i=1}^{n} -(Y_i - \widehat{Y}_i)^2}{\mathrm{n}}\right)^{0.5} \tag{4}$$

Where $\widehat{Y}_i$ and Y_i are the predicted and reference values of a sample (i); $\bar{Y}$ is the mean of reference values of all samples.

3. Results and discussions

3.1. Physicochemical characteristics of muscle-to-meat conversion

Fig. 2 shows, the pH evolution of the RFN and DFD samples during the muscle-to-meat conversion. The RFN samples show a decrease in pH from 6.21 to 5.71 and from 6.20 to 5.71 in male and female pigs, respectively, until 24 hpm, which is attributed to the degradation of glycogen produced by glycolysis, besides the production of lactate and phosphate, which are responsible for the denaturation of sarcoplasmic and myofibrillar proteins; this particular case is characterized by following a normal (Faucitano et al., 2010, Huff-Lonergan, 2010; M. V. Traffano-Schiffo et al., 2018). Similarly, our results of the RFN muscle-to-meat conversion kinetics, shown in Fig. 1a-b, are similar to those obtained by Chmiel et al. (2014), Liu et al. (2021), and Maganhini et al. (2007), whose pH decrease was from 6.10 to 5.52 for male pigs and to those by Castro-Giraldez et al. (2010), Furtado et al. (2019) and Qiao et al. (2007), whose pH decrease was from 5.99 to 5.5 for male and female pigs, during 24 hpm; however, several authors describe that such difference is due to intrinsic factors such as genetics, breed, age, sex, weight, and muscle type, and extrinsic factors such as production system, climatic conditions, antemortem management, and postmortem management (Čandek-Potokar et al., 2024; Trevisan and Brum, 2020).

In the case of DFD meats, the samples show a slight decrease in pH from 6.55 to 6.18 and from 6.58 to 6.15 for male and female pigs, respectively, due to the abnormal biochemical process in glycolysis during the muscle-to-meat conversion, caused by prolonged chronic stress in the animals during fasting, loading and unloading, transport, resting, and stunning (Jerez-Timaure et al., 2020; M. V. Traffano-Schiffo, Castro-Giraldez, Colom, et al., 2018). This stress generates glycogen depletion, low lactic acid production, low protein denaturation, and high water retention capacity (Čobanović et al., 2016; Jerez-Timaure et al., 2020; M. V. Traffano-Schiffo, Castro-Giraldez, Colom, et al., 2018). Likewise, our results shown in Fig. 1a- b are similar to those reported by Castro-Giraldez et al. (2010), whose pH decrease was from 6.22 to 5.90 in male and female pigs, and to those by Maganhini et al. (2007), who reported a pH of 5.80 ± 0.16, at 24 hpm.

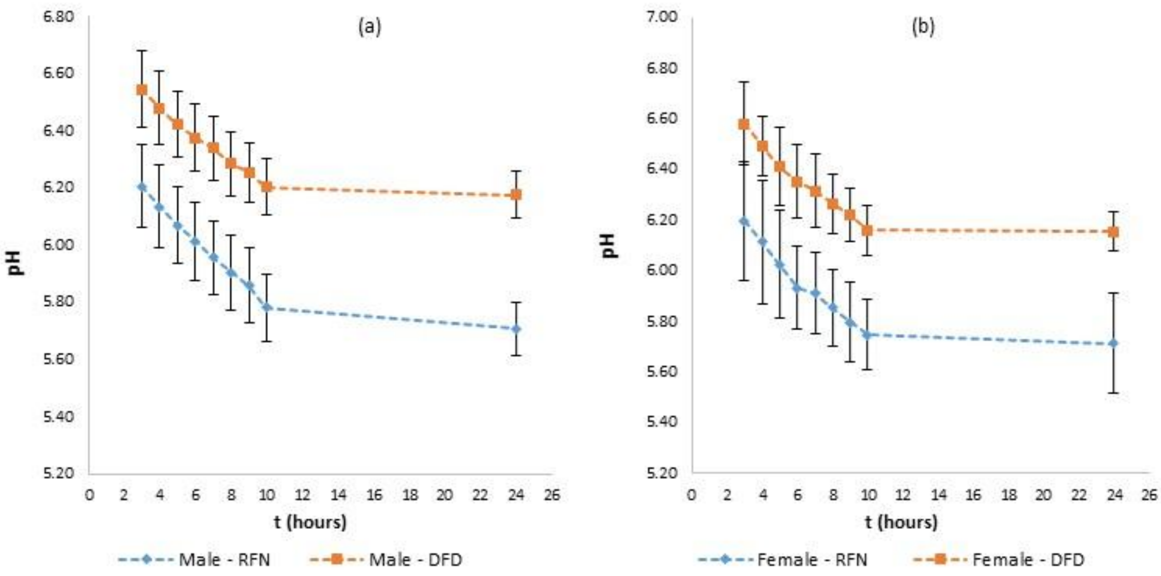

Fig. 2. Evolution of pH of RFN and DFD samples during the muscle-to-meat conversion: (a) for male pigs and (b) for female pigs.

The color kinetics in the L*, a*, b* and coordinates of male and female pig samples during the muscle-to-meat conversion are shown in Fig. 3, Fig. 4, Fig. 5. In obtaining RFN meats, it has been observed that the L* coordinate (lightness) gradually increases in male pigs from 41.11 to 48.73; and in female pigs, from 41.05 to 48.63 until 10 hpm and decreases to 43.34 in the case of male pig samples and to 43.69 in female pigs, respectively, at 24 hpm, as can be seen in Fig. 3a-b. Likewise, it is evident that our results of L* at 24 hpm are different from those reported by Chmiel et al. (2014), Liu et al. (2021) and Maganhini et al. (2007), who reported L* in the range from 46.85 to 50.34 at 24 hpm in male pigs and those by Castro-Giraldez et al. (2010) who obtained L* = 51.8 ± 1.8 at 24 hpm in male and female pigs. According to Matarneh et al. (2023), Huff-Lonergan (2010),Chmiel et al. (2014), and Gispert et al. (2000), these differences are due to light scattering and absorption during sampling and to the level of myoglobin present in the muscle, which may vary according to breed, age, sex, castration, weight, feeding, type of cut, type of muscle, and temperature. On the other hand, coordinate a* (Red-green) for RFN meats presents a slight increase between 3 and 27 hpm, from 14.25 to 14.89 and 13.88–14.05 for male and female pigs, respectively. In addition, coordinate b* (Yellow-blue) shows similar behavior of a* from 8.21 to 9.99 and 8.07–9.20 for male and female pigs, respectively, as shown in Fig. 3a-b and 4 a-b, results that are different from those acquired by Chmiel et al. (2014) and Maganhini et al. (2007), who obtained values from 1.34 to 2.2 and from 7.93 to 10.8 in the a* and b* coordinates in male pigs, during the 24 hpm.

For DFD samples, coordinate L* increases progressively in male pigs from 41.29 to 48.83 and female pigs from 40.09 to 48.51 during the 10 hpm. It then decreases at 24 hpm to 40.91 and 40.15, respectively. Our results, see Fig. 2a - b, coincide with those obtained by Faucitano et al. (2010) and Maganhini et al. (2007), who obtained L* values from 40.54 to 43.95 for male pigs at 24 hpm, but differ from those reported by Castro-Giraldez et al. (2010), who obtained L* of 49.4 ± 0.2 at 24 hpm in male and female pigs. Likewise, it can be observed that coordinate a* presents a slight increase in male pigs from 13.92 to 14.86 and a slight decrease in female pigs from 15.35 to 15.02 during the 27 hpm (see Fig. 3a - b). In the same way, coordinate b* shows an increase in male pigs from 8.06 to 9.20 and female pigs from 9.03 to 10.00 during the 27 hpm (see Fig. 4a - b). Our results are different from those acquired by Maganhini et al. (2007), who obtained in male pigs values of 1.17 ± 0.74 and 6.37 ± 0.63 in the a * and b* coordinates at 24 hpm. These differences are mainly due to the increase of myoglobin because of the advanced age and prolonged chronic stress, which generates low oxygen scattering, glycogen reduction, high pH, slow protein denaturation, low light scattering, and bacterial contamination (Castro de Jesús et al., 2021; Huff-Lonergan, 2010; Matarneh et al., 2023; M. V. Traffano-

Schiffo et al., 2018).

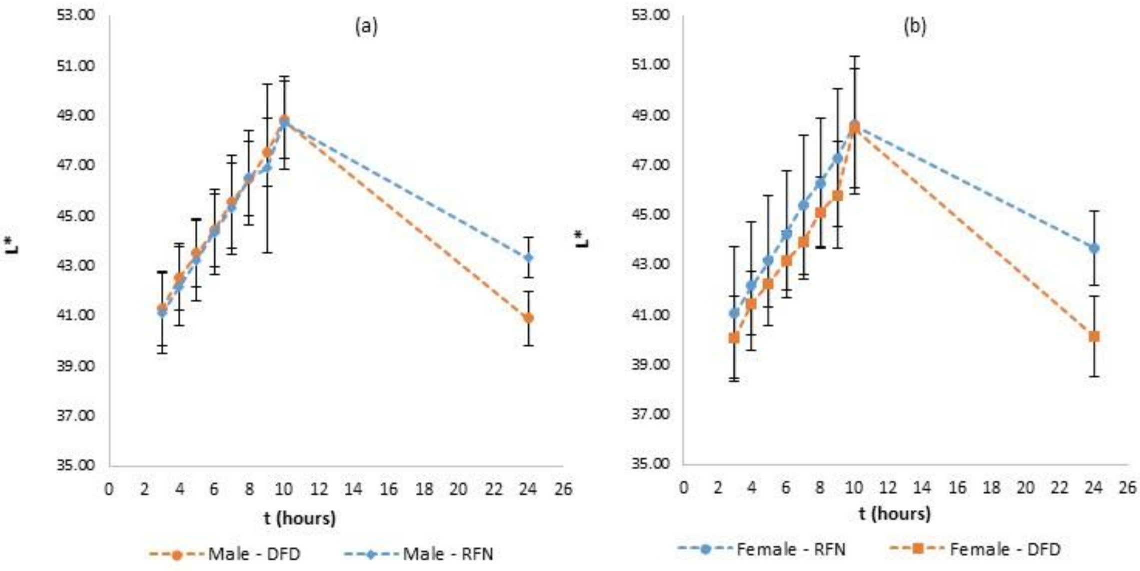

Fig. 3. Evolution of the L* coordinate of RFN and DFD samples during the muscle-to-meat conversion: (a) for male pigs and (b) for female pigs.

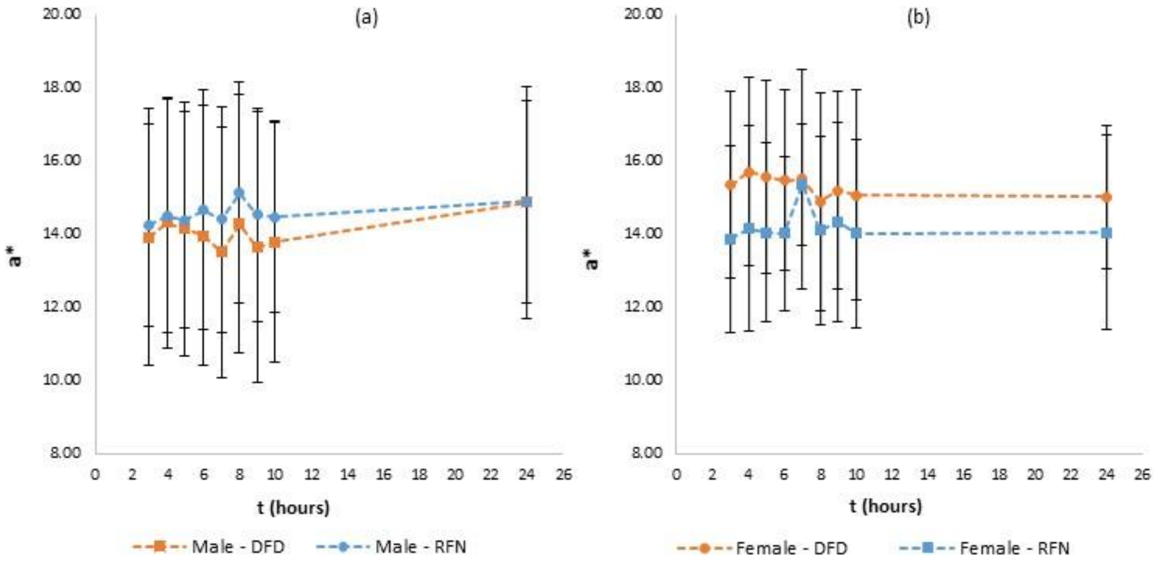

Fig. 4. Evolution of the a* coordinate of RFN and DFD samples during the muscle-to-meat conversion: (a) for male pigs and (b) for female pigs.

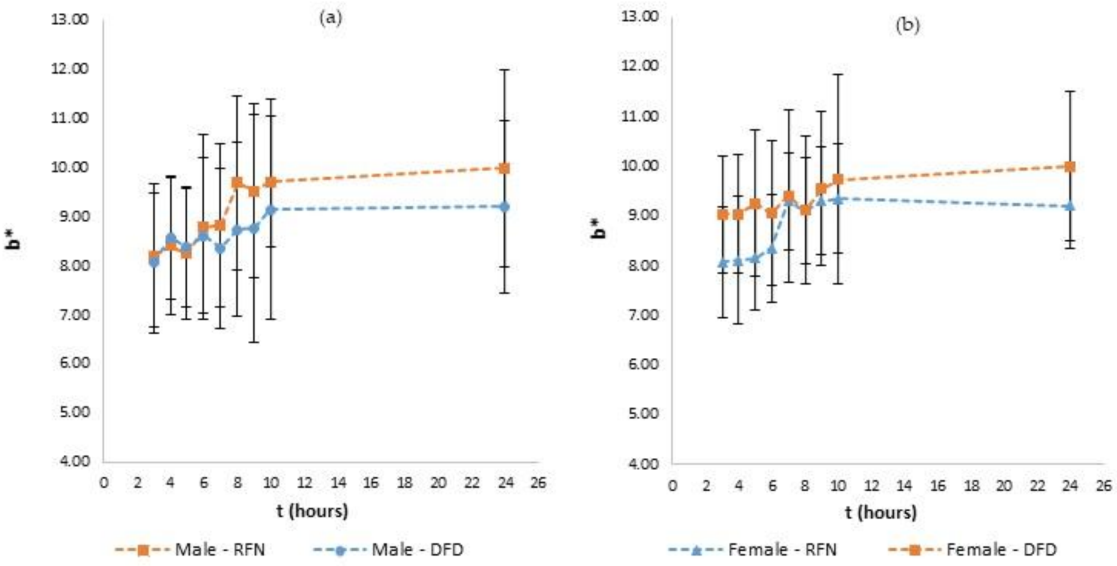

Figure 5. Evolution of the b* coordinate of RFN and DFD samples during the muscle-to-meat conversion: (a) for male pigs and (b) for female pigs.

Regarding chroma (C*) and hue (h*), it has been observed that in RFN samples, chroma increases in a range from 16.48 to 17.96 for male pigs and in a range from 16.09 to 16.83 for female pigs, during the 24 hpm. 83 for female pigs, during the 24 hpm; something similar can be observed in the tone, since it increases from 3 hpm to 24 hpm in a range of 30.28–33.90 for male pigs and in a range of 30.47–33.69 for female pigs, as shown in Fig. 6a-b and 7 a-b. In the DFD samples, both chroma and hue increased from 3 hpm to 24 hpm; in the case of chroma, it increased in a range of 16.48–17.96 for males and 16.09–16.83 for females; something similar happened with hue, which increased in a range of 30.28–33.90 and 30.47–43.34 for males and females, respectively. These results were different from those obtained by Barbin et al. (2013) who obtained values in the range of 45.95–8.36 for chroma and values of 10.91–3.50 for tone (he does not specify the type of meat); likewise, our results were different from those reported by Castro-Giraldez et al. (2010) who obtained values of 70.39 for RFN samples and 68.29 for DFD samples, in relation to tone. These differences are attributed to the physicochemical changes produced during the conversion of muscle to meat, which can generate variations in pH content, myoglobin, oxygen dispersion, light diffusion and, above all, protein denaturation (Castro de Jesús et al., 2021; Matarneh et al., 2023; M. V. Traffano-Schiffo, Castro-Giraldez, Herrero, et al., 2018).

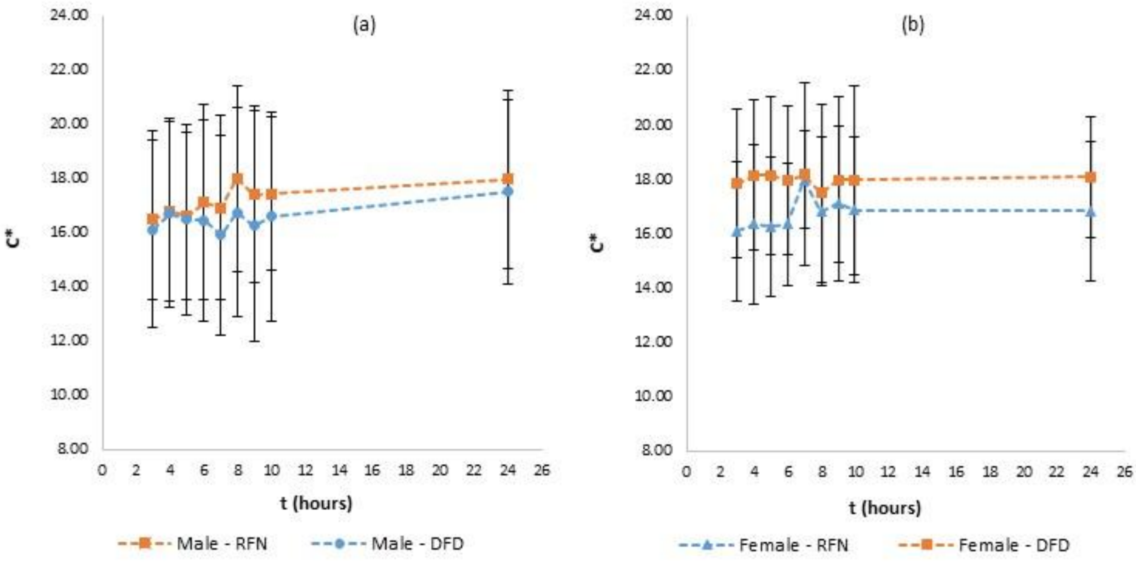

Fig. 6. Evolution of chroma (C*) of RFN and DFD samples during muscle-to-meat conversion: (a) for male pigs and (b) for female pigs.

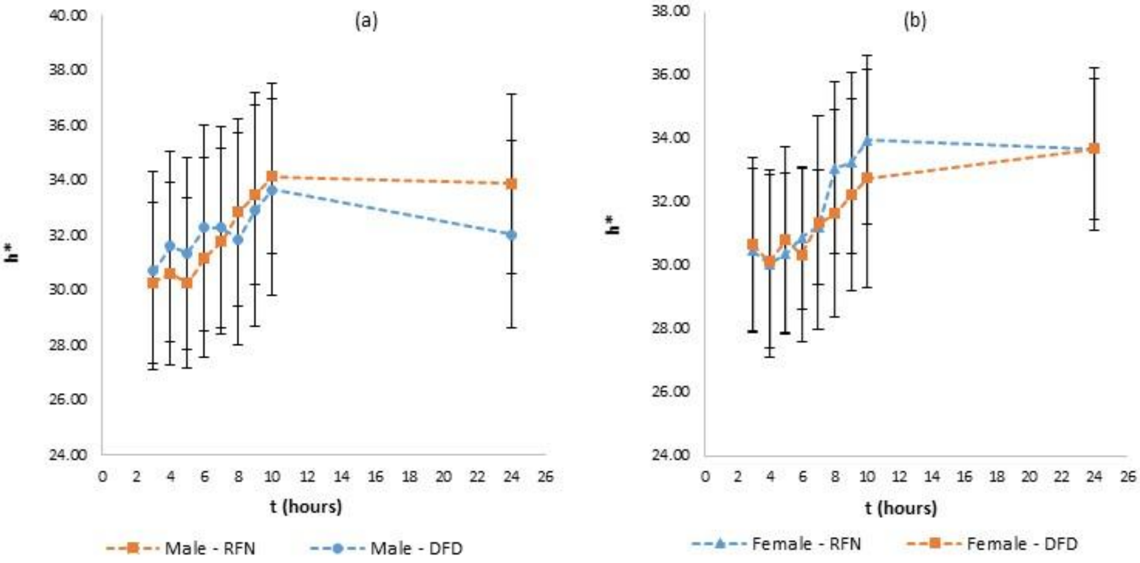

Fig. 7. Pitch evolution (h*) of RFN and DFD samples during muscle-to-meat conversion: (a) for male pigs and (b) for female pigs.

Then, the pH and color of pork meat undergo changes during post-mortem processing, with slight differences influenced by the sex of the animal for both RFN and DFD samples.

3.2. Classification of pork according to physicochemical parameters

Table 1 shows the physicochemical parameters obtained at 24 hpm and Tukey's test for RFN and DFD samples. For the RFN samples, pH < 6, L* > 40, C* > 15, h* > 30, H% > 60 and drip loss < 2 can be observed for both male and female pigs; for the DFD samples, pH > 6, L* > 40, C* > 15, h* > 30, H% > 60 and drip loss < 2 can be observed. Regarding the results obtained according to the Tukey test, a significant difference (p> 0.05) can be observed for the parameters of pH and color in the *L chordate for both RFN and DFD samples; however, for the parameters of chroma, tone, humidity and drip loss, no significant difference was found; it is worth mentioning that the parameters of pH, L* and drip loss are the ones that will allow us to classify the quality of the meat.

Table 1. Physicochemical parameters obtained at 24 hpm for RFN and DFD samples and tukey's test.

Parameters		pH_{3h}	pH_{24h}	L^*_{24h}	C^*_{24h}	h^*_{24h}	Moisture (%)	Drip loss (%)
RFN	Female	6.197 ± 0.235^a	5.714 ± 0.197^a	43.692 ± 1.486^a	16.827 ± 2.557^a	33.691 ± 4.116^a	68.857 ± 1.230^a	1.655 ± 1.004^a
	Male	6.208 ± 0.145^a	5.708 ± 0.094^a	43.341 ± 0.802^a	17.964 ± 3.269^a	33.898 ± 3.333^a	69.604 ± 1.823^a	1.833 ± 1.060^a
DFD	Female	6.581 ± 0.162^b	6.154 ± 0.077^b	40.152 ± 1.634^b	18.073 ± 2.236^a	33.684 ± 3.336^a	69.900 ± 1.524^a	1.129 ± 0.417^a
	Male	6.547 ± 0.135^b	6.177 ± 0.084^b	41.910 ± 1.075^b	17.522 ± 3.410^a	32.035 ± 3.984^a	69.032 ± 1.892^a	1.693 ± 1.037^a
p_value		0.000^*	0.000^*	0.000^*	0.734^*	0.237^*	0.287^*	0.162^*

*Analisys of variance of one-away (α=0.05); the superscripts of the same letters of the mean values in each physicochemical parameter of the types of male and female pork, indicate the existence of no significant differences according to the Tukey test (pvalue < 0.05).

Table 2 shows the meat type classification for male and female pigs based on the parameters of pH, color (L*), and drip loss at 24 hpm, resulting in 0 PSE samples, 0 RSE samples, 33 RFN samples, and 47 DFD samples, for a total of 80 samples.

Meat type	Male pigs	Female pigs	total
PSE	0	0	0
RSE	0	0	0
RFN	23	10	33
DFD	32	15	47
Total	55	25	80

Meat pH and meat colour are effective indicators for the identification of RFN and DFD pork.

3.3. Dielectric spectra during muscle-to-meat conversion.

Fig. 8, Fig. 9 show the dielectric constant (ε') values of the RFN and DFD male and female samples from 3 to 24 h post-mortem, which decrease with increasing frequency. This behavior is similar to that reported by Castro-Giráldez, Aristoy, et al. (2010). The behavior of the ε' spectra of males and females is a product of biochemical and structural changes, which include a series of oxidative, electrolyte, proteolytic, and other processes. Similarly, the before-mentioned changes are attributed to lactic acid accumulation, pH decrease, and protein denaturation, causing a decrease in water retention capacity, the release of ions (Mg^{2+}, Ca^{2+}, K^{+}, Cl^{-} and Na^{+}), and the formation of myosin-actin cross-links in the samples (Paredi et al., 2012), similar biochemical behavior in chicken meat (M. V. Traffano-Schiffo et al., 2021).

In DFD samples, the behavior of the ε' spectra of male and female pigs is due to the low availability of ATP, lactic acid, and phosphate ions, the slow decrease in pH, high water retention capacity, protein denaturation, and degradation of the muscle structure, which affect ionic conductivity and the dipolar relaxation phenomenon (Castro-Giráldez, Aristoy, et al., 2010; M. V. Traffano-Schiffo, Castro-Giraldez, Colom, et al., 2018). Due to the lower availability of glucose and the limited glycogen content, the glycolysis route is limited, which causes this type of meat to take alternative sources of energy production, such as the degradation of amino acids, mainly alanine, and glycine. Due to these processes, ε' is lower for DFD samples in contrast to the other quality classes (M. V. Traffano-Schiffo, Castro-Giraldez, Colom, et al., 2018).

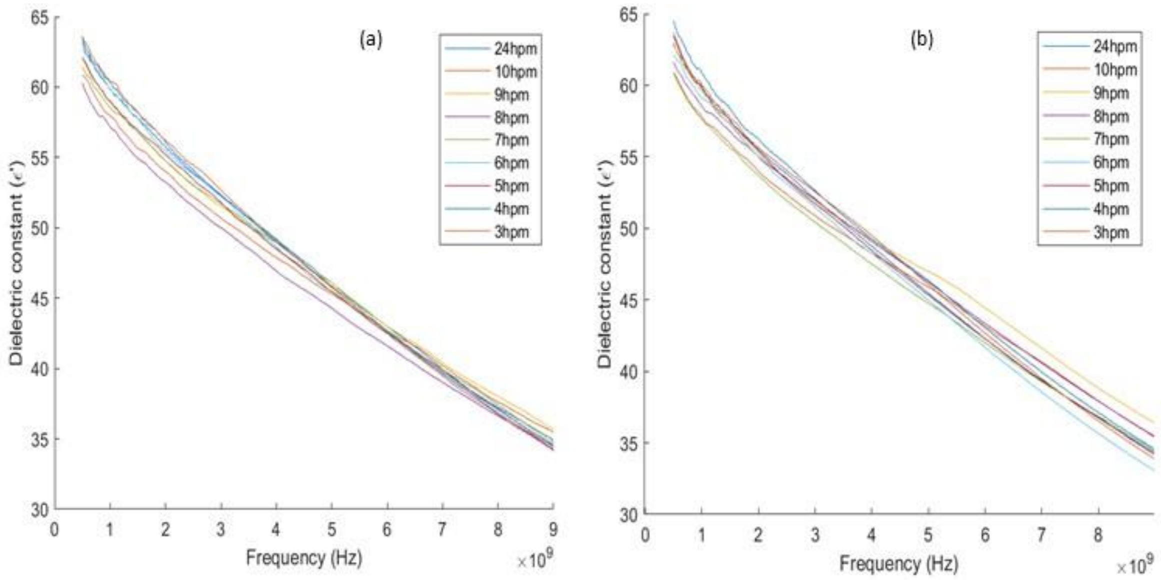

Fig. 8. Evolution of the dielectric constant of RFN samples during 10 hours post-mortem: (a) for male pigs and (b) for female pigs.

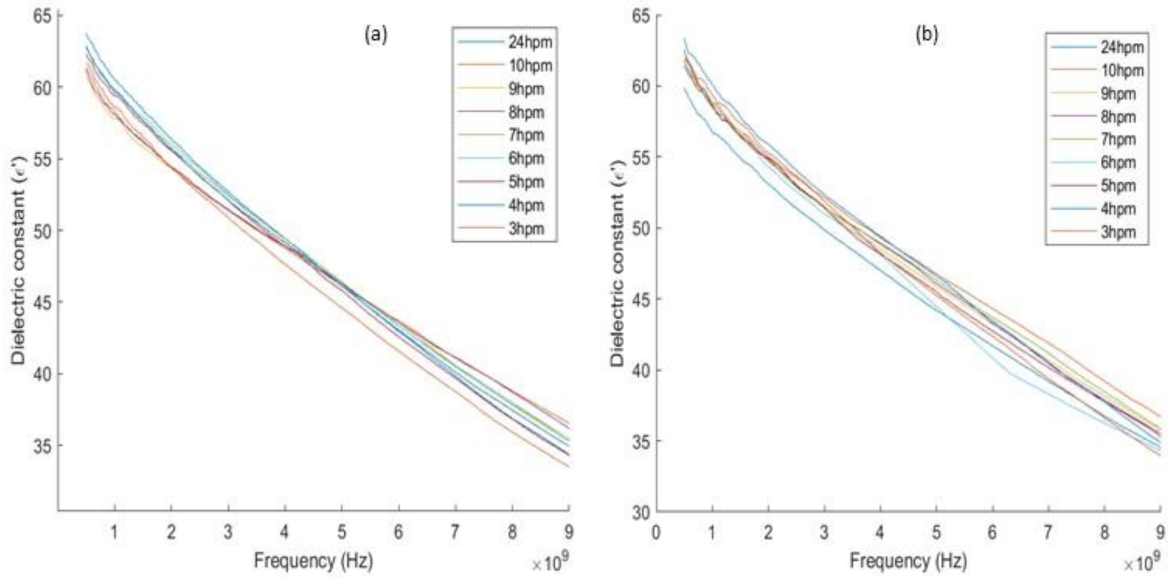

Fig. 9. Evolution of the dielectric constant of DFD samples, from 3 to 10 hours post-mortem: (a) for male pigs and (b) for female pigs.

Fig. 10, Fig. 11 show the intensity values of the loss factor (ε") along the electromagnetic spectrum (0.5–9 GHz) of the RFN and DFD samples of males and females from 3 to 24 h post-mortem. In both figures, the intensity values ε" decrease from 0.5 to 2 GHz and then increase until 9 GHz, forming a "U"- shaped spectrum. This U-shape is because, after slaughter, the muscle cells reduce the production of nutrients and oxygen, increasing ionic strength and osmotic pressure from the animal's death until rigor mortis. When the pH approaches its isoelectric point (pH close to 5.4), the proteins start to become disabled, and their capacity for absorbing cations (Mg^{2+} and Ca^{2+}) decreases, thus increasing the free ions in the sarcoplasm and the ionic conductivity (Castro-Giráldez, Aristoy, et al., 2010). Likewise, the dielectric spectra formed from the intensity values of ε" for RFN samples are similar to those reported, showing that the behavior of ε" spectra in males and females is due to ATP depletion and pH decrease, causing the release of free ions from proteins and the increase of metabolites, such as lactate and nucleotides (Castro-Giráldez, Aristoy, et al., 2010). In DFD samples, the behavior of the intensity values of the ε" spectra is due to the low lactic acid content and the late onset of rigor mortis in contrast to the other types of samples.

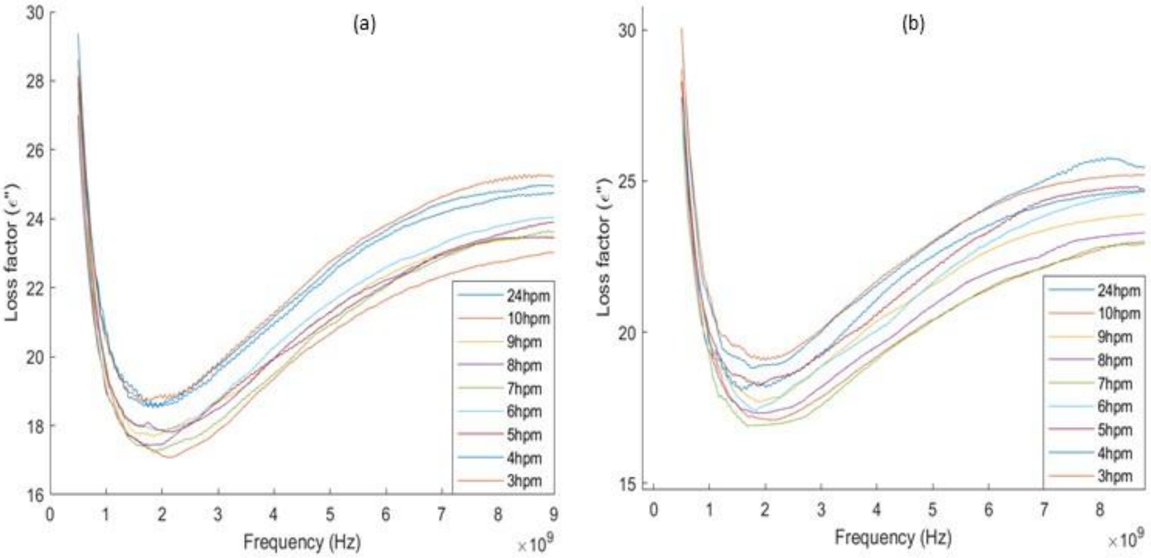

Fig. 10. Evolution of the loss factor of RFN samples, from 3 to 10 hours post-mortem: (a) for male pigs and (b) for female pigs.

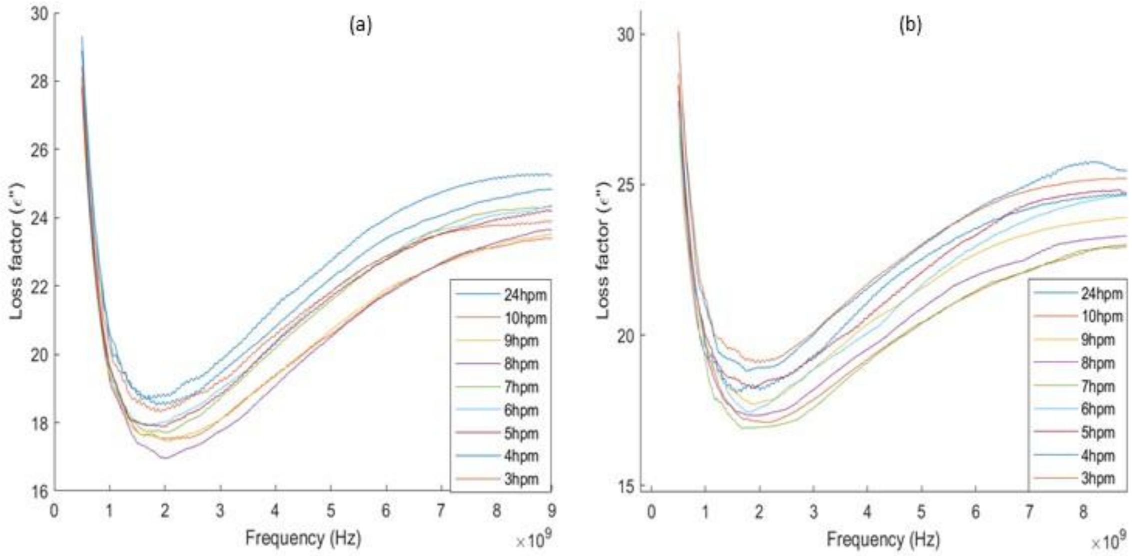

Fig. 11. Evolution of the loss factor of DFD samples, from 3 to 10 hours post-mortem: (a) for male pigs and (b) for female pigs.

3.4. Prediction of quality parameters by dielectric spectroscopy.

3.4.1. Relevant frequencies for the optimization of the prediction model

The coefficient β allows finding the highest absolute values, which measure the level of relationship between variables X and Y (Khan et al., 2020). In this investigation, a total of 15 relevant or specific frequencies of 401 were found from the intensity values of ε' and ε'', referred to pH values. In the case of RFN samples, three relevant frequency subgroups have been observed in the ranges of 0.5–1 GHz, 3–5 GHz and 8.5–9.0 GHz for male pigs and for female pigs two subgroups have been observed in the ranges of 0.5–3 GHz and 4.0–7.0 GHz, as evidenced in Fig. 12 a - b. The DFD samples also present three relevant frequency subgroups in the ranges of 1.5–6.0 GHz, 4.5–7.5 GHz and 7.2–8.9 GHz for male pigs and two subgroups in the ranges of 2.5–4.0 GHz and 5.3–9.0 GHz for female pigs, as shown in Fig. 13 a-b.Unlike those reported by Andersen et al. (2018), who obtained 3 relevant variables (RVs) in the range from 400 to 1850 nm; Andersen et al. (2021), who obtained 5 RVs in the range from 400 to 1800 cm−1; and Balage et al. (2015), who obtained 105 RVs in the range from 390 to 1380 nm through Marten's uncertainty test; Barbin et al. (2012) has found 5 RV out of 237 bands, and Barbin et al. (2013) obtained 14 RV out of 237 bands in the range from 928 to 1645 nm and from 947 to1680 nm through weighted regression coefficient; Geesink et al. (2003) found two subgroups of RVs in the range from 1000 to 1860 nm and from 2100 to 2450 nm through the multiplicative scattering correlation (MSC); Qiao et al. (2007) found 6 RVs out of 80 spectra in the range from 494 to 978 nm through the simple correlation coefficient. The differences between our research and the others are mainly due to the selection methods of relevant variables and the data collection technique, which were performed using hyperspectral imaging, near-infrared, and Raman spectroscopy, among others, in different ranges of the electromagnetic spectrum.

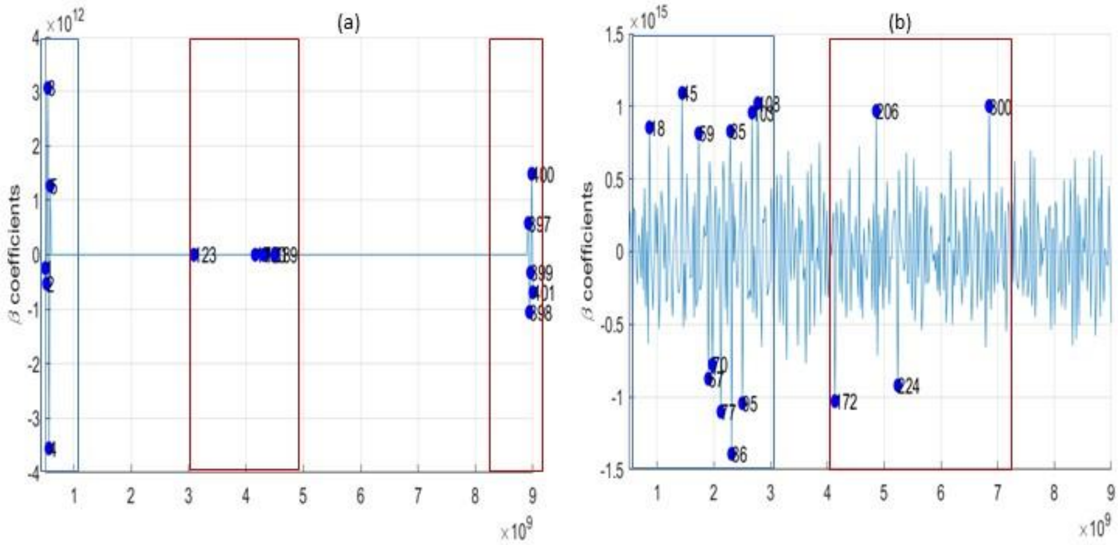

Fig. 12. β Coefficient of pH of RFN samples: (a) for male pigs and (b) for female pigs.

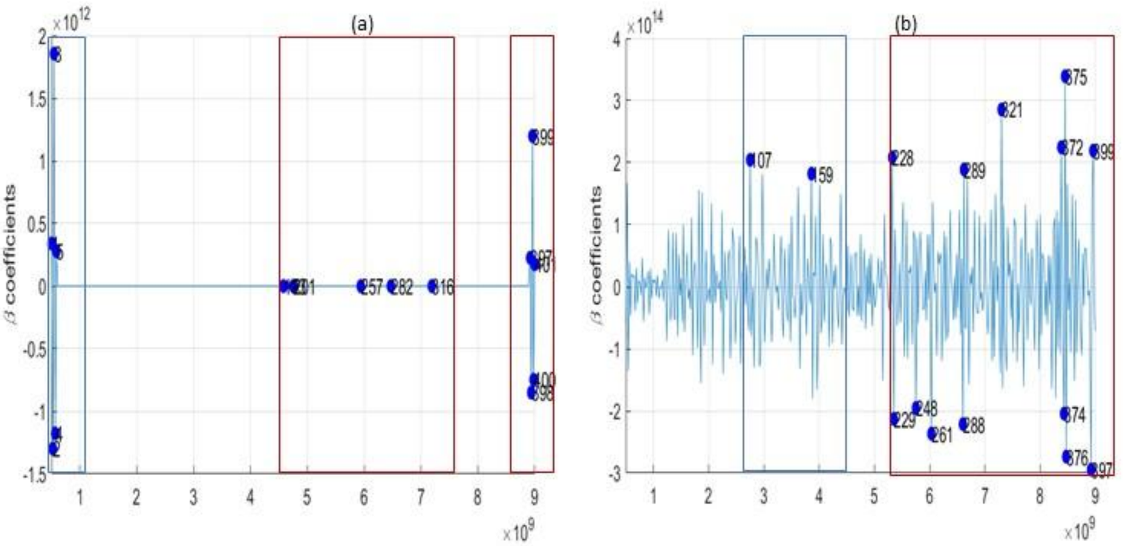

Figure 13. β Coefficient of pH of DFD samples: (a) for male pigs and (b) for female pigs.

Fig. 14, Fig. 15 show the most relevant frequencies for color prediction (L*) of the RFN and DFD samples for males and females. In the case of the RFN samples, three subgroups with relevant values (RV) are observed in the ranges of 0.5–1.0 GHz, 5.2–7.0 GHz and 8.5–9.0 GHz for male pigs and in the ranges of 0.5–2.5 GHz, 3.0–5.2 GHz and 7.5–9.0 GHz for female pigs, as shown in Fig. 14 a-b. Similarly, the DFD samples present three RV subgroups in the ranges of 0.5–1.0 GHz, 2.8–4.0 GHz and 8.5–9.0 GHz for male pigs and for female pigs two subgroups in the ranges of 2.0–4.5 GHz and 5.5–8.5 GHz, as evidenced in Fig. 15 a - b. In our research, 15 specific frequencies have been found for color(L*) prediction, unlike those reported by Balage et al. (2015), who obtained 63 RVs in the range from 405 to 1365 nm through the Martens' uncertainty test; Barbin et al., 2012, Barbin et al., 2013, who reported 6 RVs in the range of 947–1654 nm and 14 RVs in the range from 928 to 1645 nm, respectively, through the weighted regression coefficient; Geesink et al. (2003) found two major frequency subgroups in the range from 1000 to 1860 nm and 2100–2450 nm through the multiplicative scatter correlation; and Qiao et al. (2007) found 6 RVs in the range from 434 to 703 nm through the simple correlation coefficient.

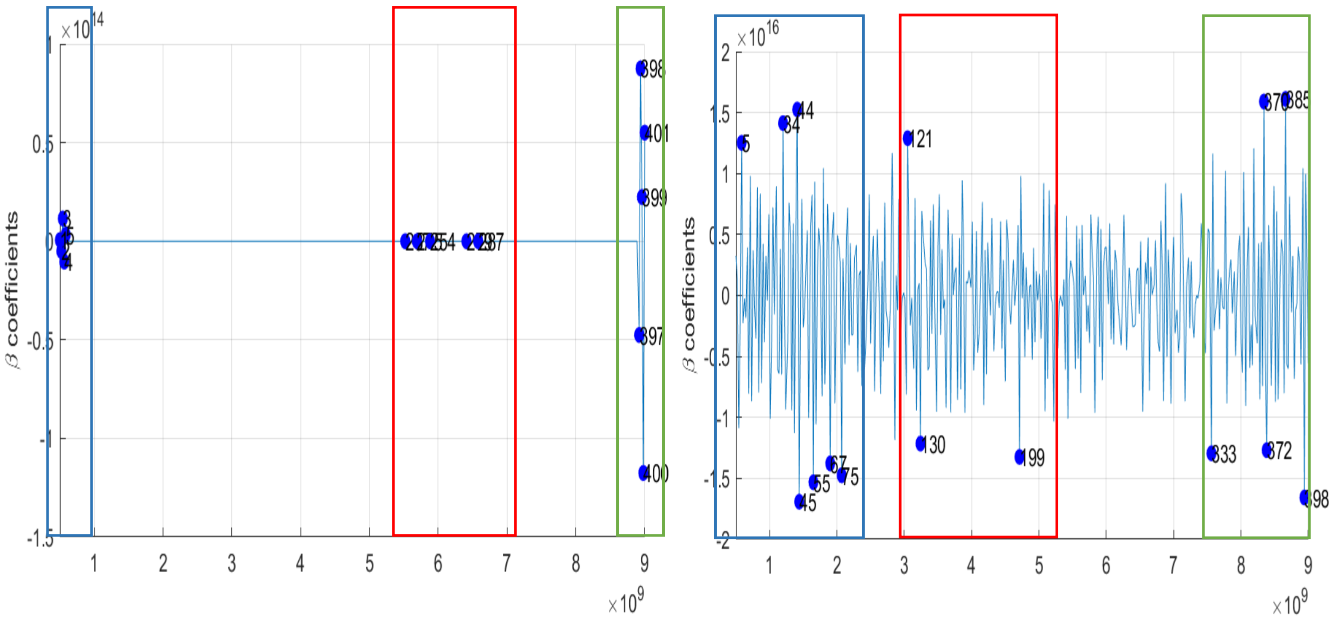

(a) (b)

Fig. 14. β Coefficient of color (L*) of RFN samples: (a) for male pigs and (b) for female pigs.

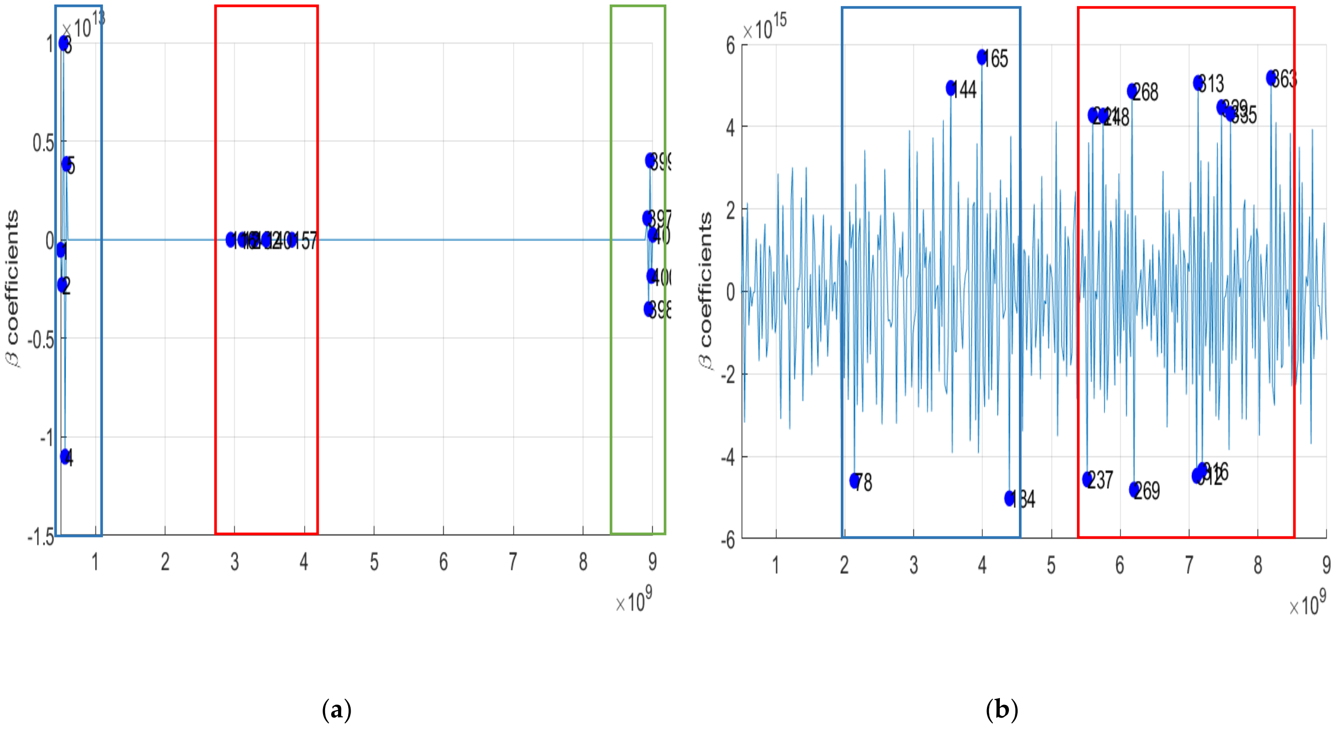

Fig. 15. β Coefficient of color (L*) of DFD samples: (a) for male pigs and (b) for female pigs.

Fig. 16, Fig. 17 show the most relevant frequencies for chroma (C*) prediction of RFN and DFD samples for male and female pigs. In the case of RFN samples, three subgroups with relevant values (RV) are observed in the ranges 0.5–1.3 GHz, 5.5–7.0 GHz and 8.5–9.0 GHz for males and in the ranges 0.5–1.5 GHz, 3.0–5.3 GHz and 6.5–9 GHz for females, as shown in Fig. 15 a-b. Similarly, DFD samples present three RV subgroups in the ranges of 0.5–1.0 GHz, 2.8–4.0 GHz and 8.5–9.0 GHz for males and for females in the ranges of 0.5–1.8 GHz, 3.2–5.0 and 6.5–9.0 GHz, as evidenced in Fig. 16 a - b. In our research, 15 specific frequencies have been found for chroma (C*) prediction, unlike those reported by Barbin et al. (2012), who obtained 6 RVs in the range of 947–1214 nm using the weighted regression coefficient.

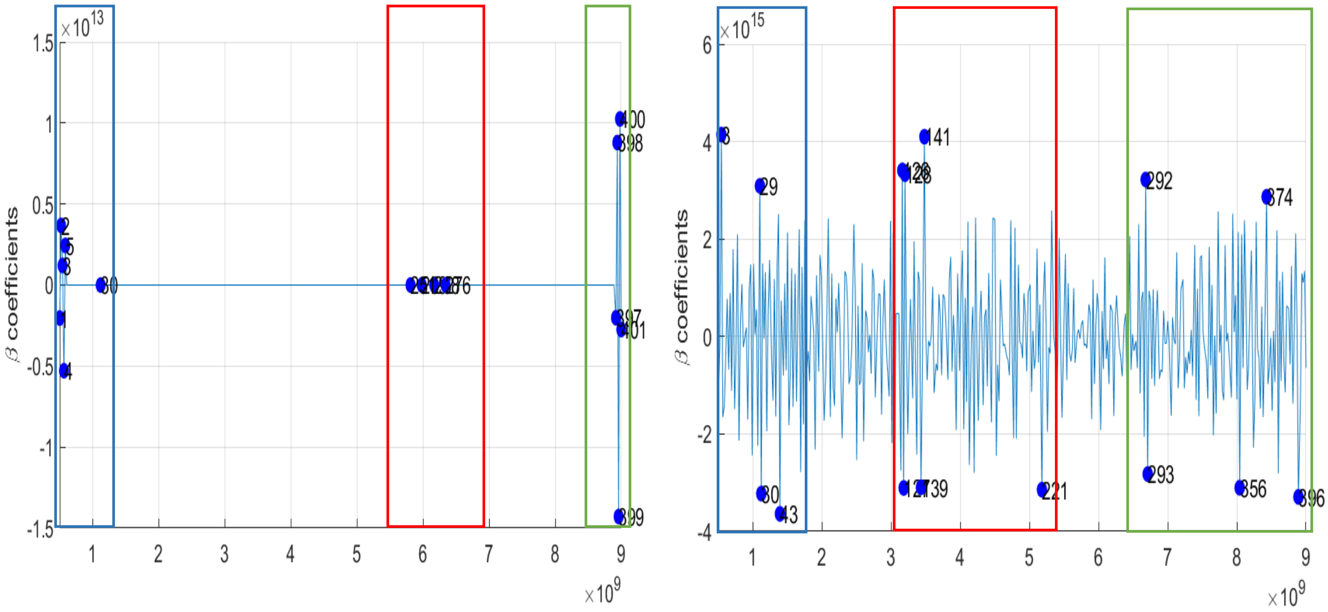

(**a**) (**b**)

Fig. 16. β Coefficient of color (C*) of RFN samples: (a) for male pigs and (b) for female pigs.

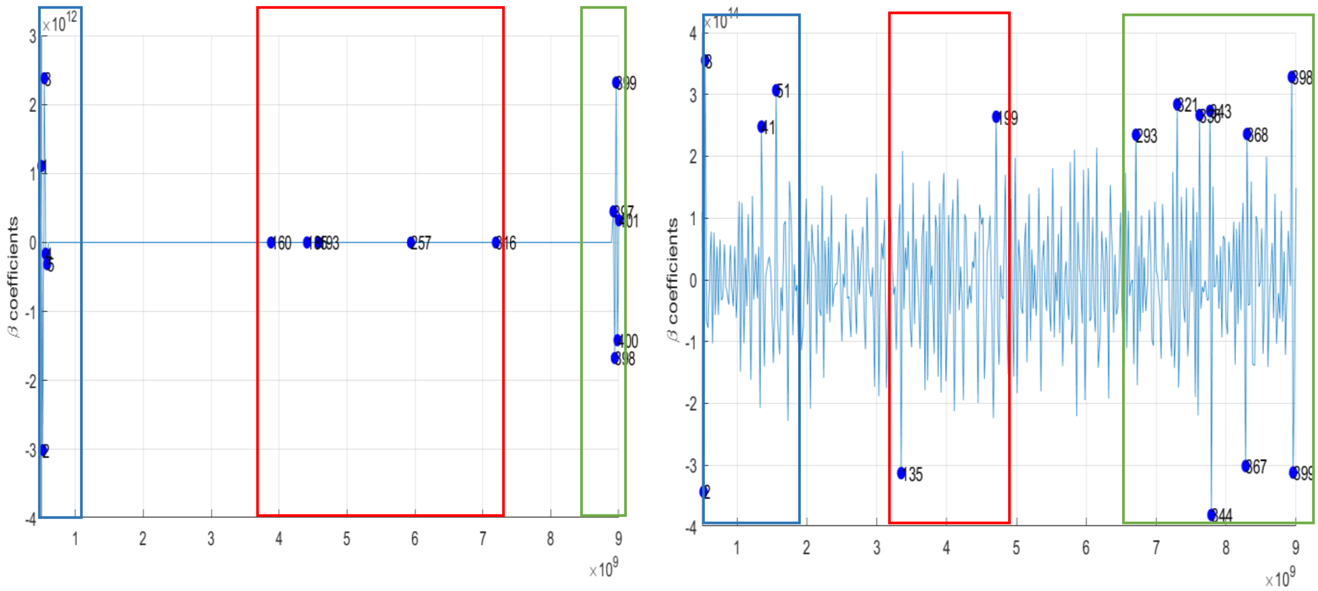

(**a**) (**b**)

Fig. 17. β Coefficient of color (L*) of DFD samples: (a) for male pigs and (b) for female pigs.

3.4.2. Prediction of physicochemical parameters during the muscle-to-meat conversion: modeling using e' for the prediction of physicochemical parameters.

Table 3 shows the values obtained from the full and optimised PLSR for each of the parameters determined (pH, L* and C*) according to the type of meat. The results show that the optimised PLSR gives better results than the full PLSR for the parameters pH and L* in both types of meat and sex; however, for the parameter C*, the full PLSR gives high values for male pigs in both types of meat and the optimised PLSR gives low values.

Table 3. Summary of PLSR values obtained for pH, L* and C* according to type of meat

PLSR			Male		Female	
			RFN	DFD	RFN	DFD
pH	Full	R^2_{cv}	0.310 ± 0.059	**0.743 ± 0.018**	0.052 ± 0.039	0.0436 ± 0.029
		RMSE	0.033 ± 0.021	0.013 ± 0.009	***	***
	Optimized	R^2_{cv}	**0.359 ± 0.012**	0.399 ± 0.012	**0.418 ± 0.030**	**0.412 ± 0.009**
		RMSE	0.004 ± 0.002	0.002 ± 0.002	0.002 ± 0.002	0.001 ± 0.001
L*	Full	R^2_{cv}	0.403 ± 0.077	**0.811 ± 0.032**	0.061 ± 0.044	0.048 ± 0.040
		RMSE	0.745 ± 0.513	0.450 ± 0.313	***	***
	Optimized	R^2_{cv}	**0.558 ± 0.007**	0.614 ± 0.007	**0.637 ± 0.009**	**0.536 ± 0.011**
		RMSE	0.068 ± 0.035	0.107 ± 0.064	0.043 ± 0.017	0.011 ± 0.007
C*	Full	R^2_{cv}	**0.289 ± 0.037**	**0.603 ± 0.017**	0.043 ± 0.037	0.045 ± 0.033
		RMSE	0.148± 0.070	0.019 ± 0.020	***	***
	Optimized	R^2_{cv}	0.284 ± 0.016	0.366 ± 0.008	**0.307 ± 0.028**	**0.285 ± 0.020**
		RMSE	0.016 ± 0.010	0.010 ± 0.006	0.0144 ± 0.005	0.0194 ± 0.020

***High error value; the stability of the prediction models was tested through 30 repetitions.

Fig. 18, Fig. 19 show the prediction of pH from the dielectric constant (ε') for the RFN and DFD male and female samples. For RFN samples, a pH prediction of R_{cv}^2 = 0.36 for male pigs and R_{cv}^2 = 0.43 for female pigs was obtained (Fig. 18 a - b); and for DFD samples, R_{cv}^2 = 0.40 for male pigs and R_{cv}^2= 0.42 for female pigs could be predicted (Fig. 19 a - b), different to the results reported by Andersen [8], who obtained an R^2 = 0.72 for male pigs; (Balage et al., 2015), (Furtado et al., 2019) and (Savenije et al., 2006), who recorded an R^2 in the range from 0.67 to 0.71 for male and female pigs; and (Kapper et al., 2012) and (Qiao et al., 2007), who recorded an R^2 in the range from 0.55 to 0.70 for pigs (not specifying sex). These similarities occur even though they have used different techniques to obtain spectra, such as Raman spectroscopy (RS), Fourier transformation infrared spectroscopy (FT - IR), visible reflectance spectroscopy (VIS), near-infrared spectroscopy (NIR), and hyperspectral imaging (HSI). When comparing our results of pork quality prediction with those performed on other types of meats, it can be observed that our results are similar to those by (Y. Yang et al., 2021), who obtained a pH prediction of R^2 = 0.80 in chicken, beef, pork, and turkey meat, but lower than those by (Hashem et al., 2021), who obtained a pH prediction of R^2 = 0.95 in beef meat. These similarities and/or differences are due to the above-mentioned in Fig. 2.

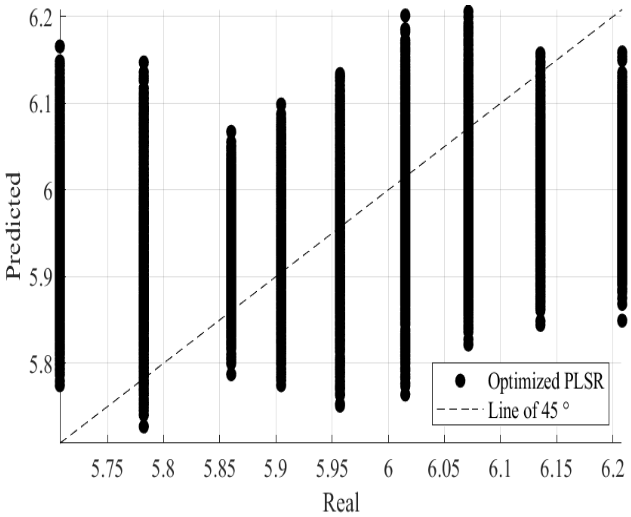

(a)

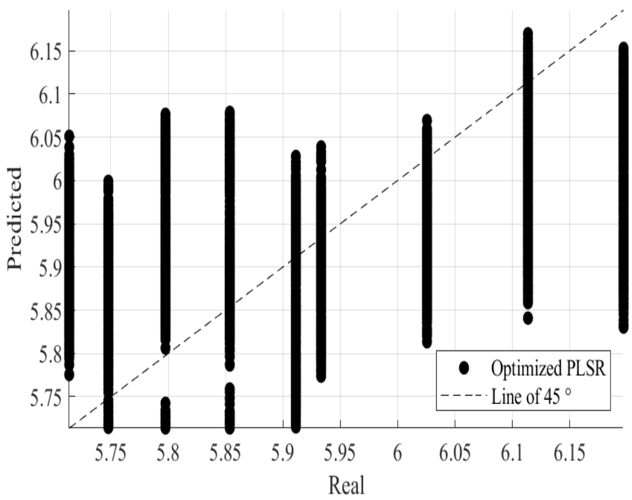

(b)

Fig. 18. Results of PLSR model prediction for pH of RFN samples: (a) R_{CV}^2 = 0.36 for male pigs and (b) R_{CV}^2 = 0.43 for female pigs.

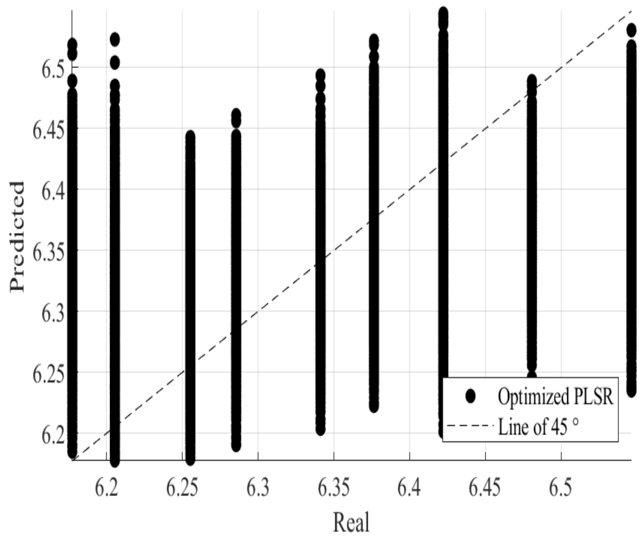

(**a**)

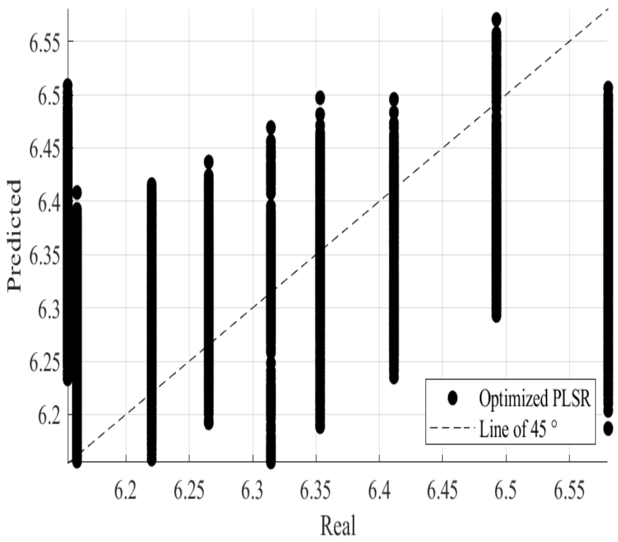

(**b**)

Fig. 19. Results of PLSR model prediction for pH of DFD samples: (a) R_{CV}^2 = 0.40 for male pigs and (b) R_{CV}^2 = 0.42 for female pigs.

Fig. 20, Fig. 21 show the color prediction (L*) from the dielectric constant e' for RFN and DFD samples for males and females, respectively. For RFN samples, an L* prediction of R_{CV}^2 = 0.57 for male pigs and R_{cv}^2 = 0.64 for female pigs was obtained; and for DFD samples, R_{CV}^2 = 0.62 for male pigs and R_{CV}^2 = 0.54 for female pigs could be predicted, similar to the reported results by Balage et al. (2015), Furtado et al. (2018) and Savenije et al. (2006), who recorded an R^2 in the range from 0.63 to 0.84 for male and female pigs through VIS/NIR spectroscopy; and those obtained by other authors (Barbin et al., 2012; Kapper et al., 2012; Qiao et al., 2007), who recorded an R_{CV}^2 in the range from 0.75 to 0.91 for pigs (not specifying sex) through FT – IR, NIR and HIS spectroscopy. When comparing our results of pork quality prediction with those performed on other types of meats, it can be observed that our results are lower than those by Yang et al. (2021), who obtained an L* prediction of R^2 = 0.93 in chicken, beef, pork, and turkey meat; and those by Hashem et al. (2021), who obtained a pH prediction of R^2 = 0.96 in beef meat, summarizing Fig. 3.

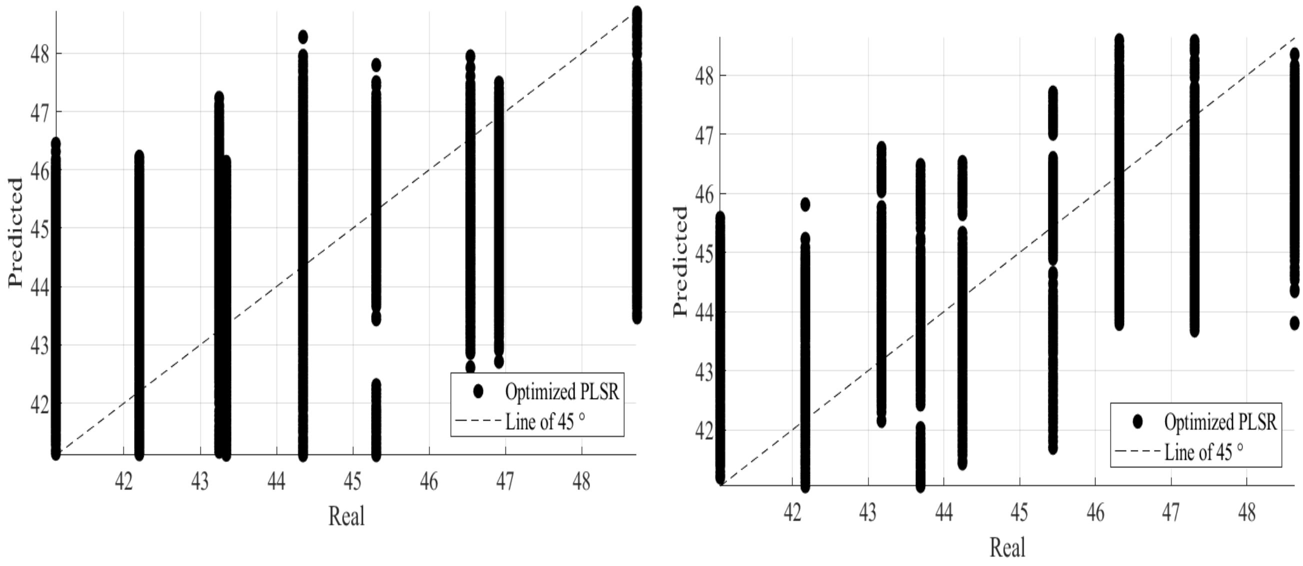

(**a**) (**b**)

Fig. 20. Results of PLSR model prediction for color (L*) of RFN samples: (a) R_{CV}^2 = 0.57 for male pigs and (b) R_{CV}^2 = 0.64 for female pigs.

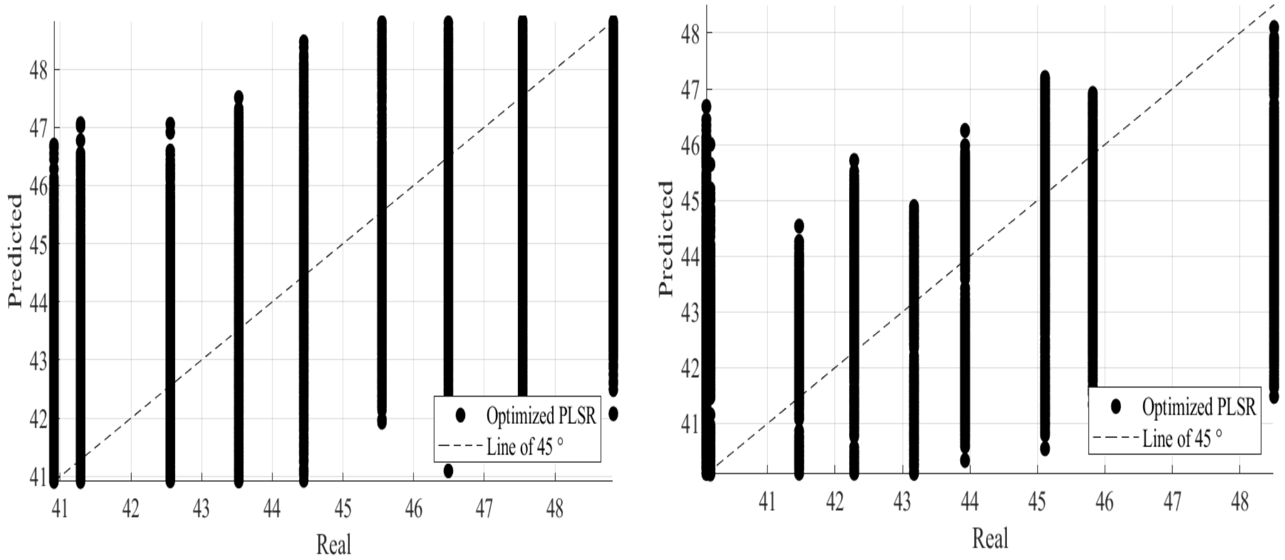

(**a**) (**b**)

Fig. 21. Results of PLSR model prediction for color (L*) of DFD samples: (a) R_{CV}^2 = 0.62 for male pigs and (b) R_{CV}^2 = 0.51 for female pigs.

Fig. 22, Fig. 23 show the color prediction (C*) from the dielectric constant e' for RFN and DFD samples for male and female pigs, respectively. For RFN samples, a C* prediction of R_{CV}^2 = 0.29 for male pigs and R_{CV}^2 = 0.32 for female pigs was obtained; and for DFD samples, it was possible to predict R_{CV}^2 = 0.35 for male pigs and R_{CV}^2 = 0.28 for female pigs, different from the results reported by Barbin et al. (2012) who recorded an R_{CV}^2 = 0.83 for pigs (no sex specified) by NIR and HIS spectroscopy, due to the reflection of surface light that the sample offers, however, for the case of prediction from dielectric properties the performance is low due to the degradation of tissue structure and reduction - oxidation of myoglobin due to the decrease in pH during the transformation from muscle to meat (Castro-Giráldez, Aristoy, et al., 2010; Castro-Giráldez, Fito, et al., 2010; Castro-Giráldez et al., 2011).

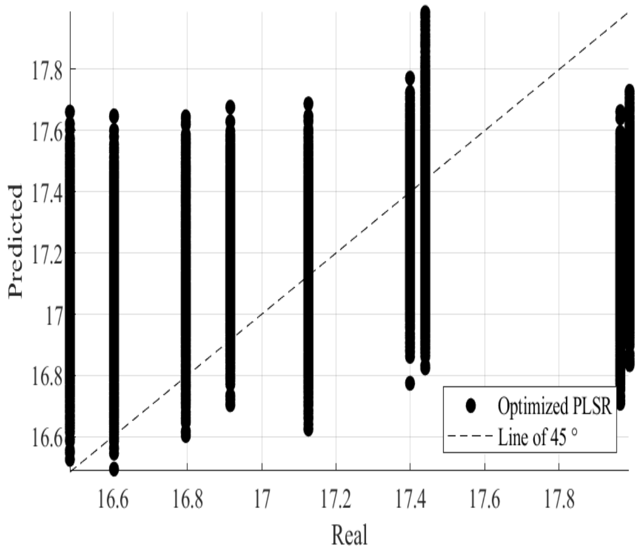

(a)

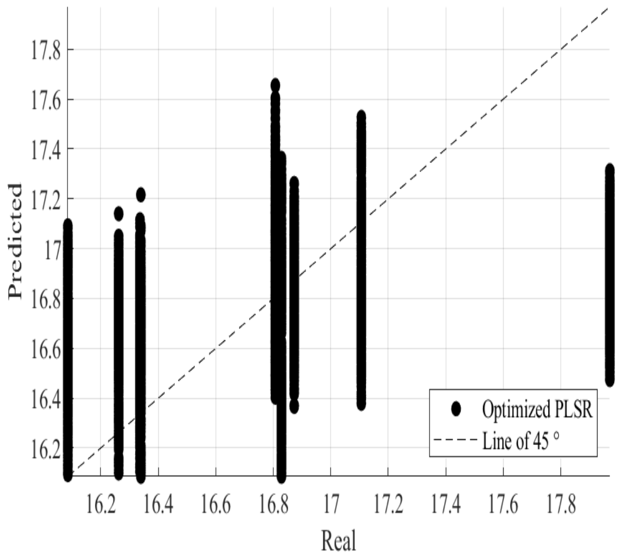

(b)

Fig. 22. Results of PLSR model prediction for color (C*) of RFN samples: (a) R_{CV}^2 = 0.29 for male pigs and (b) R_{CV}^2 = 0.32 for female pigs.

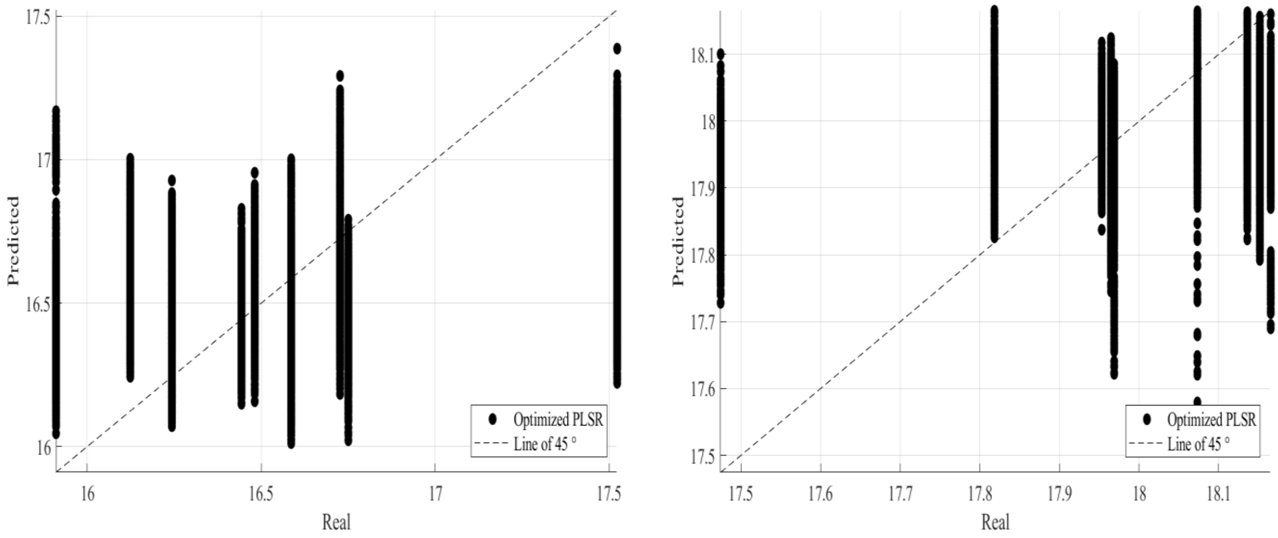

(a) (b)

Fig. 23. Results of PLSR model prediction for color (C*) of DFD samples: (a) R_{CV}^2 = 0.36 for male pigs and (b) R_{CV}^2 = 0.28 for female pigs.

The partial least squares regression (PLSR) technique has the capacity to predict significant characteristics of post-mortem pork, thereby enabling the identification of the quality grade of pork.

4. Conclusion

The transformation of muscle into meat for males and females has shown that the intensity values of the dielectric constant and loss factor decrease as the frequency increases. This allows the types of DFD and RFN meat for samples of males and females to be differentiated at 24 hpm.

Robust models were created using PLSR to predict internal quality during muscle to meat transformation. Performance was moderate for male pig meat. R^2 of 0.743 (pH), 0.811 (L*) and 0.603 (C*) for DFD meat with PLSR (full) and R^2 of 0.359 (pH), 0.558 (L*) and 0.284 (C*) for RNF meat with PLSR (optimized). R_{CV}^2 of 0.412 - 0.637 for pH, L* and C* for RFN and DFD meat from female sows with PLSR (optimized). New chemometric models are needed to improve the prediction of internal pork meat quality.

Funding

This research received funding for the payment of APC from the Vice-Rectorate of Research of the Toribio Rodríguez de Mendoza National University of Amazonas.

CRediT authorship contribution statement

Tony Chuquizuta: Project Administration, Writing – original draft, Validation, Resources, Investigation, Formal analysis, Conceptualization. Magaly Peralta: Writing – review & editing, Writing – original draft, Investigation. Sideli Medina: Writing – review & editing, Writing – original draft, Investigation: Hubert Arteaga: Validation. Supervision, Methodology. Jimy Oblitas: Validation. Supervision, Methodology. Segundo G. Chavez: Writing – review & editing, Resourses. Wilson Castro: Conceptualization, Data curation, Writin-review & editing. Marta Castro-Giraldez: Conceptualization, Data curation, Writin-review & editing. Pedro J. Fito: Validation. Supervision, Methodology.

Declaration of Competing Interest

The authors declare that they have no known competing financial interests or personal relationships that could have appeared to influence the work reported in this paper.

5. References

Andersen, P. V., Afseth, N. K., Gjerlaug-Enger, E., & Wold, J. P. (2021). Prediction of water holding capacity and pH in porcine longissimus lumborum using Raman spectroscopy. Meat Science, 172, 108357. https://doi.org/10.1016/J.MEATSCI.2020.108357

Andersen, P.V., Wold, J.P., Gjerlaug-Enger, E., Veiseth-Kent, E., 2018. Predicting post- mortem meat quality in porcine longissimus lumborum using Raman, near infrared and fluorescence spectroscopy. *Meat Sci*. 145, 94–100. https://doi.org/10.1016/j. meatsci.2018.06.016.

Balage, J. M., da Luz e Silva, S., Gomide, C. A., Bonin, M. de N., & Figueira, A. C. (2015). Predicting pork quality using Vis/NIR spectroscopy. Meat Science, 108, 37–43. https://doi.org/10.1016/J.MEATSCI.2015.04.018

Barbin, D. F., Elmasry, G., Sun, D. W., & Allen, P. (2012). Predicting quality and sensory attributes of pork using near-infrared hyperspectral imaging. Analytica Chimica Acta, 719, 30–42. https://doi.org/10.1016/J.ACA.2012.01.004

Barbin, D. F., Elmasry, G., Sun, D. W., & Allen, P. (2013). Non-destructive determination of chemical composition in intact and minced pork using near-infrared hyperspectral imaging. Food Chemistry, 138(2–3), 1162–1171. https://doi.org/10.1016/J.FOODCHEM.2012.11.120

Barbut, S., Sosnicki, A.A., Lonergan, S.M., Knapp, T., Ciobanu, D.C., Gatcliffe, L.J., Huff- Lonergan, E., Wilson, E.W., 2008. Progress in reducing the pale, soft and exudative (PSE) problem in pork and poultry meat. *Meat Sci.* 79 (1), 46–63. https://doi.org/ 10.1016/j.meatsci.2007.07.031.

Blakey, R.T., Morales-Partera, A.M., 2016. Microwave dielectric spectroscopy – a versatile methodology for online, non-destructive food analysis, monitoring and process control. *Eng. Agric. Environ. Food* 9 (3), 264–273. https://doi.org/10.1016/ j.eaef.2016.02.001.

Castro-Giraldez, M., Fito, P.J., Toldr´ a, F., Fito, P., 2010. Use of visible spectroscopy to assess colour development during ageing of fresh pork from different quality classes. *Int. J. Food Sci. Technol*. 45 (8), 1710–1716. https://doi.org/10.1111/j.1365- 2621.2010.02325.x.

Castro-Giráldez, M., Aristoy, M. C., Toldrá, F., & Fito, P. (2010). Microwave dielectric spectroscopy for the determination of pork meat quality. *Food Research International*, 43(10), 2369–2377. https://doi.org/10.1016/J.FOODRES.2010.09.003

Castro-Giráldez, M., Botella, P., Toldrá, F., Fito, P., 2010. Low-frequency dielectric spectrum to determine pork meat quality. *Innov. Food Sci. Emerg. Technol*. 11 (2), 376–386. https://doi.org/10.1016/j.ifset.2010.01.011.

Castro-Giráldez, M., Dols, L., Toldrá, F., Fito, P., 2011. Development of a dielectric spectroscopy technique for the determination of key biochemical markers of meat quality. *Food Chem*. 127 (1), 228–233. https://doi.org/10.1016/j. foodchem.2010.12.089.

Castro-Giráldez, M., Fito, P. J., & Fito, P. (2010). Application of microwaves dielectric spectroscopy for controlling pork meat (Longissimus dorsi) salting process. Journal of Food Engineering, 97(4), 484–490. https://doi.org/10.1016/j.jfoodeng.2009.11.005

Chmiel, M., Słowiñski, M., & Janakowski, S. (2014). The quality evaluation of RFN and PSE pork longissimus lumborum muscle considering its microstructure. Annals of Animal Science, 14(3), 737–747. https://doi.org/10.2478/AOAS-2014-0035

Chuquizuta, T. S., Florián, G., Castro, W. M., & Fito, P. (2017). Efecto de las condiciones de proceso en el desarrollo del color durante la elaboración de pan: uso de técnicas de análisis de imagen para evaluación del color. Revista Científica UNTRM: Ciencias Naturales e Ingeniería, 2(1), 32. https://doi.org/10.25127/UCNI.V2I1.223

Faucitano, L., Ielo, M. C., Ster, C., Lo Fiego, D. P., Methot, S., & Saucier, L. (2010). Shelf life of pork from five different quality classes. Meat Science, 84(3), 466–469. https://doi.org/10.1016/J.MEATSCI.2009.09.017

Flores, E. P., Torres, J. R. D., Del Valle, R. G., & Villarreal, A. E. (2017). Development of an automated laser induced breakdown spectroscopy system for compositional mapping of surfaces. Conference Proceedings of the Society for Experimental Mechanics Series, 2017-Janua(August), 159–164. https://doi.org/10.1007/978-3-319-28513-9_22

Furtado, E. J. G., Bridi, A. M., Barbin, D. F., Barata, C. C. P., Peres, L. M., Barbon, A. P. A. da C., Andreo, N., Giangareli, B. de L., Terto, D. K., & Batista, J. P. (2018). Prediction of pH and color in pork meat using VIS-NIR Near-infrared Spectroscopy (NIRS). Food Science and Technology, 39(1), 88–92. https://doi.org/10.1590/FST.27417

Geesink, G. H., Schreutelkamp, F. H., Frankhuizen, R., Vedder, H. W., Faber, N. M., Kranen, R. W., & Gerritzen, M. A. (2003). Prediction of pork quality attributes from near infrared reflectance spectra. Meat Science, 65(1), 661–668. https://doi.org/10.1016/S0309-1740(02)00269-3

Gispert, M., Faucitano, L., Oliver, M.A., Guardia, M.D., Coll, C., Siggens, K., Harvey, K., Diestre, A., 2000. A survey of pre-slaughter conditions, halothane gene frequency, and carcass and meat quality in five spanish pig commercial abattoirs. *Meat Sci*. 55 (1), 97–106. https://doi.org/10.1016/S0309-1740(99)00130-8.

Hashem, M., Tule, S., Khan, M., Rahman, M., Azad, M., & Ali, M. (2021). Prediction of beef quality traits through mini NIR spectrophotometer and multivariate analyses. Meat Research, 1(1). https://doi.org/10.55002/MR.1.1.6

Huff-Lonergan, E., 2010. Chemistry and biochemistry of meat. In Handbook of Meat Processing. Wiley, pp. 3–24. https://doi.org/10.1002/9780813820897.ch1.

Jerez-Timaure, N., Trompiz, J., Mendoza, E., Arenas de Moreno, L., Jerez-Timaure, N., Trompiz, J., Mendoza, E., & Arenas de Moreno, L. (2020). Evaluación del método de aturdimiento y tiempo de reposo corto sobre las características de la canal y la carne de cerdo. Revista de Investigaciones Veterinarias Del Perú, 31(3). https://doi.org/10.15381/RIVEP.V31I3.18722

Kapper, C., Klont, R. E., Verdonk, J. M. A. J., Williams, P. C., & Urlings, H. A. P. (2012). Prediction of pork quality with near infrared spectroscopy (NIRS) 2. Feasibility and robustness of NIRS measurements under production plant conditions. Meat Science, 91(3), 300–305. https://doi.org/10.1016/J.MEATSCI.2012.02.006

Kent, M., Peymann, A., Gabriel, C., & Knight, A. (2002). Determination of added water in pork products using microwave dielectric spectroscopy. Food Control, 13(3), 143–149. https://doi.org/10.1016/S0956-7135(01)00066-4

Khan, M., Khan, M. I., Sahar, A., & Jamil, A. (2020). Predicting authenticity and physicochemical characteristics of meat through FT-IR spectroscopy coupled with multivariate analysis. Pakistan Journal of Agricultural Sciences, 57(4), 1141–1147. https://doi.org/10.21162/PAKJAS/20.9352

Liu, R., Wu, G. Y., Li, K. Y., Ge, Q. F., Wu, M. G., Yu, H., Wu, S. L., & Bao, W. Bin. (2021). Comparative study on pale, soft and exudative (Pse) and red, firm and non-exudative (rfn) pork: Protein changes during aging and the differential protein expression of the myofibrillar fraction at 1 h postmortem. Foods, 10(4), 733. https://doi.org/10.3390/FOODS10040733/S1

Maganhini, M. B., Mariano, B., Soares, A. L., Guarnieri, P. D., Shimokomaki, M., & Ida, E. I. (2007). Carnes PSE (Pale, Soft, Exudative) e DFD (Dark, Firm, Dry) em lombo suíno numa linha de abate industrial. Food Science and Technology, 27(SUPPL.1), 69–72. https://doi.org/10.1590/S0101-20612007000500012

Matarneh, S.K., Scheffler, T.L., Gerrard, D.E., 2023. The conversion of muscle to meat. *In Lawrie's Meat Science*. Elsevier, pp. 159–194. https://doi.org/10.1016/B978-0-323- 85408-5.00010-8.

MIDAGRI. (2020, January). Panorama y perspectivas de la producci´on de carne de cerdo en el Perú. Http://Hdl.Handle.Net/20.500.13036/721.

Novgorodska, N., Verbytskyi, S., 2023. Theoretical basics and technological characteristics of pork with typical syndromes. *Agric. Sci*. (2), 60–65. https://doi. org/10.55505/sa.2022.2.07.

Paredi, G., Raboni, S., Bendixen, E., de Almeida, A. M., & Mozzarelli, A. (2012). "Muscle to meat" molecular events and technological transformations: The proteomics insight. Journal of Proteomics, 75(14), 4275–4289. https://doi.org/10.1016/J.JPROT.2012.04.011

Qiao, J., Wang, N., Ngadi, M. O., Gunenc, A., Monroy, M., Gariépy, C., & Prasher, S. O. (2007). Prediction of drip-loss, pH, and color for pork using a hyperspectral imaging technique. Meat Science, 76(1), 1–8. https://doi.org/10.1016/J.MEATSCI.2006.06.031

Savenije, B., Geesink, G.H., Van Der Palen, J.G.P., Hemke, G., Hopkins, D., Ouali, A., 2006. Prediction of pork quality using visible/near-infrared reflectance spectroscopy. *Meat Sci*. 73 (1), 181–184. https://doi.org/10.1016/J. MEATSCI.2005.11.006.

Torres Filho, R., de, A., Silva, V.M., da, Rodrigues, L.M., Fontes, P.R., Ramos, A., de, L.S., Ramos, E.M., 2018. Classification of pork quality by hierarchical cluster analysis. Br. Food J. 120 (7), 1446–1456. https://doi.org/10.1108/BFJ-10-2017-0589.

Traffano-Schiffo, M., Castro-Giraldez, M., Colom, R., Fito, P., 2017. Development of a spectrophotometric system to detect White striping physiopathy in whole chicken carcasses. *Sensors* 17 (5), 1024. https://doi.org/10.3390/s17051024.

Traffano-Schiffo, M. V., Castro-Giraldez, M., Colom, R. J., & Fito, P. J. (2018). Innovative photonic system in radiofrequency and microwave range to determine chicken meat quality. Journal of Food Engineering, 239, 1–7. https://doi.org/10.1016/J.JFOODENG.2018.06.029

Traffano-Schiffo, M. V., Castro-Giraldez, M., Colom, R. J., Talens, P., & Fito, P. J. (2021). New methodology to analyze the dielectric properties in radiofrequency and microwave ranges in chicken meat during postmortem time. Journal of Food Engineering, 292, 110350. https://doi.org/10.1016/J.JFOODENG.2020.110350

Traffano-Schiffo, M.V., Castro-Giraldez, M., Herrero, V., Colom, R.J., Fito, P.J., 2018. Development of a non-destructive detection system of deep pectoral myopathy in poultry by dielectric spectroscopy. *J. Food Eng*. 237, 137–145. https://doi.org/ 10.1016/j.jfoodeng.2018.05.023.

Trevisan, L., Brum, J.S., 2020. Incidence of pale, soft and exudative (PSE) pork meat in reason of extrinsic stress factors. An. Da Acad. Bras. De. Ciencias 92 (3). https://doi. org/10.1590/0001-3765202020190086.

Yang, H.-S., Hwang, Y.-H., Joo, S.-T., Park, G.-B., 2009. The physicochemical and microbiological characteristics of pork jerky in comparison to beef jerky. Meat Sci. 82 (3), 289–294. https://doi.org/10.1016/j.meatsci.2009.01.029.

Yang, Y., Wang, W., Zhuang, H., Yoon, S. C., & Jiang, H. (2021). Prediction of quality traits and grades of intact chicken breast fillets by hyperspectral imaging. British Poultry Science, 62(1), 46–52. https://doi.org/10.1080/00071668.2020.1817326

Zhao, M., Downey, G., & O'Donnell, C. P. (2016). Exploration of microwave dielectric and near infrared spectroscopy with multivariate data analysis for fat content determination in ground beef. Food Control, 68, 260–270. https://doi.org/10.1016/J.FOODCONT.2016.03.031

4.6. Determinación de la cinética de hidratación de frejoles pinto: una aplicación de imágenes hiperespectrales.

ELSEVIER

Measurement: Food
Volume 14, June 2024, 100161

Determination of hydration kinetic of pinto beans: A hyperspectral images application

Tony Chuquizuta [a d], Segundo G. Chavez [b], Alberto Claudio Miano [c], Marta Castro-Giraldez [d], Pedro J. Fito [d], Hubert Arteaga [e], Wilson Castro [f]

Show more

Add to Mendeley Share Cite

https://doi.org/10.1016/j.meafoo.2024.100161 Get rights and content

Condición	DOI
Publicado (25 de marzo, 2024)	**https://doi.org/10.1016/j.meafoo.2024.100161**

DETERMINATION OF HYDRATION KINETIC OF PINTO BEANS: A HYPERSPECTRAL IMAGES APPLICATION

Tony Chuquizuta [a,d]*, Segundo G. Chavez [b], Alberto Claudio Miano [c], Marta Castro-Giraldez [d], Pedro J. Fito [d], Hubert Arteaga [e], Wilson Castro [f]

[a] Instituto de Investigación del Mejoramiento Productivo, Universidad Nacional Autónoma de Chota, Chota 06120, Perú

[b] Facultad de Ciencias Agrarias, Universidad Nacional Toribio Rodríguez de Mendoza de Amazonas, Chachapoyas 01001, Perú

[c] Dirección de Investigación, Innovación y Responsabilidad Social, Universidad privada del Norte (UPN), Peru

[d] Instituto Universitario de Ingeniería de Alimentos FoodUPV, Universitat Politècnica de València, Camino de Vera s/n, Valencia 46022, Spain

[e] Instituto de Ciencia y Tecnología de Alimentos (ICTA), Universidad Nacional de Jaén, Jaén 06800, Perú

[f] Facultad de Ingeniería de Industrias Alimentarias y Biotecnología, Universidad Nacional de Frontera, Sullana 20100, Perú

* Correspondence: tchuquizuta@unach.edu.pe

Abstract

Hydration is a typical operation applied to legumes before cooking, reducing time and the associated energy cost. To monitor the process, mass balance method is the most used methodology, despite this method is destructive, repetitive, and time-consuming. For that reason. hyperspectral techniques are presented as an alternative for assessing the hydration process since it is a noninvasive method. Therefore, the objective of this work was to evaluate the technique of hyperspectral imaging for studying the hydration kinetics of pinto beans. For this purpose, a sample of pinto beans was hydrated in distilled water, determining moisture content during the process and taking hyperspectral images by reflectance mode, in the range 400 to 800 nm until constant mass. The moisture content was modelled using Peleg and a sigmoidal model. Next, the images were pre-treated and the median spectral profile for each bean was obtained. Then, a regression model was fitted, using the wavelength that maximized the coefficient of determination (R^2) and minimized the root mean square error ($RMSE$). The results show that Peleg model fit experimental data with R^2 in the range of 0.974 to 0.989 while sigmoidal model of 0.997 to 0.999. On other hand, mean spectral profiles at 632 nm and sigmoidal model give the higher metrics 0.997 and 38.3 for R^2 and RMSE respectively. The results showed that hyperspectral imaging in reflectance mode is a tool capable of measuring the hydration level of beans with higher performance at 632 nm, with a determination coefficient R^2 higher than 0.98.

Keywords: Hyperspectral image, reflectance, pinto beans, hydration kinetics

Highlights

- Hyperspectral images as a rapid and non-invasive tool for monitoring of the hydration process.
- Devolvement of an algorithm for determination of relevant wavelength
- The reflectance values as a new physical variable for modeling hydration kinetics.

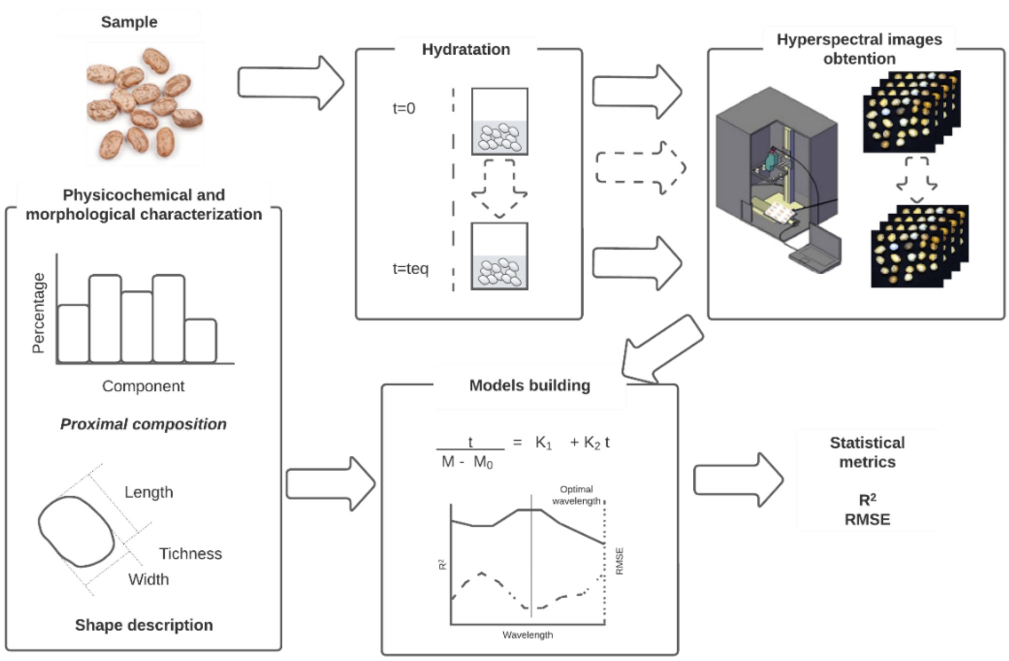

Figure 1. Summary graph of bean hydration kinetics by HSI.

1. Introduction

Legume grains are a rich source of protein, fiber, and iron, whose consumption has increased in the last decades, mainly due to their health benefits, long shelf life, and easy transport (Sánchez-Arteaga, Urías-Silvas, Espinosa-Andrews and García-Márquez, 2015). Although, before its consumption, it is necessary to increase their moisture by hydration before cooking, malting, and germination for tendering tissues, activating enzymes, and/or eliminating antinutritional components (Abu-Ghannam, 1998; Lovato, Kowaleski, Silva and Heldt, 2017). Consequently, it is important to perform the hydration process and its kinetics.

The hydration kinetics of legume grains is characterized by the determination of water absorption, equilibrium moisture, and the time required for grain softening (Miano and Augusto, 2018). In this sense, knowing the kinetics parameters of hydration allows evaluating the use of new approaches to improve the process optimizing factors such as cooking time, starch gelatinization, protein denaturation, and release of other compounds (Chapwanya and Misra, 2015).

The modeling of hydration kinetics of legume grains uses phenomenological, semi-empiric, and empiric equations such as Peleg and Kaptso's models, the most common equations for moisture modeling (Miano, Saldaña, Campestrini, Chiorato and Augusto, 2018). These models require performing a controlled-hydration process where the mass of the grains should be recorded during the soaking time, for the next calculus. Indeed, this procedure must continue until equilibrium between moisture inside grains and the media (Garvín, Augusto, Ibarz and Ibarz, 2019; Miano, García and Augusto, 2015). However, this method can be disadvantageous in industry, where quick results are desirable. Therefore, other methods, fast and nondestructive, should be studied to obtain the moisture content of grains during the hydration process for performing kinetics studies.

An interesting approach is hyperspectral system imaging (HSI) to monitor the hydration process. HSI is a nondestructive technique that has multiple applications, for instance, the assessment and prediction of moisture content in foods, which was recently studied. Yang, He, Lu, Ren and Wang (2017) applied HSI to predict moisture content in cooked beef, and Ma, Sun and Pu (2017) applied this technique for predicting moisture content in pork at diverse methods of drying. On the other hand, Caponigro, Marini and Gowen (2018) combined NIR-HSI for assessing moisture content on hydrogels composed of agar, starch, gelatin, and blended.

In fact, HSI is a tool with high potential for use in agriculture and quality control of agri-food products; with a wide range of applications from satellite images to macroscopic and cellular levels (Dale et al., 2013; Wang et al., 2023). Its application has been tested in obtaining crop field information, even considering environmental variables for decision making up to the detection of ingredients used in processed food formulations (Zhu et al., 2020; Benelli et al., 2020). More recent work explores applications combined with other tools such as visible/near-infrared spectrum imaging (Xu et al., 2023) and artificial intelligence (An et al., 2023). Taghinezehad et al. (2023) mention that HSI can be a powerful technique for controlling food drying processes.

Consequently, the main objective of this study was to evaluate the use of HSI for moisture modeling in legumes grain, which could allow us to predict the degree of hydration of pinto beans.

2. Materials and methods

The experimental procedure is shown in Figure 2. Likewise, each step of the flowchart is explained in the following paragraphs.

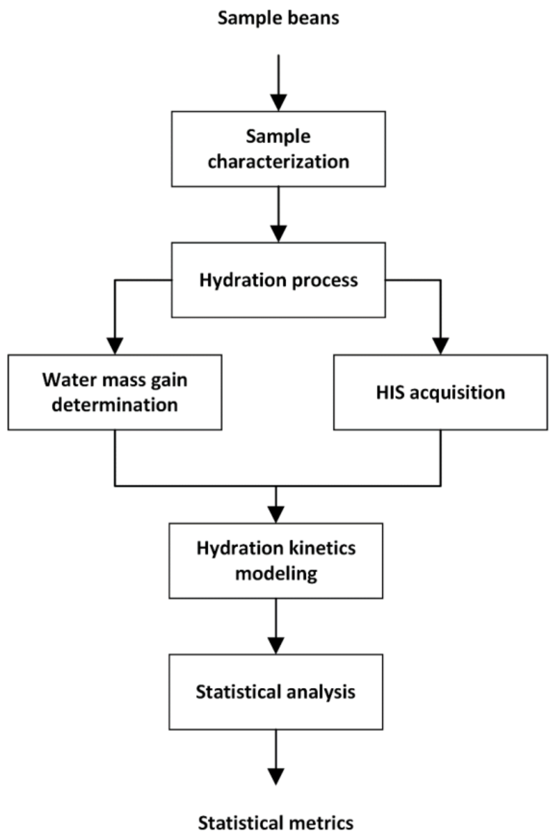

Figure 2. Experimental procedure in hydration process of beans.

2.1. Sample beans.

For the present study, 3 kg of common beans (*Phaseolus vulgaris*) of the "*Pinto*" variety were purchased from the local market in Chachapoyas, Peru. First, the beans were selected according to their homogeneity in size, color, and weight, discarding beans that presented mechanical and biological damage. Next, the samples were stored in a clean and dry plastic container at 15 ºC for two weeks to get homogeneous moisture in the beans until processing.

2.2. Sample characterization.

Samples (250 grains) of "Pinto" beans (*Phaseolus vulgaris*) were characterized by obtaining mean values for width (W), length (L), and thickness (T) using a vernier caliper (Stanley co, standard). Using these values surface (S), volume (V), and specific surface (Sps) were calculated using the Equation 1 to 3 (Miano and Augusto, 2018).

$$S \approx \pi * \sqrt[a]{\frac{(L*W)^a + (L*T)^a + (T*W)^a}{3}} \wedge a = 1.6075 \quad (1)$$

$$V = \frac{\pi * L * W * T}{6} \quad (2)$$

$$S_{sp} = \frac{S}{V} \quad (3)$$

In addition, moisture, protein, fat, and ash were determined according to AOAC (2010) in a similar way to the works of Miano and Augusto (2018), and Kaptso, Njintang, Komnek, Hounhouigan, Scher and Mbofung (2008).

2.3. Hydration process

For the hydration process, 15g (19 to 20 grains approximately per each repetition) of the sample were placed in an Erlenmeyer glass of 500 mL which contained double-distilled water at 20 ºC, controlled by constant temperature water bath (Heating Bath B-305, Buchi). The mass of each sample was controlled every 15 minutes during the first two hours and every 30 minutes until it reached equilibrium. Each sampling time, the beans were drained, dried superficially, and weighed immediately, as described by Oroian (2017), and Ulloa, Rosas-Ulloa, Ramírez-Ramírez and Ulloa-Rangel (2016).

The moisture content at each time step (M_t) was calculated by mass balance, considering the initial sample mass (m_0), the moisture (M_0), and the obtained mass at each time step. Likewise, researchers like Miano et al. (2018), Ulloa, Enríquez López, Contreras Morales, Rosas Ulloa, Ramírez Ramírez and Ulloa Rangel (2015) and Oliveira, Colnaghi, da Silva, Gouvêa, Vieira and Augusto (2013) despise the transfer of soluble solids between beans grain and water for considered not significant in the mass balance. This process was realized in triplicate.

2.4. Hyperspectral images acquisition

Previous to obtaining hyperspectral image of the grains, the parameters of functioning of the camera were programmed (Pika XC; Resonon Inc. Montana, USA), as follow: speed of sample platform = 0.5 cm/s, diaphragm aperture = 6.4 mm and distance to surface = 28.3 cm (Vásquez, Magán, Oblitas, Chuquizuta, Avila-George and Castro, 2018). After that, calibration procedure was conducted using white and black references as described in the investigation performed by Castro, Prieto, Guerra, Chuquizuta, Medina, Acevedo-Juárez and Avila-George (2018) and Vásquez et al. (2018). Subsequently, hyperspectral images of the grains of beans were acquired, being able to obtain fifty-seven images of fifty-nine grains in each hydration time by SpectrononPro 2.62 software (Resonon Inc. Montana, USA) (Castro et al., 2018). The system was operated in reflectance mode with line-by-line scanning in the 400-800 nm range (see Figure 3).

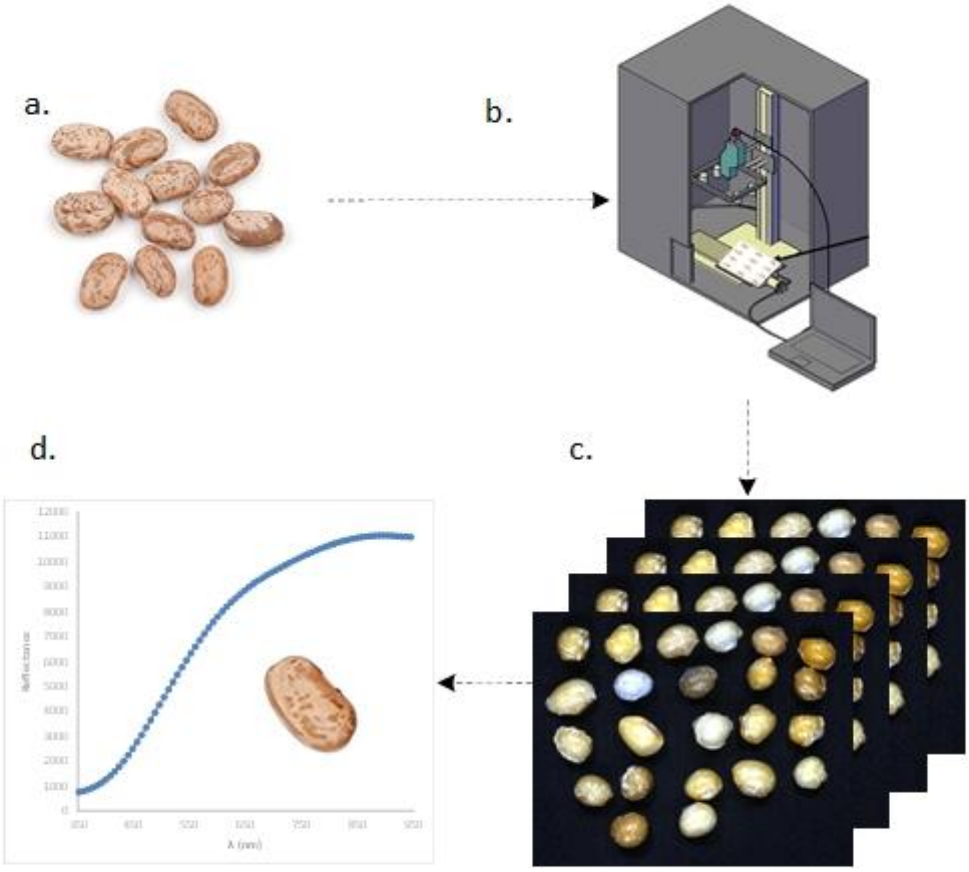

Figure 3. Hyperspectral imaging system: (a) samples, (b) camera HSI, (c) imagen spectral and (d) spectral mean.

For the extraction of the average spectral information (reflectance) of each bean's hyperspectral image throughout the hydration process, a guide created in Matlab by Castro et al. (2018) was used, obtaining a total of 1121 spectra. Finally, the mean spectra were pre-treated using a second-order Savitsky-Golay filter with 11 frames to eliminate any noise generated when images were obtained.

2.5. Modeling hydration kinetic and HIS

2.5.1. Modelling hydration kinetic

The *Peleg* model (Peleg, 1988) and a *sigmoidal* model (Kaptso et al., 2008) were used for modeling the hydration kinetics of the pinto bean. For this, the moisture contents (% dry basis) were tabulated against the hydration time (min). The Peleg model describes hydration behavior with downward concave shape through its parameters with physical explanation (Equation 4) and the sigmoidal model (semi-empiric) describes hydration kinetics behavior with a sigmoid shape, characterized by beans with low-permeability-to-water seed coat (Equation 5).

$$M_t = M_0 + \frac{t}{k_1+(k_2*t)} \tag{4}$$

$$M_t = \frac{M_{eq}}{1+\exp[-k_k*(t*\tau)]} \tag{5}$$

Where, M_0 is the initial moisture content in the dried base (% d.b.), k_1 is the hydration rate (min· (% d.b.$^{-1}$)) and k_2 is the parameter related to the equilibrium moisture content (% d.b.$^{-1}$), k_k related to hydration rate (min^{-1}), τ time to achieve the inflection point of the hydration curve (min) and M_{eq} which is the equilibrium moisture content (% d.b.).

2.5.2. Modelling hydration by reflectance

Modeling of hydration by reflectance was done using HSI technology. Previously, the reflectance and moisture content values of the beans “Pinto” were ordered and saved in *.xlsx format during each time of hydration. A sequence was implemented in MatLab 2021b to select an optimal wavelength from the maximization of determination coefficient (R^2) and minimization of mean square root deviation (RMSE) by linear regression between moisture content and reflectance (Mendoza, Wiesinger, Lu, Nchimbi-Msolla, Miklas, Kelly and Cichy, 2018). Finally, the hydration kinetics was modeled using the Peleg and Sigmoidal models using the moisture content and reflectance value at optimized wavelength instead of moisture content as the dependent variable, both in relation to hydration time (min). The functions carried out in Matlab was uploaded to Matlab files interchange web in the following link “https://es.mathworks.com/matlabcentral/fileexchange/158986-algorithm-for-modelling-pinto-bean-hydration-kinetics”.

2.5.3. Fitting and statistical analysis

The Levenberg–Marquardt algorithm implemented in MatLab 2021b - MathWorks software was used to fit data in the Peleg and Sigmoidal models (see Figure 4). For statistical analysis, the regression value R^2, the values of the root mean square error

($RMSE$), with a confidence level of 95% were evaluated using the Equation 6 and 7 (Miano et al., 2015; Miano and Augusto, 2018; Miano et al., 2018).

$$R^2 = \frac{\sum_{i=1}^{n}(\hat{y}_i - y_i)^2}{\sum_{i=1}^{n}(\hat{y}_i - y_t)^2} \tag{6}$$

$$RMSE = \sqrt{\frac{1}{n}\sum_{i=1}^{n}(y_i - \hat{y}_i)^2} \tag{7}$$

Where, $\hat{y_i}$ is the experimental value, y_i is the predicted value and n is the number of observations.

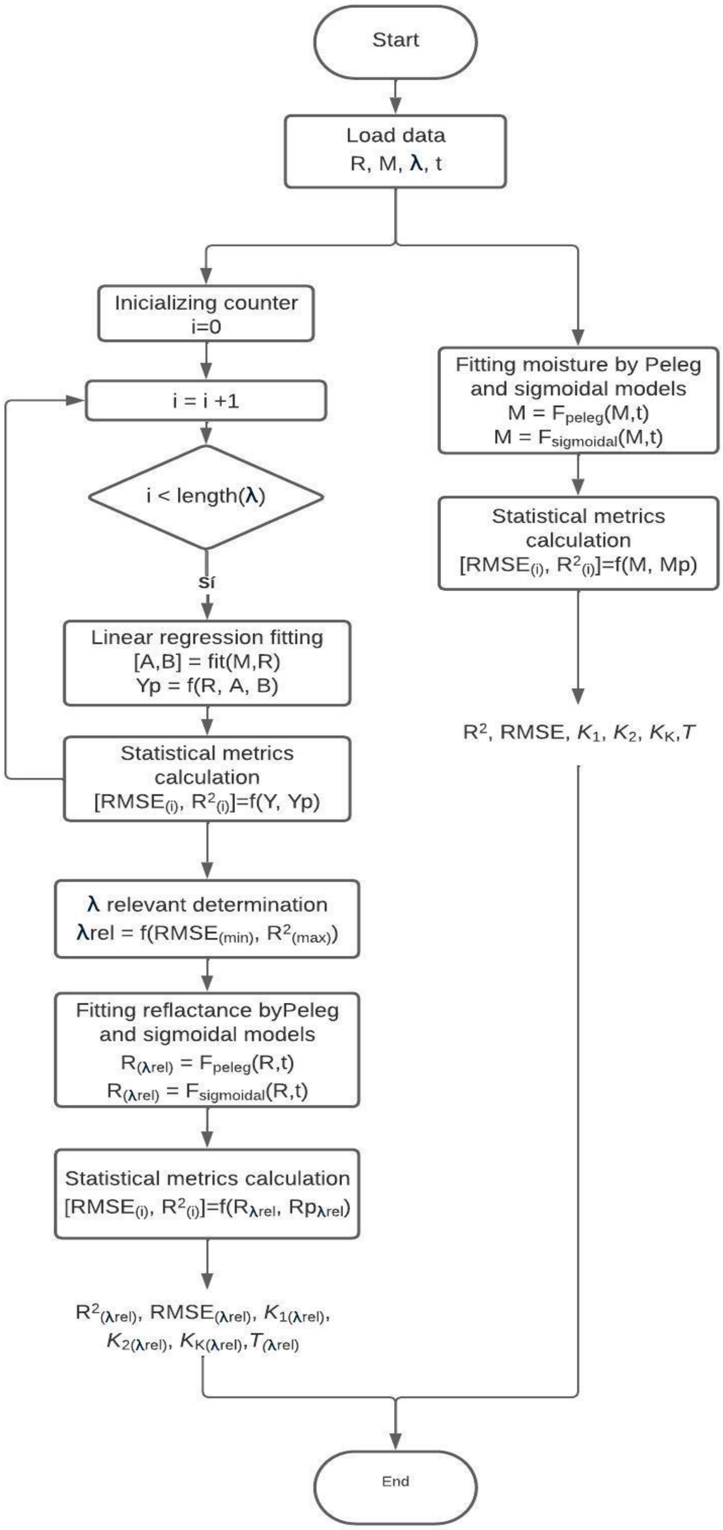

Figure 4. Pseudocode for wavelength selection algorithm

3. Results and discussion

3.1. Physicochemical analysis during fermentation

Table 1 shows the characteristic dimensions of beans and their chemical composition. The results of the dimensions are slightly different to other varieties such as Azufrado, Peruano bola, Mayacoba, and Canario, as reported by Ulloa et al. (2015) even for the same variety presented slight differences as reported by Ulloa et al. (2016). While chemical composition in moisture, protein, lipid, and ash are similar to those reported by Ovando-Martínez, Osorio-Díaz, Whitney, Bello-Pérez and Simsek (2011), Anino, Onyango, Imathiu, Maina and Onyangore (2019), and SánchezArteaga et al. (2015).

Table 1. The physicochemical values of the bean sample.

Physical properties		Chemical composition	
Thickness-T (mm)	8.49 ± 0.93	Moisture (% d.b)	13.42 ± 0.02
Width-W (mm)	9.64 ± 0.85	Protein (%)	22.25 ± 0.03
Length-L (mm)	12.40 ± 1.09	Fat (%)	1.47 ± 0.05
Surface-S (mm^3)	580.10 ± 91.19	Ash (%)	5.85 ± 0.07
Volume-V (mm^3)	540.02 ± 128.50		
Specific surface-Sps (mm^{-1})	1.10 ± 0.11		

3.2. Spectral profiles

Figure 5 shows the spectral profile of the pinto beans for different times of hydration from 0 to 1200 s, evidencing a sigmoidal shape with a higher slope in the range of 400 to 800 nm. Likewise, an upward shift of the spectrum is shown when hydration time increases. Despite being a different food matrix in beef cuts, when it was dehydrated, the spectrum has a downward shift by increasing the dehydration time Ren and Sun (2022), which shows that when a sample has higher water content, the spectrum in terms of reflectance presents higher values, evidencing a causal relationship between these two variables.

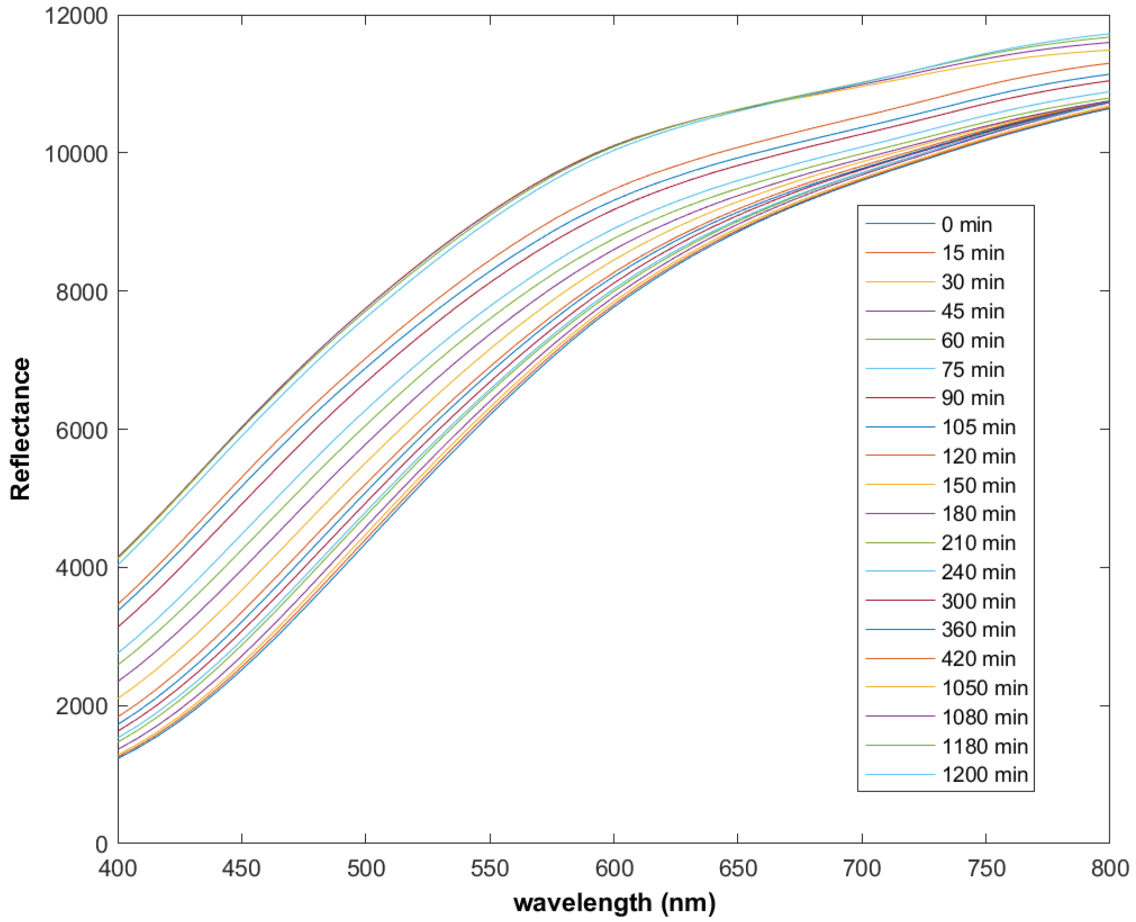

Figure 5. Mean spectral profile at different soaking times.

3.3. Hydration kinetics modeling

The hydration kinetics of Pinto beans were suitably fitted to both Peleg and Sigmoidal Model. Table 2, shows that both models present high values of R^2, being higher when sigmoidal model was used. This evidences that the pinto bean has a sigmoidal behavior of hydration kinetics, which is commonly in legume grains. In fact, legume grains such as pinto beans mostly present sigmoidal behavior due to the seed coat's impermeability to water (Miano and Augusto, 2018). This causes water to get into through the micropyle and hilum (Korban, Coyne and Weihing, 1981), and slowly hydrating the grains from inside. As the seed coat gets hydrated from the inside, its permeability to water increases, letting water enter through the seed coat and accelerating hydration (Miano et al., 2018). From this point, hydration continues until it reaches equilibrium.

Table 2. Fitting parameters from Peleg model and Sigmoidal model for moisture content and reflectance.

Peleg Model					
Parameters	k_1	k_2	-	R^2	$RSME$
Moisture	4.2856 ± 0.0925	0.0058 ± 0.0003	-	0.974 ± 0.0078	5.94 ± 1.0191
Reflectance	0.2101 ± 0.0145	$3.0x10^{-4}$ ± $1.0x10^{-4}$	-	0.988 ± 0.008	76.0 ± 15.6930
Sigmoidal Model					
Parameters	τ	k_k	M_{eq}	R^2	$RSME$
Moisture	241.5861 ± 41.0452	0.0081± *	117.5608± 7.6253	0.999± 0.1727	1.18 ± *
Reflectance	-46.818 ± 39.9971	0.003 ± 0.0005	$1.0555x10^{4}$ ± 158.1031	0.997 ± 0.0025	40.2 ± 7.3078

There are three published works where the pinto bean was used. One of them, used the Peleg model to fit hydration kinetics, reporting values of 1.56 for k_1 and 0.0071 for k_2 (Zanella-Díaz, Müjica-Paz, Soto-Caballero, Welti-Chanes and Valdez-Fragoso, 2014). These parameters are different from the used pinto beans in the present work, especially for k_1, which is related to the reciprocal of hydration rate. Besides that, thew work of Carvalho et. al (2022) also reported pinto beans hydration kinetics with downward concave shape behavior, using Peleg model to fit the data. Nevertheless, they reported the data at 30, 40 and 50°C, which can also affect to the hydration kinetics behavior since higher soaking temperatures can reduce lag phase of sigmoidal shape behavior (Kaptso et al., 2008).

In other work, pinto bean presented sigmoidal behavior with a long lag phase (Kinyanjui, Njoroge, Makokha, Christiaens, Ndaka and Hendrickx, 2015); however, without fitting data to a model. All these works and the current work show different hydration kinetics for pinto beans. This corroborates the fact that despite the same variety of beans, hydration kinetics can be very different. This is due to the intrinsic properties of the grains as initial moisture content and/or composition differences (Miano et al., 2018) caused by different growth conditions and storage conditions (Kinyanjui et al., 2015). This result suggests that hyperspectral imaging for moisture monitoring should be evaluated for beans with different storage and growth conditions.

3.4. Hyperspectral analysis for hydration kinetics evaluation

First, the optimum wavelength which better detects moisture of pinto beans was searched. In Figure 6, the relationship between the R^2 and the RMSE of the correlation between moisture content and reflectance is presented. The optimum wavelength was 632 nm, which obtained a maximum determination coefficient (R^2), and minimum root means square error (RMSE). This indicates that 632 nm is the most suitable wavelength to predict the moisture content of pinto beans. In other words, by taking images using 632 nm of wavelength, moisture content can be predicted without using a destructive method. Caponigro et al. (2018) reported that samples with very high moisture content absorb a large quantity of NIR light resulting in signal saturation above 1384 nm, while samples with very low moisture content absorb only a small quantity of light, resulting in a low signal.

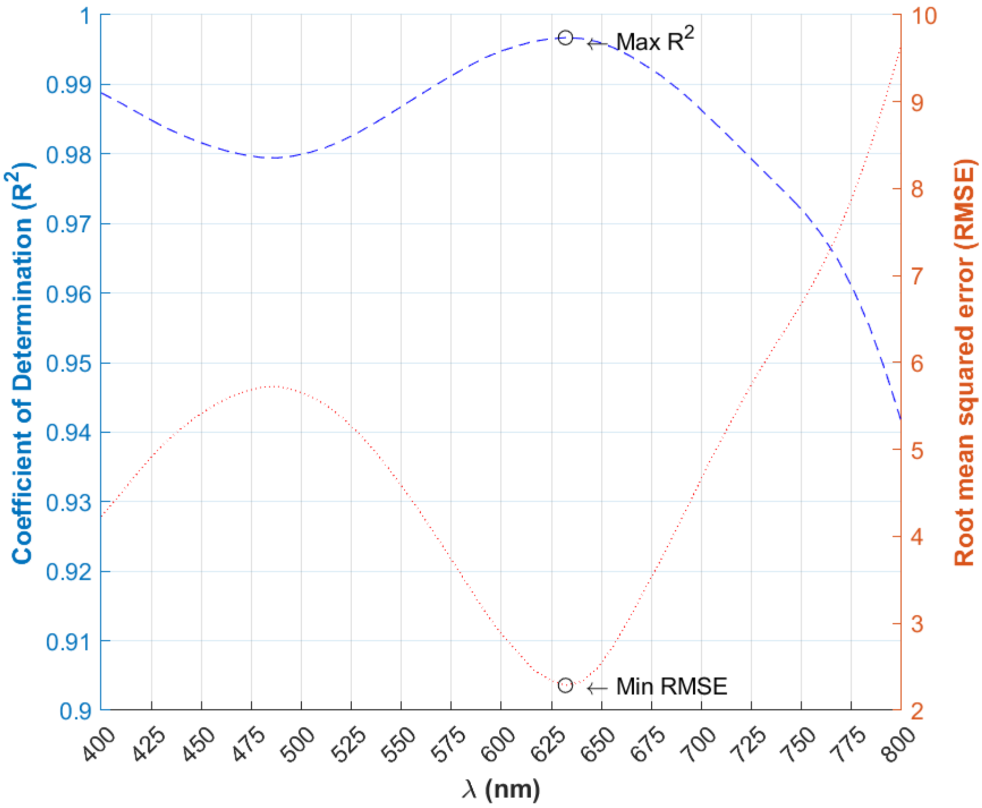

Figure 6. Relevant wavelength selection by mean of $RMSE$ and R^2

The relationship between the reflectance and the moisture content of the bean grains during hydration was R^2 = 0.9966, evidencing the existence of a similarity between both physical parameters. This value is higher than the one reported by Mendoza et al. (2018) who obtained 0.789 as the determination coefficient for the prediction of water uptake and reflectance of other common beans. This low prediction value is due to using a linear fit model such as PLSR. In contrast, Ren and Sun (2022), who determined a high relationship between water and reflectance values of a R^2 = 0.92 in the range of 1000 to 1500 nm in rehydrated samples of meat slices, due to the excitation of $O - H$ bonds that particularly the water molecule counts.

Using reflectance and the optimum wavelength, hydration kinetics can be plotted and described. Figure 7 shows the hydration kinetics evaluated using the moisture content behavior against hydration time and using reflectance of beans against hydration time. Further, Figure 7 demonstrated the sigmoidal behavior of hydration kinetics, corroborating the best-fitting goodness of the sigmoidal model (Table 1). Regarding the use of reflectance, hydration kinetics was described almost the same as using moisture content no matter which model was considered, evidencing a high correlation between moisture and reflectance.

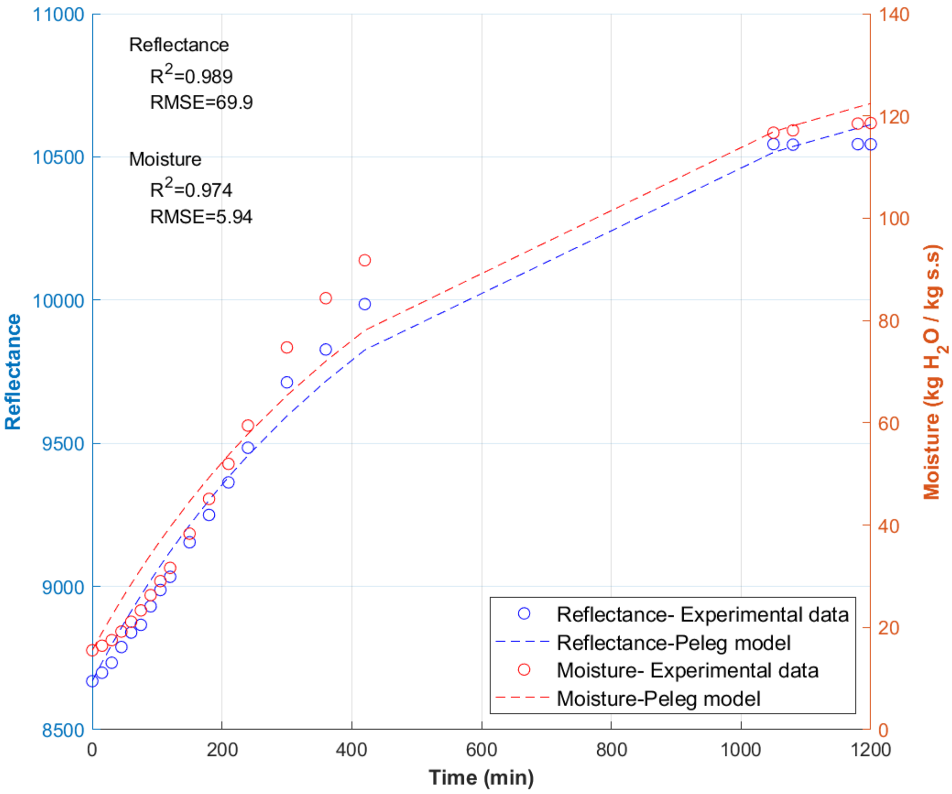

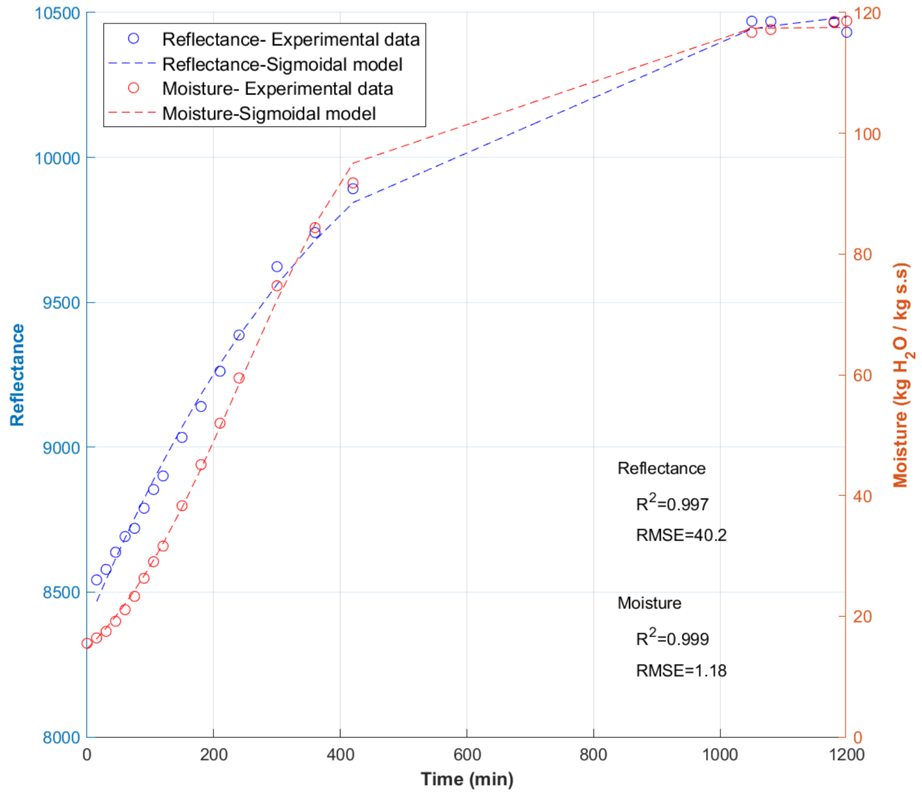

Figure 7. Hydration kinetics and reflectance models of Pinto beans. The dots represent the mean of data and discontinuous lines represent the model fitting

4. Conclusions

The hyperspectral imaging technique was used to monitor the hydration of pinto beans. Mean reflectance spectra were obtained in the 400 to 800 nm range. The best relationship between moisture content and reflectance value was identified at 632 nm, with a goodness of fit of $R^2 = 0.9966$ and RMSE = 2.30. The hydration kinetics were subsequently modelled using the Peleg and Sigmoidal equations, resulting in high goodness of fit of $R^2 = 0.989$ and $R^2 = 0.996$, respectively. Hyperspectral imaging is a promising tool for monitoring and modelling the hydration kinetics of pinto beans. This technique is useful for beans with both sigmoidal and concave downward shapes of hydration kinetics. Consequently, future studies using more grains are required to validate the optimal wavelength.

5. Bibliographical references

Abu-Ghannam, N., 1998. Modelling textural changes during the hydration process of red beans. *Journal of Food Engineering 38,* 341–352.

Aghinezhad, E., Szumny, A., & Figiel, A. (2023). The Application of Hyperspectral Imaging Technologies for the Prediction and Measurement of the Moisture Content of Various Agricultural Crops during the Drying Process. *Molecules, 28(7),* 2930. https://doi.org/10.3390/molecules28072930

An, D., Zhang, L., Liu, Z., Liu, J., & Wei, Y. (2023). Advances in infrared spectroscopy and hyperspectral imaging combined with artificial intelligence for the detection of cereals quality. Critical Reviews in *Food Science and Nutrition, 63(29),* 9766-9796. https://doi.org/10.1080/10408398.2022.2066062

Anino, C., Onyango, A.N., Imathiu, S., Maina, J., Onyangore, F., 2019. Chemical composition of the seed and 'milk'of three common bean (*phaseolus vulgaris* l) varieties. *Journal of Food Measurement and Characterization 13*, 1242–1249.

Benelli, A., Cevoli, C., & Fabbri, A. (2020). In-field hyperspectral imaging: An overview on the ground-based applications in agriculture. *Journal of Agricultural Engineering, 51(3),* 129-139. https://doi.org/10.4081/jae.2020.1030

Carvalho, V. S., de Oliveira, L. C., de Matos Jorge, L. M., & Jorge, R. M. M. (2022). Periodic operation as an alternative to intensify the hydration process of common beans (Phaseolus vulgaris). *Journal of Food Process Engineering, 45(9),* e14114. https://doi.org/10.1111/jfpe.14114

Caponigro, V., Marini, F., Gowen, A., 2018. Hydration of hydrogels studied by near-infrared hyperspectral imaging. *Journal of Chemometrics 32,* e2972.

Castro, W., Prieto, J.M., Guerra, R., Chuquizuta, T., Medina, W.T., Acevedo-Juárez, B., Avila-George, H., 2018. Feasibility of using spectral profiles for modeling water activity in five varieties of white quinoa grains. *Journal of Food Engineering 238*, 95–102.

Chapwanya, M., Misra, N., 2015. A soft condensed matter approach towards mathematical modelling of mass transport and swelling in food grains. *Journal of Food Engineering 145*, 37–44.

Dale, L. M., Thewis, A., Boudry, C., Rotar, I., Dardenne, P., Baeten, V., & Pierna, J. A. F. (2013). Hyperspectral imaging applications in agriculture and agro-food product quality and safety control: A review. *Applied Spectroscopy Reviews, 48(2),* 142-159. https://doi.org/10.1080/05704928.2012.705800

Garvín, A., Augusto, P., Ibarz, R., Ibarz, A., 2019. Kinetic and thermodynamic compensation study of the hydration of faba beans (*Vicia faba* l.). *Food Research International 119*, 390–397.

Kaptso, K., Njintang, Y., Komnek, A., Hounhouigan, J., Scher, J., Mbofung, C., 2008. Physical properties and rehydration kinetics of two varieties of cowpea (*Vigna unguiculata*) and bambara groundnuts (voandzeia subterranea) seeds. *Journal of Food Engineering 86*, 91–99.

Kinyanjui, P.K., Njoroge, D.M., Makokha, A.O., Christiaens, S., Ndaka, D.S., Hendrickx, M., 2015. Hydration properties and texture fingerprints of easy-and hard-to-cook bean varieties. *Food Science & Nutrition 3*, 39–47.

Korban, S., Coyne, D., Weihing, J., 1981. Rate of water uptake and sites of water entry in seeds of different cultivars of dry bean. *HortScience 16*, 545–546.

Lovato, F., Kowaleski, J., Silva, S.Z.d., Heldt, L.F.S., 2017. Composição centesimal e conteúdo mineral de diferentes cultivares de feijão biorfortificado (*Phaseolus vulgaris* l.). *Brazilian Journal of Food Technology 21*.

Ma, J., Sun, D.W., Pu, H., 2017. Model improvement for predicting moisture content (mc) in pork longissimus dorsi muscles under diverse processing conditions by hyperspectral imaging. Journal of Food Engineering 196, 65–72.

Mendoza, F.A., Wiesinger, J.A., Lu, R., Nchimbi-Msolla, S., Miklas, P.N., Kelly, J.D., Cichy, K.A., 2018. Prediction of cooking time for soaked and unsoaked dry beans (*Phaseolus vulgaris* l.) using hyperspectral imaging technology. *The Plant Phenome Journal 1*, 1–9.

Miano, A.C., Augusto, P.E.D., 2018. The hydration of grains: A critical review from description of phenomena to process improvements. *Comprehensive Reviews in Food Science and Food Safety 17*, 352–370.

Miano, A.C., García, J.A., Augusto, P.E.D., 2015. Correlation between morphology, hydration kinetics and mathematical models on andean lupin (lupinus mutabilis sweet) grains. *LWT-Food Science and Technology 61*, 290–298.

Miano, A.C., Saldaña, E., Campestrini, L.H., Chiorato, A.F., Augusto, P.E.D., 2018. Correlating the properties of different carioca bean cultivars (*Phaseolus vulgaris*) with their hydration kinetics. *Food Research International 107,* 182–194.

Oliveira, A.L., Colnaghi, B.G., da Silva, E.Z., Gouvêa, I.R., Vieira, R.L., Augusto, P.E.D., 2013. Modelling the effect of temperature on the hydration kinetic of adzuki beans (*Vigna angularis*). *Journal of Food Engineering 118*, 417–420.

Oroian, M., 2017. The temperature hydration kinetics of lens culinaris. *Journal of the Saudi Society of Agricultural Sciences 16*, 250–256.

Ovando-Martínez, M., Osorio-Díaz, P., Whitney, K., Bello-Pérez, L.A., Simsek, S., 2011. Effect of the cooking on physicochemical and starch digestibility properties of two varieties of common bean (*Phaseolus vulgaris* l.) grown under different water regimes. *Food chemistry 129*, 358–365.

Peleg, M., 1988. An empirical model for the description of moisture sorption curves. *Journal of Food science 53*, 1216–1217.

Ren, Y., Sun, D.W., 2022. Monitoring of moisture contents and rehydration rates of microwave vacuum and hot air dehydrated beef slices and splits using hyperspectral imaging. *Food Chemistry 382*, 132346.

Sánchez-Arteaga, H., Urías-Silvas, J., Espinosa-Andrews, H., García-Márquez, E., 2015. Effect of chemical composition and thermal properties on the cooking quality of common beans (*Phaseolus vulgaris*). *CyTA-Journal of Food* 13, 385–391.

Santos, J.R., Sarraguça, M.C., Rangel, A.O., Lopes, J.A., 2012. Evaluation of green coffee beans quality using near infrared spectroscopy: A quantitative approach. *Food Chemistry 135*, 1828–1835.

Ulloa, J.A., Enríquez López, K.V., Contreras Morales, Y.B., Rosas Ulloa, P., Ramírez Ramírez, J.C., Ulloa Rangel, B.E., 2015. Effect of ultrasound treatment on the hydration kinetics and cooking times of dry beans (*Phaseolus vulgaris*). *CyTA-Journal of Food 13*, 588–596.

Ulloa, J.A., Rosas-Ulloa, P., Ramírez-Ramírez, J.C., Ulloa-Rangel, B.E., 2016. Modelación matemática de las cinéticas de hidratación a diferentes temperaturas de cuatro variedades de frijol (*Phaseolus vulgaris* l) producidas en méxico. CienciaUAT 10, 52–62.

Vásquez, N., Magán, C., Oblitas, J., Chuquizuta, T., Avila-George, H., Castro, W., 2018. Comparison between artificial neural network and partial least squares regression models for hardness modeling during the ripening process of swiss-type cheese using spectral profiles. *Journal of Food Engineering 219*, 8–15.

Wang, B., Sun, J., Xia, L., Liu, J., Wang, Z., Li, P., ... & Sun, X. (2023). The applications of hyperspectral imaging technology for agricultural products quality analysis: A review. *Food Reviews International, 39(2),* 1043-1062. https://doi.org/10.1080/87559129.2021.1929297

Xu, H., Ren, J., Lin, J., Mao, S., Xu, Z., Chen, Z., ... & Wang, P. (2023). The impact of high-quality data on the assessment results of visible/near-infrared hyperspectral imaging and development direction in the food fields: a review. *Journal of Food Measurement and Characterization, 1-17*. https://doi.org/10.1007/s11694-023-01822-x

Yang, D., He, D., Lu, A., Ren, D., Wang, J., 2017. Combination of spectral and textural information of hyperspectral imaging for the prediction of the moisture content and storage time of cooked beef. *Infrared Physics & Technology 83*, 206–216.

Zanella-Díaz, E., Mújica-Paz, H., Soto-Caballero, M., Welti-Chanes, J., Valdez-Fragoso, A., 2014. Quick hydration of tepary (*Phaseolus acutifolius* gray) and pinto beans (*Phaseolus vulgaris* l.) driven by pressure gradients. *LWT-Food Science and Technology 59*, 800–805.

Zhu, M., Huang, D., Hu, X. J., Tong, W. H., Han, B. L., Tian, J. P., & Luo, H. B. (2020). Application of hyperspectral technology in detection of agricultural products and food: A Review. *Food science & nutrition*, *8(10)*, 5206-5214. https://doi.org/10.1002/fsn3.1852

4.7. Impacto de la bioestimulación magnética y las condiciones ambientales en la calidad agronómica y la composición bioactiva del maíz morado INIA 601.

Open Access Article

Impact of Magnetic Biostimulation and Environmental Conditions on the Agronomic Quality and Bioactive Composition of INIA 601 Purple Maize

by Tony Chuquizuta [1,2], Cesar Lobato [1], Franz Zirena Vilca [3], Nils Leander Huamán-Castilla [4], Wilson Castro [5], Marta Castro-Giraldez [2], Pedro J. Fito [2], Segundo G. Chavez [6,*] and Hubert Arteaga [7,*]

1 Instituto de Investigación del Mejoramiento Productivo, Universidad Nacional Autónoma de Chota, Chota 06120, Peru

2 Instituto Universitario de Ingeniería de Alimentos Food UPV, Universitat Politècnica de València, Camino de Vera s/n, 46022 Valencia, Spain

3 Laboratory of Organic Pollutants and Environment of the IINDEP of the Universidad Nacional de Moquegua, Urb Ciudad Jardín-Pacocha-Ilo, Moquegua 18001, Peru

4 Laboratorio de Tecnologías Sustentables para la Extracción de Compuestos de Alto Valor, Instituto de Investigación para el Desarrollo del Perú, Universidad Nacional de Moquegua, Moquegua 18001, Peru

5 Facultad de Ingeniería de Industrias Alimentarias y Biotecnología, Universidad Nacional de Frontera, Sullana 20100, Peru

6 Instituto de Investigación para el Desarrollo Sustentable de Ceja de Selva INDES-CES, Universidad Nacional Toribio Rodríguez de Mendoza de Amazonas, Chachapoyas 01001, Peru

7 Grupo de Investigación Innovación Tecnológica en Productos y Procesos Alimentarios (GIITPA), Instituto de Investigación de Ciencia y Tecnología de Alimentos (ICTA), Universidad Nacional de Jaén, Jaén 06800, Peru

* Authors to whom correspondence should be addressed.

Foods **2025**, *14*(12), 2045; https://doi.org/10.3390/foods14122045

Condición	DOI
Publicado (04 de junio, 2024)	**https://doi.org/10.3390/foods14122045**

IMPACT OF MAGNETIC BIOSTIMULATION AND ENVIRONMENTAL CONDI-TIONS ON THE AGRONOMIC QUALITY AND BIOACTIVE COMPOSITION OF PURPLE MAIZE INIA 601

Tony Chuquizuta [1,2], Cesar Lobato [1], Franz Zirena Vilca [3], Nils Leander Huamán-Castilla [4], Wilson Castro [5], Marta Castro-Giraldez [2], Pedro J. Fito [2], Segundo G. Chavez [6,*] and Hubert Arteaga [7,*]

[1] Instituto de Investigación del Mejoramiento Productivo, Universidad Nacional Autónoma de Chota,

Chota 06120, Peru; tchuquizuta@unach.edu.pe (T.C.); 2016041020@unach.edu.pe (C.L.)

[2] Instituto Universitario de Ingeniería de Alimentos Food UPV, Universitat Politècnica de València, Camino de Vera s/n, 46022 Valencia, Spain; marcasgi@upv.es (M.C.-G.); pedfisu@tal.upv.es (P.J.F.)

[3] Laboratory of Organic Pollutants and Environment of the IINDEP of the Universidad Nacional de Moquegua, Urb Ciudad Jardín-Pacocha-Ilo, Moquegua 18001, Peru.; fzirenav@unam.edu.pe

[4] Laboratorio de Tecnologías Sustentables para la Extracción de Compuestos de Alto Valor, Instituto de Investigación para el Desarrollo del Perú, Universidad Nacional de Moquegua, Moquegua 18001, Peru; nhuamanc@unam.edu.pe

[5] Facultad de Ingeniería de Industrias Alimentarias y Biotecnología, Universidad Nacional de Frontera, Sullana 20100, Peru; wcastro@unf.edu.pe

[6] Instituto de Investigación para el Desarrollo Sustentable de Ceja de Selva INDES-CES, Universidad Nacional Toribio Rodríguez de Mendoza de Amazonas, Chachapoyas 01001, Peru

[7] Grupo de Investigación Innovación Tecnológica en Productos y Procesos Alimentarios (GIITPA), Instituto de Investigación de Ciencia y Tecnología de Alimentos (ICTA), Universidad Nacional de Jaén, Jaén 06800, Peru

* Correspondence: segundo.quintana@untrm.edu.pe (S.G.C.); hubert.arteaga@unj.edu.pe (H.A.)

Abstract

The utilization of magnetic fields in agricultural contexts has been demonstrated to exert a beneficial effect on various aspects of crop development, including germination, growth, and yield. The present study investigates the impact of magnetic biostimulation on seeds of purple maize (Zea mays L.), variety INIA 601, cultivated in Cajamarca, Peru, with a particular focus on their physical characteristics, yield, bioactive compounds, and antioxidant activity. The results demonstrated that seeds treated with pulsed (8 mT at 30

Hz for 30 min) and static (50 mT for 30 min) magnetic fields exhibited significantly longer cobs (16.89 and 16.53 cm, respectively) compared with the untreated control (15.79 cm). Furthermore, the application of these magnetic fields resulted in enhanced antioxidant activity in the bract, although the untreated samples exhibited higher values (110.56 µg/mL) compared with the pulsed (91.82 µg/mL) and static (89.61 µg/mL) treatments. The geographical origin of the samples had a significant effect on the physical development and the amount of total phenols, especially the antioxidant activity in the coronet and bract. Furthermore, a total of fourteen phenols were identified in various parts of the purple maize, with procyanidin B2 found in high concentrations in the bract and crown. Conversely, epicatechin, kaempferol, vanillin, and resveratrol were found in lower concentrations. These findings underscore the phenolic diversity of INIA 601 purple maize and its potential application in the food and pharmaceutical industries, suggesting that magnetic biostimulation could be an effective tool to improve the nutritional and antioxidant properties of crops.

Keywords: antioxidants; Andean crops; biofortification strategies; bioactive yields in plants; phenolic biosynthesis

Graphical Abstract

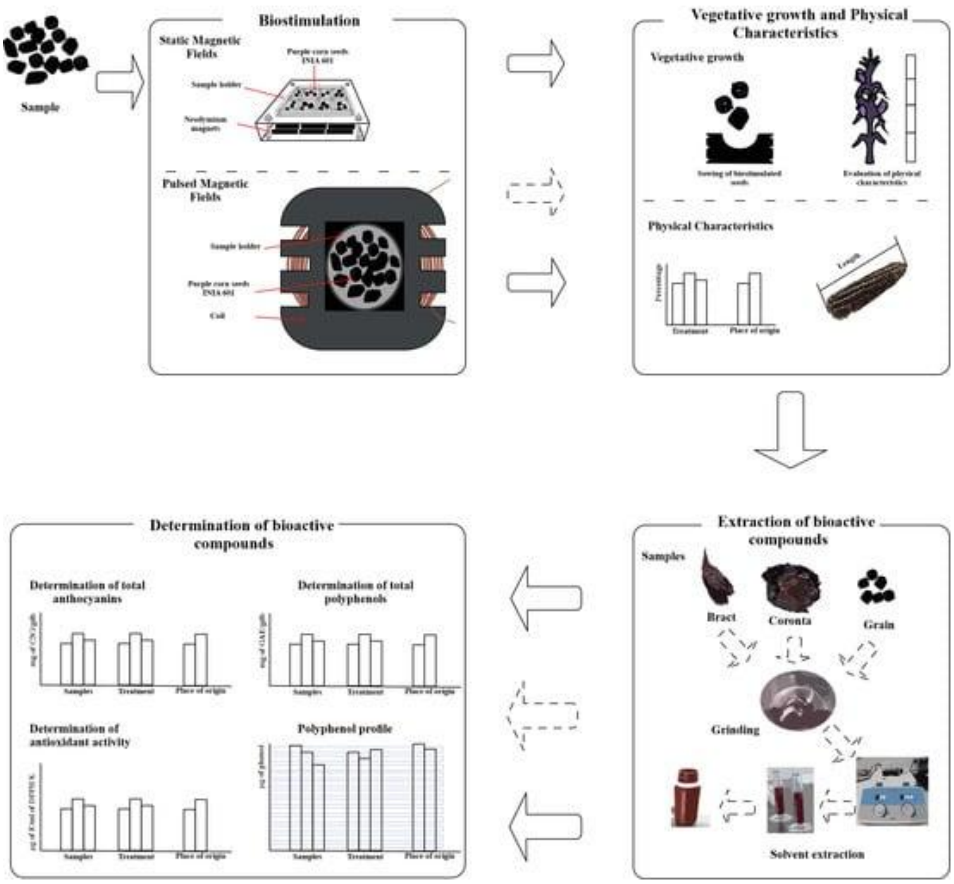

1. Introduction

The significance of purple corn extends both nationally and internationally. During the initial quarter of 2024, the marketing of grain, bracts, and crowns enabled the export of 281 tons of corn on the cob. The United States constitutes its primary market [1]. This variety of corn is utilized in the production of various baked goods, gastronomy, whiskey, and in the extraction of anthocyanin compounds. Noteworthy among the most cultivated varieties are the following: Cuzco, Caraz, Arequipa, Negro de Junín, Huancavelicano, UNC-47, PM-581, PM-582, INIA-615 black Canaan, and INIA-601. The latter variety is of particular interest due to its bioactive compounds, particularly anthocyanin, which possesses significant antioxidant activity. This bioactive compound has been shown to offer numerous health benefits, including a reduction in the risk of developing diabetes [2]. It has been demonstrated that it is instrumental in preventing obesity and being overweight, colon cancer and cardiovascular diseases, and ocular degeneration and contributes to the formation of cells and tissues. The efficacy of these benefits has been substantiated by numerous research studies. Conversely, improper seed selection has been shown to result in diminished levels of phytochemicals, such as anthocyanins and flavonoids, which are pivotal for the health benefits associated with purple corn [3]. This, in turn, has been observed to diminish the quality and economic value of purple corn [4].

In the pursuit of enhancing the germination and physical characteristics of corn, various technologies have been employed, including precision agriculture, which utilizes specialized software and hardware such as GPS and Geographic Information Systems (GISs). These technologies enable farmers to meticulously manage inputs, including fertilizers, pesticides, and irrigation water, thereby minimizing waste and reducing the environmental impact [5]. Conversely, Genetically Modified Organisms (GMOs) have been linked to an augmentation in the area and yield of maize [6]. Another method is ultrasonic priming of seeds, in which ultrasonic waves at about 20 kHz are applied in water or other suitable nutrient solutions to improve germination and early growth [7] as well as uniformity [8]. However, due to its competitive cost advantages, its varied application, and its positive effects on crops, the application of magnetic fields stands out. These fields have been shown to improve growth and yield, mitigate abiotic stress factors that affect vegetative development [9] and seed quality [10], and increase the availability of some minerals, such as phosphorus, in the soil [11].

Magnetic fields have been demonstrated to promote the germination and growth of diverse agricultural seeds. The interaction of magnetic fields with biological systems within the spectrum below 1 MHz is referred to as charge induction, which involves the transfer of charges from ions at low frequencies to the induction of metal centers (Fe^{3+}, Cu^{2+}, and Mn^{2+}) in proteins that play a crucial role in cellular functioning at higher frequencies. Molecules such as ferritins, plastocyanins, cytochrome C oxidase, and superoxide dismutase, which are crucial for plant growth [12], are affected by paramagnetic relaxation in seeds. In the cases of maize and soybean, an intensity of 200 mT for 1 h has been shown to enhance germination and essential enzyme activities, even in saline soils [13]. Furthermore, the application of 10 mT at 25 °C for 1 h to brown rice seeds resulted in an augmentation of α-amylase activity and germination, along with enhancements of shoot and root length and weight [14]. In broad beans, this treatment increased amylolytic activity and production of indole-3-acetic and gibberellic acids [15]. Furthermore, water subjected to magnetic fields exhibited a propensity to promote maize growth, yielding outcomes that surpassed those of conventional water [16]. The underlying mechanism of this phenomenon is attributed to the ability of magnetic fields to modify apical cells, thereby enhancing nutrient uptake [17]. However, these treatments have not yet been applied to purple corn seeds of the INIA 601 variety. Consequently, this study evaluated the effect of magnetic biostimulation of INIA 601 purple corn seeds on their physical characteristics, production yield, concentration of bioactive compounds, and antioxidant activity.

2. Materials and Methods

2.1. Vegetal material

The experiment utilized 3 kg of purple corn (*Zea mays* L. var. INIA 601) seeds, kindly provided by the "Baños del Inca" Experimental Station of the Instituto Nacional de Innovación Agraria (INIA), located in Cajamarca, Peru.

2.2. Regents

Hydrochloric acid, ethanol (99.7%), potassium chloride (0.025 M), sodium acetate, concentrated hydrochloric acid, Folin Ciocalteu, gallic acid, sodium carbonate (95.5%), formic acid, and methanol (99.7%) were obtained from Merck KGaA (Darmstadt, Alemania); 2,2-diphenyl-1-picrylhydrazyl (DPPH) was also acquired (Burlington, MA, USA), along with HPLC-grade methanol (JT Baker, Madrid, Spain).

2.3. Experimental location

The experiment was conducted at two locations in the department of Cajamarca. These were Cajabamba and Cochamarca, whose geographical locations and climatological characteristics for 2022 and 2023 growing seasons are shown in Table 1.

Table 1. Geographical location and climatological characteristics of the planting locations.

Location	Political Location	Geographic Coordinates		
		Altitude (masl)	Latitude	Longitude
Cajabamba	Plot of land of INIA Pampa Grande Annex, district and province of Cajabamba	2640	7°36′39″	78°04′15″
Cochamarca	INIA land lot, Gregorio Pita district, San Marcos province	2864	7°16′52″	78°13′09″

	Climatic characteristics					
	Minimum daily temperature (°C)	Maximum daily temperature (°C)	Average daily precipitation (mm)	Daily relative humidity (%)	Hours of sun/day (h)	Wind speed (m/s)
Cajabamba	12.82	23.33	3.53	74.96	5.47	0.37
Cochamarca	7.94	20.49	2.87	82.22	3.20	0.60

2.4. Methods

2.4.1. Biostimulation of INIA 601 purple corn seeds

The static and pulsed magnetic field prototypes were designed and constructed at the Emerging Technologies Laboratory of the Research Institute of the Universidad Nacional Autónoma de Chota and the Food Engineering Laboratory of the Universidad Nacional de Jaén. The static magnetic field (SMF) prototype consisted of an array of neodymium magnets, which were placed on PLA printed plates. The pulsed magnetic field (PMF) prototype consisted of a solenoid coil, pulse controllers, and a voltage source. Prior to the application of the magnetic fields, the seeds were meticulously selected, ensuring the exclusion of any seeds exhibiting signs of mechanical or biological damage. The seeds were subsequently transferred to the equipment for biostimulation with static magnetic fields, with an induction of 50 mT for 30 min and pulsed magnetic fields at a frequency of 30 Hz for 30 min (Figure 1).

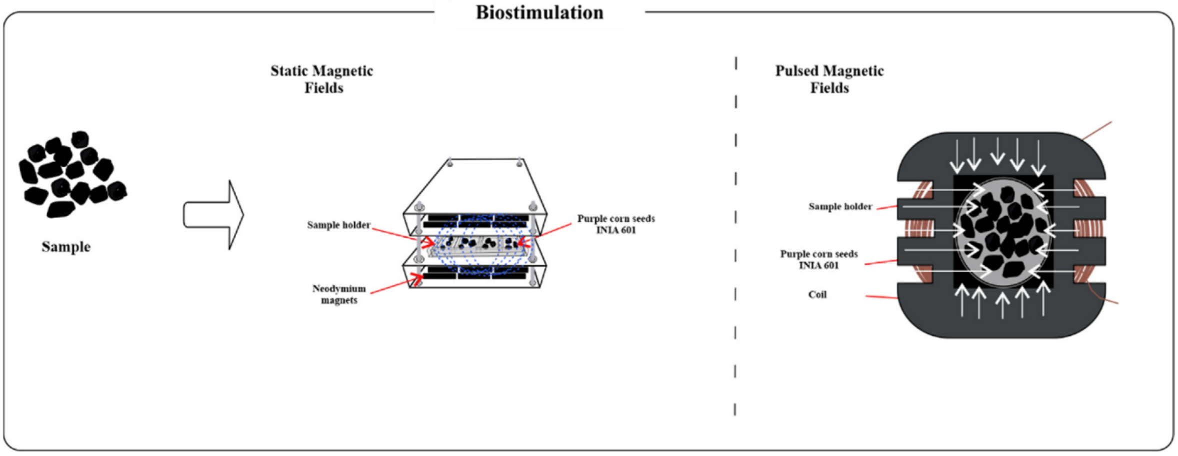

Figure 1. Application of static and pulsed magnetic fields to INIA 601 purple corn seeds.

In both experimental plots, a control treatment was installed that was not subjected to a magnetic field (NMF). All experimental plots were prepared and conducted in a homogeneous manner so that the only sources of variation were the treatments and the location.

2.4.2. Evaluation of the physical characteristics of INIA 601 purple corn

From the six central furrows of each experimental unit, the days to 50% male flowering, the days to 50% female flowering, and the number of ears harvested per plant were recorded. From ten randomly selected plants, the plant height and ear height were determined; from ten randomly selected ears from the six central furrows, the ear length was measured. A six-class scale devised by the Maize and Wheat Research Center-CIMMYT [18]. was used to ascertain the percentage of rotting.

2.4.3. Production yield of INIA 601 purple corn

The production yield of INIA 601 purple corn was determined in accordance with the procedure established by Medina et al. [19]. This procedure involved the consideration of various factors, including 14% grain moisture, the field weight, the failure correction factor, the failure factor, the shelling factor, and the factor used to express the yield in tons per hectare (t/ha).

2.4.4. Obtaining INIA 601 ourple corn extracts

The method of Lao and Giusti [20] was used, with some modifications. Cobs were shelled to separate bracts, crowns, and kernels; they were reduced in size in a multifunctional pulverizer (Henkel, WFA-GR1000, Düsseldorf, Germany) and passed through a N° 35 sieve (500 µm). The moisture of the samples was determined using a moisture balance (AND MX-50) at 105 °C; 1 g of each sample was used, along with 20 mL of 50% ethanol solvent acidified with 0.01% hydrochloric acid (HCl) at 6 N, placed in a magnetic stirrer (Cimarec+ Thermo Scientific, Saint Louis, MO, USA) at 350 rpm for 30 min at 30 °C, and centrifuged (CENTURION-Scientific Limited, Chichester, UK) at 4000 rpm for 10 min. The supernatant was filtered using Wattman No. 1 paper, placed in amber containers, and stored at −24 °C.

2.4.5. Determination of total anthocyanin content (TAC)

The total anthocyanin content was determined via the differential pH method described by Lee et al. [21], using potassium chloride buffer 0.025 M at pH 1 and sodium acetate 0.4 M at pH 4.5. The extracts obtained were as follows: for the corn cob, the dilution factor (DF) was 100, with 30 µL of extract used; for the bract, the DF was 50, with 60 µL of extract used; for the grain, the DF was 10, with 300 µL of extract needed. The difference for each extract was augmented with buffers up to 3 mL. The samples were vortexed for 1 min and left to react for 30 min in the absence of light at room temperature. Subsequently, the absorbance was read at 520 and 700 nm using a Genesys 150 UV–Visible spectrophotometer. It is imperative to note that each sample was subjected to analysis in triplicate.

2.4.6. Determination of total phenol content (TPC)

The Folin–Ciocalteu method, as described by Albarici et al. [22] and Jin et al. [23]), was employed to ascertain the total phenol content. The experimental setup involved the utilization of 0.2 mL of the diluted samples, 0.1 mL of Folin–Ciocalteu reagent, and 0.2 mL of 10% sodium carbonate. These components were allowed to react in a dark environment for a duration of 1 h. Subsequently, the reaction was measured at 765 nm using a Genesys 150 UV–Visible spectrophotometer. Prior to this, a standard curve was constructed using different dilutions of gallic acid to obtain a linear equation (y: a + bx; $R^2 > 0.998$). The results were expressed as mg of AGE/g db.

2.4.7. Profile of phenolic compounds by HPCL

The experimental procedure was executed in accordance with the protocol established by Ramos-Escudero et al. [24]. The extracts were subjected to analysis using an ultra-high-performance chromatograph (UHPLC) (Agilent 1290 Infinity II, Santa Clara, CA, USA) equipped with a Diode Array Detector (DAD) and a Poroshell C18 column. The analysis was conducted at 30 °C. The chromatographic separation was achieved through the use of a mobile phase consisting of acetonitrile and 0.1% formic acid (phase A) and water with 0.1% formic acid (phase B). The separation was conducted using a programmed gradient, which involved an initial 95% A + 5% B for 15 min, followed by a transition to 60% A + 40% B for 18 min. The final step involved a return to 95% A + 5% B for 20 min, with all steps occurring at a constant flow rate of 0.3 mL/min. The results were expressed as µg/g db. Table 2 shows the detection and quantification limits for the phenolic compounds studied. The calibration curves had an R^2 greater than 0.995.

Table 2. LOD and LOQ of the HPLC system for the phenolic compounds studied.

Compound	LOD (µg mL^{-1})	LOQ (µg mL^{-1})
Hydroxytyrosol	0.0017	0.0051
Tyrosol	0.0002	0.0007
Catechin	0.0029	0.0087
Procyanidin B2	0.0057	0.0171
Epicatechin	0.0009	0.0026
Vanillin	0.0003	0.0008
Routine	0.0001	0.0003
Procyanidin A2	0.0005	0.0014
Resveratrol	0.0076	0.0229
Kersetrin	0.0088	0.0264
Aspecinine	0.0007	0.0022
Kaempferol	0.0049	0.0147

2.4.8. Determination of antioxidant activity

The quantification of the 2,2 diphenyl, 1 picrylhydrazyl (DPPH) radical uptake method was performed in accordance with the methodology established by Ratha et al. [25], with certain modifications. The extraction process involved the dilution of 1.0 mL of the extract with methanol (200 µM), followed by the addition of 1 mL of the methanolic solution of DPPH. Subsequently, the mixture was permitted to stand for a period of 30 min in conditions of darkness. Ultimately, readings were obtained at 517 nm utilizing a Genesys 150 UV–Visible spectrophotometer. The IC50 was determined from the graph of the percentage of inhibition versus the concentrations used to inhibit 50% of the free radicals of DPPH. The results were expressed as µg sample/mL of the DPPH solution.

2.4.9. Statistical analysis

The data were tabulated and presented in figures prepared in Microsof Excel spreadsheets. To determine statistical differences between groups (treatments), an analysis of variance (ANOVA) and Tukey's post hoc test were performed, using Statgraphics Centurion V.19 software.

3. Results

3.1. Physical characteristics

The application of magnetic fields to purple corn seeds did not yield substantial modifications in the male flowering day (MFD) and female flowering day (FFD), plant height, number of corn cobs per plant, degree of rotting, and yield. However, significant variations in corn-cob length were observed, with treatments subjected to magnetic fields exhibiting lengths exceeding 16.5 cm. The planting locations exerted a substantial influence on the characteristics previously mentioned, with the exception of corn-cob length. The Cajabamba experimental plot exhibited the most optimal outcomes in terms of MFD, FFD, and plant height (Table 3), attributable to its higher sunlight exposure, which averaged 5.4 h per day (Table 1). In contrast, the Cochamarca plot demonstrated superior characteristics in the number of corn cobs per plant (prolificacy), the incidence of root lodging and stem lodging, and yield. This was due to the fact that taller plants were obtained in Cajabamba, which were more prone to the effects of weather conditions, resulting in a high percentage of root and stem lodging (20.8 and 10%, respectively).

Table 3. Physical characteristics of INIA 601 purple corn.

Variable Means			MFD (Days)	FFD (Days)	Plant Height (m)	N° of Cobs/Plant	Cob Length (cm)	Rot (%)	Root Canker (%)	Stem Canker (%)	Yield (t/ha)
Treatment	**NMF**	$\bar{x}$	99.100 [a]	105.100 [a]	2.245 [a]	0.849 [a]	15.791 [a]	14.992 [a]	7.448 [a]	7.208 [a]	4.155 [a]
		SD	2.211	2.809	0.055	0.073	0.429	3.356	2.639	3.979	0.699

	SMF	$\bar{x}$	98.800 [a]	103.400 [a]	2.304 [a]	0.856 [a]	16.526 [b]	13.982 [a]	14.515 [a]	8.102 [a]	4.107 [a]
		SD	1.506	2.125	0.118	0.086	0.481	3.625	7.426	2.701	0.738
	PMF	$\bar{x}$	98.400 [a]	103.000 [a]	2.290 [a]	0.871 [a]	16.889 [b]	15.491 [a]	10.383 [a]	7.713 [a]	4.117 [a]
		SD	1.587	1.842	0.098	0.091	0.426	3.676	2.802	3.634	0.944
Place	**Cajabamba**	$\bar{x}$	92.200 [a]	98.933 [a]	2.342 [b]	0.723 [a]	16.475 [a]	19.992 [b]	20.837 [b]	10.846 [b]	3.353 [a]
		SD	2.709	3.786	0.102	0.111	0.534	4.938	7.627	5.171	0.828
	Cochamarca	$\bar{x}$	105.333 [b]	108.733 [b]	2.217 [a]	0.994 [b]	16.329 [a]	9.651 [a]	0.727 [a]	4.503 [a]	4.899 [b]
		SD	0.827	0.730	0.078	0.055	0.356	2.167	0.950	1.704	0.759
p-Value (Place)			0.000	0.000	0.000	0.000	0.393	0.000	0.000	0.000	0.000
p-Value (Treatment)			0.720	0.165	0.233	0.866	0.000	0.665	0.071	0.864	0.991

NMF: nonmagnetic field; SMF: static magnetic field; PMF: pulse magnetic field; MFD: male flowering day; FFD: female flowering day; x : average; SD: standard deviation. Different letters indicate statistically different groups ($p \leq 0.05$).

3.2. Bioactive composition

As demonstrated in Figure 2, the magnetic fields exerted an influence on the total phenol content of the bracts of INIA 601 purple corn. The most effective treatment was identified as CMP, yielding 28.253 mg EAG/gss. The planting locations exhibited a significant impact on the phenol content, with Cajabamba and Cochamarca registering levels of 25 and 28 mg EAG/g db, respectively.

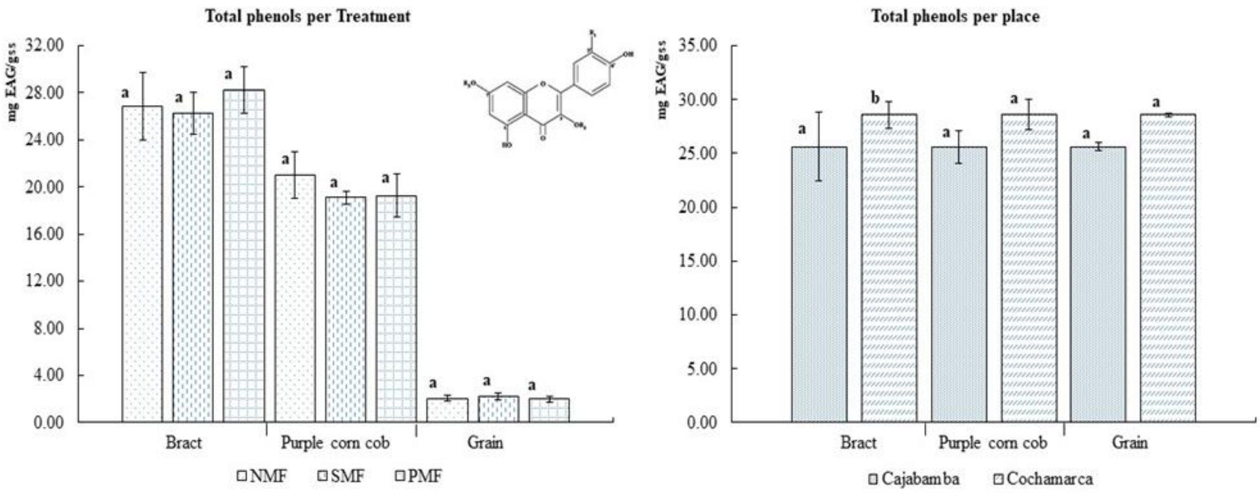

Figure 2. Total phenol content of INIA 601 purple corn samples. NMF: nonmagnetic field; SMF: static magnetic field; PMF: pulse magnetic field. Different letters indicate statistically different groups ($p \leq 0.05$).

As illustrated in Figure 3, the application of magnetic fields to INIA 601 purple corn seeds did not result in substantial variations in total anthocyanin content. Given the greater variation in temperatures between day and night at Cochamarca (see Table 1), there was a propensity for increased anthocyanin content in the bract and corn cob, with levels of 7.6 mg and 9.4 mg of Cyanidin-3-O-glucoside (C3G)/gss, respectively. This was in comparison to the samples from Cajabamba, which exhibited 6.5 mg of C3G/gss in the bract and 9.3 mg of C3G/gss in the cob.

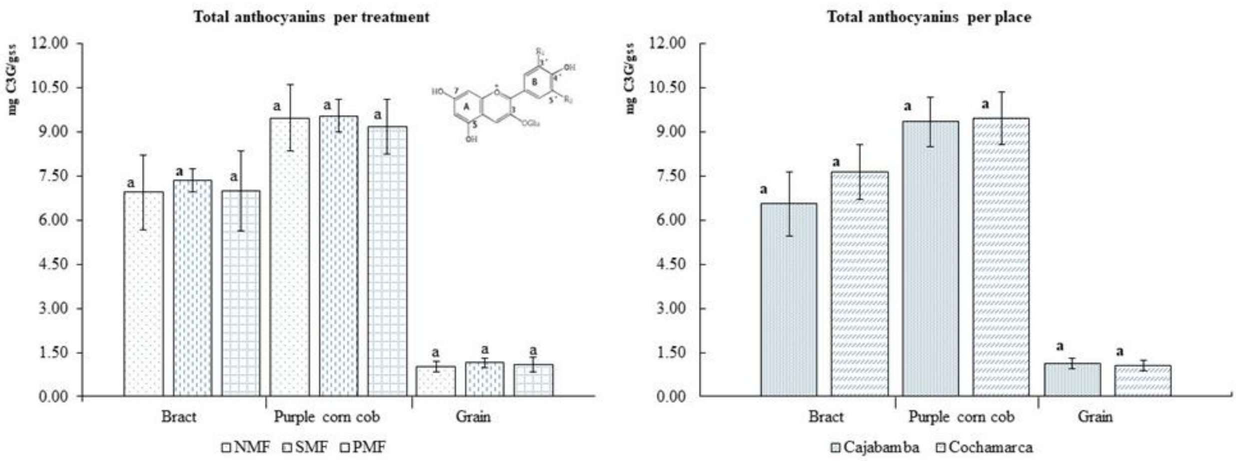

Figure 3. Total anthocyanin content of INIA 601 purple corn samples. NMF: nonmagnetic field; SMF: static magnetic field; PMF: pulse magnetic field. Different letters indicate statistically different groups ($p \leq 0.05$).

3.3. Phenolic compound profile

In Figure 4, we can observe the phenols found in the INIA 601 purple corn ear kernels. The most important were procyanidin B2, which exceeded 25 mg/L, and resveratrol, which exceeded 15 mg/L. In addition, the treatment with the pulsed magnetic field was able to increase the amount of catechin compared with the other treatments. The mean values and standard deviations are presented in Table 4.

Phenols grain

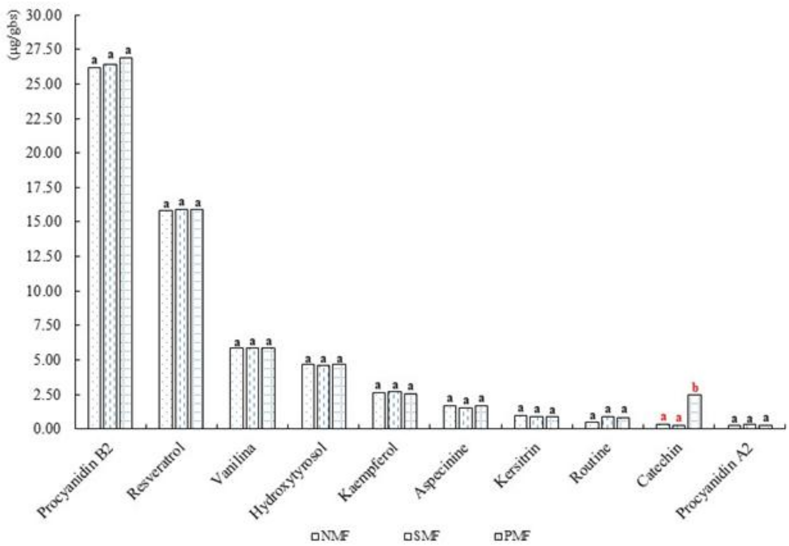

Figure 4. Phenolic content of INIA 601 purple corn kernels. NMF: nonmagnetic field; SMF: static magnetic field; PMF: pulse magnetic field. Different letters indicate statistically different groups ($p \leq 0.05$).

Table 4. Content of 12 phenolic compounds in corn cobs produced from each treatment and cultivation site (µg/gdb).

Part of the Corn Cob	Phenolic Compound	Cajabamba			Cochamarca		
		NMF	SMF	PMF	NMF	SMF	PMF
Grain	Tyrosol	*	*	*	*	*	*
	Routine	*	*	*	0.696 ± 0.043	1.089 ± 0.264	0.938 ± 0.299
	Kersetrin	0.882 ± 0.092	0.865 ± 0.046	0.923 ± 0.01	1.038 ± 0.151	0.928 ± 0.01	0.911 ± 0.026
	Hydroxytyrosol	4.695 ± 0.039	4.585 ± 0.129	4.65 ± 0.005	4.635 ± 0.006	4.674 ± 0.027	*
	Catechin	0.29 ± 0.129	0.19 ± 0.012	*	*	*	*
	Procyanidin B2	24.954 ± 1.574	26.157 ± 0.821	26.038 ± 0.507	27.408 ± 1.414	27.683 ± 1.678	26.839 ± 1.959
	Epicatechin	*	*	*	*	*	*
	Vanilina	5.903 ± 0.171	5.921 ± 0.182	5.807 ± 0.058	5.819 ± 0.106	5.884 ± 0.087	5.974 ± 0.112
	Procyanidin A2	0.309 ± 0.153	0.277 ± 0.084	0.256 ± 0.142	0.275 ± 0.022	0.338 ± 0.051	0.231 ± 0.159
	Resveratrol	*	*	15.88 ± 0.024	15.9 ± 0.003	15.934 ± 0.053	15.978 ± 0.106
	Aspecinine	1.039 ± 0.312	1.106 ± 0.208	1.601 ± 0.499	2.274 ± 0.631	1.897 ± 0.706	1.771 ± 0.526
	Kaempferol	2.16 ± 0.334	2.679 ± 0.197	2.514 ± 0.349	3.142 ± 0.627	2.798 ± 0.412	2.637 ± 0.483
	Tyrosol	*	*	*	*	*	*

Purple corn cob	Routine	*	*	*	0.696 ± 0.043	1.089 ± 0.264	0.938 ± 0.299
	Kersetrin	0.882 ± 0.092	0.865 ± 0.046	0.923 ± 0.01	1.038 ± 0.151	0.928 ± 0.01	0.911 ± 0.026
	Hydroxytyrosol	4.695 ± 0.039	4.585 ± 0.129	4.65 ± 0.005	4.635 ± 0.006	4.674 ± 0.027	*
	Catechin	0.29 ± 0.129	0.19 ± 0.012	*	*	*	*
	Procyanidin B2	24.954 ± 1.574	26.157 ± 0.821	26.038 ± 0.507	27.408 ± 1.414	27.683 ± 1.678	26.839 ± 1.959
	Epicatechin	*	*	*	*	*	*
	Vanilina	5.903 ± 0.171	5.921 ± 0.182	5.807 ± 0.058	5.819 ± 0.106	5.884 ± 0.087	5.974 ± 0.112
	Procyanidin A2	0.309 ± 0.153	0.277 ± 0.084	0.256 ± 0.142	0.275 ± 0.022	0.338 ± 0.051	0.231 ± 0.159
	Resveratrol	*	*	15.88 ± 0.024	15.9 ± 0.003	15.934 ± 0.053	15.978 ± 0.106
	Aspecinine	1.039 ± 0.312	1.106 ± 0.208	1.601 ± 0.499	2.274 ± 0.631	1.897 ± 0.706	1.771 ± 0.526
	Kaempferol	2.16 ± 0.334	2.679 ± 0.197	2.514 ± 0.349	3.142 ± 0.627	2.798 ± 0.412	2.637 ± 0.483
Bract	Tyrosol	0.976 ± 0.651	0.613 ± 0.282	0.985 ± 0.582	0.878 ± 0.307	0.764 ± 0.168	0.511 ± 0.336
	Routine	3.697 ± 0.293	3.375 ± 1.175	6.025 ± 2.843	4.405 ± 0.994	1.343 ± 0.788	3.954 ± 0.422
	Kersetrin	3.049 ± 0.025	3.233 ± 0.839	3.905 ± 0.788	3.028 ± 0.226	2.959 ± 0.759	3.474 ± 0.237
	Hydroxytyrosol	5.145 ± 0.181	5.054 ± 0.062	5.741 ± 1.324	5.522 ± 0.751	5.311 ± 0.289	5.305 ± 0.376
	Catechin	0.336 ± 0.063	0.343 ± 0.105	0.345 ± 0.035	0.275 ± 0.034	0.338 ± 0.032	0.268 ± 0.115
	Procyanidin B2	42.133 ± 2.873	40.484 ± 1.53	37.286 ± 1.289	41.687 ± 0.352	37.685 ± 1.71	41.668 ± 1.329
	Epicatechin	*	*	6.762 ± 6.86	*	6.523 ± 6.322	5.934 ± 5.957
	Vanilina	10.114 ± 2.438	5.218 ± 0.407	5.658 ± 1.135	6.625 ± 1.775	6.806 ± 2.451	5.677 ± 0.41
	Procyanidin A2	1.857 ± 0.003	2.414 ± 0.347	2.24 ± 0.246	2.155 ± 0.502	2.292 ± 1.121	2.35 ± 0.061
	Resveratrol	16.276 ± 0.115	16.096 ± 0.047	16.17 ± 0.245	16.131 ± 0.169	16.064 ± 0.066	16.1 ± 0.027
	Aspecinine	1.869 ± 0.503	*	*	*	*	*
	Kaempferol	2.552 ± 0.704	2.268 ± 0.323	4.347 ± 3.586	4.714 ± 4.453	2.576 ± 0.5	2.103 ± 0.101

Figure 5 shows the phenols present in the crown of INIA 601 purple corn, among which procyanidin B2 stood out, which exceeded 40 mg/L, as well as resveratrol, aspecinine, and catechin, the latter being affected by the pulsed magnetic field of square waves.

Phenols Purple corn cob

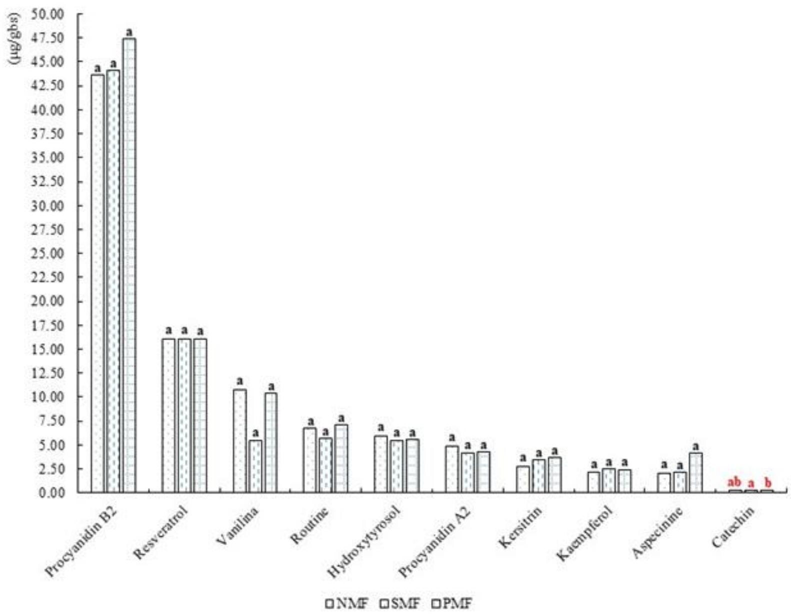

Figure 5. Phenols of INIA 601 purple corn crowns. NMF: nonmagnetic field; SMF: static magnetic field; PMF: pulse magnetic field. Different letters indicate statistically different groups ($p \leq 0.05$).

Figure 6 shows that the phenols present in the INIA 601 purple corn bract. A considerable amount of procyanidin B2 was found, exceeding 50 mg/L in the samples that had CMP applied, as well as resveratrol, which exceeded 10 mg/L. In addition, two phenols, epicatechin and tyrosol, were found only in the bract compared with the grain and coronet samples.

Phenols bract

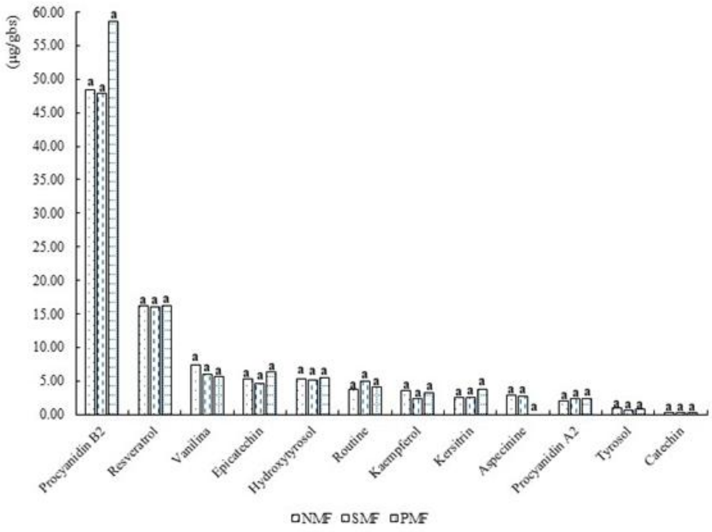

Figure 6. Phenols of INIA 601 purple corn bract. NMF: nonmagnetic field; SMF: static magnetic field; PMF: pulse magnetic field. Different letters indicate statistically different groups ($p \leq 0.05$).

3.4. Antioxidant activity

As illustrated in Figure 7, the magnetic fields exerted a substantial influence on the bract, with CME and CMP requiring 89.612 µg and 91.816 µg/mL of DPPH solution, respectively, in comparison to SCM, which necessitated an extract concentration 110.556 µg/mL higher to achieve the equivalent inhibition of free radicals. In the cob, significant differences were also observed, with CMP requiring 161.136 µg/mL compared with CME and SCM. In the grain, no significant differences were observed; however, a slight variation was noted, with CMP yielding a more favorable result.

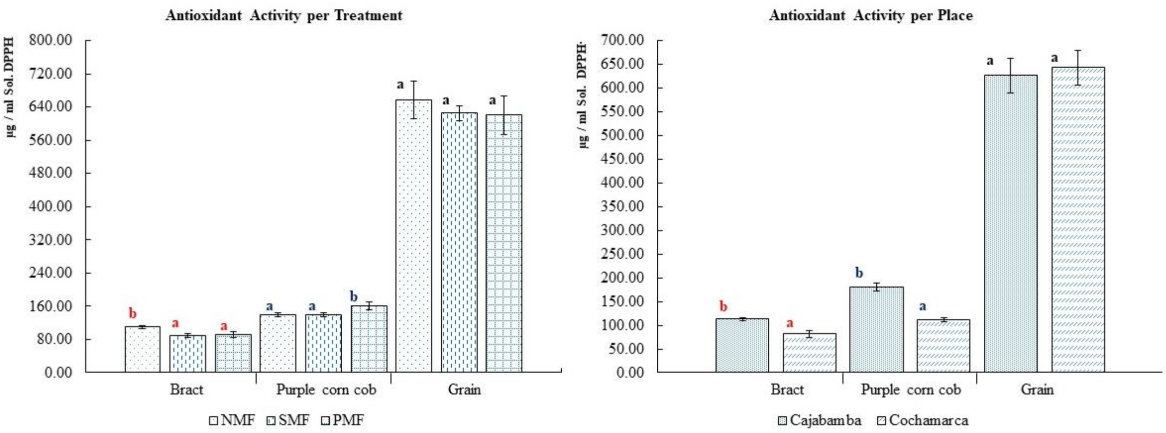

Figure 7. Antioxidant activity of INIA 601 purple corn samples. NMF: nonmagnetic field; SMF: static magnetic field; PMF: pulse magnetic field. Different letters and color indicate statistically different groups ($p \leq 0.05$).

The geographical provenance of the samples exhibited a substantial influence on the outcomes, with the bract samples from Cochamarca demonstrating superior antioxidant activity, with an average of 81.5 µg/mL, in comparison to those from Cajabamba, which exhibited an average of 113.081 µg/mL.

4. Discussion

The outcomes for the corn-cob length (16.5 cm) aligned with those reported by Huaychani [26]. The length of a corn cob is closely associated with the optimal utilization of fertilizers containing nitrogen, phosphorus, and potassium as well as heightened sunlight intensity linked to elevated photosynthesis stimulation [27]. The impact of the insect Euxesta sp. is particularly problematic as it attacks the ears from the pistil formation stage and continues during the development of the grain [19]. This resulted in a high rotting percentage of 19.99% in Cajabamba compared with Cochamarca, which was 9.65%. The aforementioned factors directly affected the low yield (3.35 t/ha) in Cajabamba compared with Cochamarca (4.89 t/ha). However, high fertilization is possible, with yields of up to 6.6 t/ha according to the results reported by Huaychani (2022) [26].

The observed variation in phenol content could be attributed to the temperature fluctuations experienced during the day and night, which have been shown to induce stress in the crop, thereby stimulating the biosynthesis of anthocyanin and phenolic compounds in the crown and the pod of the cob [27]. Previous studies have examined the impact of magnetic fields on soybean, revealing their regulatory role in protein metabolism and leading to an augmentation in globulin and lipid production [28]. Additionally, these fields have been observed to enhance the levels of phenols and flavonoids in the shoots of lemon balm [29] and concentrate the mineral compounds in certain parts of a plant, as observed in Castlerock tomato, where P was found in the leaves of the plant [30].

Given the high content of bioactive compounds found in purple corn on the cob, it is necessary to specify that foods high in phenolic compounds are responsible for the stimulation of muscle tissue and the production of nitric oxide, necessary for the dilation of blood vessels [31].

Ramos-Escudero et al. [24] obtained an extract of INIA 601 purple corn grain with 80% methanol and 20% water and acidified with 1% HCl, and identified eight phenolic compounds. These were chlorogenic acid, caffeic acid, rutin, ferulic acid, morin, quercetin, naringenin, and kaempferol, the latter being the highest at 2240 mg/kg of the sample. Such studies highlight the presence of procyanidin B2 as the predominant phenol in various parts of INIA 601 purple corn, although the extraction and analytical methods used could influence the detection of other specific phenolic compounds.

The antioxidant activity is associated with the variety of plant samples utilized, the solvents employed, and the extraction techniques used for the bioactive compounds [32]. The outcomes significantly diverged from those reported by Ramos-Escudero et al. [24], who conducted an extraction using 80% methanol and 20% water acidified with 1% HCl (1 N), yielding a DPPH concentration of 66.3 µg/mL for the INIA 601 variety.

Variations by place of culture can be attributed to the diurnal temperature fluctuations, which have been observed to enhance bioactive compounds and, consequently, antioxidant activity [27].

Recent studies suggest that phytohormones have a direct influence on the gene expression of the biosynthetic pathways related to flavonoids and anthocyanins [33,34]. According to Shan et al. [35] the JAZ protein (jasmonate) is ubiquitinated by COI1 and subsequently degraded by the 26S proteasome, thereby promoting the release of bHLH and MYB transcription factors and reforming the stable MBW complex. This complex, in turn, promotes anthocyanin synthesis and accumulation in plants. Similarly, the auxin concentration has been observed to exert a promoting or inhibiting effect on anthocyanin production, with this effect being contingent upon the specific plant species [36]. A comparable phenomenon has been documented in the context of the phytohormone gibberellin [37]. Subsequent research endeavors could involve the investigation of the impact of magnetic fields on the activity of these phytohormones.

Finally, these findings allow the demonstration of the future applications of magnetic biostimulation in the high production of bioactive compounds in purple corn cultivation under different agro–climatic conditions. A larger experiment with a larger number of experimental units and different conditions could better clarify the results found in this work.

5. Conclusions

The utilization of magnetic fields on INIA 601 purple corn seeds prior to planting did not exert a substantial influence on the agronomic characteristics under consideration, with the exception of the length of the corn cob, which exceeded 16.5 cm. Furthermore, it was associated with the adequate fertilization of the soil. Conversely, the planting location exerted an influence on the crop characteristics, with Cajabamba exhibiting a greater propensity to experience adverse conditions, thereby exerting a negative effect on yield, in contrast to Cochamarca, which demonstrated superior results due to more favorable environmental conditions and a reduced incidence of pests and diseases.

The application of magnetic fields demonstrated the exertion of a substantial influence on the concentration of bioactive compounds, including total phenols and anthocyanins, within the corn cob. Conversely, the planting location exerted a discernible influence on the phenol content, with Cajabamba exhibiting 25.6 mg AGE/gss and Cochamarca registering 28.6 mg AGE/gss. Temperature variations were observed to stimulate anthocyanin biosynthesis, with higher levels recorded in the bract in Cochamarca (7.6 mg C3G/gss) as well as in the crown (9.4 mg C3G/gss). In contrast, lower levels of anthocyanin were detected in Cajabamba, with 6.5 mg C3G/gss in the bract and 9.3 mg C3G/gss in the crown. These findings underscore the pivotal role of environmental and climatic factors on the synthesis and composition of bioactive compounds in INIA 601 purple corn.

The analysis of 12 phenol compounds in various parts of the cob of INIA 601 purple corn highlighted the presence of procyanidin B2, especially in the bract and the crown, where it exceeded 50 and 40 mg/L, respectively. The analysis also identified the presence of resveratrol, epicatechin, kaempferol, and vanillin, among other phenols, although in lower concentrations. These findings underscore the remarkable diversity of phenols in INIA 601 purple corn across its various corn cobs, which could have significant ramifications for its utilization in the food and pharmaceutical sectors.

Author contributions

Conceptualization, T.C., C.L. and H.A.; methodology, T.C., F.Z.V., W.C. and P.J.F.; software, W.C., M.C.-G., P.J.F. and S.G.C.; formal analysis, F.Z.V., W.C. and N.L.H.-C.; investigation, T.C., C.L. and H.A.; writing—original draft preparation, T.C., C.L. and H.A.; writing—review and editing, N.L.H.-C., M.C.-G. and S.G.C.; visualization, H.A. All authors have read and agreed to the published version of the manuscript.

Funding

The APC was funded by Universidad Nacional Toribio Rodríguez de Mendoza de Amazonas, Perú, and the National Program for Scientific Research and Advanced Studies (PROCIENCIA)–CONCYTEC for financing within the framework of the call for Applied Research and Technological Development Projects 2020-02—Phase II [Contract No. 205-2020-FONDECYT].

Data availability statement

The original contributions presented in the study are included in the article, further inquiries can be directed to the corresponding author.

Conflicts of interest

The authors declare no conflicts of interest.

References

1. Ministerio de Desarrollo Agrario y Riego [MIDAGRI] MIDAGRI Impulsa Consumo y Comercialización de Maíz Peruano con Exitoso Festival que Reunió a Pequeños Productores de 9 Regiones. Available online: https://www.gob.pe/institucion/midagri/noticias/948885-midagri-impulsa-consumo-y-comercializacion-de-maiz-peruano-con-exitoso-festival-que-reunio-a-pequenos-productores-de-9-regiones (accessed on 5 May 2024).

2. Kang, M.K.; Lim, S.S.; Lee, J.Y.; Yeo, K.M.; Kang, Y.H. Anthocyanin-Rich Purple Corn Extract Inhibit Diabetes-Associated Glomerular Angiogenesis. PLoS ONE 2013, 8, 1–10. https://doi.org/10.1371/journal.pone.0079823.

3. Kim, H.Y.; Lee, K.Y.; Kim, M.; Hong, M.; Deepa, P.; Kim, S. A Review of the Biological Properties of Purple Corn (Zea mays L.). Sci. Pharm. 2023, 91, 6. https://doi.org/10.3390/scipharm91010006.

4. León-Perez, D.; Domínguez-Perles, R.; Collado-González, J.; Cano-Lamadrid, M.; Durand, T.; Guy, A.; Galano, J.M.; Carbonell-Barrachina, Á.; Londoño-Londoño, J.; Ferreres, F.; et al. Bioactive Plant Oxylipins-Based Lipidomics in Eighty Worldwide Commercial Dark Chocolates: Effect of Cocoa and Fatty Acid Composition on Their Dietary Burden. Microchem. J. 2020, 157, 105083. https://doi.org/10.1016/J.MICROC.2020.105083.

5. Barbosa, M.R.; Moreira, B.R.; Carreira, V.; Brito, A.; Trentin, C.; Pereira, F.; Tedesco, D.; Setiyono, T.; Flores, J.; Ampatzidis, Y.; et al. Precision Agriculture in the United States: A Comprehensive Meta-Review Inspiring Further Research, Innovation, and Adoption. Comput. Electron. Agric. 2024, 221, 108993. https://doi.org/10.1016/j.compag.2024.108993.

6. Effland, A.; Saavoss, M.; Capehart, T.; McBride, W.D.; Boline, A. Innovations in Seed and Farming Technologies Drive Productivity Gains and Costs on Corn Farms; USDA: New York, NY, USA, 2022; 18p.

7. Amir, M.; Prasad, D.; Khan, F.A.; Khan, A.; Ahamd, B.; Astha Seed Priming: An Overview of Techniques, Mechanisms, and Applications. Plant Sci. Today 2024, 11, 553–563. https://doi.org/10.14719/pst.2828.

8. Dadlani, M.; Yadava, D.K. Seed Science and Technology: Biology, Production, Quality; Springer: Cham, Switzerland, 2023; ISBN 9789811958885.

9. Lasso-Rivas, N. Efectos Positivos Del Campo Magnético En Plantas Cultivadas. Intropica 2019, 14, 160–170. https://doi.org/10.21676/23897864.3066.

10. Martinez, E.; Florez, M.; Carbonell, M.V. Stimulatory Effect of the Magnetic Treatment on the Germination of Cereal Seeds. Int. J. Environ. Agric. Biotechnol. 2017, 2, 375–381. https://doi.org/10.22161/ijeab/2.1.47.

11. Zhang, Y.; Yang, L.; Sun, W.; Ruan, Y.; Dou, H.; Song, M.; Long, H.; Zhang, Y.; Wang, Y.; Guo, J.; et al. An Effective Method of Magnetic Field Treatment in Increasing Soil Phosphorus Availability in Wheat Rhizosphere. Rhizosphere 2023, 27, 100760. https://doi.org/10.1016/j.rhisph.2023.100760.

12. Gollan, P.J.; Tikkanen, M.; Aro, E.M. Photosynthetic Light Reactions: Integral to Chloroplast Retrograde Signalling. Curr. Opin. Plant Biol. 2015, 27, 180–191. https://doi.org/10.1016/j.pbi.2015.07.006.

13. Kataria, S.; Baghel, L.; Guruprasad, K.N. Pre-Treatment of Seeds with Static Magnetic Field Improves Germination and Early Growth Characteristics under Salt Stress in Maize and Soybean. Biocatal. Agric. Biotechnol. 2017, 10, 83–90. https://doi.org/10.1016/j.bcab.2017.02.010.

14. Luo, L.; Zhu, M.; Jia, L.; Xie, Y.; Wang, Z.; Xuan, W. Ammonium Transporters Cooperatively Regulate Rice Crown Root Formation Responding to Ammonium Nitrogen. J. Exp. Bot. 2022, 73, 3671–3685. https://doi.org/10.1093/jxb/erac059.

15. Podleśna, A.; Bojarszczuk, J.; Podleśny, J. Effect of Pre-Sowing Magnetic Field Treatment on Some Biochemical and Physiological Processes in Faba Bean (Vicia

Faba L. Spp. Minor). J. Plant Growth Regul. 2019, 38, 1153–1160. https://doi.org/10.1007/s00344-019-09920-1.

16. Alattar, E.; Elwasife, K.; Radwan, E. Effects of Magnetic Field Treated Water on Some Growth Parameters of Corn (Zea mays) Plants. AIMS Biophys. 2021, 8, 266–288. https://doi.org/10.3934/biophy.2021021.

17. Pietruszewski, S.; Martínez, E. Magnetic Field as a Method of Improving the Quality of Sowing Material: A Review. Int. Agrophys. 2015, 29, 377–389. https://doi.org/10.1515/intag-2015-0044.

18. Castro, C.; McNab, A. Enfermedades del Maíz: Una Guía para su Identificación en el Campo; Food and Agriculture Organization: Rome, Italy, 2019; Volume 11, ISBN 9788578110796.

19. Medina-Hoyos, A.; Narro-León, L.A.; Chávez-Cabrera, A. Purple Corn (Zea Mays L.) Crop in the Peruvian Highlands: Adaptation and Identification of High-Yield and High Anthocyanin Content Cultivars. Sci. Agropecu. 2020, 11, 291–299. https://doi.org/10.17268/sci.agropecu.2020.03.01.

20. Lao, F.; Giusti, M.M. Extraction of Purple Corn (Zea Mays L.) Cob Pigments and Phenolic Compounds Using Food-Friendly Solvents. J. Cereal Sci. 2018, 80, 87–93. https://doi.org/10.1016/j.jcs.2018.01.001.

21. Lee, J.; Durst, R.W.; Wrolstad, R.E. Determination of Total Monomeric Anthocyanin Pigment Content of Fruit Juices, Beverages, Natural Colorants, and Wines by the PH Differential Method: Collaborative Study. J. AOAC Int. 2005, 88, 1269–1278. https://doi.org/10.1093/jaoac/88.5.1269.

22. Albarici, T.R.; De Freitas, D.; Cruz, J.D. Empresa Brasileira de Pesquisa Agropecuária Ministério da AgricProtocolos de Análises para Polpa de Açaí: Um Guia Prático de Consulta; Embrapa Instrumentação: Sao Carlos, Brazil, 2009; ISBN 9788586463198.

23. Jin, T.Z.; Yu, Y.; Gurtler, J.B. Effects of Pulsed Electric Field Processing on Microbial Survival, Quality Change and Nutritional Characteristics of Blueberries. LWT 2017, 77, 517–524. https://doi.org/10.1016/j.lwt.2016.12.009.

24. Ramos-Escudero, F.; Muñoz, A.M.; Alvarado-Ortíz, C.; Alvarado, Á.; Yáñez, J.A. Purple Corn (Zea Mays L.) Phenolic Compounds Profile and Its Assessment as an Agent against Oxidative Stress in Isolated Mouse Organs. J. Med. Food 2012, 15, 206–215. https://doi.org/10.1089/jmf.2010.0342.

25. Ratha, J.; Yongram, Chawalit Panyatip, Panyada Powijitku, P.; Siriparu, P.; Datham, Suthida Priprem, Aroonsri Srisongkram, Tarapong and Puthongking, P. (Zea Mays L .) Variety KND and Butterfly Pea (Clitoria ternatea). Plants 2023, 12, 1–16.

26. Huaychani, F.E. Evaluación del Comportamiento del Maíz Morado INIA 601 (Zea mays L.) con Tres Niveles de Fertilización en Condiciones de 3450 Msnm en Huanchac-Independencia-Huaraz-2019. Bachelor's Thesis, Universidad Nacional Santiago Antunez de Mayolo, Huaraz, Peru, 2022.

27. Mohamed, G.; Lertrat, K.; Suriharn, B. Phenolic Compound, Anthocyanin Content, and Antioxidant Activity in Some Parts of Purple Waxy Corn across Maturity Stages and Locations. Int. Food Res. J. 2017, 24, 490–497.

28. Radhakrishnan, R. Seed Pretreatment with Magnetic Field Alters the Storage Proteins and Lipid Profiles in Harvested Soybean Seeds. Physiol. Mol. Biol. Plants 2018, 24, 343–347. https://doi.org/10.1007/s12298-018-0505-8.

29. Ulgen, C.; Yildirim, A.B.; Sahin, G.; Turker, A.U. Do Magnetic Field Applications Affect in Vitro Regeneration, Growth, Phenolic Profiles, Antioxidant Potential and Defense Enzyme Activities (SOD, CAT and PAL) in Lemon Balm (Melissa officinalis L.)? Ind. Crops Prod. 2021, 169, 113624. https://doi.org/10.1016/j.indcrop.2021.113624.

30. Abou El-Yazied, A.; El-Gizawy, A.M.; Khalf, S.M.; El-Satar, A.; Shalaby, O.A. Effect of Magnetic Field Treatments for Seeds and Irrigation Water as Well as N, P and K Levels on Productivity of Tomato Plants. J. Appl. Sci. Res. 2012, 8, 2088–2099.

31. Socci, V.; Tempesta, D.; Desideri, G.; De Gennaro, L.; Ferrara, M. Enhancing Human Cognition with Cocoa Flavonoids. Front. Nutr. 2017, 4, 1–7. https://doi.org/10.3389/fnut.2017.00019.

32. Žilić, S.; Serpen, A.; Akillioğlu, G.; Gökmen, V.; Vančetović, J. Phenolic Compounds, Carotenoids, Anthocyanins, and Antioxidant Capacity of Colored Maize (Zea mays L.) Kernels. J. Agric. Food Chem. 2012, 60, 1224–1231. https://doi.org/10.1021/jf204367z.

33. Shi, L.; Li, X.; Fu, Y.; Li, C. Environmental Stimuli and Phytohormones in Anthocyanin Biosynthesis: A Comprehensive Review. Int. J. Mol. Sci. 2023, 24, 1–17. https://doi.org/10.3390/ijms242216415.

34. Wang, L.; Yang, S.; Ni, J.; Teng, Y.; Bai, S. Advances of Anthocyanin Synthesis Regulated by Plant Growth Regulators in Fruit Trees. Sci. Hortic. 2023, 307, 111476. https://doi.org/10.1016/j.scienta.2022.111476.

35. Shan, X.; Zhang, Y.; Peng, W.; Wang, Z.; Xie, D. Molecular Mechanism for Jasmonate-Induction of Anthocyanin Accumulation in Arabidopsis. J. Exp. Bot. 2009, 60, 3849–3860. https://doi.org/10.1093/jxb/erp223.

36. Li, Z.; Ahammed, G.J. Hormonal Regulation of Anthocyanin Biosynthesis for Improved Stress Tolerance in Plants. Plant Physiol. Biochem. 2023, 201, 107835. https://doi.org/10.1016/j.plaphy.2023.107835.

37. LaFountain, A.M.; Yuan, Y.W. Repressors of Anthocyanin Biosynthesis. New Phytol. 2021, 231, 933–949. https://doi.org/10.1111/nph.17397.

V. Conclusiones

✓ **Prediction of physico-chemical parameters of goldenberry**

The technique of dielectric spectroscopy has proven to be a promising tool for the prediction of soluble solids ($R^2 = 0.7760$, RMSE = 0.5185), acidity ($R^2 = 0.479$, RMSE = 0.2391), and pH ($R^2 = 0.9994$, RMSE = 0.0221) of goldenberry fruits at point frequencies of 915, 5800, and 2450 MHz, respectively. This enables the future development of miniaturised dielectric sensors for the rapid and non-destructive evaluation of the internal quality of goldenberry fruits

✓ **Non-invasive monitoring of aguaymanto drying**

A drying monitoring system using infrared thermography has been developed to follow the drying process of goldenberry to optimum conditions. To this end, the evolution of the emissivity of the fruit surface during the process was obtained.

The evolution of the phenomenological coefficient of goldenberry drying during the process has been obtained, which will allow this operation to be predicted in the future.

The mechanical effect (internal fractures, plasmolysis and storage of mechanical energy) in the goldenberry dehydration process has been observed. This will allow both the rehydration capacity of the fruit and its effect on a formulated food system to be predicted.

Engineering tools such as the sorption isotherm, emissivity and phenomenological coefficient were obtained, which will facilitate future modelling of goldenberry drying.

The integration of infrared thermography with thermodynamic modeling provides a powerful tool for improving the efficiency and control of convective drying processes in the food industry. By enabling non-invasive, real-time monitoring of surface temperature and emissivity, this system allows for better identification of critical drying stages and optimization of process parameters. Furthermore, the quantification of water flux and chemical potential gradients supports a more accurate prediction of moisture migration, which is crucial for minimizing energy consumption, reducing drying time, and preserving product quality. These findings offer a valuable basis for the development of more sustainable and cost-effective drying protocols for high-moisture fruits such as goldenberry.

✓ Non-invasive monitoring of aguaymanto freezing

The findings indicate that infrared thermography is a viable method for monitoring the freezing process of goldenberry, as it facilitates the observation of surface temperature variations. This tool facilitates the identification of critical points in the process, such as the glass transition, from the estimation of the emissivity at different stages of freezing; supercooling stage: Detected by a continuous temperature drop without phase change, and a sharp decrease in emissivity from ~0.959 to 0.837. This stage ends with the onset of nucleation. Ice nucleation and crystallization stage: Identified by a plateau or slight rebound in temperature due to latent heat release, along with stable emissivity (~0.845) and changes in dielectric α- and β-dispersions, reflecting structural changes (β) and cryoconcentration (α). And finally, Vitrification stage: Occurs after ice crystallization is completed. Emissivity increases again (~0.93 to 0.951) as the system approaches the glass transition. The glass transition temperature (−35.8 °C) marks the point where molecular mobility becomes severely restricted, thus preserving cellular structure by preventing further ice growth and solute migration. This enhances long-term structural and biochemical stability during frozen storage.

Conversely, the utilization of sensors founded upon radiofrequency spectrophotometry facilitates the acquisition of not merely surface information, as is the case in thermography, but also the internal properties of samples undergoing the freezing process. This is imperative for the precise detection of the critical points of the process (melting point and glass transition), thereby ensuring uniform and efficient freezing of the goldenberry.

✓ Identification of cold chain breakage in mackerel fillets

The findings of this study indicate that the LSTM networks were superior to the RBNN networks for discriminating between fish fillets subjected to different FTC, achieving an average F-measure greater than 0.89 and accuracy greater than 0.93. Based on these findings, it is feasible to implement systems that utilize this technique to manage the transportation and preservation of this particular type of food. In order to improve the effectiveness of the LSTM networks, it would be beneficial for future research to investigate how modifying their layers and adjusting the training parameters can impact their training speed. It is crucial to develop an automated system to keep a check on the condition of fish fillets while they are being transported and stored. The system can notify the authorities immediately in case of any abnormalities to guarantee compliance with food safety regulations.

✓ **Pork Quality Prediction**

The transformation of muscle into meat for males and females has shown that the intensity values of the dielectric constant and loss factor decrease as the frequency increases. This allows the types of DFD and RFN meat for samples of males and females to be differentiated at 24 hpm.

Robust models were created using PLSR to predict internal quality during muscle to meat transformation. Performance was moderate for male pig meat. R^2 of 0.743 (pH), 0.811 (L*) and 0.603 (C*) for DFD meat with PLSR (full) and R^2 of 0.359 (pH), 0.558 (L*) and 0.284 (C*) for RNF meat with PLSR (optimized). R_{cv}^2 of 0.412 - 0.637 for pH, L* and C* for RFN and DFD meat from female sows with PLSR (optimized). New chemometric models are needed to improve the prediction of internal pork meat quality.

✓ **Bean hydration monitoring**

The hyperspectral imaging technique was used to monitor the hydration of pinto beans. Mean reflectance spectra were obtained in the 400 to 800 nm range. The best relationship between moisture content and reflectance value was identified at 632 nm, with a goodness of fit of R2 = 0.9966 and RMSE = 2.30. The hydration kinetics were subsequently modelled using the Peleg and Sigmoidal equations, resulting in high goodness of fit of R2 = 0.989 and R2 = 0.996, respectively. Hyperspectral imaging is a promising tool for monitoring and modelling the hydration kinetics of pinto beans. This technique is useful for beans with both sigmoidal and concave downward shapes of hydration kinetics. Consequently, future studies using more grains are required to validate the optimal wavelength.

✓ Application of magnetic fields to purple maize INIA 601

The utilization of magnetic fields on INIA 601 purple corn seeds prior to planting did not exert a substantial influence on the agronomic characteristics under consideration, with the exception of the length of the corn cob, which exceeded 16.5 cm. Furthermore, it was associated with the adequate fertilization of the soil. Conversely, the planting location exerted an influence on the crop characteristics, with Cajabamba exhibiting a greater propensity to experience adverse conditions, thereby exerting a negative effect on yield, in contrast to Cochamarca, which demonstrated superior results due to more favorable environmental conditions and a reduced incidence of pests and diseases.

The application of magnetic fields demonstrated the exertion of a substantial influence on the concentration of bioactive compounds, including total phenols and anthocyanins, within the corn cob. Conversely, the planting location exerted a discernible influence on the phenol content, with Cajabamba exhibiting 25.6 mg AGE/gss and Cochamarca registering 28.6 mg AGE/gss. Temperature variations were observed to stimulate anthocyanin biosynthesis, with higher levels recorded in the bract in Cochamarca (7.6 mg C3G/gss) as well as in the crown (9.4 mg C3G/gss). In contrast, lower levels of anthocyanin were detected in Cajabamba, with 6.5 mg C3G/gss in the bract and 9.3 mg C3G/gss in the crown. These findings underscore the pivotal role of environmental and climatic factors on the synthesis and composition of bioactive compounds in INIA 601 purple corn.

The analysis of 12 phenol compounds in various parts of the cob of INIA 601 purple corn highlighted the presence of procyanidin B2, especially in the bract and the crown, where it exceeded 50 and 40 mg/L, respectively. The analysis also identified the presence of resveratrol, epicatechin, kaempferol, and vanillin, among other phenols, although in lower concentrations. These findings underscore the remarkable diversity of phenols in INIA 601 purple corn across its various corn cobs, which could have significant ramifications for its utilization in the food and pharmaceutical sectors.

VI. Bibliografía

Abdel Latef, A. A. H., Dawood, M. F. A., Hassanpour, H., Rezayian, M., & Younes, N. A. (2020). Impact of the Static Magnetic Field on Growth, Pigments, Osmolytes, Nitric Oxide, Hydrogen Sulfide, Phenylalanine Ammonia-Lyase Activity, Antioxidant Defense System, and Yield in Lettuce. *Biology*, *9*(7), 172. https://doi.org/10.3390/biology9070172

Amigo, J. M., Martí, I., & Gowen, A. (2013). Hyperspectral Imaging and Chemometrics: A Perfect Combination for the Analysis of Food Structure, Composition and Quality. Data Handling in Science and Technology, 28, 343–370. https://doi.org/10.1016/B978-0-444-59528-7.00009-0

Aviara, N. A., Liberty, J. T., Olatunbosun, O. S., Shoyombo, H. A., & Oyeniyi, S. K. (2022). Potential application of hyperspectral imaging in food grain quality inspection, evaluation and control during bulk storage. Journal of Agriculture and Food Research, 8, 100288. https://doi.org/10.1016/J.JAFR.2022.100288

Bezerra, E. A., Carvalho, C. P. S., Costa Filho, R. N., Silva, A. F. B., Alam, M., Sales, M. V., Dias, N. L., Gonçalves, J. F. C., Freitas, C. D. T., & Ramos, M. V. (2023). Static magnetic field promotes faster germination and increases germination rate of Calotropis procera seeds stimulating cellular metabolism. Biocatalysis and Agricultural Biotechnology, 49, 102650. https://doi.org/10.1016/J.BCAB.2023.102650

Blas Saavedra, R., Cruz-Tirado, J. P., Figueroa-Avalos, H. M., Barbin, D. F., Amigo, J. M., & Siche, R. (2024). Prediction of physicochemical properties of cape gooseberry (Physalis peruviana L.) using near infrared hyperspectral imaging (NIR-HSI). Journal of Food Engineering, 371, 111991. https://doi.org/10.1016/j.jfoodeng.2024.111991

Castro Giraldez, M. (2010). Estudio de los espectros dieléctricos para el control de calidad de alimentos [Universitat Politècnica de València]. https://doi.org/10.4995/Thesis/10251/8550

Castro-Giráldez, M., Aristoy, M.-C., Toldrá, F., & Fito, P. (2010). Microwave dielectric spectroscopy for the determination of pork meat quality. Food Research International, 43(10), 2369–2377. https://doi.org/10.1016/j.foodres.2010.09.003

Castro-Giráldez, M., Balaguer, N., Hinarejos, E., & Fito, P. J. (2014). Thermodynamic approach of meat freezing process. Innovative Food Science & Emerging Technologies, 23, 138–145. https://doi.org/10.1016/j.ifset.2014.03.007

Castro-Giráldez, M., Fito, P. J., Chenoll, C., & Fito, P. (2010). Development of a Dielectric Spectroscopy Technique for Determining Key Chemical Components of Apple Maturity. Journal of Agricultural and Food Chemistry, 58(6), 3761–3766. https://doi.org/10.1021/jf903338b

Castro-Giráldez, M., Fito, P. J., & Fito, P. (2010). Application of microwaves dielectric spectroscopy for controlling pork meat (Longissimus dorsi) salting process. Journal of Food Engineering, 97(4), 484–490. https://doi.org/10.1016/j.jfoodeng.2009.11.005

Castro Silupu, W. M. (2016). Aplicación de la tecnología de imágenes hiperespectrales al control de calidad de productos agroalimentarios de la región de Amazonas (Perú) [Universitat Politècnica de València]. https://doi.org/10.4995/Thesis/10251/63250

Castro, W., Prieto, J. M., Guerra, R., Chuquizuta, T., Medina, W. T., Acevedo-Juárez, B., & Avila-George, H. (2018). Feasibility of using spectral profiles for modeling water activity in five varieties of white quinoa grains. Journal of Food Engineering, 238, 95–102. https://doi.org/10.1016/j.jfoodeng.2018.06.012

Castro, W., Saavedra, M., Castro, J., Tech, A. R. B., Chuquizuta, T., & Avila-George, H. (2024). Using recurrent neural networks to identify broken-cold-chain fish fillet from spectral profiles. Neural Computing and Applications, 36(8), 4377–4386. https://doi.org/10.1007/s00521-023-09311-4

Castro, W., Tene, B., Castro, J., Guivin, A., Ruesta, N., & Avila-George, H. (2024). Mango varietal discrimination using hyperspectral imaging and machine learning. Neural Computing and Applications, 36(30), 18693–18703. https://doi.org/10.1007/s00521-024-10218-x

Chandra Roychoudhuri, A. F. K. K. C. (2017). The Nature of Light What is a Photon? (Thompson Brian J., Ed.). CRC Press.

Cheng, J. H., Nicolai, B., & Sun, D. W. (2017). Hyperspectral imaging with multivariate analysis for technological parameters prediction and classification of muscle foods: A review. Meat Science, 123, 182–191. https://doi.org/10.1016/J.MEATSCI.2016.09.017

Cheng, J.-H., Sun, D.-W., Pu, H.-B., Chen, X., Liu, Y., Zhang, H., & Li, J.-L. (2015). Integration of classifiers analysis and hyperspectral imaging for rapid discrimination of fresh from cold-stored and frozen-thawed fish fillets. Journal of Food Engineering, 161, 33–39. https://doi.org/10.1016/j.jfoodeng.2015.03.011

Chuquizuta, T., Castro, W., Castro-Giraldez, M., & Fito, P. J. (2025). Non-invasive monitoring of goldenberry freezing using infrared thermography and radiofrequency dielectric spectroscopy. Innovative Food Science & Emerging Technologies, 104, 104134. https://doi.org/10.1016/J.IFSET.2025.104134

Chuquizuta, T., Castro, W., Castro-Giraldez, M., & Fito, P. J. (2026). Thermodynamic model and infrared thermography monitoring system for convective drying of goldenberry (Physalis peruviana). Journal of Food Engineering, 404, 112773. https://doi.org/10.1016/J.JFOODENG.2025.112773

Chuquizuta, T., Chavez, S. G., Miano, A. C., Castro-Giraldez, M., Fito, P. J., Arteaga, H., & Castro, W. (2024). Determination of hydration kinetic of pinto beans: A hyperspectral images application. Measurement: Food, 14, 100161. https://doi.org/10.1016/J.MEAFOO.2024.100161

Chuquizuta, T., Colunche, Y., Rubio, M., Oblitas, J., Arteaga, H., & Castro, W. (2022). Prediction of Quality Attributes of Fresh Unpasteurized Milk Using Dielectric Spectroscopy Coupled to Chemometric Tools. 2022 Photonics & Electromagnetics Research Symposium (PIERS), 776–782. https://doi.org/10.1109/PIERS55526.2022.9792687

Chuquizuta, T., Lobato, C., Zirena Vilca, F., Huamán-Castilla, N. L., Castro, W., Castro-Giraldez, M., Fito, P. J., Chavez, S. G., & Arteaga, H. (2025). Impact of Magnetic Biostimulation and Environmental Conditions on the Agronomic Quality and Bioactive Composition of INIA 601 Purple Maize. Foods, 14(12), 2045. https://doi.org/10.3390/foods14122045

Chuquizuta, T., Oblitas, J., Arteaga, H., Yarleque, M., & Castro, W. (2021). Dielectric Spectral Profiles for Andean Tubers Classification: A Machine Learning Techniques Application. 2021 International Conference on Electromagnetics in Advanced Applications, ICEAA 2021. https://doi.org/10.1109/ICEAA52647.2021.9539623

Chuquizuta, T., Peralta, M., Medina, S., Arteaga, H., Oblitas, J., Chavez, S. G., Castro, W., Castro-Giraldez, M., & Fito, P. J. (2025). Dielectric spectroscopy for the prediction of pork quality during the post-mortem time. Journal of Food Composition and Analysis, 148, 108128. https://doi.org/10.1016/J.JFCA.2025.108128

Cuibus, L., Castro-Giráldez, M., Fito, P. J., & Fabbri, A. (2014). Application of infrared thermography and dielectric spectroscopy for controlling freezing process of raw potato. Innovative Food Science & Emerging Technologies, 24, 80–87. https://doi.org/10.1016/j.ifset.2013.11.007

Dale, L. M., Thewis, A., Boudry, C., Rotar, I., Dardenne, P., Baeten, V., & Pierna, J. A. F. (2013). Hyperspectral Imaging Applications in Agriculture and Agro-Food Product Quality and Safety Control: A Review. Applied Spectroscopy Reviews, 48(2), 142–159. https://doi.org/10.1080/05704928.2012.705800

Demirel, Y., & Gerbaud, V. (2019a). Fundamentals of Nonequilibrium Thermodynamics. Nonequilibrium Thermodynamics, 135–186. https://doi.org/10.1016/B978-0-444-64112-0.00003-4

Demirel, Y., & Gerbaud, V. (2019b). Heat and Mass Transfer. Nonequilibrium Thermodynamics, 337–379. https://doi.org/10.1016/B978-0-444-64112-0.00007-1

Demirel, Y., & Gerbaud, V. (2019c). Thermodynamics and Biological Systems. Nonequilibrium Thermodynamics, 489–571. https://doi.org/10.1016/B978-0-444-64112-0.00011-3

Demirel, Y., & Sandler, S. I. (2001). Linear-nonequilibrium thermodynamics theory for coupled heat and mass transport. International Journal of Heat and Mass Transfer, 44(13), 2439–2451. https://doi.org/10.1016/S0017-9310(00)00291-X

El Khaled, D., Castellano, N., Gázquez, J., Perea-Moreno, A.-J., & Manzano-Agugliaro, F. (2016). Dielectric Spectroscopy in Biomaterials: Agrophysics. Materials, 9(5), 310. https://doi.org/10.3390/ma9050310

Elmasry, G., Kamruzzaman, M., Sun, D.-W., & Allen, P. (2012). Principles and Applications of Hyperspectral Imaging in Quality Evaluation of Agro-Food Products: A Review. Critical Reviews in Food Science and Nutrition, 52(11), 999–1023. https://doi.org/10.1080/10408398.2010.543495

Feldman, Y., Ishai, P. Ben, Puzenko, A., & Raicu, V. (2015). Elementary Theory of the Interaction of Electromagnetic Fields with Dielectric Materials. In Dielectric Relaxation in Biological Systems (pp. 32–59). Oxford University Press. https://doi.org/10.1093/acprof:oso/9780199686513.003.0002

Fletcher, N. H. (1970). The Chemical Physics of Ice. Cambridge University Press. https://doi.org/10.1017/CBO9780511735639

Fodor, M., Matkovits, A., Benes, E. L., & Jókai, Z. (2024). The Role of Near-Infrared Spectroscopy in Food Quality Assurance: A Review of the Past Two Decades. Foods, 13(21), 3501. https://doi.org/10.3390/foods13213501

Gonçalves, B. J., Giarola, T. M. de O., Pereira, D. F., Vilas Boas, E. V. de B., & de Resende, J. V. (2016). Using infrared thermography to evaluate the injuries of cold-stored guava. Journal of Food Science and Technology, 53(2), 1063–1070. https://doi.org/10.1007/s13197-015-2141-4

Gowen, A. A., O'Donnell, C. P., Cullen, P. J., Downey, G., & Frias, J. M. (2007). Hyperspectral imaging – an emerging process analytical tool for food quality and safety control. Trends in Food Science & Technology, 18(12), 590–598. https://doi.org/10.1016/J.TIFS.2007.06.001

Greenebaum, B., & Barnes, F. (Eds.). (2018). Bioengineering and Biophysical Aspects of Electromagnetic Fields. CRC Press. https://doi.org/10.1201/9781315186580

Grigelmo-Miguel, N., Soliva-fortuny, R., Barbosa-Cánovas, G. V., & Martín-Belloso, O. (2010). Use of Oscillating Magnetic Fields in Food Preservation. In Nonthermal Processing Technologies for Food (pp. 222–235). Wiley. https://doi.org/10.1002/9780470958360.ch16

Guo, L., Azam, S. M. R., Guo, Y., Liu, D., & Ma, H. (2022). Germicidal efficacy of the pulsed magnetic field against pathogens and spoilage microorganisms in food processing: An overview. Food Control, 136, 108496. https://doi.org/10.1016/J.FOODCONT.2021.108496

Guo, W., Fang, L., Liu, D., & Wang, Z. (2015). Determination of soluble solids content and firmness of pears during ripening by using dielectric spectroscopy. Computers and Electronics in Agriculture, 117, 226–233. https://doi.org/10.1016/j.compag.2015.08.012

Harrap, M. J. M., Hempel de Ibarra, N., Whitney, H. M., & Rands, S. A. (2018). Reporting of thermography parameters in biology: a systematic review of thermal imaging literature. Royal Society Open Science, 5(12), 181281. https://doi.org/10.1098/rsos.181281

Hassoun, A., Jagtap, S., Garcia-Garcia, G., Trollman, H., Pateiro, M., Lorenzo, J. M., Trif, M., Rusu, A. V., Aadil, R. M., Šimat, V., Cropotova, J., & Câmara, J. S. (2023). Food quality 4.0: From traditional approaches to digitalized automated analysis. Journal of Food Engineering, 337, 111216. https://doi.org/10.1016/J.JFOODENG.2022.111216

Huang, H., Liu, L., & Ngadi, M. (2014a). Recent Developments in Hyperspectral Imaging for Assessment of Food Quality and Safety. Sensors, 14(4), 7248–7276. https://doi.org/10.3390/s140407248

Huang, H., Liu, L., & Ngadi, M. (2014b). Recent Developments in Hyperspectral Imaging for Assessment of Food Quality and Safety. Sensors, 14(4), 7248–7276. https://doi.org/10.3390/s140407248

Hu, J. you, Zhang, J., Mei, M., Yang, W. min, & Shen, Q. (2019). Quality control of a four-echelon agri-food supply chain with multiple strategies. Information Processing in Agriculture, 6(4), 425–437. https://doi.org/10.1016/J.INPA.2019.05.002

Hussain, M. S., Dastgeer, G., Afzal, A. M., Hussain, S., & Kanwar, R. R. (2020). Eco-friendly magnetic field treatment to enhance wheat yield and seed germination growth. Environmental Nanotechnology, Monitoring & Management, 14, 100299. https://doi.org/10.1016/j.enmm.2020.100299

Ibarz, A., & Barbosa-Canovas, G. V. (2002). Unit Operations in Food Engineering. CRC Press. https://doi.org/10.1201/9781420012620

Kang, R., Park, B., Ouyang, Q., & Ren, N. (2021). Rapid identification of foodborne bacteria with hyperspectral microscopic imaging and artificial intelligence classification algorithms. Food Control, 130, 108379. https://doi.org/10.1016/J.FOODCONT.2021.108379

Kataria, S., Baghel, L., & Guruprasad, K. N. (2017). Pre-treatment of seeds with static magnetic field improves germination and early growth characteristics under salt stress in maize and soybean. Biocatalysis and Agricultural Biotechnology, 10, 83–90. https://doi.org/10.1016/J.BCAB.2017.02.010

Kuang, W., & Nelson, S. O. (1998). Low-frequency dielectric properties of biological tissues: A review with some new insights. Transactions of the American Society of Agricultural Engineers, 41(1), 173–184.

Kumari, K., Chakraborty, S., Kishore, A., John, H., & Sinha, C. (2025). Dielectric Spectroscopy: Process and Quality Monitoring of Dairy Products: A Review. Agricultural Research, 14(1), 47–69. https://doi.org/10.1007/s40003-025-00840-z

Liu, D., & Guo, W. (2017). Nondestructive determination of soluble solids content of persimmons by using dielectric spectroscopy. International Journal of Food Properties, 20(sup3), S2596–S2611. https://doi.org/10.1080/10942912.2017.1381114

Liu, D., Sun, D.-W., & Zeng, X.-A. (2014). Recent Advances in Wavelength Selection Techniques for Hyperspectral Image Processing in the Food Industry. Food and Bioprocess Technology, 7(2), 307–323. https://doi.org/10.1007/s11947-013-1193-6

Marín-Méndez, J. J., Luri Esplandiú, P., Alonso-Santamaría, M., Remirez-Moreno, B., Urtasun Del Castillo, L., Echavarri Dublán, J., Almiron-Roig, E., & Sáiz-Abajo, M. J. (2024). Hyperspectral imaging as a non-destructive technique for estimating the nutritional value of food. Current Research in Food Science, 9, 100799. https://doi.org/10.1016/J.CRFS.2024.100799

Martínez-Domingo, M. Á., Valero-Benito, E. M., & Hernández-Andrés, J. (2024). Multispectral and Hyperspectral Imaging. In Non-invasive and Non-destructive Methods for Food

Integrity (pp. 175–201). Springer Nature Switzerland. https://doi.org/10.1007/978-3-031-76465-3_9

McClelland, A., & Mankin, M. (2018). Optical Measurements for Scientists and Engineers. Cambridge University Press. https://doi.org/10.1017/9781316779613

Miñano, H. L. A., Silva, A. C. de S., Souto, S., & Costa, E. J. X. (2020). Magnetic Fields in Food Processing Perspectives, Applications and Action Models. Processes, 8(7), 814. https://doi.org/10.3390/pr8070814

Nelson, S. O. (2005). Dielectric spectroscopy in agriculture. Journal of Non-Crystalline Solids, 351(33–36), 2940–2944. https://doi.org/10.1016/J.JNONCRYSOL.2005.04.081

Okpala, C. O. R., & Korzeniowska, M. (2023). Understanding the Relevance of Quality Management in Agro-food Product Industry: From Ethical Considerations to Assuring Food Hygiene Quality Safety Standards and Its Associated Processes. Food Reviews International, 39(4), 1879–1952. https://doi.org/10.1080/87559129.2021.1938600

Onsager, L. (1931a). Reciprocal Relations in Irreversible Processes. I. Physical Review, 37(4), 405–426. https://doi.org/10.1103/PhysRev.37.405

Onsager, L. (1931b). Reciprocal Relations in Irreversible Processes. II. Physical Review, 38(12), 2265–2279. https://doi.org/10.1103/PhysRev.38.2265

Patel, D., Bhise, S., Kapdi, S. S., & Bhatt, T. (2024). Non-destructive hyperspectral imaging technology to assess the quality and safety of food: a review. Food Production, Processing and Nutrition, 6(1), 69. https://doi.org/10.1186/s43014-024-00246-4

Pearsall, T. P. (2020). Photons (pp. 19–53). https://doi.org/10.1007/978-3-030-47325-9_2

Peskin, M. E. (2018). An Introduction To Quantum Field Theory. CRC Press. https://doi.org/10.1201/9780429503559

Podleśna, A., Bojarszczuk, J., & Podleśny, J. (2019). Effect of Pre-sowing Magnetic Field Treatment on Some Biochemical and Physiological Processes in Faba Bean (Vicia faba L. spp. Minor). Journal of Plant Growth Regulation, 38(3), 1153–1160. https://doi.org/10.1007/s00344-019-09920-1

Poirier-Pocovi, M., Volder, A., & Bailey, B. N. (2020). Modeling of reference temperatures for calculating crop water stress indices from infrared thermography. Agricultural Water Management, 233, 106070. https://doi.org/10.1016/j.agwat.2020.106070

Raymer, M. G., & Polakos, P. (2023). States, Modes, Fields, and Photons in Quantum Optics. Acta Physica Polonica A, 143(6), S28–S41. https://doi.org/10.12693/APhysPolA.143.S28

Reyes, A., Yarleque, M., Castro, W., & Chuquizuta, S. (2017). Determination of dielectric properties of the red delicious apple and its correlation with quality parameters. 2017 Progress in Electromagnetics Research Symposium - Fall (PIERS - FALL), 2067–2072. https://doi.org/10.1109/PIERS-FALL.2017.8293478

Reyes, A., Yarleque, M., Castro, W., & Chuquizuta, S. (2018). Determination of Permittivity Values Using Microwave Dielectric Spectroscopy for Assessing Apple and Purple Sweet Potato Quality Parameters. 2018 International Conference on Electromagnetics in Advanced Applications (ICEAA), 593–596. https://doi.org/10.1109/ICEAA.2018.8520427

Saha, D., & Manickavasagan, A. (2021). Machine learning techniques for analysis of hyperspectral images to determine quality of food products: A review. Current Research in Food Science, 4, 28–44. https://doi.org/10.1016/J.CRFS.2021.01.002

Saleh, B. E., & Teich, M. C. (2019). Fundamentals of photonics (Vol. 2). Wiley.

Schwartz, M. D. (2013). Quantum Field Theory and the Standard Model. Cambridge University Press. https://doi.org/10.1017/9781139540940

Shammi, S., Sohel, F., Diepeveen, D., Zander, S., & Jones, M. G. K. (2023). Machine learning-based detection of frost events in wheat plants from infrared thermography. European Journal of Agronomy, 149, 126900. https://doi.org/10.1016/j.eja.2023.126900

Shammi, S., Sohel, F., Diepeveen, D., Zander, S., Jones, M. G. K., Bekuma, A., & Biddulph, B. (2022). Machine learning-based detection of freezing events using infrared thermography. Computers and Electronics in Agriculture, 198, 107013. https://doi.org/10.1016/j.compag.2022.107013

Shen, X., Xing, L., Pan, L., Miao, Y., & Zhang, W. (2025). Prediction of chicken breast meat freshness based on hyperspectral imaging technique and high-throughput sequencing. Poultry Science, 104(4), 104999. https://doi.org/10.1016/J.PSJ.2025.104999

Taghinezhad, E., Szumny, A., Figiel, A., Latifi Amoghin, M., Mirzazadeh, A., Blasco, J., Mazurek, S., & Castillo-Gironés, S. (2025). The potential application of HSI and VIS/NIR spectroscopy for non-invasive detection of starch gelatinization and head rice yield during parboiling and drying process. Journal of Food Composition and Analysis, 142, 107443. https://doi.org/10.1016/J.JFCA.2025.107443

Talens, C., Castro-Giraldez, M., & Fito, P. J. (2016a). A thermodynamic model for hot air microwave drying of orange peel. Journal of Food Engineering, 175, 33–42. https://doi.org/10.1016/j.jfoodeng.2015.12.001

Talens, C., Castro-Giraldez, M., & Fito, P. J. (2016b). Study of the effect of microwave power coupled with hot air drying on orange peel by dielectric spectroscopy. LWT - Food Science and Technology, 66, 622–628. https://doi.org/10.1016/j.lwt.2015.11.015

Tirado-Kulieva, V., Quijano-Jara, C., Avila-George, H., & Castro, W. (2024a). Predicting the evolution of pH and total soluble solids during coffee fermentation using near-infrared spectroscopy coupled with chemometrics. Current Research in Food Science, 9, 100788. https://doi.org/10.1016/J.CRFS.2024.100788

Tirado-Kulieva, V., Quijano-Jara, C., Avila-George, H., & Castro, W. (2024b). Predicting the evolution of pH and total soluble solids during coffee fermentation using near-infrared spectroscopy coupled with chemometrics. Current Research in Food Science, 9, 100788. https://doi.org/10.1016/J.CRFS.2024.100788

Tomás Egea, J. Á. (2022). Fotónica aplicada a la monitorización de procesos y al desarrollo de sensores en la industria agroalimentaria [Universitat Politècnica de València]. https://doi.org/10.4995/Thesis/10251/182292

Tomas-Egea, J. A., Castro-Giraldez, M., Colom, R. J., & Fito, P. J. (2022). New technique for determining the critical freezing temperatures of chicken breast based on radiofrequency photospectrometry. Journal of Food Engineering, 333, 111155. https://doi.org/10.1016/j.jfoodeng.2022.111155

Tomas-Egea, J. A., Fito, P. J., & Castro-Giraldez, M. (2019). Analysis of Apple Candying by Microwave Spectroscopy. Foods, 8(8), 316. https://doi.org/10.3390/foods8080316

Tomas-Egea, J. A., Traffano-Schiffo, M. V., Castro-Giraldez, M., & Fito, P. J. (2021). Hot Air and Microwave Combined Drying of Potato Monitored by Infrared Thermography. Applied Sciences, 11(4), 1730. https://doi.org/10.3390/app11041730

Trabelsi, S., & Nelson, S. O. (2016). Microwave sensing of quality attributes of agricultural and food products. IEEE Instrumentation & Measurement Magazine, 19(1), 36–41. https://doi.org/10.1109/MIM.2016.7384959

Traffano Schiffo, M. V. (2017). Espectrofotometría de baja frecuencia aplicada a sistemas alimentarios [Universitat Politècnica de València]. https://doi.org/10.4995/Thesis/10251/90441

Traffano-Schiffo, M. V., Castro-Giraldez, M., Colom, R. J., & Fito, P. J. (2018a). Innovative photonic system in radiofrequency and microwave range to determine chicken meat quality. Journal of Food Engineering, 239, 1–7. https://doi.org/10.1016/j.jfoodeng.2018.06.029

Traffano-Schiffo, M. V., Castro-Giraldez, M., Colom, R. J., & Fito, P. J. (2018b). Innovative photonic system in radiofrequency and microwave range to determine chicken meat quality. Journal of Food Engineering, 239, 1–7. https://doi.org/10.1016/j.jfoodeng.2018.06.029

Traffano-Schiffo, M. V., Castro-Giraldez, M., Colom, R. J., & Fito, P. J. (2018c). New Spectrophotometric System to Segregate Tissues in Mandarin Fruit. Food and Bioprocess Technology, 11(2), 399–406. https://doi.org/10.1007/s11947-017-2019-8

Traffano-Schiffo, M. V., Castro-Giraldez, M., Colom, R. J., Talens, P., & Fito, P. J. (2021). New methodology to analyze the dielectric properties in radiofrequency and microwave ranges in chicken meat during postmortem time. Journal of Food Engineering, 292, 110350. https://doi.org/10.1016/j.jfoodeng.2020.110350

Traffano-Schiffo, M. V., Castro-Giráldez, M., Fito, P. J., & Balaguer, N. (2014). Thermodynamic model of meat drying by infrarred thermography. Journal of Food Engineering, 128, 103–110. https://doi.org/10.1016/j.jfoodeng.2013.12.024

Traffano-Schiffo, M. V., Castro-Giraldez, M., Herrero, V., Colom, R. J., & Fito, P. J. (2018). Development of a non-destructive detection system of Deep Pectoral Myopathy in poultry by dielectric spectroscopy. Journal of Food Engineering, 237, 137–145. https://doi.org/10.1016/j.jfoodeng.2018.05.023

Traffano-Schiffo, M. V., Chuquizuta, T., Castro-Giraldez, M., & Fito, P. J. (2021). Development of a methodology to categorize poultry meat affected by deep pectoral myopathy. Journal of Food Processing and Preservation, 45(3). https://doi.org/10.1111/jfpp.15226

Usamentiaga, R., Venegas, P., Guerediaga, J., Vega, L., Molleda, J., & Bulnes, F. (2014). Infrared Thermography for Temperature Measurement and Non-Destructive Testing. Sensors, 14(7), 12305–12348. https://doi.org/10.3390/s140712305

Vásquez, N., Magán, C., Oblitas, J., Chuquizuta, T., Avila-George, H., & Castro, W. (2018a). Comparison between artificial neural network and partial least squares regression models for hardness modeling during the ripening process of Swiss-type cheese using spectral profiles. Journal of Food Engineering, 219, 8–15. https://doi.org/10.1016/J.JFOODENG.2017.09.008

Vásquez, N., Magán, C., Oblitas, J., Chuquizuta, T., Avila-George, H., & Castro, W. (2018b). Comparison between artificial neural network and partial least squares regression models for hardness modeling during the ripening process of Swiss-type cheese using spectral profiles. Journal of Food Engineering, 219. https://doi.org/10.1016/j.jfoodeng.2017.09.008

Vega-Gálvez, A., López, J., Ah-Hen, K., Torres, M., & Lemus-Mondaca, R. (2014). Thermodynamic Properties, Sorption Isotherms and Glass Transition Temperature of Cape Gooseberry (Physalis peruviana L.). Food Technology and Biotechnology, 52(1), 83–92.

Velazquez Varela, J. (2014). ESTUDIO DE LOS ESPECTROS DIELECTRICOS EN ALIMENTOS CON ESTRUCTURA COLOIDAL [Universitat Politècnica de València]. https://doi.org/10.4995/Thesis/10251/37196

Vera, W., Avila-George, H., Mogollón, J., Chuquizuta, T., & Castro, W. (2025). Food fraud detection in Octopus mimus using hyperspectral imaging and machine learning techniques. Neural Computing and Applications, 37(4), 2369–2381. https://doi.org/10.1007/s00521-024-10750-w

Wang, B., Sun, J., Xia, L., Liu, J., Wang, Z., Li, P., Guo, Y., & Sun, X. (2023). The Applications of Hyperspectral Imaging Technology for Agricultural Products Quality Analysis: A Review. Food Reviews International, 39(2), 1043–1062. https://doi.org/10.1080/87559129.2021.1929297

Wang, S., Zhang, L., Wang, H., Fan, W., Hu, Y., & Tu, Z. (2024). Magnetic field: A non-thermal technology in food processing. Food Control, 166, 110692. https://doi.org/10.1016/J.FOODCONT.2024.110692

Witteveen, M., Sterenborg, H. J. C. M., van Leeuwen, T. G., Aalders, M. C. G., Ruers, T. J. M., & Post, A. L. (2022). Comparison of preprocessing techniques to reduce nontissue-related variations in hyperspectral reflectance imaging. Journal of Biomedical Optics, 27(10). https://doi.org/10.1117/1.JBO.27.10.106003

W. Kuang, & S. O. Nelson. (1998). Low-frequency dielectric properties of biological tissues: a review with some new insights. Transactions of the ASAE, 41(1), 173–184. https://doi.org/10.13031/2013.17142

Workman, J. (2014, June 30). An Introduction to Near Infrared Spectroscopy. Https://Analyticalscience.Wiley.Com/Content/Article-Do/Introduction-near-Infrared-Spectroscopy.

Ye, Z., Ren, Y., Yang, M., Cheng, M. M.-C., & Chen, P.-Y. (2023). Food Quality Monitoring Using A Low-Profile Multiplexed Harmonic Sensor. 2023 IEEE SENSORS, 1–4. https://doi.org/10.1109/SENSORS56945.2023.10324978

Yoplac, I., Avila-George, H., Vargas, L., Robert, P., & Castro, W. (2019). Determination of the superficial citral content on microparticles: An application of NIR spectroscopy coupled with chemometric tools. Heliyon, 5(7), e02122. https://doi.org/10.1016/j.heliyon.2019.e02122

Yuan, W., Zhou, H., Zhang, C., Zhou, Y., Jiang, X., & Jiang, H. (2024). Prediction of oil content in Camellia oleifera seeds based on deep learning and hyperspectral imaging. Industrial Crops and Products, 222, 119662. https://doi.org/10.1016/J.INDCROP.2024.119662

Zhu, M., Huang, D., Hu, X., Tong, W., Han, B., Tian, J., & Luo, H. (2020). Application of hyperspectral technology in detection of agricultural products and food: A Review. Food Science & Nutrition, 8(10), 5206–5214. https://doi.org/10.1002/fsn3.1852

VII. Anexos

Artículos de conferencia

Prediction of Quality Attributes of Fresh Unpasteurized Milk Using Dielectric Spectroscopy Coupled to Chemometric Tools

Prediction of Quality Attributes of Fresh Unpasteurized Milk Using Dielectric Spectroscopy Coupled to Chemometric Tools

Publisher: IEEE

T. Chuquizuta ; Y. Colunche ; M. Rubio ; J. Oblitas ; H. Arteaga ; W. Castro All Authors

Abstract:
The objective of this research is to predict the quality attributes of fresh unpasteurized milk using dielectric spectroscopy coupled to chemometric tools. For the fulfillment of the purpose, we have worked with fresh unpasteurized milk of the Brown Swiss breed, obtained from the "La lechera" stable; dilutions of water — fresh milk were obtained, from 70 to 100% at $25^{\circ}C$, followed by the physicochemical characterization (density, total solids, freezing point, fatty solids, proteins and added water) and dielectric properties in the range of 0.5 to 9 GHz using an open ended coaxial probe (N1501A-001), connected to a Vector Network Analyzer, model N9915A-Keysight Technologies. Likewise, the partial least squares regression was used to correlate the physicochemical properties with the dielectric properties; the results obtained in the prediction of freezing point, proteins, fatty solids and added water from fresh milk unpasteurized have presented a coefficient of determination and a mean square error in the range of [0.95-0.98] and $[2.57 \times 10^{-7} - 7.46 \times 10^{-2}]$ respectively. Consequently, it is concluded that the technique of dielectric spectroscopy and machine learning presents potential for prediction of physicochemical characteristics of fresh milk unpasteurized, being able to be implemented in the production lines to quickly and reliably evaluate the quality of cow's milk.

Published in: 2022 Photonics & Electromagnetics Research Symposium (PIERS)

Date of Conference: 25-29 April 2022

DOI: 10.1109/PIERS55526.2022.9792687

Date Added to IEEE *Xplore*: 16 June 2022

Publisher: IEEE

ISBN Information:

Conference Location: Hangzhou, China

Electronic ISSN: 1559-9450

Congreso Internacional	DOI
Progress in Electromagnetic Research Symposium (PIERS)	**DOI: 10.1109/PIERS55526.2022.9792687**

PREDICTION OF QUALITY ATTRIBUTES OF FRESH UNPASTEURIZED MILK USING DIELECTRIC SPECTROSCOPY COUPLED TO CHEMOMETRIC TOOLS

T. Chuquizuta[1], Y. Colunche[1], M. Rubio[1], J. Oblitas[2], H. Arteaga[3] and W. Castro[4]

[1] Instituto de investigación del Mejoramiento Productivo, Universidad Nacional Autónoma de Chota, Perú

[2] Facultad de Ingeniería, Universidad Privada del Norte, Perú

[3] Escuela Profesional de Ingeniería Agroindustrial, Universidad Nacional Autónoma de Chota, Perú

[4] Facultad de Ingeniería de Industrias Alimentarias, Universidad Nacional de Frontera, Perú

Abstract

The objective of this research is to predict the quality attributes of fresh unpasteurized milk using dielectric spectroscopy coupled to chemometric tools. For the fulfillment of the purpose, we have worked with fresh unpasteurized milk of the Brown Swiss breed, obtained from the "La lechera" stable; dilutions of water - fresh milk were obtained, from 70 to 100% at 25 ºC, followed by the physicochemical characterization (density, total solids, freezing point, fatty solids, proteins and added water) and dielectric properties in the range of 0.5 to 9 GHz using an open ended coaxial probe (N1501A-001), connected to a Vector Network Analyzer, model N 9915A - Keysight Technologies. Likewise, the partial least squares regression was used to correlate the physicochemical properties with the dielectric properties; the results obtained in the prediction of freezing point, proteins, fatty solids and added water from fresh milk unpasteurized have presented a coefficient of determination and a mean square error in the range of [0.95 - 0.98] and [2.57 x 10-7 - 7.46 x 10-2] respectively. Consequently, it is concluded that the technique of dielectric spectroscopy and machine learning presents potential for prediction of physicochemical characteristics of fresh milk unpasteurized, being able to be implemented in the production lines to quickly and reliably evaluate the quality of cow's milk.

INTRODUCTION

Milk is one of the main foods of the world population; providing an important amount of nutrients such as water, proteins, lipids, disaccharides and minerals required in the human diet [1]. However; how milk is obtained from different race cows under differente feed practice changes in the composition of the samples are common. In addition to cow's metabolism intentional adulteration could produce differences during the milk chain.

In this sense to know some characteristics such as water content is critical for verifying the quality of milk, but its value varies with stage of lactation, body condition, station of year and environmental temperature [2]. The monitoring and control of the quality characteristics of the milk is traditionally carried out using methods that imply the subsequent discard of the sample as the over drying method in the case of water content that imply higher time consumption.

Therefore, it is necessary to use and develop technologies that allow characterizing the quality of milk fast or in real time, dielectric spectroscopy then becomes an alternative to carry out these tasks, which also has the advantages of being fast and non-destructive, with result satisfactory in preliminary works [2]–[4]. Consequently, the objective in this investigation was to predict the quality attributes of fresh unpasteurized milk using dielectric spectroscopy coupled to chemometric tools.

MATERIALS AND METHODS

Sample

Fresh milk samples from Brown Swiss cows were obtained from the "La lechera" stable (Chota, Cajamarca, Peru). Milk was collected at 6:00 a.m. for five days in the morning, next the milk was placed in a glass bottle of 2.5 L previously sterilized with water and transported to the “Emerging Technology Laboratory” of the Universidad Nacional Autónoma de Chota and stored at 4 ºC until next analysis.

Sample preparation

Adulterated milk solutions were prepared adding water until obtaining concentration of 70, 75, 80, 85, 90, 95 and 100% in a beaker of 250 mL. Next samples were homogenized and heated to a temperature of 25 ºC on a heating plate (F20500421 AM4 X, Velp Scientific, Italy).

Determination of physicochemical properties

Freezing point, proteins, fatty solids and added water of the fresh milk unpasteurized was performed using a milk analyzer (Master Eco, MilkoTester, Bulgaria) following the instructions done by the fabricant [5], [6]. total soluble solids were obtained by refractometry (618.23.001 - ATC, Isolab, Alemania) and the density with a lactometer of Quevenne (71384000, Nahita, Spain).

Dielectric properties measurements

The used system to obtain the dielectric properties consists in an open ended coaxial probe (N1501A-001), attached to a vector network analyzer (VNA) (N9915A FieldFox, Keysight Technologies) and finally connected to a laptop (Legion Y520, Lenovo) (Figure 1)[7].

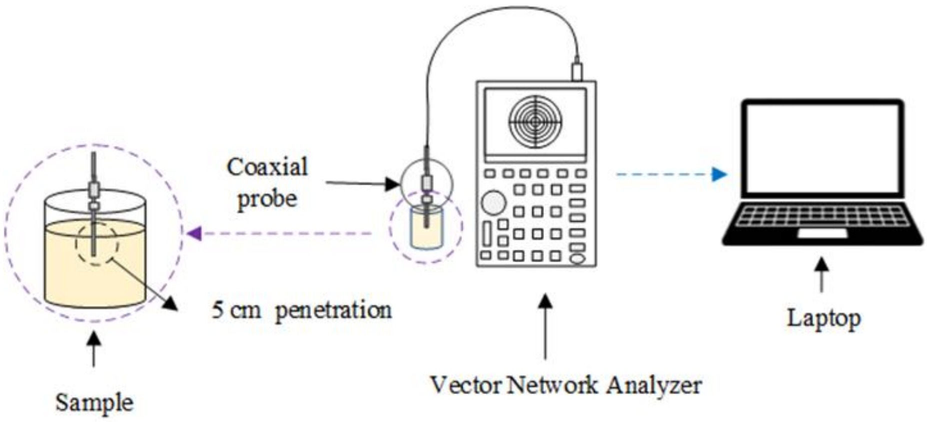

Figure 1. Dielectric properties acquisition system for fresh milk unpasteurized, using open-ended coaxial probe.

Previously to obtain the dielectric properties (dielectric constant - e' and dielectric loss factor - e") of the milk samples at different concentrations, the VNA was switched on for one hour in order to avoid instability of the signal between sensor and equipment [8]. Then the system was configured for obtaining the dielectric values in the range 0.5 to 9.0 GHz, divided it into 401 bands with a bandwidth of 1000 Hz and output power of -10 dBm. Next, the calibration was done according to the procedure described by Guo [9]; this requires a three steps calibration using air as the medium, an intentional short circuit and finally calibration with bidistilled water at 25 ºC.

Finally; using reflection coefficients, obtained with the open-ended coaxial probe and the milk, the dielectric constant and the loss factor were calculated. This required using the material measurement software N1500A-FG (Keysight Technologies), doing each measure by triplicate and ten repetitions of the treatments during the five days.

Modelling

First the dielectric data - e'' was pretreated in order to reduce electric noise by means of smoothing using a Savitzky-Golay filter with nice frames and second order [10]. Then the relationship between the dielectric spectra profile - e'' and physicochemical properties of the milk was modelizated using the Partial Least Square Regression (PLSR). PLSR generates a linear model, see Equation 1, to predict a response variable (Y), from a large set of independent variables, X with size [n x m]. For us X was a matrix of e'' loss factor values where n is the number of frequency samples and m is the number of observations; likewise density, total solids, freezing point, proteins, fatty solids and added water of the fresh milk are response variables (Y) [2].

$$Y = \beta X + e \tag{1}$$

Where Y is a quality parameter of the samples; β, matrix of coefficients; X, matrix of loss factor valius e'' and e is the model error.

In the first step, all frequencies were used for model building; however these models, called full models, preserve problems of multicollinearity. In this sense, selection of relevant variables (RV) or latent variables (LV) could be useful to reduce problems with the models, increasing model precision. This selection can be based on the β coefficient values obtained from the full model [11]–[13].

Statistical evaluation of the model

In all the cases, the models were built and validated using a K-fold cross-validation methodology, with K= 5; the complete and optimized models were evaluated comparing their coefficient of determination (R^2_{cv}) and the mean square error ($RSME_{cv}$) for cross-validation according to the equations 2 and 3 [2], [12].

$$R_{cv}^2 = \frac{\sum(\hat{y}_i - \bar{y}_i)^2}{\sum(y_i - \bar{y}_i)^2} \tag{2}$$

$$RSME_{cv} = \sqrt{\sum_{i=1}^{n} \frac{(\hat{y}_i - \bar{y}_i)^2}{n}} \tag{3}$$

RESULTS AND DISCUSSION

Physicochemical properties of the milk

Table 1, shows the physicochemical results of fresh milk unpasteurized at different concentrations of the Brown Swiss breed, these being similar to those reported by [14], [15]. However, these physicochemical values may vary according to diet, age, lactation number, phenotype, breed, environmental conditions, and the addition of water or some other milk adulterant [16]–[19]. Also, parameters such as density and freezing point are the most important to be able to identify adulteration in milk [20], [21].

Table 1. Physicochemical characteristics of fresh milk no pausteiced to different ratios

Ratio	N	Density (Kg/m^3)	Total soluble solids (°Brix)	Freezing point (°C)	Fatty solid (%)	Proteins (%)	Added water (%)
70	20	1.019 ± 0.001	6.345 ± 0.216	-0.360 ± 0.010	3.510 ± 0.085	1.480 ± 0.428	29.205 ± 1.922
75	20	1.020 ± 0.0	6.760 ± 0.256	-0.396 ± 0.015	3.820 ± 0.128	1.565 ± 0.049	22.570 ± 2.745
80	20	1.022 ± 0.0	7.316 ± 0.210	-0.428 ± 0.018	4.090 ± 0.137	1.660 ± 0.050	16.560 ± 3.311
85	20	1.023 ± 0.0	7.800 ± 0.64	-0.459 ± 0.020	4.365 ± 0.139	1.765 ± 0.049	10.660 ± 3.650
90	20	1.025 ± 0.0	8.380 ± 0.238	-0.488 ± 0.023	4.625 ± 0.168	1.860 ± 0.050	5.720 ± 4.151
95	20	1.026 ± 0.001	8.995 ± 0.307	-0.510 ± 0.019	4.835 ± 0.146	1.995 ± 0.039	2.520 ± 2.559
100	20	1.027 ± 0.0	9.820 ± 0.312	-0.546 ± 0.018	5.155 ± 0.110	2.125 ± 0.064	-

N: Number of samples evaluated

It can clearly be seen that when adding water to milk, the properties evaluated vary proportionally. The density, total soluble solids, fatty solids and proteins decrease, while the freezing point increases tending to the freezing point of water.

Dielectric spectrum of the milk

In Figure 2, the mean spectrum for each solution of milk-water is shown. These profiles show the degree of interaction of electromagnetic energy with the amount of added water to fresh milk, causing a decrease in the loss factor from 24.5 to 11.5 in the range of 0.5 to 1.5 GHz and subsequent increase as the frequency increases (1.5 to 9 GHz), giving rise to "U" shaped spectra. The “U” shape in the spectra of the loss factor found in our investigation are similar to those reported by Guo [2], Agranovich [22] and Guo [9], this behavior of the spectrum is due to ionic conductivity and subsequent dipole polarization of the chemical species and the water present in milk in the microwave range [4], [23]. Likewise, the amount of fat, protein, lactose, electrolytes and water influence the dielectric properties of fresh milk [2]–[4], [8], [24], [25].

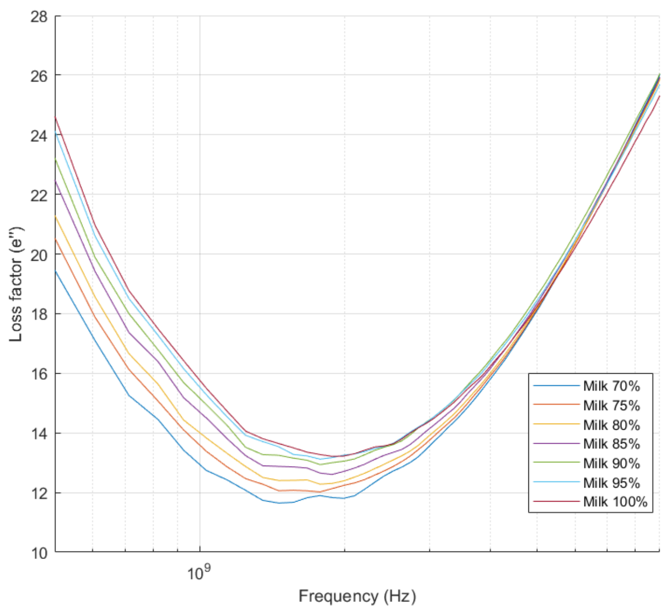

Figure 2. Dielectric spectrum of milk-water solutions

Modeling of the physicochemical properties

Figure 3, show the results of full PLSR models in the prediction of the quality parameters, in these R^2 were over 0.95 for all parameters assessment. However, as in the de works developed by [10]–[12] it is necessary to optimize the models as a previous step for industrial applications. For PLSR models one of the most common method for variable selection is based on β- coefficients [26].

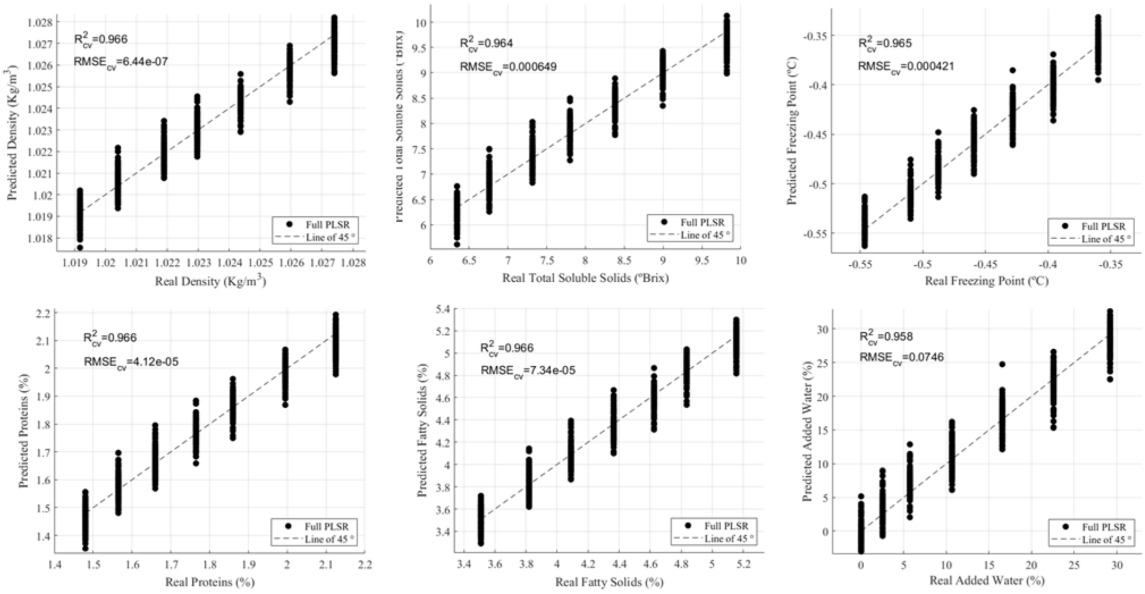

Figure 3. Full models for quality parameters in milk using dielectric spectroscopy

The results of optimization models was shown in Figure 4, in this case the $R^2$was increased for almost each variable with exception of added water. In the same way $RMSE_{cv}$ was reduced with the exception of protein content. In similar conditions another technique currently used is artificial neural network [13] which is compared to PLSR giving lighty better results.

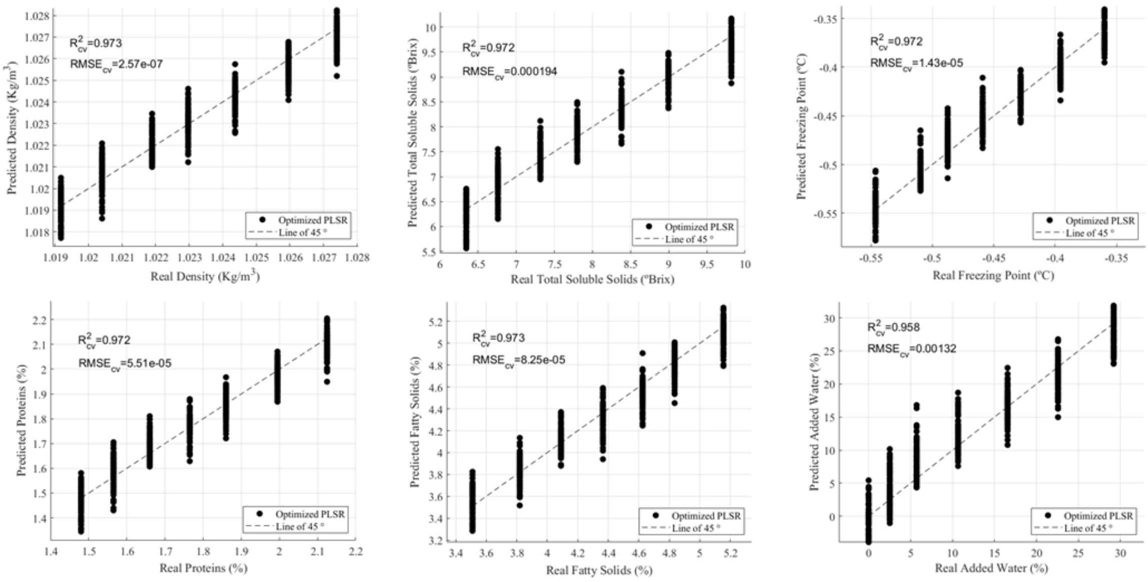

Figure 4. Optimized models for quality parameters in milk using dielectric spectroscopy

Statistical evaluation of models

Table 2 summarizes the statistical descriptors that evaluate the performance of the models full and optimized. From full model to optimized model decrease for eachs variables, thus the processing of data for prediction is streamlined, addly R_cv^2increase while 〖RSME〗_cv decreases. Likewise, several studies have used hyperspectral images and near infrared to predict the quality of pasteurized cow's milk and UHT in the visible and the near infrared in the range from 1000 to 2400 nm, resulting in fats [0.953 - 0.997] and proteins [0.552-0.946], through the use of PLSR [27]–[31]. In our case, the use of the dielectric spectroscopy technique in the determination of the physicochemical parameters of fresh milk un paustezed has presented similar values to other technologies such as those mentioned above, as well as in the investigations carried out with dielectric microwave spectroscopy in the range of 0.5 to 20 GHz [2], [9], [22].

Table 2. Prediction values of the complete and optimized PLSR model of the physicochemical characteristics of fresh milk unpasteurized.

Physicochemical properties	Full model		Optimized model *	
	R^2_{cv}	$RMSE_{cv}$	R^2_{cv}	$RMSE_{cv}$
Density (Kg/m^3)	0.966	6.44×10^{-7}	0.973	2.57×10^{-7}
Total soluble solids (°Brix)	0.964	6.49×10^{-4}	0.972	1.94×10^{-4}
Freezing point (°C)	0.965	4.21×10^{-4}	0.972	1.43×10^{-5}
Fatty solid (%)	0.966	7.34×10^{-5}	0.973	8.25×10^{-5}
Proteins (%)	0.966	4.12×10^{-5}	0.972	5.51×10^{-5}
Added water (%)	0.958	7.46×10^{-2}	0.958	1.32×10^{-3}

* Number latent variables = 15

CONCLUSION

Dielectric spectroscopy coupled with chemometric tools proved to be a useful technique to predict the quality properties of unpasteurized cow's milk, which include density, total soluble solids, fatty solids, proteins and the point of freezing. The level of prediction shows an improvement when using the optimized models compared to the full models. These results suggest that these techniques could be implemented in production lines to assess milk quality quickly and reliably.

ACKNOWLEDGMENT

The authors would like to thank Universidad Nacional Autónoma de Chota for funding with mining CANON funds the execution of the research project called "Desarrollo de un sistema no destructivo para la determinación de las propiedades fisicoquíımicas en frutas nativas y derivados de la región Cajamarca, usando espectroscopía dieléctrica" approved with resolution N° 432-2018-C.O./UNACH.

REFERENCES

[1] X. Zhang et al., "Milk consumption and multiple health outcomes: umbrella review of systematic reviews and meta-analyses in humans," Nutr. Metab. , vol. 18, no. 1, p. 7, Jan. 2021.

[2] W. Guo, B. Lin, D. Liu, and X. Zhu, "A Novel Technique on Determining Water Content in Milk Using Radio-Frequency/Microwave Dielectric Spectroscopy and Chemometrics," Food Anal. Methods, vol. 10, no. 12, pp. 3781–3789, Dec. 2017.

[3] X. Zhu, W. Guo, F. Kang, F. Kong, and Q. Zhu, "Determination of Protein Content of Raw Fresh Cow's Milk Using Dielectric Spectroscopy Combined with Chemometric Methods," Food and Bioprocess Technology, vol. 9, no. 12. pp. 2092–2102, 2016. doi: 10.1007/s11947-016-1791-1.

[4] Q. Liu, W. Guo, and X. Zhu, "Effect of lactose content on dielectric properties of whole milk and skim milk," Int. J. Food Sci. Technol., vol. 53, no. 9, pp. 2037–2044, Sep. 2018.

[5] Milkotester Ltd, "MASTER ECO." https://milkotester.com/es/products/master-eco (accessed Aug. 25, 2021).

[6] S. M. A. Sallam et al., "The effect of Saccharomyces cerevisiae live cells and Aspergillus oryzae fermentation extract on the lactational performance of dairy cows," Anim. Biotechnol., vol. 31, no. 6, pp. 491–497, Dec. 2020.

[7] T. C. Trigoso, J. O. Cruz, H. A. Miñano, and W. C. Silupu, “Application of Machine Learning in the Discrimination of Citrus Fruit Juices: Uses of Dielectric Spectroscopy,” in 2020 IEEE Engineering International Research Conference (EIRCON), Oct. 2020, pp. 1–4.

[8] X. Zhu, W. Guo, and Z. Liang, “Determination of the Fat Content in Cow’s Milk Based on Dielectric Properties,” Food and Bioprocess Technology, vol. 8, no. 7. pp. 1485–1494, 2015. doi: 10.1007/s11947-015-1508-x.

[9] W. Guo, X. Zhu, H. Liu, R. Yue, and S. Wang, “Effects of milk concentration and freshness on microwave dielectric properties,” J. Food Eng., vol. 99, no. 3, pp. 344–350, Aug. 2010.

[10] A. Reyes, M. Yarleque, W. Castro, and S. Chuquizuta, “Determination of dielectric properties of the red delicious apple and its correlation with quality parameters,” 2017 Progress in Electromagnetics Research Symposium - Fall (PIERS - FALL). 2017. doi: 10.1109/piers-fall.2017.8293478.

[11] A. Reyes, M. Yarleque, W. Castro, and S. Chuquizuta, “Determination of Permittivity Values Using Microwave Dielectric Spectroscopy for Assessing Apple and Purple Sweet Potato Quality Parameters,” 2018 International Conference on Electromagnetics in Advanced Applications (ICEAA). 2018. doi: 10.1109/iceaa.2018.8520427.

[12] W. Castro et al., “Feasibility of using spectral profiles for modeling water activity in five varieties of white quinoa grains,” J. Food Eng., vol. 238, pp. 95–102, Dec. 2018.

[13] N. Vásquez, C. Magán, J. Oblitas, T. Chuquizuta, H. Avila-George, and W. Castro, “Comparison between artificial neural network and partial least squares regression models for hardness modeling during the ripening process of Swiss-type cheese using spectral profiles,” J. Food Eng., vol. 219, pp. 8–15, 2018.

[14] R. WingChing-Jones and E. Mora Chaves, “Efecto de agregar agua sobre el punto crioscópico y componentes de la leche cruda de vacas Jersey y Holstein,” Cuadernos de Investigación, 2019, [Online]. Available: https://www.scielo.sa.cr/scielo.php?script=sci_arttext&pid=S1659-42662019000300313

[15] C. E. Rodriguez, G. F. Saavedra, and D. F. Gómez, “Efecto de la etapa de lactancia sobre la calidad fisicoquímica de leche en vacas de raza Holstein y Normando,” Zoot Trop, vol. 33, pp. 23–35, 2015.

[16] H. Jurado-Gámez, L. Muñoz-Domínguez, D. Quitiaquez-Montenegro, C. Fajardo-Argoti, and E. Insuasty-Santácruz, “Evaluación de la calidad composicional, microbiológica y sanitaria de la leche cruda en el segundo tercio de lactancia en vacas lecheras,” Revista de la Facultad de Medicina Veterinaria y de Zootecnia, vol. 66, no. 1. 2019. doi: 10.15446/rfmvz.v66n1.79402.

[17] W. Jose Brinez, E. Valbuena, G. Castro, A. Tovar, and J. Ruiz-Ramirez, “Some Composition Parameters and Quality on Raw Milk of Dual Purpose Cows in the Machiques County. Zulia State, Venezuela,” REVISTA CIENTIFICA-FACULTAD DE CIENCIAS VETERINARIAS, vol. 18, no. 5, pp. 607–617, 2008.

[18] R. WingChing-Jones and E. Mora-Chaves, “Composición de la leche entera cruda de bovinos antes y después del filtrado,” Agronomía mesoamericana, vol. 24, no. 1, pp. 203–207, 2013.

[19] J. P. G. Blanco and R. R. WingChing-Jones, “Relación del valor de urea en leche con parámetros reproductivos y productivos en vacas Holstein, Jersey y sus cruces,” UNED Research Journal, vol. 8, no. 2. pp. 175–183, 2016. doi: 10.22458/urj.v8i2.1558.

[20] J. Zagorska and I. Ciprovica, “Evaluation of factors affecting freezing point of milk,” International Journal of Biological, Biomolecular, Agricultural, Food and Biotechnological Engineering, vol. 7, no. 2, pp. 106–111, 2013.

[21] P. Senevirathne, U. L. P. Mangalika, A. Adikari, and W. A. D. Nayananjalie, “Evaluation of Cow Factors and Milk Composition on Freezing Point Depression of Cow Milk,” International Journal of Livestock Research, vol. 6, no. 5. p. 61, 2016. doi: 10.5455/ijlr.20160512114121.

[22] D. Agranovich, P. B. Ishai, G. Katz, D. Bezman, and Y. Feldman, “Microwave dielectric spectroscopy study of water dynamics in normal and contaminated raw bovine milk,” Colloids Surf. B Biointerfaces, vol. 154, pp. 391–396, Jun. 2017.

[23] T. K. Kataria, A. Corona-Chávez, J. L. Olvera-Cervantes, R. Rojas-Laguna, and M. E. Sosa-Morales, “Dielectric characterization of raw and packed soy milks from 0.5 to 20 GHz at temperatures from 20 to 70 oC,” J. Food Sci. Technol., vol. 55, no. 8, pp. 3119–3126, Aug. 2018.

[24] K. Zhao, Y. Liu, and Q. Zhang, “Dielectric behavior of adulterated milk with urea and water,” J. Mol. Liq., vol. 273, pp. 37–44, Jan. 2019.

[25] A. C. Nunes, X. Bohigas, and J. Tejada, “Dielectric study of milk for frequencies between 1 and 20GHz,” J. Food Eng., vol. 76, no. 2, pp. 250–255, Sep. 2006.

[26] D.-W. Sun, Hyperspectral Imaging for Food Quality Analysis and Control. Elsevier, 2010.

[27] B. Yang, Z. Zhu, M. Gao, X. Yan, X. Zhu, and W. Guo, “A portable detector on main compositions of raw and homogenized milk,” Comput. Electron. Agric., vol. 177, p. 105668, Oct. 2020.

[28] J. A. Diaz-Olivares, I. Adriaens, and E. Stevens, “Online milk composition analysis with an on-farm near-infrared sensor,” and Electronics in …, 2020, [Online]. Available: https://www.sciencedirect.com/science/article/pii/S0168169920311182

[29] B. Aernouts, E. Polshin, J. Lammertyn, and W. Saeys, “Visible and near-infrared spectroscopic analysis of raw milk for cow health monitoring: reflectance or transmittance?,” J. Dairy Sci., vol. 94, no. 11, pp. 5315–5329, Nov. 2011.

[30] R. Jankovská and K. Šustová, “Analysis of cow milk by near-infrared spectroscopy,” Czech Journal of Food Sciences; Prague, vol. 21, no. 4, pp. 123–128, 2003.

[31] R. Tsenkova, S. Atanassova, K. Toyoda, Y. Ozaki, K. Itoh, and T. Fearn, “Near-infrared spectroscopy for dairy management: measurement of unhomogenized milk composition,” J. Dairy Sci., vol. 82, no. 11, pp. 2344–2351, Nov. 1999.

Dielectric Spectral Profiles For Andean Tubers Classification: A Machine Learning Techniques Application


IEEE Xplore® Browse My Settings Help Institutional Sign In

All

ADVANCED SEARCH

Conferences > 2021 International Conference...

Dielectric Spectral Profiles For Andean Tubers Classification: A Machine Learning Techniques Application

Publisher: IEEE Cite This PDF

Tony Chuquizuta ; Jimy Oblitas ; Hubert Arteaga ; Manuel Yarleque ; Wilson Castro All Authors

108 Full Text Views

Abstract

Document Sections

I. Introduction

II. Materials and methods

III. Results and discussion

IV. Conclusion

Authors

Figures

References

Keywords

Metrics

Footnotes

Abstract:
Currently, the agri-food industry prioritizes the development of non-destructive methods, such as dielectric spectroscopy, for quality control. The obtained dielectric spectral properties can be coupled to multivariate statistical methods as "machine learning" when identification of attributes is wanted. However, these techniques have not been applied to andean tubers classification. Therefore, the objective of the present investigation is to evaluate the possibility of discriminating four andean tubers using dielectric spectra properties and machine learning techniques (Support Vector Machine - SVM, K-Nearest Neighbors-KNN, and Linear Discriminat - LD). For this purpose, samples of Tropaeolum tuberosum (Killu isaño), Solanum tuberosa (yellow) and two varieties of Oxalis tuberosa (Puka kamusa and Lari oqa) were acquired, 30 units per tuber. The dielectric spectral profile was extracted twice for each tubers sample, in the range from 2 to 8 GHz. Then, the dielectric constant (e') were calculated, and its dimensionality was reduced using principal component analysis. Finally, models for classification were built by employing KNN, SVM and LD techniques. The results showed that three components can explain the variance at 99.6 %. Likewise, the accuracy in the discrimination values varied between 79.17 - 83.04, being SVM the best discrimination technique. Consequently, it is concluded that the technique of dielectric spectroscopy and machine learning presents potential for andean tuber discrimination.

Published in: 2021 International Conference on Electromagnetics in Advanced Applications (ICEAA)

Date of Conference: 09-13 August 2021

DOI: 10.1109/ICEAA52647.2021.9539623

Date Added to IEEE *Xplore*: 21 September 2021

Publisher: IEEE

ISBN Information:

Conference Location: Honolulu, HI, USA

Congreso Internacional	DOI
International Conference on Electromagnetics in Advanced Applications (ICEAA)	**DOI: 10.1109/PIERS55526.2022.9792687**

DIELECTRIC SPECTRAL PROFILES FOR ANDEAN TUBERS CLASSIFICATION: A MACHINE LEARNING TECHNIQUES APPLICATION

T. Chuquizuta[1]*, J. Oblitas[2], H. Arteaga[3], M. Yarleque[4] and W. Castro[5]

[1] Universidad Nacional Autónoma de Chota, Chota, Perú; tchuquizuta@unach.edu.pe

[2] Universidad Privada del Norte, Cajamarca, Perú; jimy.oblitas@upn.edu.pe

[3] Universidad Nacional Autónoma de Chota, Chota, Perú; hlarteagam@unach.edu.pe

[4] Pontificia Universidad Católica de Perú, Lima, Perú; myarleq@pucp.edu.pe

[5] Universidad Nacional de Frontera, Sullana, Perú; wcastro@unf.edu.pe

Abstract

Currently, the agri-food industry prioritizes the development of non-destructive methods, such as dielectric spectroscopy, for quality control. The obtained dielectric spectral properties can be coupled to multivariate statistical methods as "machine learning" when identification of attributes is wanted. However, these techniques have not been applied to andean tubers classification. Therefore, the objective of the present investigation is to evaluate the possibility of discriminating four andean tubers using dielectric spectra properties and machine learning techniques (Support Vector Machine - SVM, K-Nearest Neighbors-KNN, and Linear Discriminat - LD). For this purpose, samples of Tropaeolum tuberosum (Killu isañu), Solanum tuberosa (yellow) and two varieties of Oxalis tuberosa (Puka kamusa and Lari oqa) were acquired, 30 units per tuber. The dielectric spectral profile was extracted twice for each tubers sample, in the range from 2 to 8 GHz. Then, the dielectric constant (e') were calculated, and its dimensionality was reduced using principal component analysis. Finally, models for classification were built by employing KNN, SVM and LD techniques. The results showed that three components can explain the variance at 99.6 %. Likewise, the accuracy in the discrimination values varied between 79.17 - 83.04, being SVM the best discrimination technique. Consequently, it is concluded that the technique of dielectric spectroscopy and machine learning presents potential for andean tuber discrimination.

Introduction

Nowadays, countries as Peru, Bolivia, Colombia and Ecuador have started to give importance to the recovery, conservation and production of andean tubers: native potatoes, mashua, oca and others [1]–[3], they are carbohydrates, sugars, vitamins, minerals and beneficial bioactive compounds for health [4], considered fundamental diet in the High Andean areas [5]; however, cross pollination and lack of technification in the production of andean tubers in High Andean areas give rise to the formation of new kind of tubers.

Identification of new andean tuber species has been realized through different features as anatomical-exomorphological [6], biochemicals - molecular [7] and physicochemical [8], [9], however, these techniques present disadvantages as: long sample preparation times, destructive techniques, generate products wasted and are expensive when talking about the analysis. Some andean tuber as mashua and oca have similar characteristics in your varieties, so is necessary apply rapid technical for genuine identification them. To overcome all these disadvantages, recently research works have been applying dielectric spectroscopy techniques in prediction of physicochemical properties [10], eggs freshness determination [11], identification of fresh decalcified goat milk [12], apple varieties [13] and tomatoes [14], all those come accompanied by the usage of chemometric techniques.

The usage of chemometric techniques, especially machine learning (ML), is being widely used in the developing of different models (regression, classification, grouping and dimensionality reduction) [15], those that are applied for classification, monitoring and process optimization [16]. The use of ML in the food classification has been possible thanks to the development of different algorithms (linear discriminant - LDA, quadratic discriminant - QD, K-nearest neighbor - KNN, support vector machines - SVM) [17], those that have been used in honey [18], coffee [19], peach [20], egg [11], orange [21], golden berry [22] and powdered food [23], [24].

Up to now, there has not been any work reported about the use of chemometric tools in the andean tubers classification through dielectric spectroscopy; in this way, the goal of the present research is to assess the feasibility of four kind of andean tuber through dielectric spectrums and machine learning techniques (Support Vector Machine - SVM, K-Nearest Neighbours- KNN y Linear Discriminat-LD).

Materials and methods

A. Andean tubers

The samples were constitued by three different kind of andean tubers: *Tropaeolum tuberosum* (Killu isañu), *Solanum tuberosa* (yellow) and two kinds of *Oxalis tuberosa* (Puka kamusa and Lari oqa), figure 1.

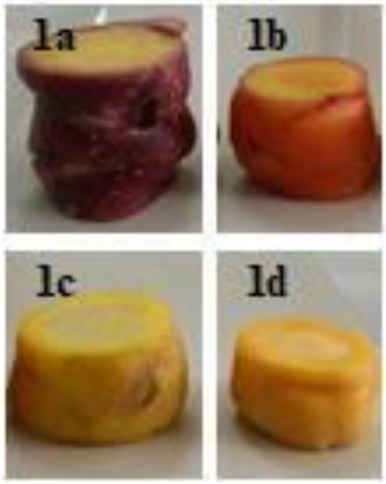

Fig. 1. Andean Tubers: Oxalis tuberosa (Puka kamusa (a) and Lari oqa (b)), *Tropaeolum tuberosum* (Killu isañu) (c), *Solanum tuberosa* (yellow) (d)

Thirty units per each tuber variety were acquired in an experimental farm of the Universidad Nacional de Cajamarca agronomists [UTM: -7.166949, -78.495392].

B. Sample preparation

In biological samples with non-uniform surfaces such as Andean tubers, it is necessary to condition the samples in order to obtain a flat surface for contact with the open ended coaxial probe (flat surface). In our case, with the help of a cutter, the ends of the tubers were cut, obtaining a length of 5 cm (see Figure 2), taking as reference the works of [25] and [26].

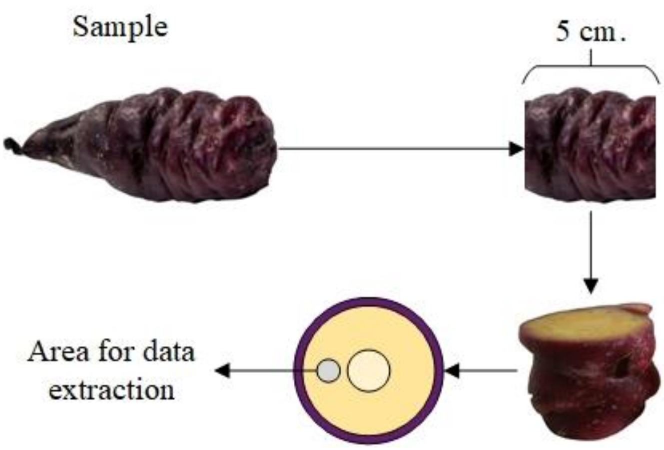

Fig. 2. Conditioning of Andean tubers samples

C. Dielectric spectrum acquisition system

The used system to obtain the dielectric spectrums (dielectric properties) consists in an open ended coaxial probe (N1501A-001), attached to a VNA (Vector Network Analyzer) (N9915A, Keysight Technologies), connected to a notebook (Legion Y520, Lenovo) (Figure 3).

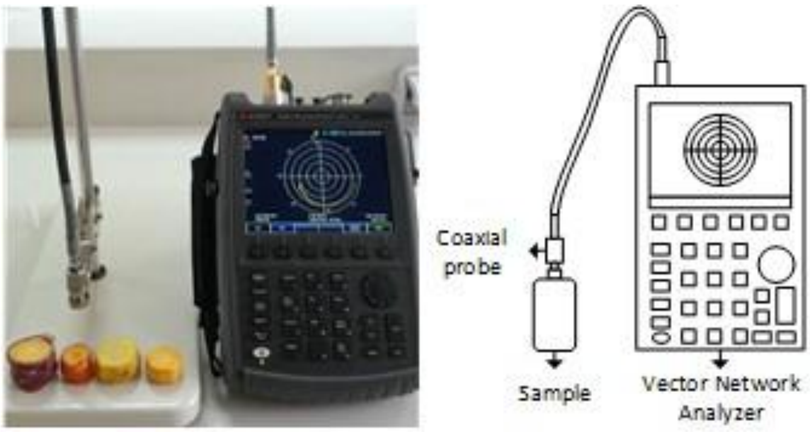

Fig. 3. Relative permittivity acquisition system for Andean Tubers, using open-ended coaxial probe

The dielectric properties were represented by the equation (1).

$$\varepsilon_r = \varepsilon' - j\varepsilon'' \quad (1)$$

Where: ε_r electrical permitivity; ε' dielectric contant (real values); ε'' loss factor (imaginary values)

Prior to obtaining the dielectric properties (dielectric constant and dielectric loss factor) of the andean tubers, the VNA was turned on for one hour, then the system was calibrated according to the procedure described by Liu [27] in three steps: calibration in an open system (air), short circuit and bi-distilled water at 20°C

At last, 274 ε' values were obtained from the reflection coefficients, between the contact of the open end coaxial probe with the surface of each tuber, using the material measurement software N1500A-FG (Keysight Technologies), in a range from 2 to 8 GHz. The measurement was carried out twice for each tuber at room temperature (20± 0.5 °C).

D. Dimensionality reduction

Dimensionality reduction used the Principal Components Analysis (PCA) technique, which consists in obtaining the new variables from the total variables by association according to its capacity to explain variances [28].

E. Classification models

Currently, various tools or techniques for linear and nonlinear classification are being used in food such as those described in the investigations of Leide [19], You [23], You [24], Khaled [28], Castro [29]. In our case, linear classification techniques were used such as: LD, SVM and KNN, whose graphical representation of these models is shown in Figure 4.

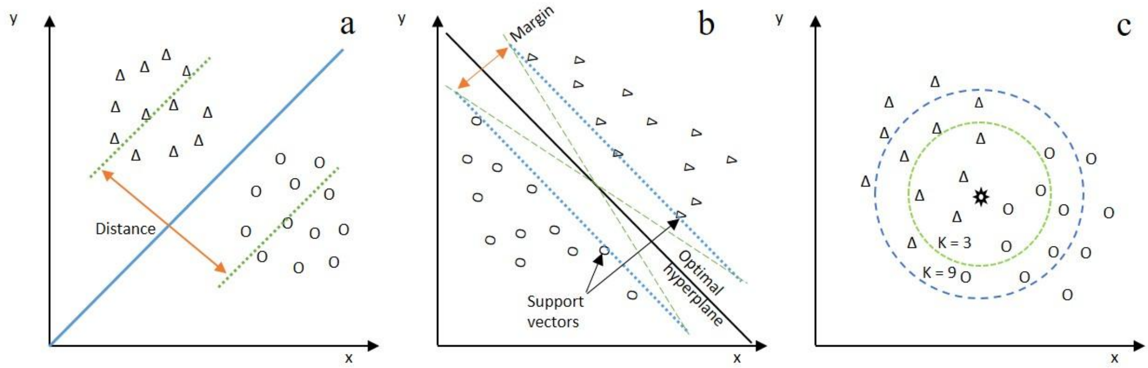

Fig. 4. Machine learning in the classification of Andean tubers: LD (a), SVM (b) y K-NN (c)

This lineal classification techniques are based on:

- LD.- distribution or grouping of alike covariance values, this guarantees their maxima separation [21]
- SVM.- built hyperplane or set of hyperplanes in a high dimension space, determining less error and increasing at its best the separation margin [11], [22], [23], [29].
- K-NN.- distance between neighboring data, this makes place to a prediction model for data classification [23].

With the tool support of the app Classification Learner of MATLAB 2020b software, the tubers were classified according to the aforementioned techniques. Likewise, a cross validation (k-fold) was used, with k = 5. The process was carried out ten times in order to verify the robustness of the model.

F. Statistical evaluation

The classification of Andean tubers, was carried out by means of the construction of the confusion matrix (4x4) has two dimensions with of real (row) and predicted (column) values, from the obtaining of the true positive (TP - correctly identified) and negative (TN - correctly rejected) values and false positives (FP - incorrectly identified) and negatives (FN - incorrectly rejected), through the equations from (2) to (5), described by Castro et al [22].

$$TP = N_{ij} \tag{2}$$

$$TN = \sum\nolimits_{j,k\neq 1}^{n} N_{jk} = \sum\nolimits_{j=1}^{n}\sum\nolimits_{k=1}^{n} N_{jk} - (TP + FP + FN) \tag{3}$$

$$FP = \sum\nolimits_{k\neq 1}^{n} N_{ki} = \sum\nolimits_{k=1}^{n} N_{ki} - TP \tag{4}$$

$$FN = \sum\nolimits_{k\neq 1}^{n} N_{ik} = \sum\nolimits_{k=1}^{n} N_{ik} - TP \tag{5}$$

Finally, the performance evaluation of the classification of Andean tubercles from the confusion matrix was based on terms of accuracy, receiver operating characteristic (ROC) and area under the curve (AUC), according to app Classification Learner of MATLAB 2020b software.

- Accuracy : This measures how many observations, both positive and negative, were correctly classified and it is defined by Equation (6).

$$Accuracy = \frac{TP + TN}{TP + TN + FP + FN} \tag{2}$$

- ROC : Curve constructed from TP versus FP at different Andean tuber classification thresholds.

- AUC: It is an evaluation metric that considers all possible classification thresholds for Andean tubers, the same one that is determined from the area under the ROC curve, see Equation (7).

$$AUC = \int_{x=0}^{1} ROC(1 - TN) \cdot d(1 - TN) \tag{2}$$

Results and discussion

A. Dielectric spectrum for Andean tubers

The figure 5, shows the mean values of the dielectric spectra of four types of Andean tubers. Similar works Kuang and Nelson [30]–[32] in the dielectric characterization of tubers have shown a decrease in the dielectric constant in the range from 2 to 8 GHz, coinciding with our results.

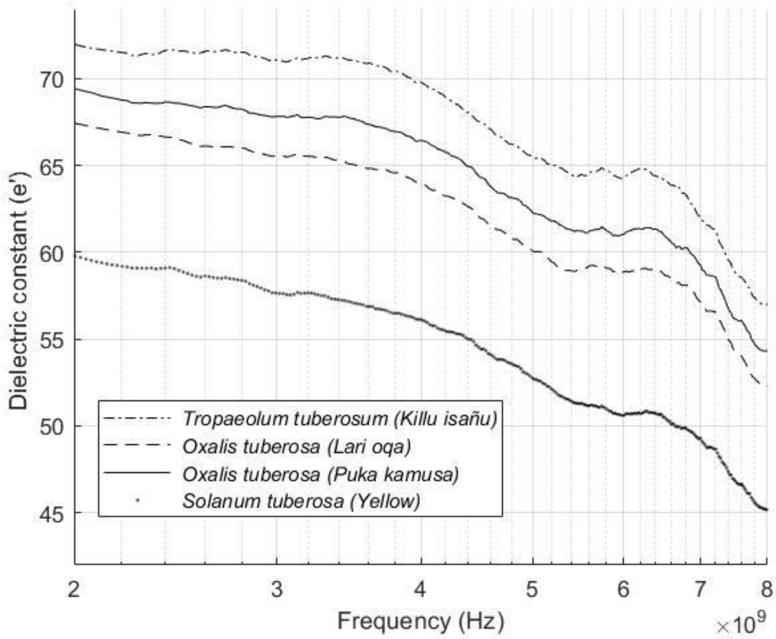

Fig. 5. Dielectric spectrums from four kinds of andean tubers

According to the graph, in the range from 6 to 7 GHz, a slight growth of the dielectric spectrum of Andean tubers is evidenced, this process is attributed to methyl groups in the β dispersion [33].

B. Dimensionality reduction

PCA has shown that three components can explain a cumulative variability of the data above 99.6% (figure 6), in the reduction of variables. Similar works with different techniques for obtaining spectral information and images support our study: oil palm [28], food powdered [23], green arabica coffee [19], tomatoes [34], muskmelons [35] and multiple food ingredients [36].

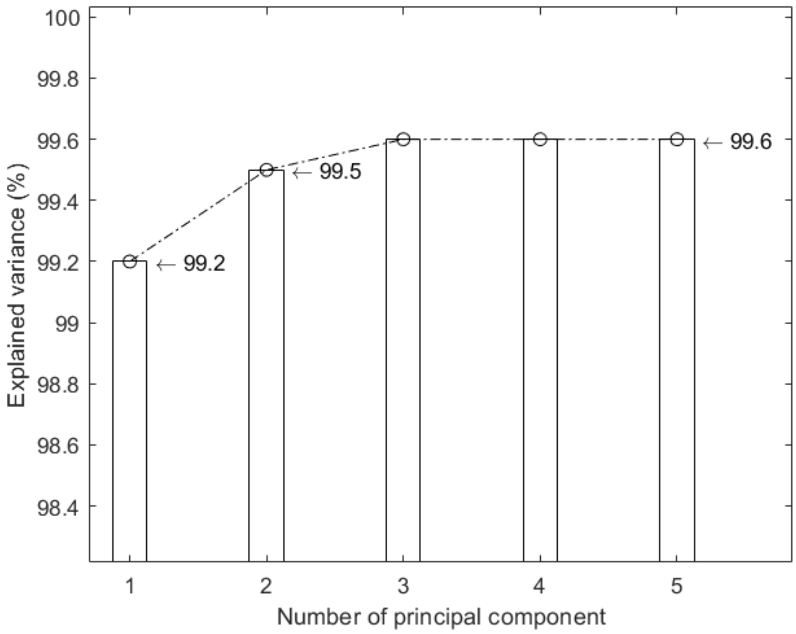

Fig. 6. Variance explained for principal component

C. Classification methods

The Table I, shows confusion matrices for each classifier model. Although the values for correct classification, values in diagonal cells, shown percents from 65.0 to 95.5 % with high variations among the accuracy from each class. In addition, in all the models the best classification was obtained for S. tuberosa (yellow) and T. tuberosum (Killa isaña).

TABLE I Confusion matrix for each classifier

a) LD

		Predicted class			
		1	2	3	4
Real class	1	93.3	-	6.7	-
	2	-	75.0	21.7	3.3
	3	15.0	-	68.3	-
	4	-	-	-	95.0

b) SVM

		Predicted class			
		1	2	3	4
Real class	1	86.7	-	13.3	-
	2	1.7	83.3	11.7	3.3
	3	11.7	18.3	70.0	-
	4	-	5.0	1.7	93.3

c) KNN

		Predicted class			
		1	2	3	4
Real class	1	85.0	-	15.0	-
	2	-	76.7	18.3	5.0
	3	18.3	16.7	65.0	-
	4	-	1.7	3.3	95.5

Cumulative values or accuracy percentage on andean tubers classification may be seen in Table I, considering a good classification over the 80 % as described in You [23].

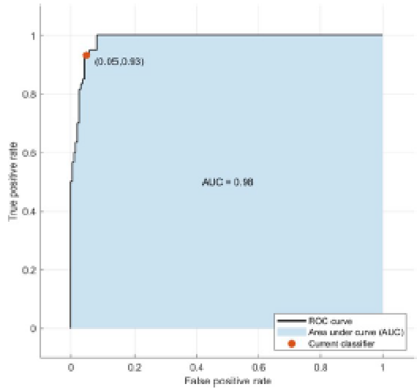

(a)

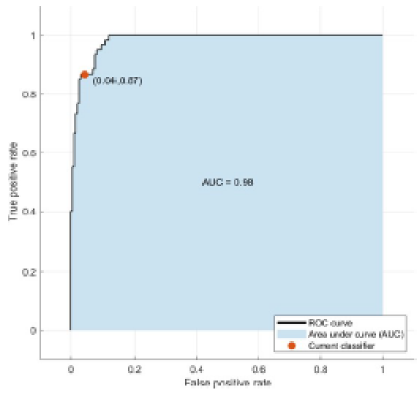

(b)

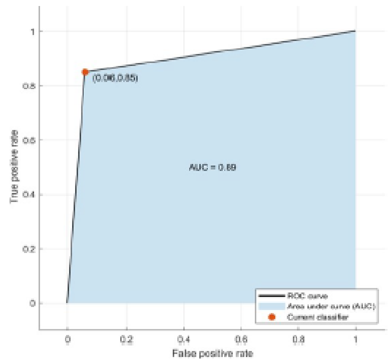

(c)

Fig. 7. RUC for a) LD, b) SVM. and c) KNN

D. Performance

In this study the best classification model based on dielectric properties (ϵ') for Andean tubers was the SVM (Table II) which is similar to reported by Suphamitmongkol [21], in the classification of orange, reporting that the PCA - SVM as the best classification model, this results reinforce that the non-invasive techniques coupled with chemometric classification tools have great potential of application in the industry [19].

The Figure 7, show the probability to find the correct classification based in AUC terms, varying between 0.85 to 0.98, see Table II. In this case LD and SVM proving to be valid and viable, as long as the AUC is higher than 0.90 in concordance with [37],

TABLE II Classification model for andean tubers

Technique	Accuracy (%)	AUC
Linear Discriminant	80.89 ± 2.49	0.968 ± 0.027
Support Vector Machine	83.04 ± 0.66	0.984 ± 0.005
K- Nearest Neighbour	79.17 ± 1.63	0.855 ± 0.042

Conclusion

Differentiation from four kind of andean tubers based on dielectric properties (e' values), coupled to machine learning technique have allowed to observe a high precision in discrimination of andean tubers, over 80 %. Ergo, it is concluded that dielectric spectroscopy technique and machine learning together expose a great potential for the andean tubers differentiation.

ACKNOWLEDGMENT

The authors would like to thank Universidad Nacional Autónoma de Chota for funding with mining CANON funds the excecution of the research project called "Desarrollo de un sistema no destructivo para la determinatión de las propiedades físicoquímicas en frutas nativas y derivados de la región Cajamarca, usando espectroscopía dieléctrica" approved with resolution No 432-2018-C.O./UNACH.

REFERENCES

[1] E. O. Leidi, A. M. Altamirano, G. Mercado, J. P. Rodriguez, A. Ramos, G. Alandia, M. Sørensen, and S.-E. Jacobsen, "Andean roots and tubers crops as sources of functional foods," Journal of Functional Foods, vol. 51, pp. 86–93, 2018.

[2] A. M. Fries and M. E. Tapia, Gu´ıa de campo de los cultivos andinos. FAO, ANPE-PERÚ, 2007.

[3] S. E. Jacobsen, A. Mujica, and R. Ortiz, "La importancia de los cultivos andinos," Fermentum. Revista Venezolana de Sociolog´ıa Y Antropología, vol. 13, no. 36, pp. 14–24, 2003.

[4] A. Chandrasekara and T. Josheph Kumar, "Roots and tuber crops as functional foods: a review on phytochemical constituents and their potential health benefits," International journal of food science, vol. 2016, 2016.

[5] W.-H. Su and D.-W. Sun, "Advanced analysis of roots and tubers by hyperspectral techniques," in Advances in food and nutrition research. Elsevier, 2019, vol. 87, pp. 255–303.

[6] P. Melchiorre, "Identificacion de tuberculos andinos (oxalis tuberosa, ullucus tuberosus y tropaeobim tuberosum) mediante caracteres anatomicos y exomorfologicos," 1985.

[7] C. Mohan, V. Prasannakumary, and A. G. Nair, "Tropical roots and tubers: Impact on environment, biochemical, molecular characterization of different varieties of tropical roots and tubers," Tropical Roots and Tubers: Production, Processing and Technology, pp. 138–182, 2016.

[8] F. F. Velásquez-Barreto and C. Velezmoro, “Propiedades reológicas y viscoelásticas de almidones de tubérculos andinos,” Scientia Agropecuaria, vol. 9, no. 2, pp. 189–197, 2018.

[9] F. F. Vel´asquez-Barreto, L. A. Bello-P´erez, H. Yee-Madeira, and C. E. Velezmoro S´anchez, “Esterification and characterization of starch from andean tubers,” Starch-St¨arke, vol. 71, no. 1-2, p. 1800101, 2019.

[10] A. Reyes, M. Yarlequ´e, W. Castro, and S. Chuquizuta, “Determination of dielectric properties of the red delicious apple and its correlation with quality parameters,” in 2017 Progress in Electromagnetics Research Symposium-Fall (PIERS-FALL). IEEE, 2017, pp. 2067–2072.

[11] M. Soltani and M. Omid, “Detection of poultry egg freshness by dielectric spectroscopy and machine learning techniques,” LWT-Food Science and Technology, vol. 62, no. 2, pp. 1034–1042, 2015.

[12] Z. Zhu, X. Zhu, F. Kong, and W. Guo, “A rapid method on identifying disqualified raw goat’s milk based on total bacterial count by using dielectric spectra,” Journal of Food Engineering, vol. 239, pp. 40–51, 2018.

[13] L. Shang, W. Guo, and S. O. Nelson, “Apple variety identification based on dielectric spectra and chemometric methods,” Food Analytical Methods, vol. 8, no. 4, pp. 1042–1052, 2015.

[14] G. W. G. K. Z. Xinhua, “Application of dielectric properties in identifying species of tomatoes and apples [j],” Transactions of the Chinese Society for Agricultural Machinery, vol. 8, 2006.

[15] K. G. Liakos, P. Busato, D. Moshou, S. Pearson, and D. Bochtis, “Machine learning in agriculture: A review,” Sensors, vol. 18, no. 8, p. 2674, 2018.

[16] T. Wuest, D. Weimer, C. Irgens, and K.-D. Thoben, “Machine learning in manufacturing: advantages, challenges, and applications,” Production & Manufacturing Research, vol. 4, no. 1, pp. 23–45, 2016.

[17] W. Zheng, X. Fu, and Y. Ying, "Spectroscopy-based food classification with extreme learning machine," Chemometrics and Intelligent Laboratory Systems, vol. 139, pp. 42–47, 2014.

[18] A. Noviyanto and W. H. Abdullah, "Honey dataset standard using hyperspectral imaging for machine learning problems," in 2017 25th European Signal Processing Conference (EUSIPCO). IEEE, 2017, pp. 473–477.

[19] E. Bona, I. Marquetti, J. V. Link, G. Y. F. Makimori, V. da Costa Arca, A. L. G. Lemes, J. M. G. Ferreira, M. B. dos Santos Scholz, P. Valderrama, and R. J. Poppi, "Support vector machines in tandem with infrared spectroscopy for geographical classification of green arabica coffee," LWT-Food Science and Technology, vol. 76, pp. 330–336, 2017.

[20] W. Guo, J. Gu, D. Liu, and L. Shang, "Peach variety identification using near-infrared diffuse reflectance spectroscopy," Computers and Electronics in Agriculture, vol. 123, pp. 297–303, 2016.

[21] W. Suphamitmongkol, G. Nie, R. Liu, S. Kasemsumran, and Y. Shi, "An alternative approach for the classification of orange varieties based on near infrared spectroscopy," Computers and electronics in agriculture, vol. 91, pp. 87–93, 2013.

[22] W. Castro, J. Oblitas, M. De-La-Torre, C. Cotrina, K. Baz´an, and H. Avila-George, "Classification of cape gooseberry fruit according to its level of ripeness using machine learning techniques and different color spaces," IEEE Access, vol. 7, pp. 27 389–27 400, 2019.

[23] H. You, Y. Kim, J. H. Lee, and S. Choi, "Classification of food powders using handheld nir spectrometer," in 2017 Ninth International Conference on Ubiquitous and Future Networks (ICUFN). IEEE, 2017, pp. 732–734.

[24] H. You, H. Kim, D.-K. Joo, S. M. Lee, J. Kim, and S. Choi, "Classification of food powders with open set using portable vis-nir spectrometer," in 2019 International Conference on Artificial Intelligence in Information and Communication (ICAIIC). IEEE, 2019, pp. 423–426.

[25] A. Kjær, G. Nielsen, S. Stærke, M. R. Clausen, M. Edelenbos, and B. Jørgensen, "Prediction of starch, soluble sugars and amino acids in potatoes (solanum

tuberosum l.) using hyperspectral imaging, dielectric and lf-nmr methodologies," Potato research, vol. 59, no. 4, pp. 357–374, 2016.

[26] A. y. K. "o. s. B. y. H. P. L. y. S. A. C. y. J. o. r. B. Nielsen, Glenn Gunner Brink y Kj ae r, "Espectroscopía diel´ectrica para evaluar el contenido de materia seca de los tubérculos de papa," Journal of Food Engineering.

[27] D. Liu and W. Guo, "Nondestructive determination of soluble solids content of persimmons by using dielectric spectroscopy," International journal of food properties, vol. 20, no. sup3, pp. S2596–S2611, 2017.

[28] A. Y. Khaled, S. Abd Aziz, S. K. Bejo, N. M. Nawi, I. A. Seman, and M. A. Izzuddin, "Development of classification models for basal stem rot (bsr) disease in oil palm using dielectric spectroscopy," Industrial Crops and Products, vol. 124, pp. 99–107, 2018.

[29] W. Castro, J. Oblitas, M. De-la Torre, C. Cotrina, K. Bazán, and H. Avila-George, "Using machine learning techniques and different color spaces for the classification of cape gooseberry (physalis peruviana l.) fruits according to ripeness level," PeerJ Preprints, vol. 7, p. e26691v2, 2019.

[30] W. Kuang and S. Nelson, "Low-frequency dielectric properties of biological tissues: a review with some new insights," 1998.

[31] S. Nelson, W. Forbus, and K. Lawrence, "Permittivities of fresh fruits and vegetables at 0.2 to 20 ghz," Journal of Microwave Power and Electromagnetic Energy, vol. 29, no. 2, pp. 81–93, 1994.

[32] L. Cuibus, M. Castro-Gir´aldez, P. Fito, and A. Fabbri, "Application of infrared thermography and dielectric spectroscopy for controlling freezing process of raw potato," Innovative Food Science & Emerging Technologies, vol. 24, pp. 80–87, 2014.

[33] J. Einfeldt, D. Meißner, and A. Kwasniewski, "Polymerdynamics of cellulose and other polysaccharides in solid state-secondary dielectric relaxation processes," Progress in Polymer Science, vol. 26, no. 9, pp. 1419–1472, 2001.

[34] L. Xie, Y. Ying, and T. Ying, “Classification of tomatoes with different genotypes by visible and short-wave near-infrared spectroscopy with least-squares support vector machines and other chemometrics,” Journal of food engineering, vol. 94, no. 1, pp. 34–39, 2009.

[35] Z. Wang, C. Zhao, L. Shang, F. Kong, and X. Weng, “Nondestructive testing of muskmelons varieties based on dielectric spectrum technology,” Transactions of the Chinese Society of Agricultural Engineering, vol. 33, no. 9, pp. 290–295, 2017.

[36] L. Pan, S. Pouyanfar, H. Chen, J. Qin, and S.-C. Chen, “Deepfood: Automatic multi-class classification of food ingredients using deep learning,” in 2017 IEEE 3rd international conference on collaboration and internet computing (CIC). IEEE, 2017, pp. 181–189.

[37] A. P. Bradley, “The use of the area under the roc curve in the evaluation of machine learning algorithms,” Pattern recognition, vol. 30, no. 7, pp. 1145–1159, 1997.

Application of Machine Learning in the Discrimination of Citrus Fruit Juices: Uses of Dielectric Spectroscopy


IEEE Xplore® Browse My Settings Help Institutional Sign In

All

ADVANCED SEARCH

Conferences > 2020 IEEE Engineering Interna...

Application of Machine Learning in the Discrimination of Citrus Fruit Juices: Uses of Dielectric Spectroscopy

Publisher: IEEE Cite This PDF

Tony Chuquizuta Trigoso ; Jimy Oblitas Cruz ; Hubert Arteaga Miñano ; Wilson Castro Silupu All Authors

Abstract:

Nowadays, process control in the juice industry requires fast, safe and easily applicable methods. In this regard, the use of dielectric spectroscopy is being coupled to statistical methods such as machine learning in order to develop new methods to identify adulteration. However, there is a small number of scientific reports above the application of the aforementioned methods when citric fruit juices is being identified. Therefore, the objective of this research was to evaluate dielectric spectroscopy and four different classification techniques (Support Vector Machine - SVM, K-nearest neighbor-KNN, Linear Discriminat -LD and Quadratic Discriminat-QD) to discriminate between three citrus juices. For this purpose, samples of Citrus limetta, Citrus limettioides and Citrus reticulata were evaluated; obtaining its dielectric spectral profiles in the range of 5 to 9 GHz. Then from the spectral profiles the loss factor (e") was calculated using the reflection coefficient. Next e" value was pretreated, reducing noise through a savitzky golay filter, and new variables created through Principal Component Analysis (PCA). Finally, the models for classification were constructed with the previously mentioned techniques and the principal components. The results shown that using four components the variance can be explained in 97%; likewise, the discrimination values vary between 88.9 and 100.0%, with SVM, LD and QD the best discrimination techniques all successfully at 100.0 %. Therefore; It is concluded that the technique of dielectric spectroscopy and machine learning presents potential for the discrimination of citrus fruit juices.

Published in: 2020 IEEE Engineering International Research Conference (EIRCON)

Date of Conference: 21-23 October 2020

DOI: 10.1109/EIRCON51178.2020.9253756

Date Added to IEEE *Xplore*: 17 November 2020

Publisher: IEEE

ISBN Information:

Conference Location: Lima, Peru

Congreso Internacional	DOI
Engineering International Research Conference (EIRCON)	**DOI: 10.1109/EIRCON51178.2020.9253756**

Das

APPLICATION OF MACHINE LEARNING IN THE DISCRIMINATION OF CITRUS FRUIT JUICES: USES OF DIELECTRIC SPECTROSCOPY

Tony Chuquizuta Trigoso[1]; Jimy Oblitas Cruz[2]; Hubert Arteaga Miñano[3]; Wilson Castro Silupu[4]

[1] Instituto de Investigación del Mejoramiento Productivo, Universidad Nacional Autónoma de Chota, Chota, Cajamarca, Perú

[2] Facultad de Ingeniería, Universidad Privada del Norte, Cajamarca, Perú

[3] Escuela Profesional de Ingeniería Agroindustrial, Universidad Nacional Autónoma de Chota, Chota, Cajamarca, Perú

[4] Facultad de Ingenieria de Industrias Alimentarias, Universidad Nacional de Frontera, Sullana, Perú

Abstract:

Nowadays, process control in the juice industry requires fast, safe and easily applicable methods. In this regard, the use of dielectric spectroscopy is being coupled to statistical methods such as machine learning in order to develop new methods to identify adulteration. However, there is a small number of scientific reports above the application of the aforementioned methods when citric fruit juices is being identified. Therefore, the objective of this research was to evaluate dielectric spectroscopy and four different classification techniques (Support Vector Machine - SVM, K-nearest neighbor-KNN, Linear Discriminat -LD and Quadratic Discriminat-QD) to discriminate between three citrus juices. For this purpose, samples of Citrus limetta, Citrus limettioides and Citrus reticulata were evaluated; obtaining its dielectric spectral profiles in the range of 5 to 9 GHz. Then from the spectral profiles the loss factor (e”) was calculated using the reflection coefficient. Next e” value was pretreated, reducing noise through a savitzky golay filter, and new variables created through Principal Component Analysis (PCA). Finally, the models for classification were constructed with the previously mentioned techniques and the principal components. The results shown that using four components the variance can be explained in 97%; likewise, the discrimination values vary between 88.9 and 100.0%, with SVM, LD and QD the best discrimination techniques all successfully at 100.0 %. Therefore; It is concluded that the technique of dielectric

spectroscopy and machine learning presents potential for the discrimination of citrus fruit juices.

Introduction

Fruit juice can be defined as extracted content from fruits or liquid content extracted from cells or tissues made when well ripened fruits are squeezed without using any solvent or heat, actually, this is one of the most important sectors in the food industry [1].

As fruit juice is a healthier option for the consumers, quality and security in the juice products is always an important topic; because they are always fraud objectives or possible adulterations, it is important to verify the juice origin and a complex job that goes beyond a simple measurement from some associated product properties [2]. Authenticity determination may be a complex job because of the variety of factors that may cause variations in an authentic food product [3].

For citrus fruit juices, the principal faking problems or wrong tagging is the full or partial substitution of the original juice for water or another lower cost juice [4]; in citrus fruits, tangerine juice (Citrus reticulata), lemon (Citrus limon) and/or pomelo (Citrus paradisi) has been detected as if it would be orange juice (Citrus sinensis) [5].

Also, the used technology for commercial bottled juices is another parameter to analyze in order to guarantee the authenticity of a citrus fruit juice. There are several studies that talk about this topic about juice authenticity using HPLC-MS (High performance liquid chromatography-mass spectrometry) [6] [7] or UHPLC/Q-TOF-MS (ultra-high performance liquid chromatography-quadrupole time-of-flight mass spectrometry) [8], that have evaluated the authenticity of these juices with the multivariate statistical analysis.

The mentioned techniques require part of the juice for the correspondant analysis, this means that those are destructive methods. In this context, the dielectric spectroscopy method is presented as an interesting method, that has been studied and applied in other products as pomegranate (Punica granatum L.) [9], apples (Malus domestica) [10], kiwi (Actinidia deliciosa) [11], melons (Cucumis melo L.) [12], among others. Knowing the juice electric properties and their relation with their structural and composition properties opens endless oportunities in the design and development of industry level equipments for quality control and processes through an adequate classification [13].

The main goal of this research was to assess the feasibility of a fast, simple and sensible method to distinguish different citrus fruit juices through the chemometric processing of the dielectric spectrometry data using the four classification models in the PCA multivariate analysis.

Materials and Methods

A. Citric Fruit Supplies

For the present investigation, 60 citrus fruits were used for each species of Citrus limetta, Citrus limettioides and Citrus reticulata, previously selected in good state of maturity, from the Paccha district in Chota, Cajamarca. The juice from the citrus fuits was obtained using an electric juicer extractor (FPSTJU4176, Oster), later, they were placed in 50 mL beakers.

B. Dielectric Spectrum Acquirement System

The used system to obtain the dielectric spectrums (dielectric properties), see Figure 1, consists in an open ended coaxial probe (N1501A-001), attached to a VNA (Vector Network Analyzer) (N9915A, Keysight Technologies), connected to a notebook (Legion Y520, Lenovo).

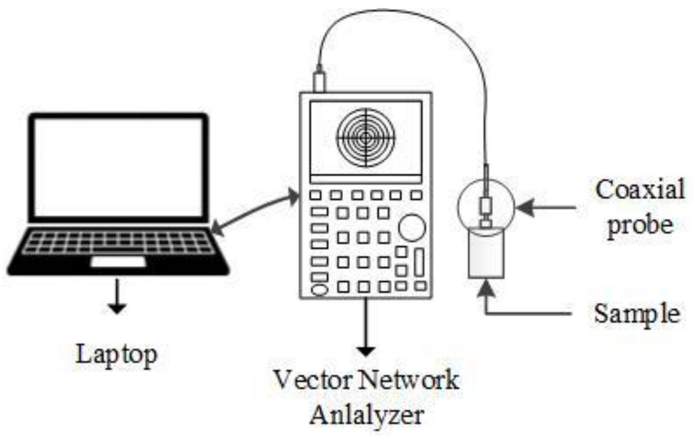

Fig. 1. Relative permittivity acquisition system for citrus

The dielectric properties were represented by the relative permittivity ($\varepsilon_r = \varepsilon' - j\varepsilon''$), were ε' is the dielectric constant and $\varepsilon''$is related to the losses, this about the real and imaginary part of ∊r, respectively. Before ε'' was obtained, the dielectric spectrum acquirement system was calibrated in air, short circuit and deionized water at 25 °C [14].

At last, ε'' was determined by obtaining the reflection coefficient between citrus juice samples with the submerged coaxial prob (5 cm), using the coaxial probe's software (N1500A-FG, Keysight Technologies), in the range 5 to 9 GHz (183 points).

C. Multivariate Analysis for Classification

The multivariate statistical analysis for classification was the non-supervised PCA technique using four different classification techniques (Support Vector Machine - SVM, K-nearest neighbor, Linear Discriminant - LD and Quadratic Discriminant- QD) using MATLAB 2018a software. Before PCA was applied, defects and anomalies present in dielectric spectrums were deleted through the proposed filtering method in [15].

Results and Discussion

The main goal from this research was to explore the possibility of using dielectric spectrometry to test the authenticity of the three kinds of juice taken from the citrus fruits used and develop qualitative tests to detect adulterated citrus juices.

A. Dielectric Spectrum for Citrus Juices

Mean values for the samples shown that loss factor (ε'') increase may be seen in the range from 5 to 9 GHz, see Figure 2. It could be due by the different content of polyphenol in each citrus fruit, concordant with they are made up mostly of flavanones, and also flavones and flavonols, this may generate dielectric relaxation because of concentration, the Maxwell-Wagner relaxation and other phenomena related with existing ions in these juices [16].

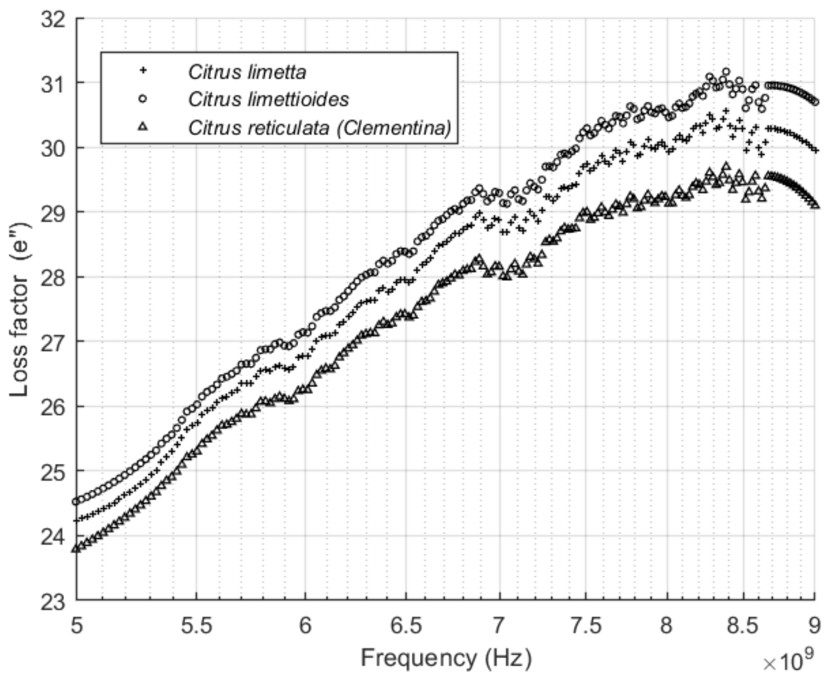

Fig. 2. Loss factor mean values vs frequency in samples

B. Classification Methods

In the data analysis, *PCA* was applied to look for any possible sample grouping for each kind of citrus fruit. The analysis was capable to distinguish them for each used model, the four principal components obtained variance values of 94.8 %, 0.8 %, 0.8 % and 0.6 % for PC1, PC2, PC3 and PC4 respectively. This evidences that variance may be explained in 97 % using four components. In this way to show the effect of first two PC in discrimination of samples the Figure 3 is shown.Developing the models accuracy values oscillate between 93.3 % and 100 % (Table I)

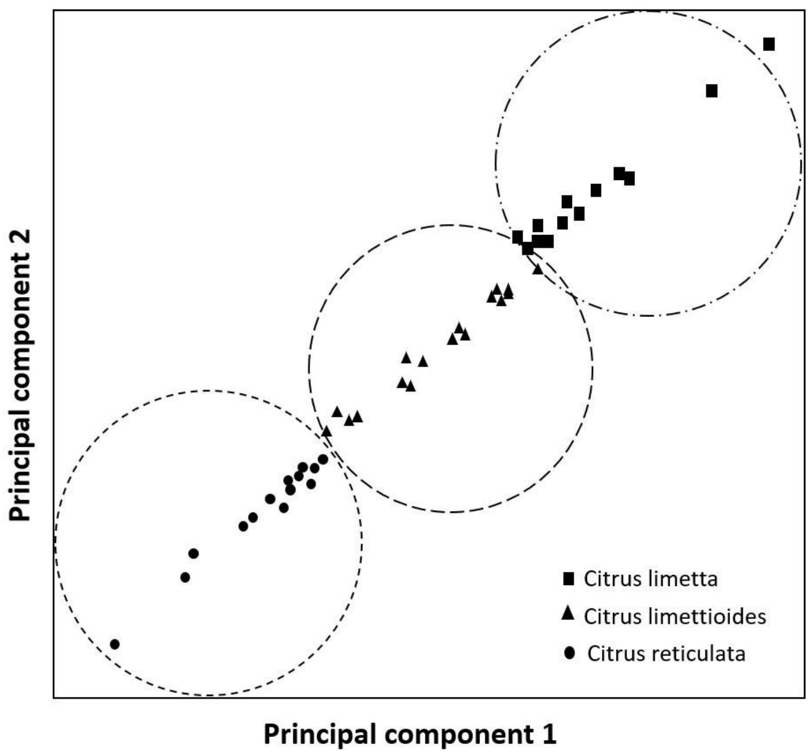

Fig. 3. Principal component

Table I Performance of the classification models for citrus juices.

Technique	Accuracy (%)
Support vecto machine - Linear	100.0
k-nearest neighbor - Fine	93.3
Linear Discriminat	100.0
Quadatic Discriminat	100.0

In our case PCA technique shown feasibility to be used, creating new variables from the initial data, coupled to dielectric spectra. Another examples of its use are the works of Zhu [17] with peach and Khaled [18] and oils properties evaluation which shown similar results. Other dielectric properties studies as the ones developed on apple classification reached an average accuracy of 99.5 % and 99 %.

It is seen that dielectric spectrometry may be used as a simple method, at low-cost and non-destructive for the citrus juice classification, this may ease the adoption of QA (quality assurance) in production line inside of the juice processing industry, because it may be attached to a real time system, it is low-cost and because of its ease of use [19], also it is seen that the obtained data has results of extensive data blocks that require suitable numerical strategies in order to obtain an adequate classification as the used in this research, furthermore it is noted that advanced chemometrics models should be developed to analyze the obtained data [20].

Conclusion

The dielectric spectroscopy analysis in citrus fruit juices with multivariate modeling shows its potential to be used as a fast classification technique to guarantee the authenticity of this kind of juices. This method is simple to apply and does not require sophisticated instrumentation; also the data is analyzed with simple classification systems, this shows that this method may be applied for an analysis in citrus fruit industry or in fast processes in order to detect frauds on fake juice replacements.

ACKNOWLEDGMENT

The authors would like to thank Universidad Nacional Autónoma de Chota for funding with mining CANON funds the excecution of the research project called “Desarrollo de un sistema no destructivo para la determinación de las propiedades físicoquímicas en frutas nativas y derivados de la región Cajamarca, usando espectroscopía dieléctrica” approved with resolution N°432-2018-C.O./UNACH.

REFERENCES

[1] G. Rajauria and B. K. Tiwari, “Chapter 1- Fruit Juices: An Overview,” in Fruit Juices (G. Rajauria and B. K. Tiwari, eds.), pp. 3–13, San Diego: Academic Press, Jan. 2018.

[2] M. M. Aung and Y. S. Chang, “Traceability in a food supply chain: Safety and quality perspectives,” Food Control, vol. 39, pp. 172–184, May 2014.

[3] Z. Jandri´c and A. Cannavan, “An investigative study on differentiation of citrus fruit/fruit juices by UPLC-QToF MS and chemometrics,” Food Control, vol. 72, pp. 173–180, Feb. 2017. [4] J. C. Moore, J. Spink, and M. Lipp, “Development and

application of a database of food ingredient fraud and economically motivated adulteration from 1980 to 2010," Journal of Food Science, vol. 77, pp. R118–126, Apr. 2012

[5] E. Muntean, "Simultaneous Carbohydrate Chromatography and Unsuppressed Ion Chromatography in Detecting Fruit Juices Adulteration," Chromatographia, vol. 71, pp. 69–74, June 2010.

[6] L. Vaclavik, A. Schreiber, O. Lacina, T. Cajka, and J. Hajslova, "Liquid chromatography–mass spectrometry-based metabolomics for authenticity assessment of fruit juices," Metabolomics, vol. 8, pp. 793–803, Oct. 2012.

[7] S. Ehling and S. Cole, "Analysis of Organic Acids in Fruit Juices by Liquid ChromatographyMass Spectrometry: An Enhanced Tool for Authenticity Testing," Journal of Agricultural and Food Chemistry, vol. 59, pp. 2229–2234, Mar. 2011. Publisher: American Chemical Society.

[8] Z. Jandri´c, D. Roberts, M. N. Rathor, A. Abrahim, M. Islam, and A. Cannavan, "Assessment of fruit juice authenticity using UPLC-QToF MS: a metabolomics approach," Food Chemistry, vol. 148, pp. 7–17, Apr. 2014.

[9] M. Castro-Gir´ aldez, P. J. Fito, M. D. Ortol´ a, and N. Balaguer, "Study of pomegranate ripening by dielectric spectroscopy," Postharvest Biology and Technology, vol. 86, pp. 346–353, Dec. 2013.

[10] M. Castro-Gir´aldez, P. J. Fito, C. Chenoll, and P. Fito, "Development of a Dielectric Spectroscopy Technique for Determining Key Chemical Components of Apple Maturity," Journal of Agricultural and Food Chemistry, vol. 58, pp. 3761–3766, Mar. 2010. Publisher: American Chemical Society.

[11] A. Fazayeli, S. Kamgar, S. M. Nassiri, H. Fazayeli, and M. D. L. Guardia, "Dielectric spectroscopy as a potential technique for prediction of kiwifruit quality indices during storage," Information Processing in Agriculture, vol. 6, pp. 479–486, Dec. 2019. Publisher: Elsevier BV.

[12] W.-c. Guo, S. O. Nelson, S. Trabelsi, and J. K. Stanley, "Dielectric Properties of Honeydew Melons and Correlation with Quality," Journal of Microwave Power and

Electromagnetic Energy, vol. 41, pp. 44–54, Jan. 2006. Publisher: Taylor & Francis eprint: https://doi.org/10.1080/08327823.2006.11688556.

[13] M. V. Traffano-Schiffo, M. Castro-Giraldez, R. J. Colom, and P. J. Fito, "New Spectrophotometric System to Segregate Tissues in Mandarin Fruit," Food and Bioprocess Technology, vol. 11, pp. 399–406, Feb. 2018.

[14] D. Liu and W. Guo, "Nondestructive determination of soluble solids content of persimmons by using dielectric spectroscopy," International Journal of Food Properties, vol. 20, pp. S2596–S2611, Dec. 2017. Publisher: Taylor & Francis eprint: https://doi.org/10.1080/10942912.2017.1381114.

[15] W. Castro, J. Oblitas, J. Maicelo, and H. Avila-George, "Evaluation of Expert Systems Techniques for Classifying Different Stages of Coffee Rust Infection in Hyperspectral Images," International Journal of Computational Intelligence Systems, vol. 11, pp. 86–100, Jan. 2018. Publisher: Atlantis Press.

[16] S. O. Nelson, W.-c. Guo, S. Trabelsi, and S. J. Kays, "Dielectric spectroscopy of watermelons for quality sensing," Measurement Science and Technology, vol. 18, pp. 1887–1892, May 2007. Publisher: IOP Publishing.

[17] X. Zhu, L. Fang, J. Gu, and W. Guo, "Feasibility Investigation on Determining Soluble Solids Content of Peaches Using Dielectric Spectra," Food Analytical Methods, vol. 6, no. 9, pp. 1789–1798, 2016.

[18] A. Y. Khaled, S. Abd Aziz, S. Khairunniza Bejo, N. Mat Nawi, I. Abu Seman, and M. A. Izzuddin, "Development of classification models for basal stem rot (BSR) disease in oil palm using dielectric spectroscopy," Industrial Crops and Products, vol. 124, pp. 99–107, Nov. 2018.

[19] B. Panikuttira and C. P. O'Donnell, "Chapter 40- Process Analytical Technology for the Fruit Juice Industry," in Fruit Juices (G. Rajauria and B. K. Tiwari, eds.), pp. 835–847, San Diego: Academic Press, Jan. 2018.

[20] P. J. Cullen, C. P. O'Donnell, and C. C. Fagan, "Benefits and Challenges of Adopting PAT for the Food Industry," in Process Analytical Technology for the Food Industry (C. P. O'Donnell, C. Fagan, and P. Cullen, eds.), serie de, Food Engineering Series, pp. 1–5, New York, NY: Springer, 2014.

Presentación de poster

" MONITORING SYSTEM OF GOLDEN BERRY DRYING USING INFRARED THERMOGRAPHY "

Valencia, 27 de abril de 2023

Chuquizuta-Trigoso, T.S. [a,b]*; Castro-Giraldez, M. [a]; Castro, W.[c]; Fito, P.J. [a]

[a] Instituto Universitario de Ingenieria de Alimentos para el Desarrollo, Universidad Politécnica de Valencia, Camino de Vera s/n, 46022 Valencia, España

[b] Instituto de Investigación del Mejoramiento Productivo, Universidad Nacional Autónoma de Chota, Chota, Perú

[c] Facultad de Ingeniería de Industrias Alimentarias, Universidad Nacional de Frontera, Sullana 20100, Peru.

*steven_ct_20@hotmail.com

UNIVERSITAT POLITÈCNICA DE VALÈNCIA · CSIC CONSEJO SUPERIOR DE INVESTIGACIONES CIENTÍFICAS · ivia instituto valenciano de investigaciones agrarias

Introduction

At present, high Andean berries such as "aguaymanto – golden berry" have a high demand in foreign markets due to their nutritional contribution and bioactive compounds that contribute to the diet of consumers. However, the golden berry is a perishable fruit due to its high water level (78-84%), making it susceptible to fungal and bacterial attacks. For this reason, the application of dehydration processes is necessary to prolong its useful life and preserve its physicochemical properties.

During dehydration, physical phenomena of mass and heat transfer originate, such as the displacement of water from the center to the surface of the fruit (differential chemical potential of water) and the emission of heat by radiation, respectively. However, there are limited studies that allow relating these phenomena through non-invasive technologies in exotics fruits like the golden berry.

The infrared thermography technique is based on measuring the infrared radiation emitted by a surface (solid), as well as it can provide important information on heat transfer in biological systems. For this reason, the objective of the present investigation is the monitoring of golden berry drying by means of infrared thermography.

Materials and Methods

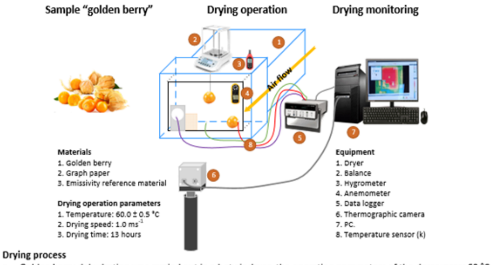

Drying process

- Golden berry dehydration was carried out in a hot air dryer, the operation parameters of the dryer were: 60 °C, 1 m/s and 13 hours. Previously, a golden berry was suspended with a nylon thread to a precision balance; A material with known emissivity (0.95 - reference) and a graph paper were placed next to the suspended golden berry, in addition to recording the surface temperature of a second golden berry. During drying, the mass (scale), volume (digital camera) and surface temperature (thermocouple K, connected to a 34901A multiplexer and recording the digital data using an Agilent data acquisition equipment 34972A) of the golden berry were recorded every 10 minutes for the first two hours, then every 30 min until 13 hours. Likewise, in parallel, the surface temperature emitted by the golden gooseberry and the reference material was recorded using a thermographic camera (Optris GmBh, Germany).

Measurements

- Moisture: Drying at 65 °C per 48 hours until mass constant.
- Water activity: Hygrometer (Aqualab CX-2)
- Volume: Image analysis was applied to calculate the volume using the ImageJ software

Results and discussion

KINETICS AND THERMODYNAMIC PROPERTIES

It has been possible to reduce the mass and volume of the golden berry up to 73 and 67 % respectively, during 13 hours of dehydration (Fig. 1-a). Likewise, a classic drying curve has been observed, with its three stages: induction period (I), constant speed period (II) and decreasing speed period (III). In the same way, the transport of water from the interior to the surface is less than the rate of evaporation of surface water and therefore changes in the structure of the vegetative tissue must originate.

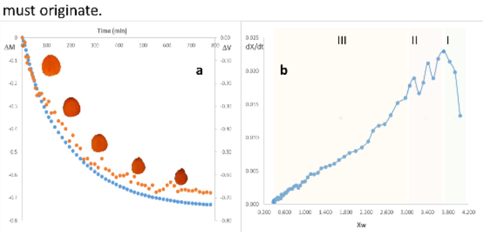

Fig. 1.a). Variation of mass and volume during dehydration of golden gooseberry. **b).** Drying speed.

To understand the variation in water transport during the drying of the golden berry, it is necessary to estimate the water flux. Previously, starting from a thermodynamic approach such as the variation of the Gibbs free energy.

$$dG = -SdT + VdP + Fdl + \psi de + \sum_i \mu_i dn_i$$

If we express the variation of the Gibbs free energy per mole of water, then we can define the extended chemical potential of water

$$\Delta\mu_w = \frac{\Delta G}{\Delta n_w}$$

To determine the existence of a relationship between the molar flow and the chemical potential, as a transporter of water through the first Onsager relationship: . $J_w = L_w \cdot \Delta\mu_w$. To determine the chemical potential without any effect of mechanical terms, the equation is used:

$$\Delta\mu_w^* = -s_w \Delta T + RTln\frac{\varphi^{air}}{a_w^{surf}}$$

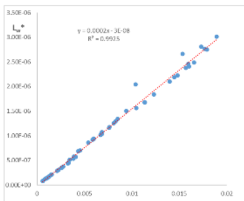

Fig. 2. Phenomenological coefficient (L_w^*) with regard to water flux (J_w).

Therefore, we can obtain the phenomenological coefficient: $L_w^* = \frac{J_w}{\Delta\mu_w^*}$

INFRARED TERMOGRAPHY: EMISSIVITY AND TEMPERATURE

It was possible to obtain the surface temperature of the golden gooseberry by means of a thermographic camera (pyroelectric sensor). However, the energy emitted by the golden gooseberry must be calculated through an energy flow balance, in order to subtract the intervention of the environment and the absorption of energy by the air.

$$E_T = F_{samp}\sigma T_{samp}^4 + (1-\varepsilon_{surr})\sigma T_{surr}^4 - (1-\tau_{air})F.\varepsilon_{samp}\sigma T_{samp}^4$$

To obtain the net emissivity of the golden gooseberry, it is necessary to determine the energy emitted by the environment, for which a reference material of known emissivity was used (Fig. 3).

$$E_T^{ref} = 0.95 \cdot \sigma \cdot T_{ref}^4 + E_{surr}$$

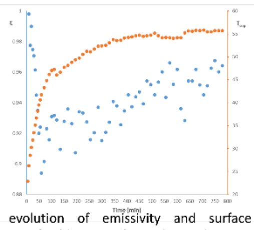

Fig. 3. evolution of emissivity and surface temperature of golden gooseberry during drying.

Conclusions

- A thermodynamic model has been developed that allows to efficiently observe the changes of the phenomenological coefficient in relation to the flow of water during the dehydration process of the golden berry.
- It has been shown that the thermographic camera is a promising tool for monitoring the golden gooseberry drying process, which provides valuable information on heat transfer in a tissue of plant origin, allowing to observe the evolution of emissivity and surface temperature.

UNIVERSITAT
POLITÈCNICA
DE VALÈNCIA

2025